Durham University
Department of Earth Sciences

The Nature, Consequences and Controls of Deformation During Superimposed Rifting: the Inner Moray Firth Basin

Alexandra Tămaș

Supervisors: Prof. Robert E. Holdsworth, Prof. John R. Underhill, Dr. Edward D. Dempsey, Dr. Dave McCarthy, Prof. Ken J.W. McCaffrey, Prof. David Selby

A thesis submitted to Durham University in partial fulfilment of the requirements for the degree of
Doctor of Philosophy

Department of Earth Sciences, Durham University (UK)
January 2022

Declaration

No part of this thesis has previously been submitted for a degree at this university or any other.
The work described in this thesis is entirely that of the author, except where reference is made to previously published or unpublished work.

Alexandra Tamas
University of Durham
Department of Earth Sciences
January 2022

Statement of Copyright

Funding

The PhD study was undertaken as part of the Natural Environment Research Council (NERC) Centre for Doctoral Training (CDT) in Oil and Gas [grant number NEM00578X/1] and was funded by Durham University and British Geological Survey (BGS) via the British University Funding Initiative (BUFI), whose support is gratefully acknowledged.

Acknowledgements

Dan, my lovely husband, your love, care and support are invaluable, and I cannot thank you enough for encouraging me to do a PhD in the first place and supporting me along the way, including being my field assistant. Sorry we had to leave your drone parked up the cliff at Shandwick, I promise I'll get it back at some point! Thanks for taking over all the responsibilities at home so I could focus on writing up and submitting on time.

Csaba, thank you for making me to love my job, thank you for being such an inspirational boss, and nonetheless, thank you for assigning me to a structural geology project and trusting I can handle such a project, although my initial knowledge in structural geology was so 'good' I had to google how to construct a cross-section… But this leads me to you, Zsolt. Thank you for being my mentor. Thanks for lighting the structural geology spark in me. Your enthusiasm and patience to make me a structural geologist led me to this point. Also, thanks for warning me that I will cry 'several times' during this PhD journey…I did (especially writing this part of the thesis).

Alex L., thanks for paving the way for me, it was fun to chase you from Cluj uni to Petrom and then to Durham uni.

Thanks to all the other amazing people I shared my time with at OMV Petrom, before coming to Durham, especially to Domnu' Olaru, Ale O., Andreea, Anca, Vali, Eve, Roxana, Alex S., Lenuta, Marian, Lorena, Emilia, Flori, Gabi.

Alex S… it wasn't in the Carpathians, as you expected, but I've done it, as you've always encouraged me. I wish you were here to see it done…

Thanks to all my PhD supervisors, especially to you, Bob, for giving me this opportunity which definitely pushed me way out of my comfort zone. Thanks for your very prompt and straightforward feedback, which really helped me structure and support my ideas. I've learned a lot from you, especially in the field, and I'm grateful for that. Thank you also for giving me the necessary trust to feel independent but letting me know you are there to help.

John, I'm really grateful I had the chance to work with you and have so many good discussions. Thanks for giving me the opportunity to come to Edinburgh and do part of my PhD at Heriot-Watt University.

Dave M., you've said that you probably can't contribute much to my PhD being at the very end of my supervisors' list, you couldn't have been more wrong. I'm very grateful for all your scientific contribution, but what I'm even more grateful for is for always making sure I was ok, for taking me out for drinks, walks, dinners and all the support and encouragements. Thanks for joining your two *favourite* PhD students for the traditional Whiskey Wednesdays, which I'm always looking forward to.

Thanks to all my other supervisors: Ken, Eddie and Dave S., for providing the necessary support to get to this point.

Special thanks to Lorna Morrow and Anna Clark for all the support during the NERC CDT trainings and during my time in Edinburgh.

Thanks to Jon Gluyas and Christine Pierce for being on my annual review panel and always making the discussions very enjoyable. Thanks for all your feedback and comments and your kind and encouraging words.

Many thanks to Jon Gluyas and Chris Jackson for the good discussions during my viva and the valuable feedback which improved my thesis.

I would also like to thank Catherine Mottram, Graham Leslie, John MacDonald, Billy J Andrews, Craig Magee, Nick Roberts and one anonymous reviewer who provided so many valuable comments on the submitted manuscripts, which ultimately led to better PhD chapters.

Alan…as usual, I can't thank you enough for being the friend I wish anyone to be that lucky to have in their life. It looks like we needed a pandemic to invent a word to better describe what you've also been for me

through all these years (and still are) - my support bubble. Thanks for all the amazing unicycling adventures, long walks, coffee, chess, juggling and also for listening to me rattle about all the struggles, frustrations, plans and dreams… Also, thanks to Carolyn for all the 'rescues', kind words, and emergency pictures with Henry to boost my mood.

Thanks to all the other friends I met through Durham City Jugglers and JUST, thanks for adopting me and bringing that much joy into my life, especially to you, John, for inviting me to spend Christmas with you when I couldn't make it home in the first year of my PhD. Roger, for your contagious positive energy that can brighten up someone's day instantly, and nonetheless, for helping me with the parcels and saving my plant! Lovely Tony, your warmth and care were and are so much needed. Thanks for checking up on me and for and the hugs and love I'm lucky to get from you. Calum, thanks for joining me for rides in Edinburgh and for all your support. Paul, Francis, Leyna, I'm grateful we got the chance to share so many great memories juggling and unicycling.

Sam, it was so great to share the office with you in Edinburgh. I had so much fun going for our lunchtime unicycling/running races in the campus, backpacking, or just chatting about anything and everything. Thanks for providing chocolate and ibuprofen when my ankle was the size of a watermelon, and I couldn't get out of the house.

Roxana, we intersected so many times randomly. We shared a mentor at OMV Petrom, a PhD supervisor, a house in Edinburgh, I think that becoming friends was unavoidable. I'm so grateful to have you. Thanks for always encouraging, supporting, and celebrating with me.

Adi, thanks for Mishu, the best PhD support companion one can have.

I would also like to thank to all my friends I've met in the Earth Sciences Department at Durham. Jack, for sharing my love for coffee and always being there when coffee is needed (especially during the CDT training). Pierce, for allowing me to become his favourite Transylvanian vampire, even if we don't support the same F1 team. Zach, for all the nice memories generally involving cakes, tea, and Kermit. Sweet Aimeé, for her inspiring constant positive attitude. I couldn't be more grateful for the time we spent together. I'm also grateful to Simon for our Saturday walks that were

always something to look forward to, and also for visiting me in Edinburgh. Nico, for all the morning hugs, which were definitely one of my favourite routines. Ilaria, for all the dinners, coffees, walks and just being such a good friend. Guillaume, for always putting a smile on my face with his dry humour, embarrassing direct questions and statements. Nuno, for all the meaningful conversations we had during our morning coffee. Dimitrios, for delicious Greek food, chocolate and accompanying me for long walks. Marie-Anne, for joining me hiking, camping, slacklining, and bringing Dodue for cuddles. Naeema, for always being so caring and thoughtful.

Thanks to Pavlos, Nikos, Max, Laura, Sean, Emma, Tim, Sarah, Miles, Eloise, Kate, Bob E., Ariane, Stella, CJ, Tom, Chris, Kit, Telemaco and all my other friends and colleagues in the department for all the necessary coffee breaks, chats, happy hour, and fun nights out.

Many thanks to all the admin staff, especially Jo Banner and Paula Elliot, for helping me figure out all the paperwork I needed for enrolling, fieldwork or training. Ian Chaplin and Sophie Edwards are thanked for the thin-section preparation.

I'm also grateful to Mirela Popa, the person responsible for my love for research, and to Sorin Filipescu. About ten years ago, I almost started a PhD in palaeontology under the supervision of you both, but things went into a different direction. However, your guidance and support didn't stop to this day, and I couldn't be more grateful for that.

Nonetheless, thanks to my loving parents (mulțumesc că mă susțineți în tot ceea ce fac și sunt), my brother, sister-in-law and nephew, grandparents and parents in low for their constant support of all my crazy decisions. Radu, Clau și Tudor mulțumesc și pentru toate întrebările (grele) despre doctorat și geologie. Mama Nuți și Tata Nelu, mulțumesc că sunteți bunici atât pentru Dan cât și pentru mine, abia aștept să răspund cu 'da' la întrebarea 'ai gătat'?

Abstract

The Inner Moray Firth Basin (IMFB) is a superimposed sedimentary basin that experienced a complex structural history with many deformation episodes of regionally or local extent. Strictly, the IMFB rift forms the western arm of the North Sea trilete rift system that initiated mainly during the Late Jurassic-Early Cretaceous, with the widespread development of major NE-SW-trending faults. However, the basin overlies older Caledonian basement, the pre-existing Devonian-Carboniferous Orcadian Basin, and part of a regionally developed Permo-Triassic basin system in the wider North Sea region. The IMFB also experienced later episodes of uplift and fault reactivation during the Cenozoic. The resulting superimposed structures can be challenging to separate and characterise.

This study uses detailed field observations of key onshore outcrops across the entire IMFB, coupled with U-Pb dating of syn-faulting calcite-mineralised veins to constrain the absolute timing of faulting events. These findings are then integrated with the offshore interpretation of 2D and selected 3D seismic reflection data to constrain the absolute timing of fault populations and decipher the kinematic history of the superimposed basin development.

This holistic approach allows up to six deformation events to be identified and characterised regionally: Devonian rifting associated with the older Orcadian Basin; Variscan inversion and regional uplift/exhumation; Permo-Triassic thermal subsidence with evidence of only minor fracturing (e.g. no clear evidence for rift-related faulting at this time); Upper Jurassic – Lower Cretaceous rifting; possible Upper Cretaceous rifting, and Cenozoic strike-slip-dominated faulting and reactivation of older syn-rift faults.

Table of Contents

Chapter 1

Introduction

1.1 Project motivation, aims and objectives

Superimposed basins are formed due to vertical juxtaposition or overlapping of different regional sedimentary basins which leads to overprinting tectonic processes and the development of complex multistage structures. Isolating and characterising different deformation events in such basins is often difficult to constrain. Regional subsurface data can give valuable insights into the relative timing of faulting. However, observations here are inevitably limited by the scale resolution of seismic reflection datasets. Also, fault kinematics can be difficult to ascertain in three dimensions so that oblique- or strike-slip faults may not be recognised unambiguously. In outcrops, these aspects are well preserved. However, limitations arise here due to restricted exposure, complex kinematic histories leading to multiple fault networks that can co-exist at the exposed stratigraphic level, which can be challenging to separate. In many cases, however, the deformation episodes may be associated with diagnostic syn-tectonic mineral fills (e.g. calcite, zeolite or base metal sulphides). Some of these can be dated using radiometric methods to constrain the absolute timing (e.g. calcite - U-Pb, Roberts et al. 2020a; sulphides - Re-Os, Dichiarante et al. 2016).

The Inner Moray Firth Basin (IMFB) is located on the North-Eastern coast of Scotland (Fig. 1.1) and is part of the larger Moray Firth Basin which lies on the western side of the Permian to Recent North Sea Basin. The IMFB is a superimposed basin overlying rocks of the Caledonian basement, the pre-existing Devonian-Carboniferous Orcadian Basin and a regionally developed Permo-Triassic basin system. Prior to this project, the IMFB was

generally thought to have opened during Permo-Triassic and Late Jurassic-Early Cretaceous rifting episodes (e.g. McQuillin et al. 1982; Underhill 1991a; Thomson and Underhill 1993). Subsequently, the area supposedly experienced inversion events associated with important episodes of Late Cretaceous to Cenozoic regional uplift and faulting (e.g. Underhill 1991a; Thomson and Underhill 1993; Le Breton et al. 2013). These events are thought to have involved localised fault reactivation, including dextral

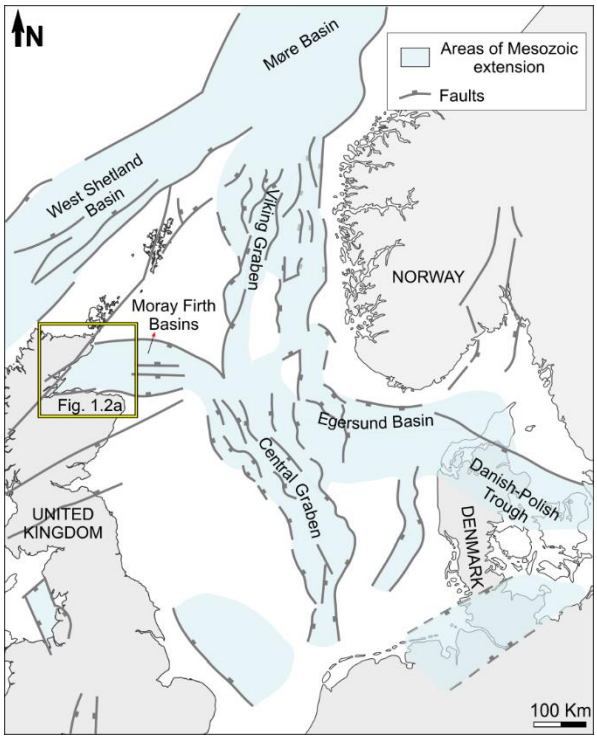

Fig. 1. 1: Generalised tectonic map of northwest Europe showing the main Mesozoic rift systems (adapted after Goldsmith et al. 2003). The yellow box shows the location of the map in Fig. 1.2a.

reactivation of the Great Glen and sinistral reactivation of the Helmsdale faults (north-western major boundary faults; e.g. Underhill 1991a; Thomson and Underhill 1993; Le Breton et al. 2013).

In the IMFB, the majority of available structural models rely on either exclusively subsurface data (e.g. McQuillin et al. 1982; Roberts et al. 1990; Davies et al. 2001) or sparse outcrop data (e.g. Pickering 1984). Little

research has attempted to integrate onshore data across the IMFB with offshore data (e.g. Thomson and Underhill 1993; Underhill and Brodie 1993; Roberts and Holdsworth 1999). Moreover, no absolute dating study of the syn-tectonic mineral fills has been carried out so far, so many of the deformation events recognised onshore are just assumed based of general geological constraints, e.g. trend, cross-cutting relationships, etc.

This situation has led to many uncertainties or contrasting models regarding the absolute and relative timing or kinematics of the basin development.

For example, some authors have considered the Permo-Triassic history to be characterised by active rifting (e.g. Frostick et al. 1988; Roberts et al. 1989), while others suggest that the Permo-Triassic history was marked by thermal subsidence (Andrews et al. 1990; Thomson and Underhill 1993). The kinematic opening of the basin during the Late Jurassic – Early Cretaceous has also been a matter of debate. Roberts et al. (1990) and other authors (e.g. McQuillin et al. 1982; Bird et al. 1987) favoured a transtensional origin for the IMFB, controlled by the dextral strike-slip movements of the Great Glen Fault. Underhill (1991a) challenged the transtensional model and proposed a new extensional model for the evolution of the IMFB. This model was reinforced by subsequent studies which support the predominance of orthogonal rifting and suggest there is little evidence of oblique-slip faulting in the basin (e.g. Davies et al. 2001; Long and Imber 2010; Lapadat et al. 2016). Relatively little is known about the cessation of rifting within the Early Cretaceous. Suggestions range from Berriasian (e.g. Underhill 1991a and b;

Davies et al. 2001), Hauterivian (Roberts et al. 1990; Argent et al. 2002), and even up to Albian (Andrews et al. 1990).

Moreover, the post-rift events that led to the reactivation of Helmsdale and Great Glen faults, traditionally viewed as Cenozoic, are assumed based on indirect evince and correlation with regional events (e.g. Le Breton et al. 2013). Very little is known about the occurrence and nature of Cenozoic faulting and fault reactivation away from these main faults (e.g. along the south coast of IMFB).

The potential influence of older rift-related faults on the kinematics of later Mesozoic basin development has been a matter of speculation. Based on offshore data, it has been suggested that Orcadian Basin structures may have been reactivated in the IMFB (e.g. Norton et al.1987; Coward et al. 1989), but little compelling evidence for this inheritance has yet emerged, and its potential importance remains uncertain.

The main goal of this project is to give new insights into the kinematics, timing and structural controls of the superimposed basin development by providing an outcrop to regional-scale structural model. Additionally, I aim to identify and characterise individual deformation events in areas affected by subsequent deformation. Likewise, I explore how the earlier-formed Orcadian Basin structures may localise deformation and interact during subsequent (Mesozoic and Cenozoic) basin development.

This was achieved by:

- Detailed field mapping of key exposures located along both coasts of the IMFB, augmented with low-level aerial photogrammetry. This provided a

high-resolution characterisation of structural geometries around key basin-bounding faults.

- Collecting samples of fault rocks and fracture fills for microscopy and U-Pb dating of syn-kinematic calcite mineralisation. These were used to place absolute age constraints on the timing of fault movements, which are critical to understanding the timing of brittle deformation and better constrain the basin development.

- Performing offshore seismic interpretation to understand the regional-scale context and timing of basin development and compare the faulting patterns with the outcrop-scale structures.

- Integrating the findings to develop conceptual models and explain the kinematic patterns and deformation histories, including the absolute timing of faulting, the role of reactivation and oblique tectonics.

Apart from the new outcrop- to basin-scale structural study of this complex superimposed rift basin, this integrated multiscale study has important potential application in other superimposed rift basin settings worldwide, and also in areas of regionally contemporaneous onshore-offshore basin development. This can provide a structural template for the subsurface areas where seismic resolution is limited and can be used to better develop the region as a training ground for subsurface geoscience teams worldwide.

1.2 Thesis Outline

The thesis is divided into ***six chapters*** which deal with key aspects of the project as follows:

Chapter 1 - Introduction

Provides information about the scope of the project, the scientific questions, and the regional geological setting of the study area prior to this work. The regional geological setting is not exhaustive and aims to provide a general overview of the study area. Additional relevant stratigraphic (e.g. detailed descriptions of lithostratigraphic units with formation names onshore and offshore) or structural details (e.g. fault characterisation at sub-basin or outcrop scale) are given in appropriate chapters to support the results.

Chapter 2 - Dataset and Methodology

In this chapter, the datasets available for this study, the multiple methods and the software used are detailed.

Chapters 3 to 5 are the results chapters. They are generally self-standing and are either published papers or prepared as manuscripts for publishing. This means they have their own scientific question, introduction, results, discussions, and conclusions sections. However, the chapters are adjusted to link with one other. Chapter 3 and 4 present the deformation events by combining onshore fieldwork along the **southern coast** of IMFB, with geochronology results (Chapter 3) or with **offshore seismic interpretation** (Chapter 4), while Chapter 5 presents a detailed study of multiple exposures along the **north-western coast** of IMFB coupled with geochronology results.

To avoid repeating information, the general geological overview and the methods section is simplified here and the reader is advised to consult the dedicated chapters for more information.

Chapter 3 - Devonian kinematic history of the Inner Moray Firth Basin and the role of the inherited faults in later stages of basin development: the Turriff Sub-basin.

This chapter provides new information concerning the earlier kinematic history of the basin and offers better constraints on the influence and timing of fault reactivation. It is based on the results of the onshore fieldwork carried out along the south coast of the IMFB and describes the faulting and associated structures cross-cutting Devonian sedimentary units associated with the Turriff Sub-basin.

Chapter 4 - Integrating onshore fieldwork with offshore interpretation of seismic profiles to decipher the Permo-Triassic to Cenozoic history of the Inner Moray Firth Basin: the Lossiemouth Fault Zone

This chapter presents a detailed structural study of the Permo-Triassic-age exposures along the southern coast of IMFB. This is coupled with the offshore interpretation of seismic 2D and 3D datasets, and structural validation techniques to decipher the Permo-Triassic development of the IMFB and subsequent Late Jurassic to Early Cretaceous and Cenozoic deformation events.

Chapter 5 - Combining geochronology and high-resolution photogrammetry to analyse the structural evolution of a superimposed basin: the northern margin of the Inner Moray Firth Basin, Scotland

The north-western margin of the IMFB is strongly controlled by major long-lived basin-boundary faults including the Great Glen and Helmsdale fault zones. Hence, the onshore exposures preserve a wide variety of fault orientations and structures.

In this chapter, new structural fieldwork augmented with drone photography and U-Pb geochronological evidence is used to constrain the absolute timing of fault populations and to decipher the kinematic history of the basin.

Chapter 6 - Summary, Conclusions and Way Forward

In this chapter, the main findings of the thesis are compiled and are summarised. It also outlines the progress made by this study and the areas for future work.

References

A single set of references is used for the whole thesis rather than at the end of each chapter to avoid repetition.

Supplementary Files

Supplementary material to all chapters are compiled here. It mostly contains the geochronology data (as provided by Hull or BGS laboratory), 3D PDFs of the studied outcrops and uninterpreted seismic profiles, maps or outcrops. The uninterpreted images (e.g seismic profiles) which are provided are annotated the same as the interpreted figure + ‘S’ (e.g. uninterpreted version of Fig. 1b will be Fig. 1bS).

1.3 The Inner Moray Firth Basin: Geological Overview

1.3.1 Introduction

The IMFB is bounded by the Banff Fault to the south, the Helmsdale and Great Glen (GGF) faults to the northwest and by the Wick fault to the north (Fig. 1.2a). The IMFB transitions eastwards into the Outer Moray Firth Basin, which links into the Central and Viking grabens in the central part of the North Sea. (Fig. 1.1).

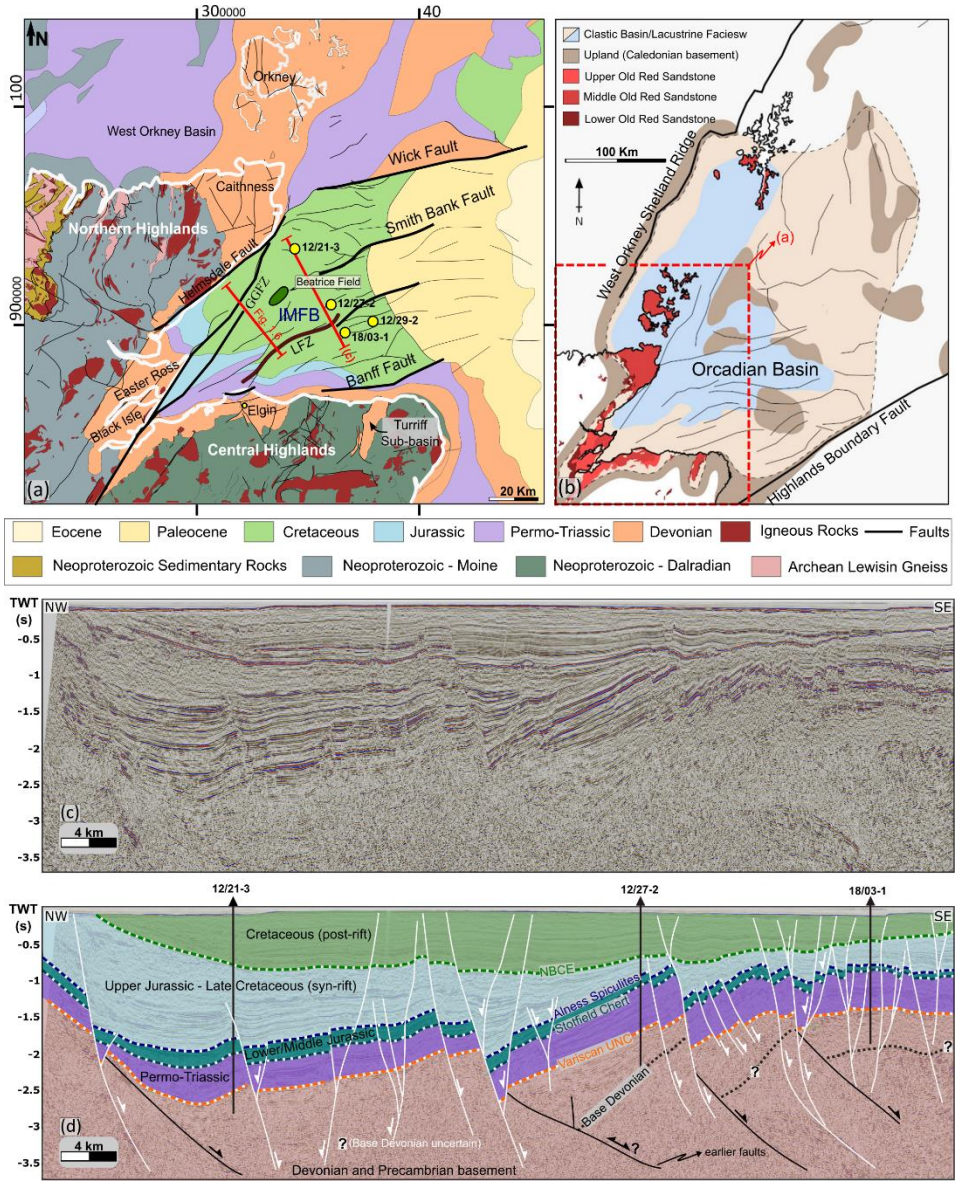

Fig. 1. 2: (a) Regional geological map of northern Scotland and associated offshore regions (after Tamas et al. 2022a). Red line shows the location of Fig. 1.8. IMFB – Inner Moray Firth Basin. LFZ – Lossiemouth Fault Zone. GGFZ – Great Glen Fault Zone. (b) Regional map of the Orcadian Basin (after Flannery-Sutherland 2021). Approximate location of (a) is indicated by the red rectangle. (c) uninterpreted and (d) interpreted stratigraphy and faults on a regional 2D seismic profile. NBCE – Near Base Cretaceous Event.

Since the discovery of coals at the end of the sixteenth century (Trewin and Hurst 2009) to the present-day subsurface exploration and hydrocarbon production, the IMFB area has been of great geological interest both economically and scientifically (e.g. Devonian fossil fish; Miller 1841). It was also the focus of offshore exploration during the early development of the North Sea as a petroleum province.

However, the geological history of the IMFB has also been a source of some controversy. In particular, the Permo-Triassic history and the kinematics of opening of the basin during the Late Jurassic – Early Cretaceous have both been matters of discussion and disagreement.

1.3.2 Stratigraphic Framework

The IMFB has been a depositional area since the Devonian, with up to 16 km of sedimentary rocks accumulated in the deepest parts of the basin (Andrews et al. 1990). The underlying Devonian-Carboniferous basin is known as the Orcadian Basin (Fig. 1.2b). The stratigraphy of the basin is known from both surface (e.g. Hurst 1981; Pickering 1984; Frostick et al. 1988) and subsurface data (e.g. Roberts et al. 1990; Andrews et al. 1990).

The outcrops in onshore regions to the north and south are dominated by Precambrian basement rocks and Silurian-Devonian Caledonian intrusions that are unconformably overlain by Palaeozoic (mainly Devonian) cover sequences. Mesozoic strata (Triassic to Jurassic) have a limited extent onshore and occur mostly along costal margins, sometimes located in the hangingwalls of major faults (Fig. 1.2a).

Offshore, the preserved stratigraphy comprises Devonian to Upper Cretaceous sedimentary rocks (Fig. 1.2d). Younger, Cenozoic stratigraphy is

preserved further east in the Outer Moray Firth. A summary of the main stratigraphy is given in Figure 1.3.

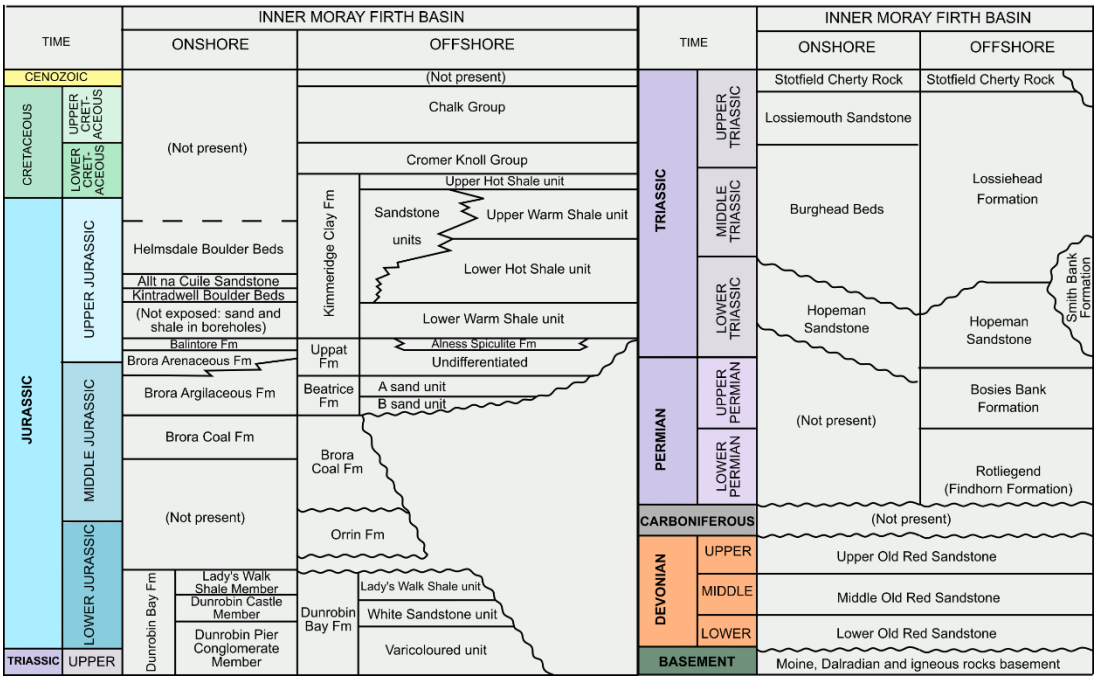

Fig. 1. 2: Summary of stratigraphy (after Andrews et al. 1990, Lovell 1991 and Goldsmith et al. 2003)

1.3.2.1 Basement

The crystalline basement of IMFB consists mainly of Proterozoic Moine and Dalradian Supergroup metasedimentary rocks deformed during the Caledonian Orogeny and earlier events (e.g. Stephenson and Gould 1995; Johnstone and Mykura 1989). The Moine Supergroup lies to the north of the basin, forming part of the Northern Highland Terrane (Fig. 1.2a). The Dalradian Supergroup lies to the south, forming part of the Central Highland Terrane (Fig. 1.2a; Woodcock and Strachan 2012). The NE-SW-trending Caledonian Great Glen Fault separates the two basement terranes passing through Inverness and through the northern part of the IMFB offshore (Fig. 1.2a). The crystalline basement is intruded by numerous granitic bodies emplaced during the Caledonian Orogeny or later, during Late Silurian – Early Devonian (e.g. Andrews et al. 1990).

1.3.2.2 Sedimentary Cover

1.3.2.2.1 Palaeozoic

Devonian-Carboniferous

The Moine and Dalradian basement terranes are unconformably overlain by the Devonian-Carboniferous deposits of the Orcadian Basin (Fig. 1.3), which extends both onshore and offshore in the IMFB, Caithness and Orkney regions (Fig. 1.2b; Johnstone and Mykura 1989; Friend et al. 2000). The Orcadian Basin belongs to a much larger system of Devonian basins that extends northwards into Shetland, western Norway and eastern Greenland (Fig. 1.2b; Seranne 1992; Duncan and Buxton 1995; Woodcock and Strachan 2012).

The Lower Devonian (Fig. 1.3) is represented by non-marine, red coloured alluvial and fluviatile breccio-conglomerates and conglomerates, medium- to coarse-grained sandstones or floodplain mudstones (e.g. Stephenson and Gould 1995; Johnstone and Mykura 1989 and references therein). They are mostly restricted to the western onshore-offshore parts of the IMFB (Rogers et al. 1989) and some areas of Caithness (NIREX 1994), but limited exposures can be seen on the southern coast in Turriff Sub-basin (e.g. Coward et al. 1989; Trewin 1987). Usually, the Lower Devonian rocks are unconformably overlying or are faulted against basement rocks. They are thought to have been deposited in a series of small fault-bounded basins of limited extent.

These strata are unconformably overlain by Middle Devonian alluvial, fluvial, lacustrine and locally marine sequences. Rocks of this age dominate the onshore sequences exposed in Caithness, Orkney and

Shetland (Marshall and Hewett 2003). They are, in turn, overlain by less widespread Upper Devonian post-rift fluvial and aeolian sedimentary rocks (Friend et al. 2000). Younger Carboniferous strata conformably overlie Devonian rocks and are restricted to offshore regions of the Outer Moray Firth Basin. The succession comprises sandstones, conglomerates, and sparse claystones and siltstones, interpreted as part of a regional fluvial depositional setting developed across the former Orcadian Basin (e.g. Marshall and Hewett 2003).

Permian

Permian deposits (Fig. 1.3) onshore are limited to a restricted series of coastal exposures along the southern coast of IMFB, north of the Elgin area (Fig. 1.2a). In general, they are characterised by aeolian, dune bedded sandstones, playa deposits and conglomerates interbedded with cross-bedded sandstones, part of a marginal fluvial system (e.g. Stepherson and Gould 1995). Offshore, they are well represented, being penetrated by many (c. 10) deep wells (e.g. Fig. 1.2d). They consist here of red-bed continental fine-grained sandstones, mudstones and anhydritic mudstone (e.g. Andrews et al. 1990). Interpretation of seismic reflection profiles by some workers has suggested that the Permian deposits show fault-controlled thickening. This minor extension is thought to attest the onset of the opening of the IMFB (e.g. Roberts et al. 1990), however this interpretation is disputed by many (see section **1.3.3.2**).

1.3.2.2.2 Mesozoic

Triassic

The Triassic rocks (Fig. 1.3) have a similar distribution as the Permian rocks. Onshore, the Triassic succession is dominated by sandstones and conglomeratic sandstones (e.g. Trewin and Hurst 2009 and reference therein) interpreted as aeolian, fluviatile and lacustrine deposits (e.g. Frostick et al. 1988). Offshore, they are generally finer-grained, characterised by siltstones, mudstones, thin limestone and evaporitic beds, part of the same general depositional environment as the onshore equivalent (e.g. Frostick et al. 1988; Roberts et al. 1990).

Jurassic

An almost complete section of Jurassic rocks crops out on the north-western coast of the IMFB, in the hangingwall of the Helmsdale fault (Fig. 1.2a). Lower Jurassic strata (Fig. 1.3) are characterised by conglomerates and cross-bedded sandstones deposited in a fresh water, alluvial fan environment. They are followed by shallow marine thin sandstones, siltstones and shales (e.g. Trewin and Hurst 2009 and reference therein). Offshore, they are predominantly represented by interbedded mudstones and siltstones, which contain rootlets, thin coal horizons and cm-thick fining-upward sandstones or laminated bituminous shales. Those strata are overlain by a medium to coarse cross-bedded sandstones with erosional bases and rip-up clasts. This offshore succession is interpreted as alluvial floodplains and levee-crevasse splay deposits (e.g. Andrews et al. 1990). The succession is considered the distal time equivalents of the coarser onshore non-marine deposits (Stephen et al. 1993).

The Middle Jurassic (Fig. 1.3), both onshore and offshore, is characterised by freshwater, continental sequence. The lithology is dominated by sideritic mudstones, passing upwards into organic-rich shales and coals followed by a thick succession of deltaic sandstones (Hurst 1981 and reference therein).

The Upper Jurassic (Fig. 1.3) is highly influenced by active tectonics in the IMFB being deposited in a series of half-grabens (Fig. 1.2d). The succession shows clear evidence of growth strata on seismic reflection profiles (Fig. 1.2c and d; e.g. Underhill 1991a). Onshore, Upper Jurassic crops out widely in the hangingwall of the Helmsdale fault. The lithology is dominated by shallow marine sandstones followed by deep marine shales, sandstones, and localised active fault-related debris flow breccias (e.g. Pickering 1984). Offshore, the sequence is finer-grained, represented by mudstones, fined grained sandstones and organic-rich mudstones (e.g. Roberts et al. 1990).

Cretaceous

The deposition of the Cretaceous strata is thought by some authors to have occurred during a period of regional thermal subsidence (Underhill 1991a and b). Onshore, Cretaceous rocks only appear as glacial erratics (Roberts et al. 1990). Offshore the Lower Cretaceous is characterised by black mudstones, fine to coarse-grained sandstone, sometimes conglomeratic. They are interpreted as having been deposited in a deep-water, open marine environment (e.g. Argent et al. 2000) with local fan deltas in the northern part of the basin. The Upper Cretaceous is represented by

thin glauconitic sandstones overlain by a thick coccolithic limestone (chalk) and mudstones succession (Roberts et al. 1990).

1.3.2.2.3 Cenozoic to Quaternary

Cenozoic sedimentary rocks are only found offshore, in the eastern part of the basin, sub-cropping beneath the Quaternary deposits. During the Cenozoic, the basin is thought to have been subjected to continuous regional uplift, eastward tilting and exhumation (e.g. Underhill and Brodie 1993). The sedimentation of chalk extended until the beginning of the Paleogene. Later in the Paleocene and Eocene, the sedimentation was followed by the development of widely distributed submarine fan sandstones (e.g. Mudge 2015) and prograding deltaic sequences. They are considered to be triggered by the uplift and sea-level drop (Roberts et al. 1990). Due to the uplift, a break in sedimentation took place between late Paleocene and Quaternary in the IMFB (e.g. Mackay et al. 2005). During Quaternary, the area is marked by alternating glacial- low salinity arctic marine or glacio-marine sedimentation (e.g. Sutherland 1984).

The deposits are present almost everywhere within the sedimentary basin of Moray Firth, thinning westwards. The lithologies are characterised by pebbly, sandy clay and muddy sand, interpreted as basal till. Laminated silty clay and calcareous mud deposits overlie the till and are interpreted to be glaciomarine sequences.

1.3.3 Structural Evolution

The IMFB developed on a Precambrian to Caledonian basement and post-orogenic Devonian-Carboniferous sedimentary rocks related to the

Orcadian Basin. It evolved as part of the North Sea trilete rift system, which some have suggested represents a failed triple junction (Whiteman et al., 1975). Prior to this study, the IMFB was generally thought to have opened during superimposed Permo-Triassic and Late Jurassic rifting episodes (e.g. McQuillin et al. 1982; Underhill 1991a; Thomson and Underhill 1993). During Late Cretaceous – Cenozoic, the basin experienced important episodes of regional uplift, strike-slip faulting and inversion (e.g. Underhill 1991a; Thomson and Underhill 1993; Le Breton et al. 2013).

1.3.3.1 Precambrian to Carboniferous

The Caledonian basement

The Palaeozoic Caledonian orogenic belt has a long and complex history that culminated in the sinistrally-dominated collision between Laurentia, Baltica, Avalonia and associated closure of the Iapetus ocean and Tornquist Sea (e.g. Soper et al. 1992; Dewey and Strachan 2003). The regionally widespread intrusion of mainly Silurian to Devonian age granites and associated rock types was associated with the later stages of Caledonian orogenesis in both basement terranes, with some plutons being directly controlled or influenced by strike-slip faulting (e.g. Jacques and Reavy 1994; Holdsworth et al. 2015). In addition, two small inliers of older (Archaean) Lewisian metamorphic rocks crop out in the Black Isle (Fig 1.2a). These rocks are thought to represent the original basement of the Moine and have been interpreted to represent an upfaulted region of deeper crustal material forced upwards in a restraining bend formed during the Silurian-age left-lateral movements along the GGF (Mendum and Noble 2010).

Devonian-Carboniferous: The Orcadian Basin and Permo-Carboniferous ('Variscan') inversion.

The origin of the Orcadian and nearby West Orkney basins has been a matter of controversy. Interpretation of seismic reflection profiles N of Scotland shows that the West Orkney Basin comprises a series of half-grabens bounded by easterly dipping normal faults (e.g. Brewer and Smythe 1984; Coward and Enfield 1987).

Earlier interpretations (e.g. McClay et al. 1986; Enfield and Coward 1987) postulated that much of the basin fill here was Devonian and that both the Orcadian - West Orkney basins formed due to the extensional collapse of the Caledonian orogen.

Later studies have cast doubt on these models showing that the fill of the West Orkney Basin is mostly Permo-Triassic (e.g. Stoker et al. 1993) and that there is only limited onshore evidence for large-scale basement reactivation along the N coast of Scotland (e.g. Roberts and Holdsworth 1999; Wilson et al. 2010). ENE-WSW rifting in northern Scotland during the Devonian is now

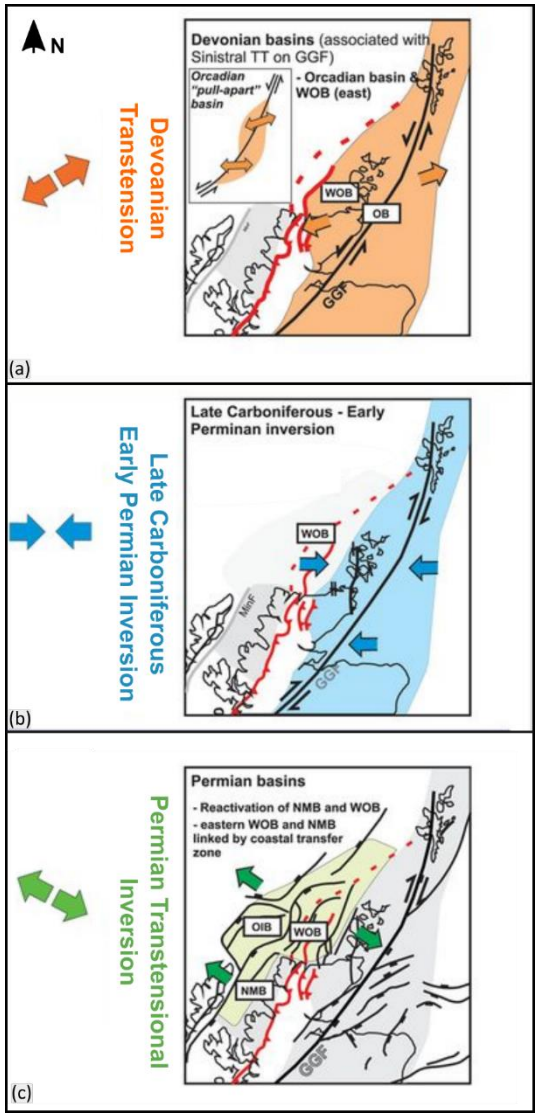

Fig. 1. 3: (a) Regional events in the northern Scotland (after Dichiarante et al. 2020): (a) development of the Orcadian Basin (OB) during Devoanian. (b) Widespread Late Carboniferous-Early Permian (Variscan) inversion events. (c) Localized Permian Transtension recognized in the West Orkney Basin (WOB), Outer Isles Basin (OIB) and North Minch Basin (NMB). GGF – Great Glen Fault.

generally considered to be related to regional sinistral transtension during left-lateral shear along the Great Glen–Walls Boundary Fault system (Fig. 1.4a; Seranne 1992; Dewey and Strachan 2003; Watts et al. 2007).

However, Norton et al. (1987) argued against the dominance of strike-slip related development of the Orcadian Basin and proposed a dip-slip evolution during NW-SE extension. The authors used Turriff Sub-basin (Fig. 1.2a) as one of their case studies to support their interpretation. The distance of this basin to the major known strike-slip faults was one of the arguments against strike-slip related development on the Orcadian Basin.

The Orcadian Basin then experienced an episode of E-W compression, which led to widespread reactivation of previously formed rift-related structures. Such compressional structures have been documented from the Scottish mainland to Shetland (e.g. Underhill and Brodie 1993; Armitage et al. 2020; Dichiarante et al. 2020, 2021). Overall, these structures are interpreted to have formed due to Late Carboniferous–Early Permian east-west inversion possibly related to dextral strike-slip reactivation of the Great Glen-Walls Boundary fault system (Fig. 1.4b; e.g. Coward et al. 1989; Seranne 1992; Watts et al. 2007; Wilson et al. 2010; Dichiarante et al. 2020, 2021). These displacements may in turn be related to the far-field effects of the Variscan orogenic event which is also thought to have caused widespread uplift and erosional exhumation of much of northern Scotland and surrounding offshore areas such as the IMFB at this time (the so called ‘Variscan unconformity’).

The Variscan structures are then everywhere cross-cut by younger, predominantly normal faults of various ages. In northern Caithness, close to

the southern margin of the West Orkney Basin, Dichiarante et al. 2016 used Re-Os geochronology to date syn-tectonic normal to transtensional fault sulphide-carbonate infills in Devonian rocks of the Dounreay area (Caithness). The sampled dextral transtensional faults yielded a mid-Permian (267.5 ± 3.4 [3.5] Ma) age of faulting, which Dichiarante et al. (2016) suggested was related to the development of the nearby West Orkney Basin (Fig. 1.4c).

1.3.3.2 Permian to Early Cretaceous Basin Opening

The IMFB is generally thought to have opened during Permo-Triassic and/or Late Jurassic- Early Cretaceous rifting episodes mainly based on interpretation of the 2D offshore seismic reflection and well data (e.g. McQuillin et al. 1982; Underhill 1991a; Thomson and Underhill 1993).

Permo – Triassic history

The Permo-Triassic history - which is widely characterised by active rifting in other parts of the North Sea (e.g. Steel and Ryseth 1990; Bell et al. 2014; Fazlikhani et al. 2020) - is debatable in the IMFB. Some authors have considered the Permo-Triassic history to be characterised by active rifting (e.g. Frostick et al. 1988; Roberts

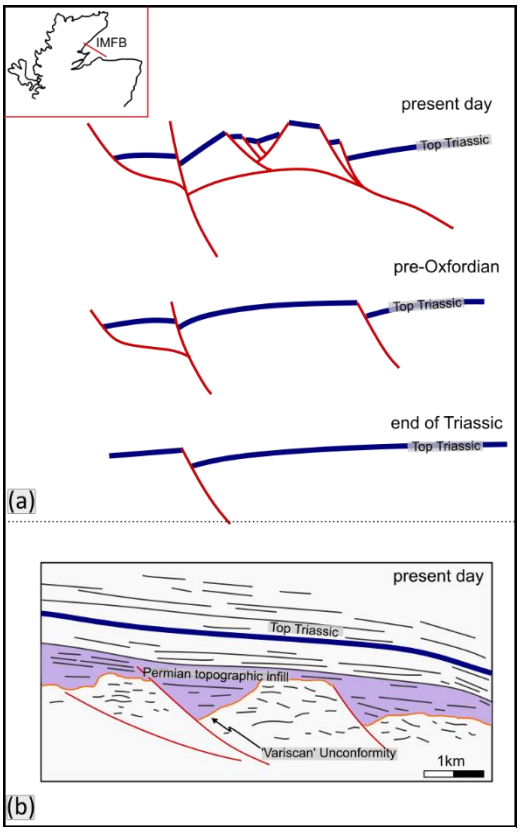

Fig. 1. 4: (a) Schematic basin development diagram after Frostick et al. 1988, suggesting Triassic onset of the rifting. (b) passive infilling of the post-Variscan topography after Thomson and Underhill (1993)

et al. 1989). Frostick et al. (1988) suggested that rifting initiated in the Triassic and that the IMFB evolved as a simple half-graben (Fig. 1.5a). They viewed the GGF as a major controlling structure, which they suggested, developed as a dip-slip normal fault, with extension later in the Triassic transferring north-westwards onto the Helmsdale Fault. Roberts et al. (1990), based on the interpretation of the regional 2D seismic profiles, argued for rift initiation in the Permian based on the supposed recognition of growth strata of this age in different parts of the basin associated with active intra-basinal faults (e.g. Wick, Halibut, Smith Bank faults; Fig. 1.2a).

Other more recent interpretations, based on interpretations of increasingly available seismic reflection data, considered that the Permo-Triassic history was dominantly marked by thermal subsidence (Andrews et al. 1990; Thomson and Underhill 1993). Thomson and Underhill (1993) document thickness variations between the Variscan unconformity and overlying lower units of the Permo-Triassic (Fig. 1.5b). However, they interpreted these to result from the passive infilling of the post-Variscan topography (Fig. 1.5b). Yet, they did not entirely rule out early syn-sedimentary faulting along reactivated structures cutting the Carboniferous and older basement rocks.

Late Jurassic – Early Cretaceous basin development

The kinematics of basin opening have been the subject of debate, with both oblique-slip (McQuillin et al. 1982; Roberts et al. 1990) and dip-slip faulting models suggested (e.g. Underhill 1991a; Davies et al. 2001; Fig. 1.6).

The transtensional model was first proposed by McQuillin et al. (1982)

and then further developed by other researchers (e.g. Bird et al., 1987, Roberts et al. 1990; Frost and Rose 1996). The models typically assume opening of the basin due to dip-slip movements along the major GGF (Fig. 1.6a), initially during Permo-Triassic, followed by about 8 km of dextral movements.

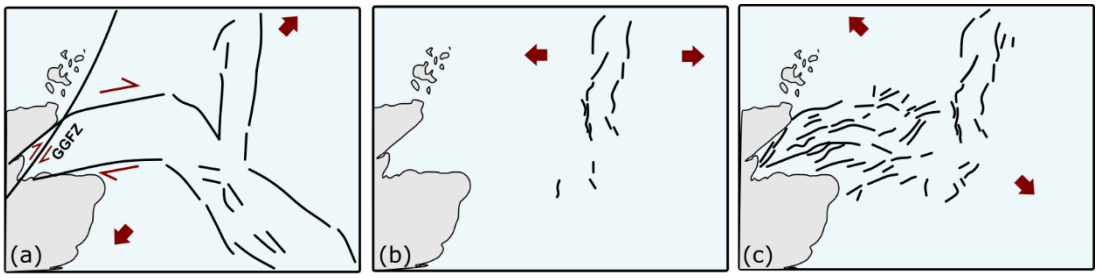

Fig. 1. 5: Schematic diagram showing the opening of the IMFB due to dextral shear along Great Glen Fault Zone (GGFZ, modified after McQuillin et al. 1982). Schematic diagram showing the North Sea rift development during (b) the Late Bathonian to Early Callovian, (c) the Oxfordian (after Davies et al. 2001).

The suggestion that a link existed between the dextral shear along the GGF and the transtensional opening of the IMFB was proposed based on the preservation of structures imaged on seismic reflection data. Supposedly, they are consistent with strike-slip/transtensional deformation, e.g. flower structures, pull-apart mini-basins, 'scissor faults', helicoidal faults, en-echelon folds and faults, and the presence of both normal and reverse slip faults or lateral offsets in the stratigraphy (Fig. 1.7; e.g. McQuillin et al. 1982; Bird et al. 1987; Roberts et al. 1990).

Also, evidence of folding and onlap within the Upper Jurassic was associated by Frost and Rose (1996) to dextral strike-slip inversion.

A dip-slip model was first proposed by Frostick et al. (1988). The authors also viewed the GGF as the major controlling fault during basin development at least in the Triassic. Based on seismic reflection profiles, they identified Triassic growth strata thickening towards the GGF, but invoked a dip-slip movement rather than strike-slip.

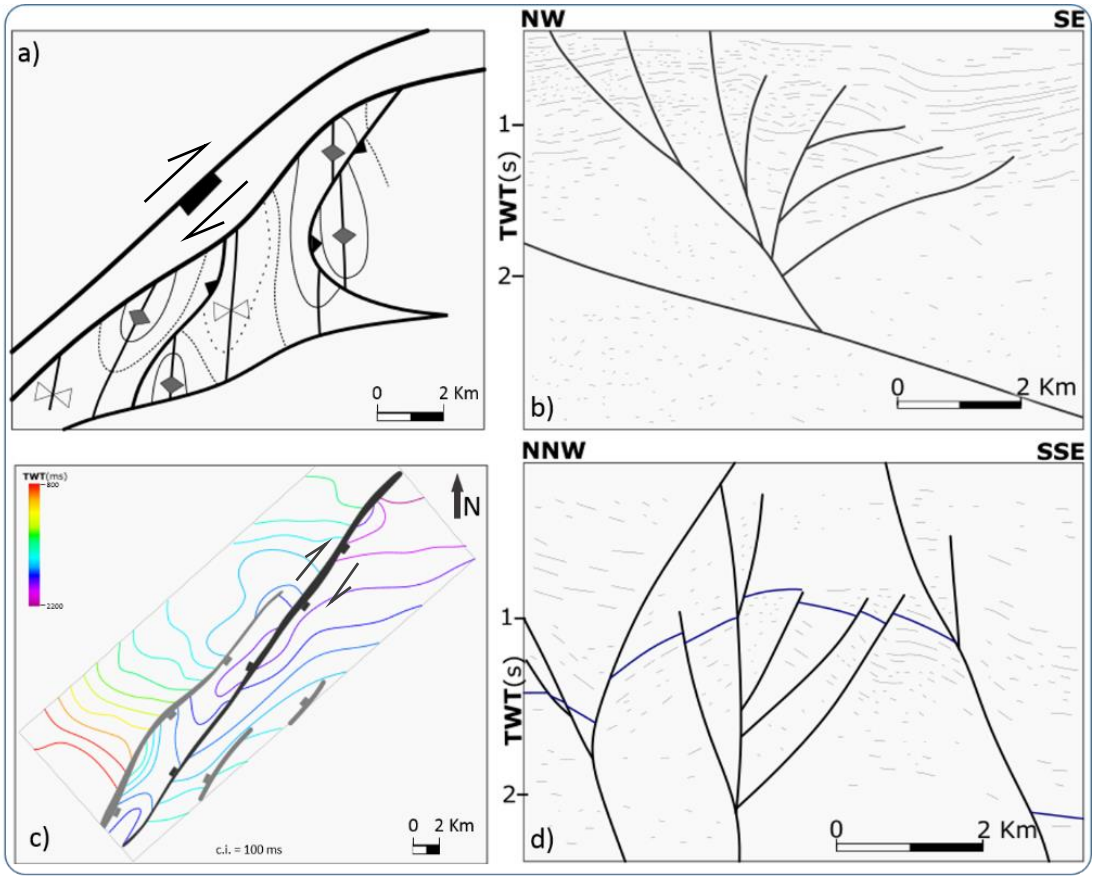

Fig. 1. 7: Evidence of oblique-slip in the basin. (a) en-echelon folds indicating dextral slip (redrawn after Bird et al. 1987). (b) interpreted seismic line displaying a positive flower structure (redrawn after Bird et al. 1987). (c) Structural map of the top Triassic in the Great Glen Fault Zone. The coloured in black fault on the map displays 'scissors' geometry (redrawn after Roberts et al. 1990). (d) interpreted seismic line displaying a positive flower structure (redrawn after Roberts et al. 1990).

Largely based on detailed interpretation of seismic profiles and construction of thickness maps between key stratigraphic intervals, Underhill (1991a) proposed a new model for the evolution of the IMFB (Fig. 1.8).

The model suggested that, after a long period of thermal subsidence during the Triassic to mid-Jurassic, the basin opened mainly during Late Jurassic under an NW-SE to NNW-SSE orthogonal extensional regime. The main rift-controlling fault displacements were interpreted to occur along the Helmsdale Fault, as the synkinematic sequence thickens without change across the GGF and towards the Helmsdale Fault. This indicates that the Great Glen Fault was inactive during the Late Jurassic. Subsequent studies of Thomson and Underhill (1993), Underhill and Brodie (1993) and Davies et al. (2001)

support the dip-slip opening of the basin as opposed to an oblique- or strike-slip history.

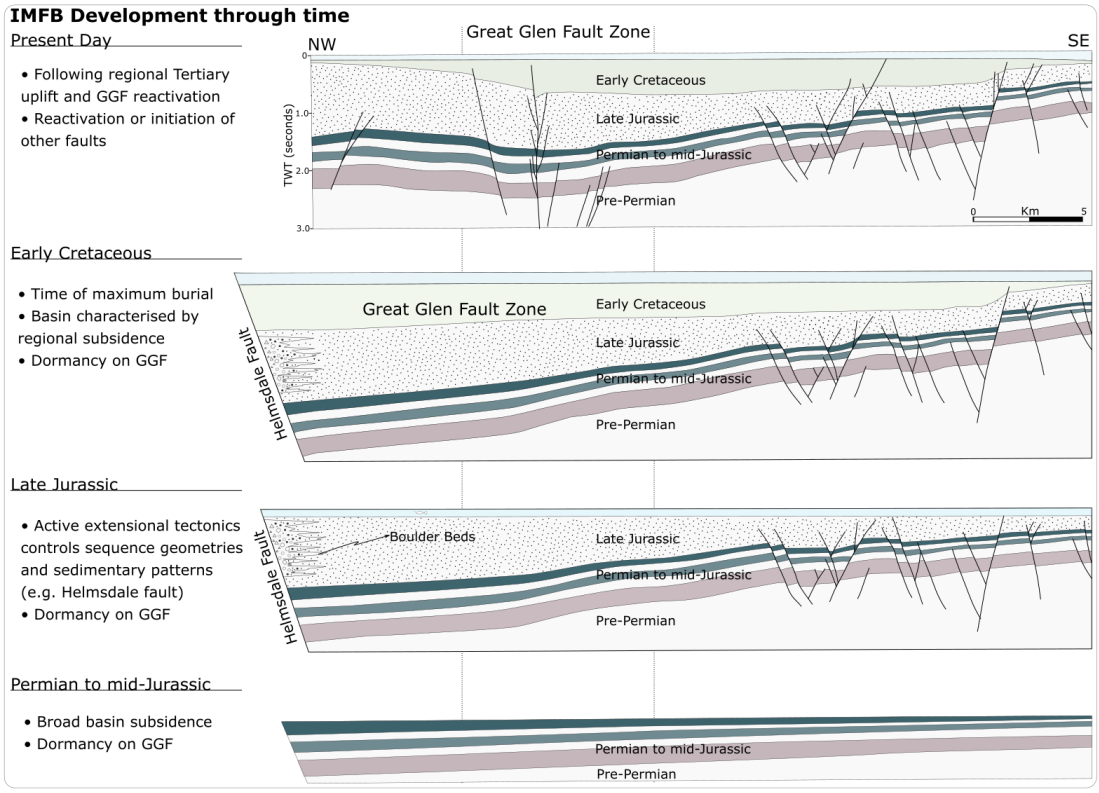

Fig. 1. 8: IMFB development through time (after Underhill 1991a) (See section location on Fig. 1.2a).

The authors consider the strike-slip structures recognised by earlier workers (Fig. 1.7) to be related to younger Cenozoic inversion (see below).

The NW-SE to NNW-SSE extension direction proposed by Underhill (1991a) is similar to that suggested by Davies et al. (2001) for the wider North Sea region during the Oxfordian and early Kimmeridgian, following a shift from E–W extension during the Bathonian and Callovian which generated N-S trending structures in the Central Graben (Fig. 1.6b, c).

Moreover, the most more recent studies of offshore 3D seismic reflection profiles (e.g. Davies et al. 2001; Long and Imber 2010; Lapadat et al. 2016) strongly support a predominance of orthogonal rifting and suggest there is little evidence of oblique-slip faulting in the basin.

3.1.1.3.2 Cenozoic

From the early Cenozoic to the present day, the basin is thought to have experienced episodes of uplift, eastward tilting and regional erosion, with some major faults undergoing reactivation (e.g. Underhill 1991a; Argent et al. 2002). The main causes for these events have been linked variously to the development of the Iceland mantle plume, the Alpine Orogeny or opening of the North Atlantic rift (e.g. Le Breton et al. 2013 and references therein). There is good evidence onshore and offshore that reactivation leading to folding and faulting has occurred during the Tertiary, particularly in the region of the GGF. The GGF is believed to be the major controlling structure in the basin at that time (Fig. 1.8; Underhill 1991a). Offshore, seismic reflection profiles show evidence for the development of strike-slip related deformation patterns (e.g. flower-structures, folds) offsetting post-rift reflectors (Fig. 1.9; e.g. Thomson and Underhill 1993; Underhill and Brodie 1993; Davies et al. 2001).

Onshore, Holgate (1969) had previously estimated c. 30 km Cenozoic dextral slip of the GGF due to the offset of the Cenozoic dykes.

Other Cenozoic onshore structures supposedly include the development of NW-SE trending large-scale folds (of about 500 m wavelength) in the hangingwall of Helmsdale Fault (Thomson and Underhill 1993; Thomson and Hillis 1995). In addition, minor folds and faults consistent with dextral kinematics, cropping out in Devonian strata along the Easter Ross coast (Fig. 1.2a), are considered to be Cenozoic and related to right-lateral slip along GGF (e.g. Underhill and Brodie 1993; Le Breton et al. 2013).

The effects of Cenozoic deformation away from the GGF, both onshore and offshore, are less certain and may be limited and/or localised.

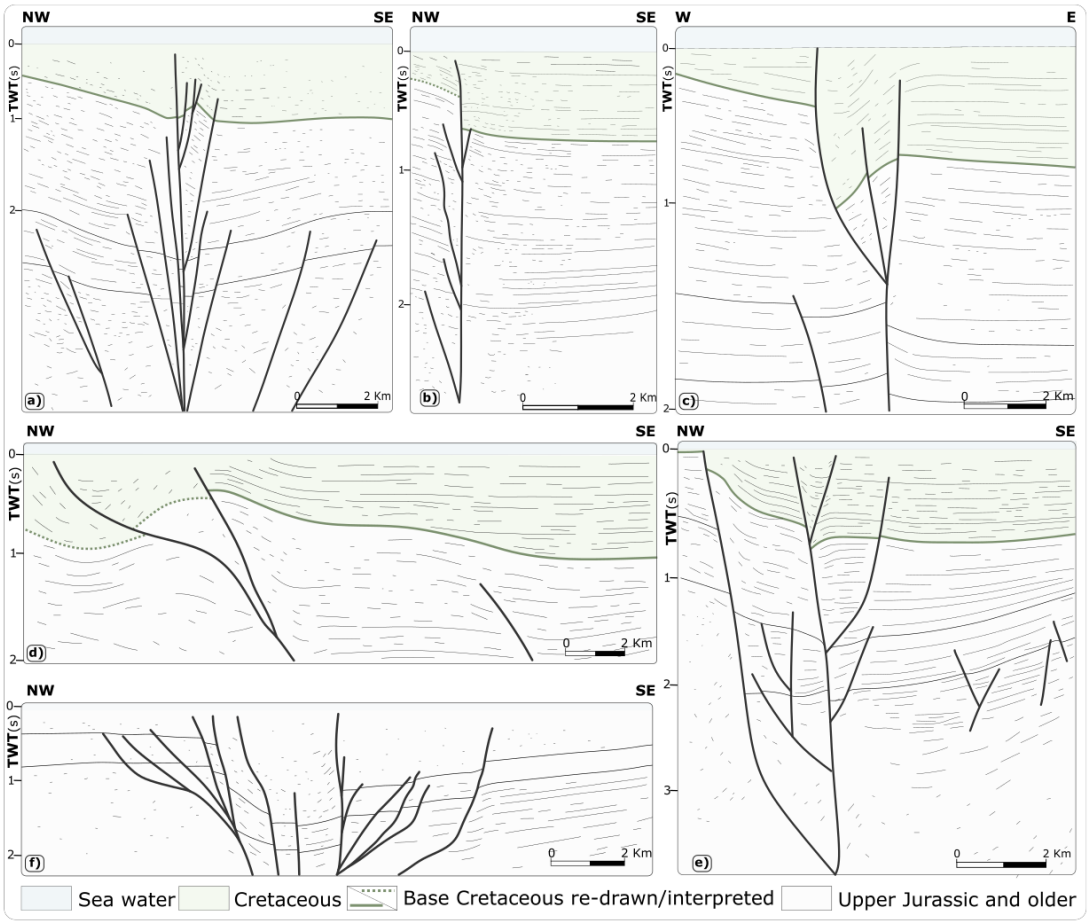

Fig. 1. 9: Evidence of post-Cretaceous basin inversion. (a) strike-slip related faults offsetting post-rift reflectors (redrawn after Underhill 1991a). (b and c) negative flower structure (redrawn after Thomson and Underhill 1993). (d) inversion-related hangingwall anticline and associated short-cut fault (redrawn after Thomson and Underhill 1993). (e) Post-rift faulting in the GGF zone (redrawn after Davies et al. 2001). (f) negative flower structures in the GGF zone (redrawn after Underhill and Brodie 1993).

1.3.4 Hydrocarbon potential

The IMFB has a history of hydrocarbon exploration dating back to 1967 (e.g. Linsley et al. 1980; David 1996). Although the first wells drilled turned out to be dry holes and the first seismic survey failed to reveal a drillable prospect (e.g. Linsley et al. 1980), the discovery of the Beatrice Field (Fig. 1.2a) proved a petroleum system and encouraged further exploration

and production. The Beatrice field reservoir-seal packages comprise Lower Jurassic to Middle Jurassic sandstones and siltstones interbedded with mudstones. The source rock is considered to be a combination of Devonian and Jurassic rocks (e.g. Peters et al. 1989; Greenhalgh 2016). The hydrocarbon trap is represented by a tilted fault block (Stevens 1991). To date, the Beatrice Field (currently decommissioned) still remains the largest hydrocarbon filed in the IMFB (16.6 Mboe total hydrocarbons produced; North Sea Transition Authority). Although subsequent smaller fields have been discovered, the IMFB has not been of much direct interest the hydrocarbon industry as no major hydrocarbon accumulations have been discovered. However, a recent licence awarded to Corallian Energy during the 31st Round award (in 2019), includes the Dunrobin prospect, located in the southern part of the basin c. 30 km offshore (Dunrobin and Golspie prospects licence P2478; Corallian Energy 2022). This consists of three large shallow Jurassic rotated fault blocks that are mapped mostly on 3D seismic data, which have direct hydrocarbon indicators (dim spot). The Dunrobin structure has c. 40 km^2 and has P50 prospective resources of 174 mmboe, with a potential for 396 mmboe (P10) (Offshore Energy 2020).

If this prospect turns out to be a significant discovery, it could restart interest in the IMFB area.

Chapter 2

Dataset and Methodology

Abstract

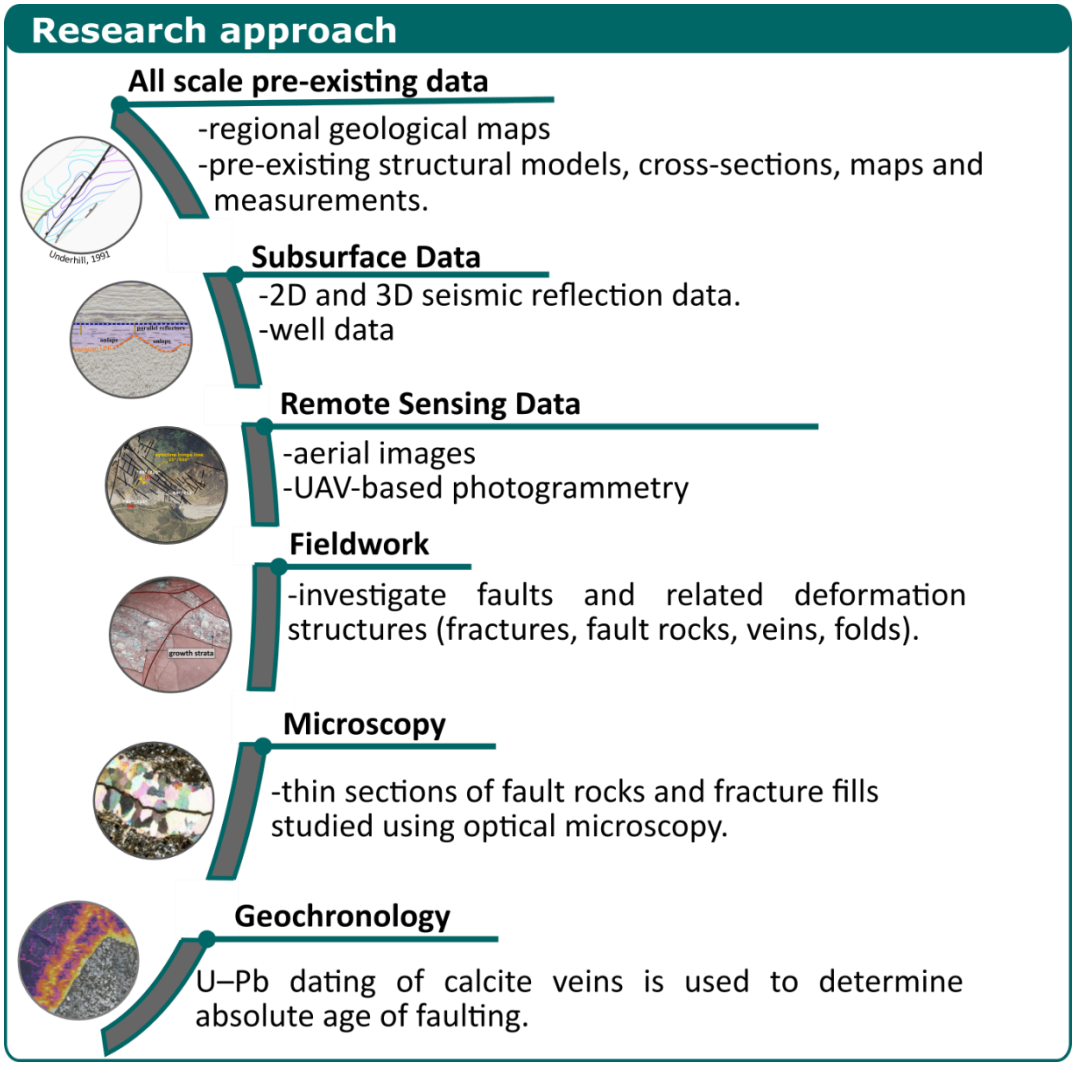

Fig. 2. 1: The multiscale and multimethod analysis used in this study.

The present study involves a multiscale and multimethod analysis, using both surface and subsurface data, integrated with the pre-existing published data and models (Fig.2.1).

New detailed onshore field observations were augmented with drone photography and the creation and interpretation of 3D digital outcrops. This onshore study was combined with the offshore interpretation of seismic reflection data and coupled with the thin section study of onshore fault rocks and U-Pb geochronology of syn-kinematic calcite veins or cements.

This holistic approach proved very effective in shedding new light on the nature, age, and significance of regional to local deformation events in the complex evolution of the Inner Moray Firth Basin (IMFB).

2.1 Pre-existing data

The present project made good use and was developed based upon a vast body of good quality work done by previous workers in the form of published research papers, PhD theses, maps and reports.

Most regional geological maps (1:250:000 to 1:50:000) used in this study were published by the British Geological Survey and are available under the Open Government Licence. They were accessed both as a digital copy via the maps portal on the BGS website (https://www.bgs.ac.uk/information-hub/bgs-maps-portal) and as vectorised layers using the Edina Digimap service (https://digimap.edina.ac.uk/geology) under licence agreement.

The extensive literature review was approached systematically to locate as much relevant literature in order to:

- understand the regional geology of the study area.
- identify what is already known and generally agreed.
- integrate results from different studies.
- identify uncertainties and define the scope of the present work.
- plan fieldwork.
- complement and illustrate findings.
- better understand structural geology concepts and techniques.

2.2 Subsurface dataset and mapping

The sub-surface dataset used in this study comprises a compilation of 2D regional and selected 3D time-migrated seismic reflection surveys (Fig. 2.2). The regional 2D seismic lines, acquired in 1997, were provided by Spectrum. Most

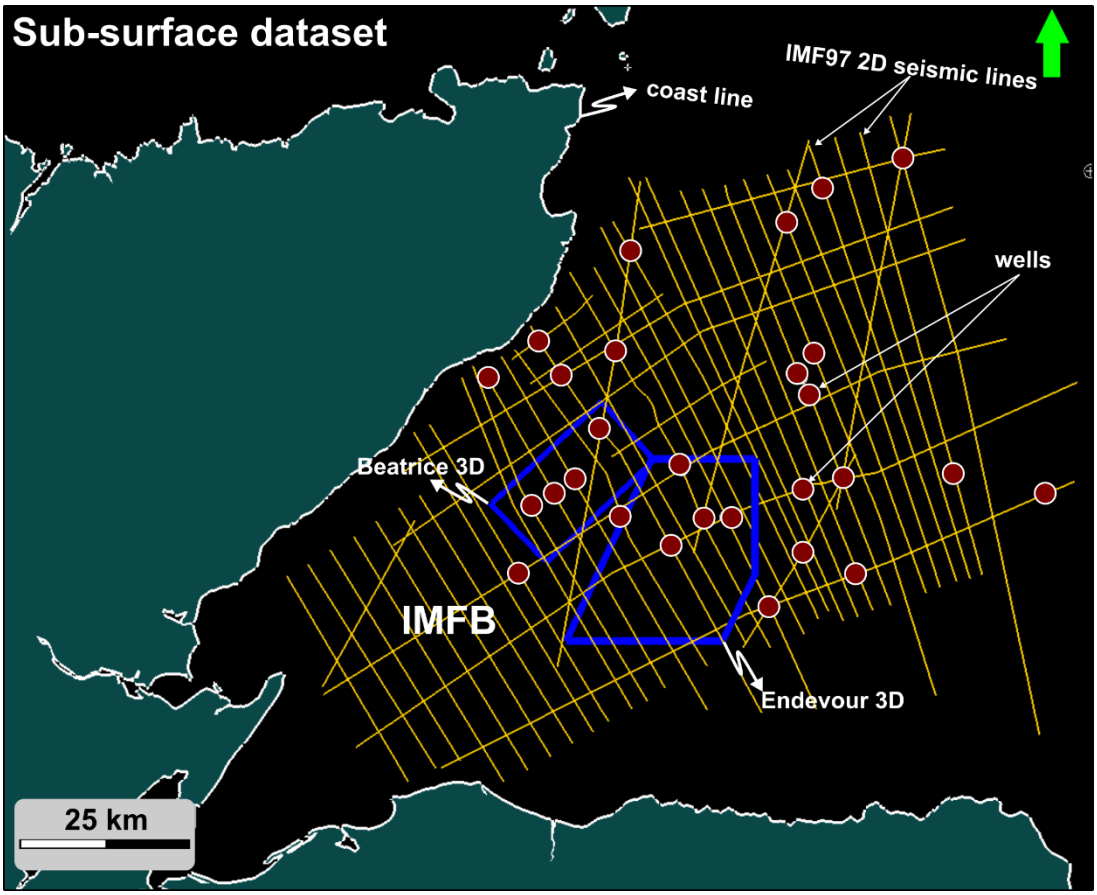

Fig. 2. 2: The sub-surface database used for this study comprising 3D and 2D seismic reflection data and wells.

lines (32 in total) are orientated NW-SE, orthogonal to the main basin-bounding structures of the IMFB (Fig. 3b) and have a 2 to 5 km line spacing. These lines are connected by eight ENE-WSW orientated lines with a spacing of between 2 to 14 km. These lines were chosen as they are ideal for regional mapping and for defining the major faults in the basin.

This study also made use of two 3D time-migrated seismic surveys (Fig. 3b). One (*Beatrice 3D*) acquired over the Beatrice Field (e.g. Fig. 1b; Linsley et al. 1980) covers an area of 11 x 22 km and has a crossline and inline bin spacing

of 12.5 m. The second (*Endeavour 3D*) is located in the central part of the basin, has an area of about 36 x 20 km and a crossline/inline bin spacing of 12.5m/25m, respectively. These high-quality seismic surveys were selected as they provide higher resolution analysis of fault networks and provided indirect insights into the fault development and kinematics.

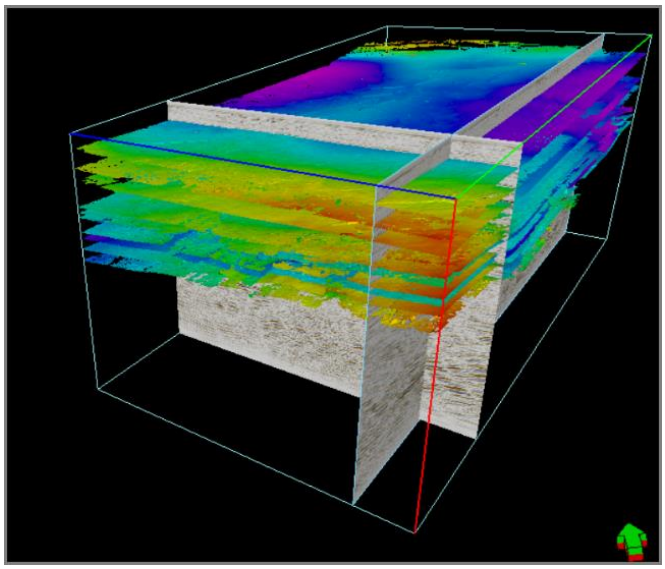

Fig. 2. 3: Example of seismic horizons interpreted from the 3D Beatrice cube.

In addition to the seismic reflection data, key exploration wells were used in this study (Fig. 2.2). Stratigraphic data and checkshot/sonic logs available allowed the determination of the age of the mapped seismic horizons, linking this to the stratigraphic framework for the study area.

The seismic and well data were obtained from the Oil and Gas Authority's National Data Repository (NDR) and from Fugro GeoTeam (regional 2D spec survey).

The seismic interpretation was undertaken in the Centre for Exploration Geoscience in the Institute of GeoEnergy Engineering (IGE) at Heriot-Watt University (HWU), UK, during two short assignments of about five months total duration during 2019 and 2020. The software used was Schlumberger's Petrel suite released to HWU under academic license.

Conventional geometrical interpretation of the seismic data usually requires the picking and lateral tracking of a seismic reflector, which usually

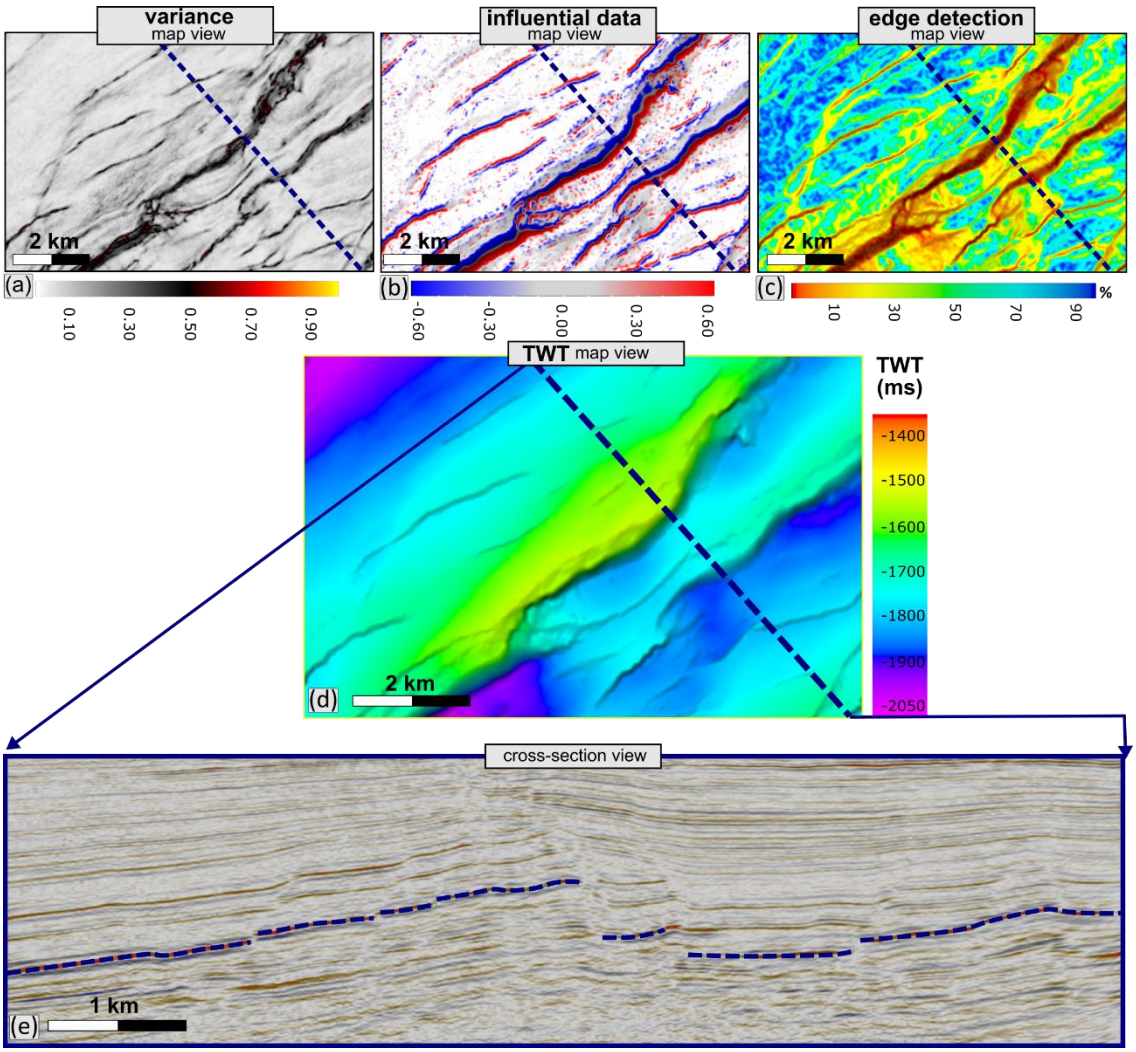

Fig. 2. 4: Comparison between (a) variance (b) influential data and (c) edge detection properties against (d) the TWT map generated at the seismic horizon shown in dashed blue line on the seismic profile in (e).

represents a bedding surface or an unconformity. Likewise, fault mapping was performed by recognising breaks and offsets in the continuity of seismic horizons. The horizon mapping has been performed using a combination of 2D/3D manual interpretation and seeded 2D and 3D autotracking.

An extensive number of seismic horizons were interpreted in order to understand the architecture of the basin fill and structural history (e.g. Fig. 2.3) and link this to the onshore interpretation. However, only a smaller number of key horizons have been selected to illustrate the findings.

Two-way time (TWT) structural maps and a TWT thickness map were generated to support structural interpretations. Multiple seismic attribute

analyses were carried out on the interpreted surfaces based on the 3D reflection seismic data to assist fault interpretation and enhance small-scale fault detection and visualisation. The seismic attributes are components extracted from seismic data (e.g. time, amplitude, frequency; Chopra and Marfurt 2007; Brown, 2011) that can be analysed in order to enhance specific geological, petrophysical and structural aspects. The present study used variance, edge detection and influential tools. Variance and Edge Detection are amongst the most useful geophysical tools used to highlight geological features and are routinely used to characterise fault and fracture networks (e.g. Chopra 2009; Chopra and Marfurt 2007; Di and Gao 2017).

Variance is possible the most used attribute in structural interpretation and is highly recommended for the identification of faults and fractures (e.g. Koson et al. 2014; Pigott et al. 2013). This attribute measures the discontinuities in the horizontal continuity of amplitude. Therefore, it converts a volume of continuity (the normal reflections) into a volume of discontinuities in the seismic data, hence highlighting faults or stratigraphic features (e.g. channels) (Fig. 2.4a; e.g. Brown 2011; Koson et al. 2014).

Edge detection is a geometrical attribute that can be generated on a map using 'structural operation'. This will create a property on the data object which highlights sharp edges where subtle changes in the surface topography occur. It can be used either to rapidly highlight a fault network, or to identify potential low throw structures not immediately discernible in the seismic sections (Fig. 2.2c; Petrel 2021).

The influential tools operation is a new feature implemented in Petrel (2021) which generates a property on the map that highlights areas of rapid 3D

geometric variation. The points highlighted in this way identify areas within the data set that are prominent on the 3D form of the data object (Fig. 2.4b; Petrel 2021).

2.3 Fieldwork

The field data described in this study focus on the brittle deformation recorded in the Devonian to upper Jurassic rocks cropping out along the southern

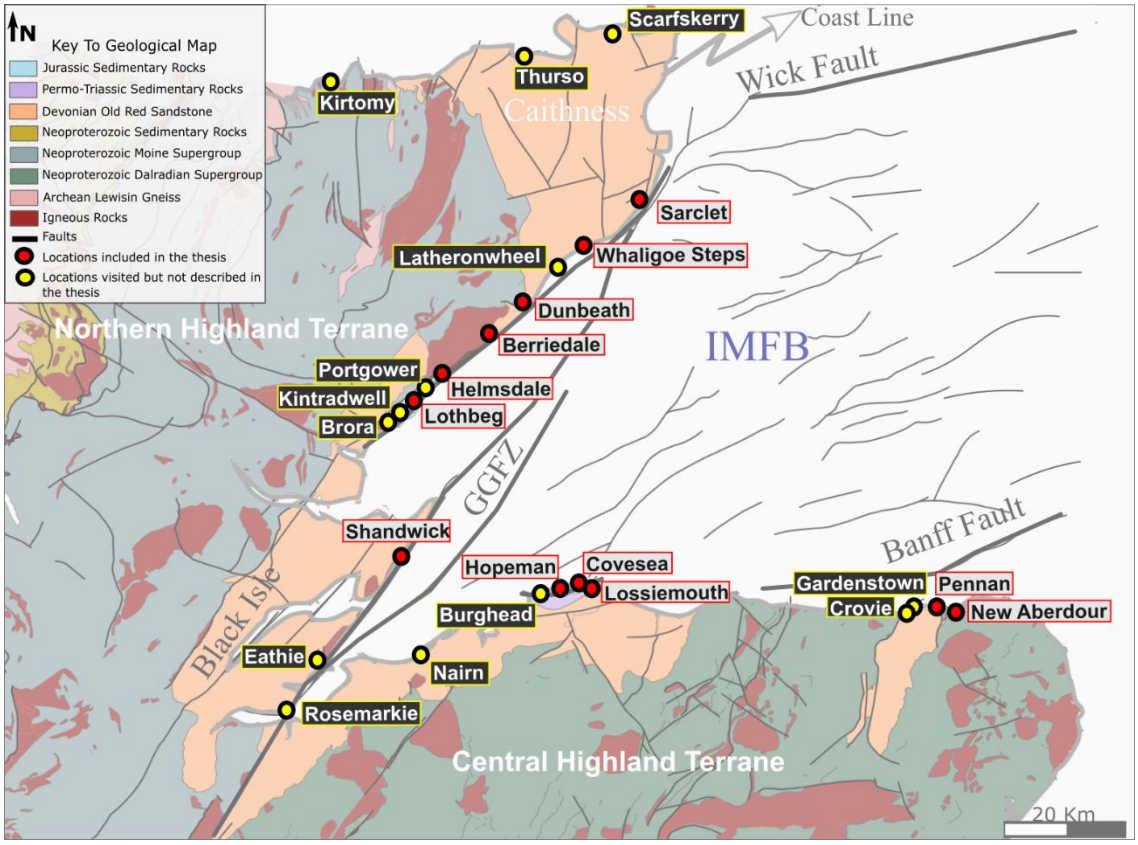

Fig. 2. 5: Localities investigated in the field.

and north-western coast of IMFB (Fig. 2.5). The onshore fieldwork is a core component of this thesis and was done during four field campaigns during 2018 and 2019 totalling c. ten weeks. A total of 26 locations (Fig. 2.5) were studied, of which 12 were selected and included in the thesis and are described in some detail. The key localities included are usually km-long exposures and were selected as they show representative sequences of events and a variety of brittle deformation structures. The outcrops are referred to based on their proximity to nearby villages or places. A grid reference (in UK National Grid) is given for each one when discussed in the chapters. Details from the other sites were not included for different reasons. Some were briefly visited to get background

information (e.g. Kirtomy, Thurso; related to north Caithness work of Dichiarante et al. 2016, 2021). Others, because the quality of the outcrop is poor and there is not enough evidence to support the structural interpretation (e.g. Nairn, Brora). Or that the features seen here are the same but less well developed compared to those seen at the red localities (e.g. Gardenstown, Portgower). To include these would simply lead to unnecessary duplication.

2.3.1 Fieldwork planning and data collection

The fieldwork started with a desk-based planning stage, where key outcrop locations were identified using pre-existing publish maps, fieldtrip guides together with Google Maps™ street view. Google Maps™ street view was a very useful tool in judging outcrop quality and accessibility, especially when a certain location was not described in a publication. The selection of the exposures was guided by the locations where major boundary or intrabasinal faults were exposed or rocks were exposed in close proximity to such faults where minor deformation can be observed and linked to the major faults.

Scoping fieldwork followed, where many of the selected localities were visited, and key exposures were identified for detailed data collection.

The data were collected in the form of structural measurements (e.g. dip/dip direction of planar structures, plunge/plunge azimuth of linear structures), notes, photographs, sketches, quick interpretation models, as well as collecting physical samples.

At each exposure, the typical workflow involved: i) locating the outcrop on the aerial/topographic map; ii) identifying the rock units and making a short description of lithologies, sedimentary structures, and measurements (dip/dip

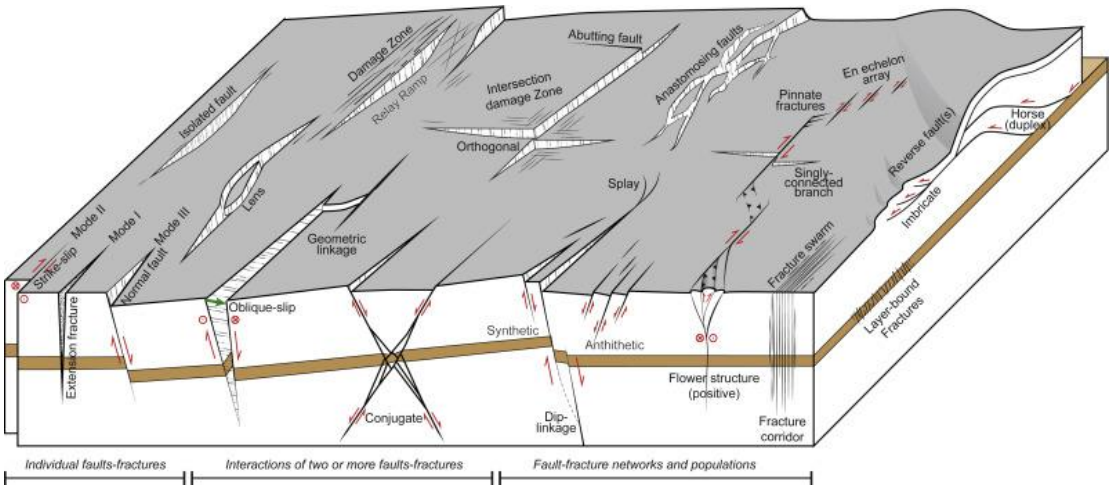

Fig. 2. 6: Schematic illustration of the range of fault and other fracture networks investigated in this study. After Peacock et al. (2016); used with permission - License Number: 5210611241789.

direction) of bedding; iii) characterising and measuring the brittle structures observed, including any kinematic information; iv) making preliminary interpretations of cross-cutting relationships and structural history; v) rock sample collection; and vi) photogrammetry data collection (see section 2.4.1).

The brittle structures investigated in this study comprises all the different types of faults, fractures or associated folds (Fig. 2.6).

Measurements of fault/fracture planes and observations of fault type, associated fault damage zone, fault rock and mineral fill were recorded.

The sense of fault movement was determined based on offset stratigraphic markers or kinematic indicators such as slickenlines, lineations, grooves and associated shear sense indicators. Fault-slip slickenline data were collected in-situ from exposed fault surfaces as both pitch and plunge/azimuth.

Folds elements were analysed and measurements of fold limb orientations, axial hinge lines and planes were taken when possible. The attitude of their hinge line/axial plane and the interlimb angle was later used to classify the folds (Fig. 2.7).

The structural measurements were taken using both a Suunto geological compass/clino and the FieldMove™ digital mapping application on an Apple iPad™ (6th Generation). FieldMove™ digital mapping application is a very powerful tool as it has a lot of useful functionalities such as:

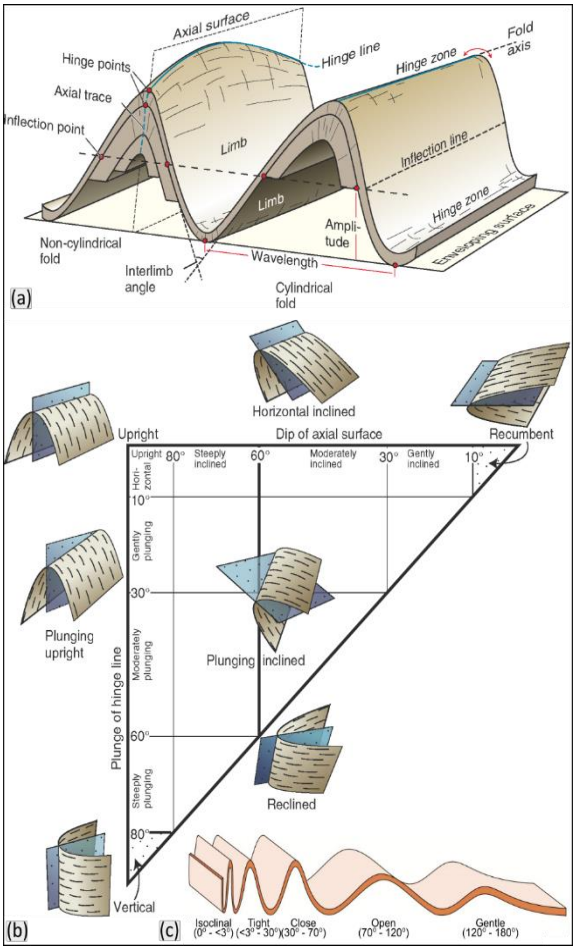

Fig. 2. 7: (a) Elements of a fold. Fold classification based on (b) the plunge of the hinge line and dip of the axial surface, and (c) interlimb angle. Compiled after (a-c) Navabi and Fossen (2021) and (b) Fossen (2011) used with permission - License Number: 5217680280028 and PLSclear Ref No: 59822.

- The ability to connect to satellite maps or import basemaps such as MBTile and GeoTiff to work offline.
- An embedded digital compass clinometer which allows the collection of structural measurements that can be directly displayed on a base map due to coordinate capture.
- A camera within the app, which allows taking photographs, which are also directly georeferenced, as well as annotating and sketching them.
- The ability to draw contacts, faults and outcrop polygons on your chosen basemap.
- A stereonet display of geological data.
- The ability to export data in different formats such as MOVE, KMZ or CSV files.

The measurements collected using FieldMove™ digital mapping were systematically double-checked with the geological compass to ensure accuracy and avoid errors. Although a lot of data were collected using the digital application, key information was also recorded in the notebook. Likewise, relevant photographs were also taken with another camera to avoid any potential data loss.

Structurally oriented samples of fault rocks and mineral fills associated with specific fault zones were collected for microscopic and geochronological analysis. Calcite mineral fills associated with faults or fractures were specifically collected for U-Pb geochronology. A key requirement in the field was to first recognise the presence of carbonate in order to make it suitable for collecting and dating. For that, a diluted solution of hydrochloric acid was used, together with analysing physical properties like colour, cleavage, or hardness.

2.3.2 Field data analysis and display

The measurements were graphically represented using both rose diagram plots of azimuth distributions (at 10° sector angles) and equal area stereonets, lower hemisphere projections using poles to planes where appropriate. The processing and visualisation were carried out using Stereonet 10 (Allmendinger et al. 2012; Cardozo and Allmendinger 2013). The contouring was done after Kamb (Kamb 1959) at 2 and 3 sigma standard deviation above a random population. Measurements of fold limbs were used to calculate axial lines/planes or interlimb angles when those elements could not be directly measured in the field.

Relevant average measurements of bedding, fault orientations or folds were illustrated on geological and/or aerial maps, photographs, or sketches.

Fault-slip slickenlines were used in order to perform a palaeostress inversion. This analysis was done in order to allow testing of previous hypotheses for the driving stress state associated with the various tectonic events or correlate the results with regional events. This analysis assumes that slip on a fault surface occurs in the direction of the maximum resolved shear stress (Wallace 1951; Bott 1959). Numerous methods have been developed to invert fault kinematic data and derive palaeostress (e.g. Spang 1972; Michael 1984; Angelier 1984,1990; Mostafa 2005) by obtaining the orientation of the three principal stress axes (σ_1, σ_2, and σ_3 which are the maximum, the intermediate, and the minimum principal stresses, respectively) and the stress ratio (R) which is defined as $(\sigma_1 - \sigma_2)/(\sigma_2 - \sigma_3)$, also called the reduced stress tensor. In this study, the fault data were analysed using the Angelier (1990) direct inversion method (INVD) implemented using the SG2PS software (Sasvári and Baharev 2014).

This method estimates the reduced stress tensor and the shear stress magnitudes from the fault-slip data (Angelier 1990). The program also graphically computes the stress regime based on the stress index (R') (Delvaux et al. 1997). The stress index is based on the identity of the vertical stress axes and the stress ratio as follows: radial extension (σ_1 vertical, 0 < R < 0.25); pure extension (σ_1

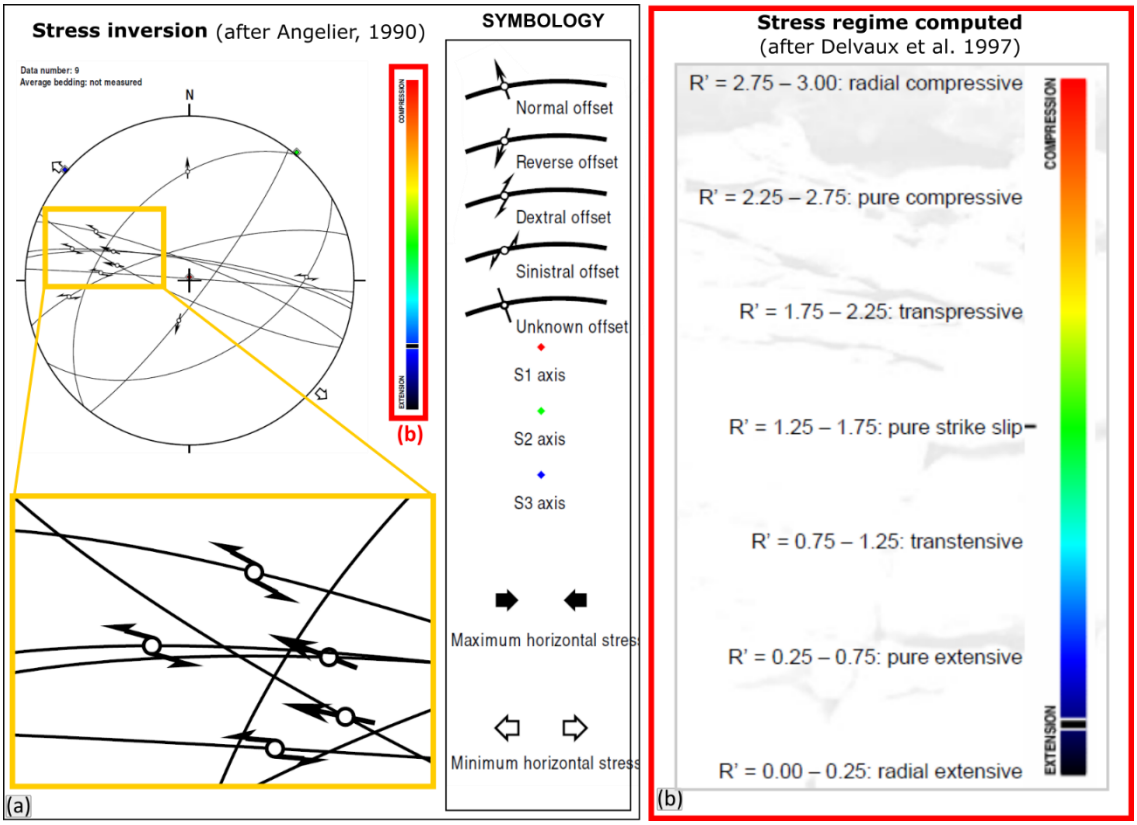

Fig. 2. 8: (a) Example of stress inversion plot and relevant symbology used by the the SG2PS softwere. (b) Stress regime computed based on the stress ratio.

vertical, 0.25 < R < 0.75); transtension (σ_2 vertical, 0.75 < R < 1 or σ_2 vertical, 1 > R > 0.75); pure strike-slip (σ_2 vertical, 0.75 > R > 0.25); transpression (σ_2 vertical, 0.25 > R > 0 or σ_3 vertical, 0 < R < 0.25); pure compression (σ_3, vertical, 0.25 < R < 0.75); and radial compression (σ_3 vertical, 0.75 < R < 1). The stress index is expressed numerically as continuous values between 0 and 3, where values ranging from 0 to 1 are defined for extensional stress regimes (R′ = R, σ_1 is vertical), 1 to 2 for strike-slip stress regimes (R′ = 2 − R, σ_2 is vertical), and

from 2 to 3 for compressional stress regimes (R′ = 2 + R, σ_3 is vertical) (Delvaux et al. 1997).

2.4 Remote sensing data

Aerial maps were used both as base maps for displaying structural data and occasionally for lineament analysis. The aerial maps were obtained using EDINA Digimap service, which provides access to high-quality 25 cm vertical ortho-photography available for Great Britain, created and licensed by Getmapping plc.

The UAV photogrammetry data were collected during the field data acquisition campaigns and were used to create 3D digital outcrops, digital elevation models, and high-resolution ortomosaic maps. These data were used for visualisation and structural data extraction.

2.4.1 Uncrewed aerial vehicle (UAV) photogrammetry

Photogrammetry, especially UAV-based photogrammetry, is a valuable and increasingly used technique (give some key references as examples). It allows a visual assessment of the spatial distribution of structures across a wide range of scales (cm to km) and gives greater access to otherwise inaccessible parts of the outcrop in cliffs. It also allows the routine extraction of structural observations and data from 3D digital outcrop models (DOM) (e.g. McCaffrey et al. 2005; Weismüller et al. 2019; Tamas et al. 2021). In this case, UAV photography was acquired using a DJI Mavic Air drone, which has a digital camera with a 12-megapixel image sensor.

A total of 23500 images were acquired from altitudes ranging from tens of centimeters to 120 meters above the lift-off ground level. Manual photograph acquisition was used for the vertical faces of some outcrops (e.g. Berridale, Dunbeath, Sarclet, Whaligoe Steps). The photographs from horizontally exposed outcrops (e.g. Crovie, Helmsdale, New Aberdour, Shandwick) were taken both using manual flight paths and automated flight paths (Fig. 2.9). The automated acquisition flight paths were flown as a double grid (two orthogonal flight grids).

Fig. 2. 9: Automated flight path grid used at New Aberdour.

For the automated data acquisition, Pix4Dcapture was used with a front overlap of 80% and a side overlap of 70%, and a 70° camera angle, which converges to orthogonal when the UAV is flying, as it slightly dips forward during flight. When flying the manual flight paths, similar photograph overlaps as with the automated acquisition are desired.

The creation of the DOM, DEM and orthomosaics, was done at Babes-Bolyai University, Romania, using Agisoft Metashape Professional. The first step in the process is aligning the photographs, generating a sparse point cloud (Fig. 2.10).

After alignment, the next step was to adjust the shape of the region, so that the following stages would generate and process data only in the region of interest, thus reducing processing time. The next step was the generation of the dense point cloud using the 'high' settings, which is a time and resource-consuming process. The 'calculate point confidence' option was enabled during this process as it was later used to filter out the highly uncertain points during the process of cleaning the dense point cloud (Fig. 2.10).

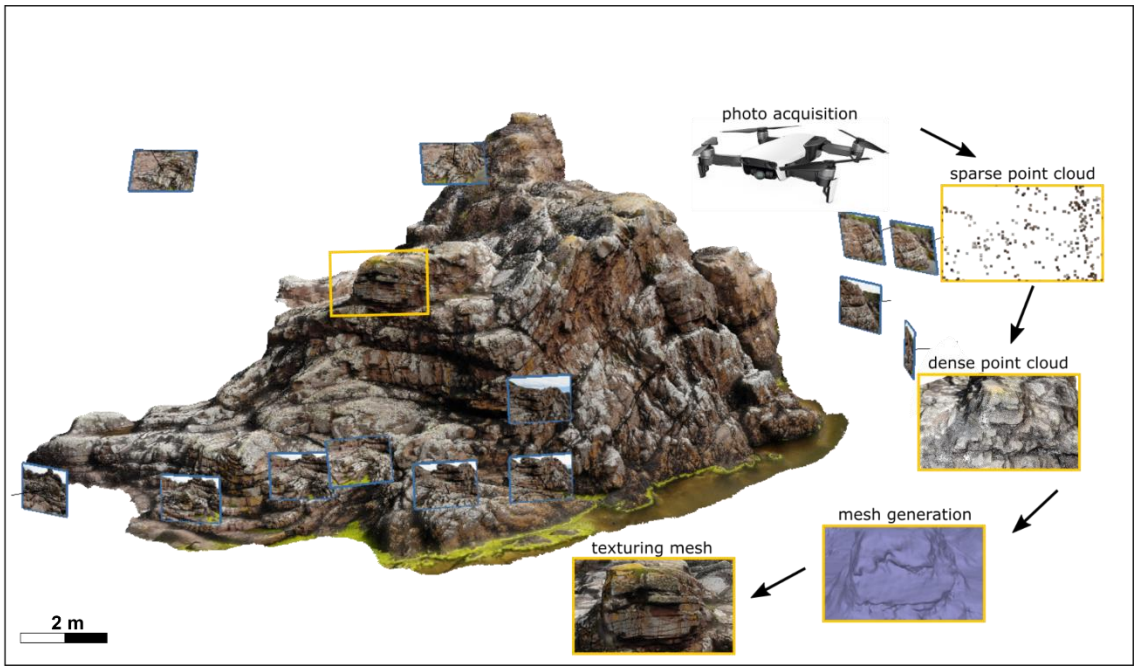

Fig. 2. 10: Photogrammetry workflow from photographs acquisition to generating texture meshes.

From the cleaned dense point cloud, both the DEM and the mesh (which was later textured) were generated (Fig. 2.10). Based on the DEM, the orthomosaic was generated, which was later imported in both Google Earth Pro and QGIS. The position match between the UAV-based orthomosaic and satellite imagery is almost exact; thus there is high confidence in the orientation of the DOM

created during the present study. Further quality control/ground truthing of each model was made by cross-checking structural measurements from the same area in both the model and in the field (where possible).

2.4.2 Structural data extraction

The DEM and orthomosaic data as well as aerial maps, were imported in QGIS, which was used to extract the visible structural features, fault and fracture orientations, etc. All the observable morphologies were traced in QGIS with the intention of extracting their orientation and dimension data. Lineament orientation analysis was performed using both FracPaQ (Healy et al. 2017), a MATLAB-based toolbox and NetworkGT (Nyberg et al. 2018), which is a QGIS plugin.

The 3D textured meshes (DOM) were imported into Virtual Reality Geological Studio software (Hodgetts et al. 2007) with the intention of interpreting them and extracting the orientation of structural features (Fig. 2.11). VRGS is a 3D data visualisation and interpretation software tool for field-based geology and geophysics (Hodgetts et al. 2007). Most of the extracted data are bedding

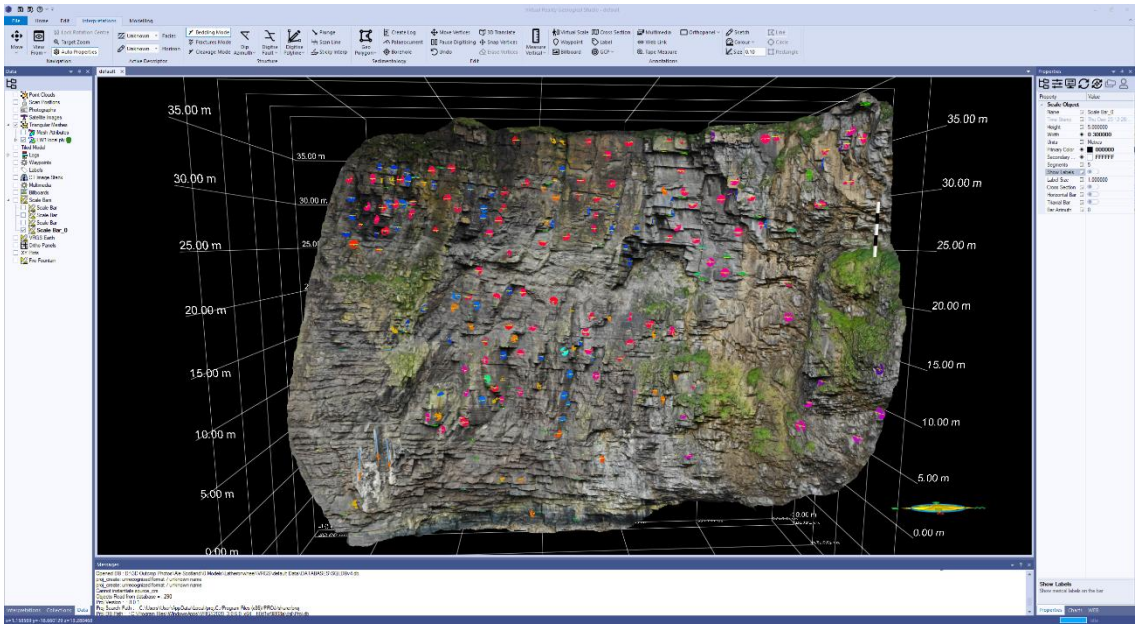

Fig. 2. 11: Example of DOM imported in VRGS for structural data extraction. The colourful circles represent measurements of planar structures while the arrows (bottom left) represent measurements of lineations.

orientations, fault orientations, fold axial planes, fold axes and sometimes even lineations on fault planes (Fig. 2.11).

Within VRGS, there are a number of tools made available for the extraction of planar (e.g. 3-point method, N-point based) and linear features (either by measuring plunge of one line or by interpreting polylines). After each measurement, the model was rotated in such a way (looking in dip direction) to assure the correctitude of the measurement, thus reducing the measurement error. In order to further reduce measurement uncertainty, the location of the measurements was also compared with the point confidence of the dense point cloud. Areas of high uncertainty (low dense point cloud confidence) were not considered for extraction of measurements.

One other valuable feature of VRGS is the possibility to use VR headsets (Oculus Rift S) to visualise the outcrops and identify features that were not previously observed both in the field and during DOM interpretation. Although VRGS has the possibility to display a stereonet window, the measurements were exported from the 3D data visualisation and interpretation software and imported into Stereonet and SG2PS software. These software were used to analyse and interpret the data and to generate the stereonet and roseplot graphics presented in this thesis. Where presented together with structural data collected by hand, these readings are shown in a different colour on stereoplots.

2.5 Microscopy and Geochronology

2.5.1 Microscopy

Thin sections were studied and photographed using an optical transmitted light microscope to ascertain the relative age of the mineral fills, any fault-related displacements and deformation. For calcite samples, a key requirement was to demonstrate whether the growth of calcite could be shown to be synchronous with fault displacements recognised during fieldwork. This was critical for interpreting the results of the geochronology data. Representative thin sections photomicrographs are used to illustrate the findings.

2.5.2 Geochronology

U-Pb analysis of calcite fracture fills was undertaken mostly at the University of Hull using in-situ laser ablation inductively coupled mass spectrometry (LA-ICP-MS). Ablation was carried out using an Applied Spectra, RESOlution-SE 193nm laser with a Laurin Technic S155 two volume cell, laser wavelength of 193 nm, pulse width of 5 ns, fluency of 5 j/cm^2, repetition rate of 10 Hz, ablation time of 30 s, 100 micron spot size. Helium and N_2 were used in the cell with Ar acting as the main carrier gas. Isotopic analyses were carried out using an Agillent 8800 ICP-MS with an RF power of 1170 W, nebuliser gas flow of 0.86 l/min with the electron multiplier in counts per second mode.

All samples were tested and mapped for uranium content (e.g. Fig. 2.12b) in order to ascertain whether they contain sufficient abundance of ^{238}U in order to yield a Model 1 U-Pb discordia age. Isotopic mapping (Fig. 2.12b) was carried out on polished chips (Fig. 2.12a) with a fluency of 5 j/cm^2, on laser energy of 6.4

mJ, square 80 x 80 µm spot size and a scan speed of 20 µm/s with a repetition rate of 10 Hz.

All uncertainties were propagated in the Iolite software package following the approach used in Holdsworth et al. (2020). The Iolite software uses the reference standard analyses to estimate the propagated analytical uncertainty. This is done by individually removing each analysis and treating it as an unknown which results in a population of pseudo-secondary standards. It does not address any potential sources of bias (e.g., nonmatrix matched standards, or measurement biases between zircon standards). Uncertainties are further propagated through the addition of the standard reference material uncertainties in quadrature. The U-Pb data is presented on Tera-Wasserburg plot (e.g. Fig. 2.12d), which shows the measured $^{207}Pb/^{204}Pb$ ratios plotted against $^{238}U/^{206}Pb$ ratios. A model 1 age calculated (with age and $Pb_{initial}$ uncertainties quoted as 1σ) using IsoplotR (Vermeesch 2018).

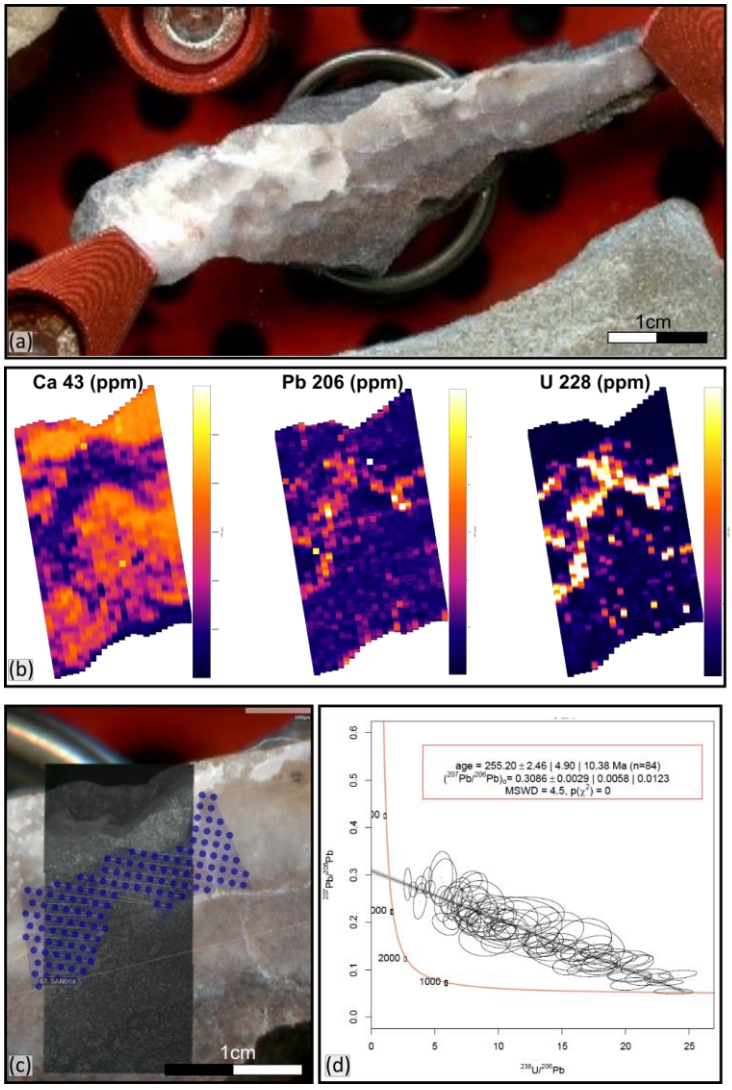

Fig. 2. 12: Example of calcite dating workflow (a) polished thick section/chips. (b) Calcium, lead, and uranium maps. (c) ablation sites (d) Tera-Wasserburg plot.

Three samples were also analysed at the BGS Isotope Geosciences Laboratory, of which one did not contain sufficient amounts of ^{238}U compared to common lead to yield suitable U/Pb ratios to produce a geologically meaningful date.

Further analytical protocols and analysed sample details are provided in the Supplementary Materials.

2.5 Structural validation techniques

Structural validation techniques are qualitative tools to assess the reliability of a structural interpretation. They usually comprise kinematic models such as structural restoration or forward modelling techniques to determine the evolution of a geometrical structural model (see Brandes and Tanner 2013 and references therein). Other methods include 'area-depth-strain', which is a non-kinematic tool for predicting fault displacement and detachment depth (see Totake et al. 2017 and references therein), or 'horizon flattening' of seismic reflection data.

In this study, 'horizon flattening' of seismic reflection and forward modelling was used to geometrically test some geological interpretations of offshore datasets.

Horizon flattening is a fast and straightforward tool implemented in Petrel software to undo the deformation (tilting, folding or faulting) and reconstruct

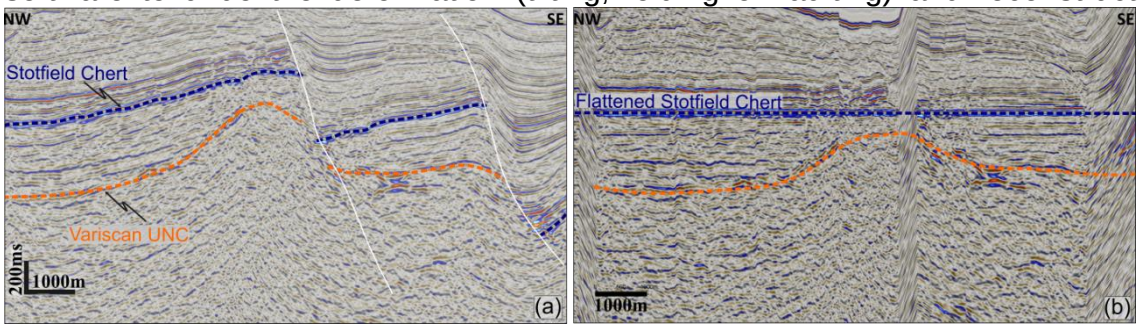

Fig. 2. 13: Example of horizon flattening operation done on the dashed blue seismic horizon (Stotfield Chert) (a) original profile and (b) seismic profile after the operation was performed.

geometries to allow better horizon correlation across faults or interpret geometries in the underlying sediment packages (e.g. Fig. 2.13).

Forward kinematic modelling is a sequential development of an initial undeformed sequence by successively adding and introducing displacement on faults as interpreted by the user to achieve the present-day geometry. As the faulted block moves progressively in relation to the fault displacement, the hanging wall changes its shape to honour the shape of the fault. Modern software like MOVE, which was used in this study, have a variety of embedded algorithms to constrain this geometrical change in shape (e.g. Suppe 1983; Egan et al. 1997; Kane et al. 1997).

The Old Red Sandstone at New Aberdour Bay.

Chapter 3

Devonian kinematic history of the Inner Moray Firth Basin and the role of the inherited faults in later stages of basin development: the Turriff sub-basin.

A version of chapter was published as: A. Tamas, R. E. Holdsworth, J. R. Underhill, D. M. Tamas, E. D. Dempsey, K. Hardman, A. Bird, D. McCarthy, K. J. W. McCaffrey, D. Selby. 2022a. ***New onshore insights into the role of structural inheritance during Mesozoic opening of the Inner Moray Firth Basin, Scotland.*** Journal of the Geological Society, https://doi.org/10.1144/jgs2021-066.
As the lead author, I conducted the fieldwork, collected and analysed the field data, integrated the microscopy and geochronology results, and wrote the first draft of the manuscript.

Abstract

The Inner Moray Firth Basin (IMFB) forms the western arm of the North Sea trilete rift system that initiated mainly during the Late Jurassic-Early Cretaceous with the widespread development of major NE-SW-trending dip-slip growth faults. The IMFB is superimposed over the southern part of the older Devonian Orcadian Basin. The potential influence of older rift-related faults on the kinematics of later Mesozoic basin opening has received little attention, partly due to the poor resolution of offshore seismic reflection data at depth. New field observations augmented by drone photography and photogrammetry, coupled with U-Pb geochronology have been used to explore the kinematic history of faulting in onshore exposures along the southern IMFB margin. Dip-slip N-S to NNE-SSW-striking Devonian growth faults are recognised that have undergone later dextral reactivation during NNW-SSE extension. The U-Pb calcite dating of a sample from the syn-kinematic calcite veins associated with this later episode shows that the age of fault reactivation is 130.99 ± 4.60 Ma (Hauterivian). The recognition of dextral-oblique Early Cretaceous reactivation of faults related to the underlying and older Orcadian Basin highlights the importance of structural inheritance in controlling basin- to sub-basin-scale architectures and how this influences the kinematics of IMFB rifting.

Key words: Inner Moray Firth Basin, Orcadian Basin, structural inheritance, reactivation, U-Pb calcite geochronology

3.1 Introduction

Many sedimentary basins worldwide are superimposed partially or completely over the sites of older, pre-existing basins, e.g. Colorado Basin (Lovecchio et al. 2018); East African Rift (Macgregor 2015; Ragon et al. 2018); the Gulf of Aden (Fournier et al. 2004); the Northeast Atlantic margin (Hansen et al. 2012; Henstra et al. 2019); East Greenland rift system (Rotevatn et al. 2018), the North Sea Rift (e.g. Tomasso et al. 2008) and the West Orkney Basin (Wilson et al. 2010). The role of inherited structures is commonly difficult to constrain in such settings due to the limited resolution of seismic data in offshore regions, whilst onshore areas may be limited by restricted surface exposure and lack of evidence to constrain the absolute age of fault movements. Yet, a better understanding of how earlier-formed faults localise deformation and interact during rifting can give key insights into basin development and potentially reduce sub-surface uncertainties. One potentially useful approach is to focus on well exposed coastal outcrops where structures imaged offshore can be traced directly or indirectly onshore. In many cases, individual faulting episodes will be associated with syn-tectonic mineral fills - such as calcite or base metal sulphides - which can then be dated using radiometric methods (e.g., U-Pb calcite) to constrain the age of specific faulting episodes (e.g. see approach used by Dichiarante et al. 2016; Roberts et al. 2020a). In particular in-situ LA-ICP-MS U-Pb calcite dating has become highly popular in recent years. Calcite can incorporate uranium upon its formation, making it a potentially suitable chronometer for U–Pb and U–Th geochronology allowing it to be used to provide direct timing constraints for a broad range of geoscience applications, including the timing of vein formation and crustal fluid

flow (Roberts et al. 2020b; Kylander-Clark 2020). Using in-situ LA-ICP-MS allows the targeting of specific microstructural features of carbonate-bearing fault rocks (Hoareau et al. 2021), giving a much more rigorous approach to calcite U-Pb dating of complex geological regions with multiple tectonic or fluid flow events.

This paper focuses on the nature, age and regional significance of faulting and fracturing present in the onshore Devonian succession of the southern IMFB and Orcadian Basin (Fig. 3.1a-c). New detailed field observations in the Turriff Sub-basin (Fig. 3.1c) coupled with U-Pb dating of syn-kinematic calcite mineralisation are used to document and characterise the kinematic history of faulting. The latter is utilised to explore the role that inherited Devonian structures played in basin development during subsequent (Mesozoic and Cenozoic) deformation. These findings reveal hitherto unrecognised evidence for interactions between younger rifting episodes and pre-existing sub-seismic-scale Devonian structures, providing a potential new structural template for interpretation of the subsurface basin architecture in the offshore IMFB and elsewhere.

3.2 Stratigraphic and structural setting

The IMFB is a superimposed basin founded on Precambrian to Caledonian metamorphic basement and post-orogenic Devonian-Carboniferous sedimentary rocks related to the Orcadian Basin. From Permian until Cretaceous it forms the western arm of the intra-continental North Sea trilete rift system (McQuillin et al. 1982; Frostick et al. 1988; Roberts et al. 1990; Andrews et al. 1990; Underhill 1991a; Thomson and Underhill 1993) that was created following a period of transient thermal doming in the

mid-Jurassic (Underhill and Partington 1993). The basin is bounded by major faults, including the Banff Fault to the south, the Helmsdale and Great Glen faults to the northwest, and the Wick Fault to the north (Fig. 3.1b).

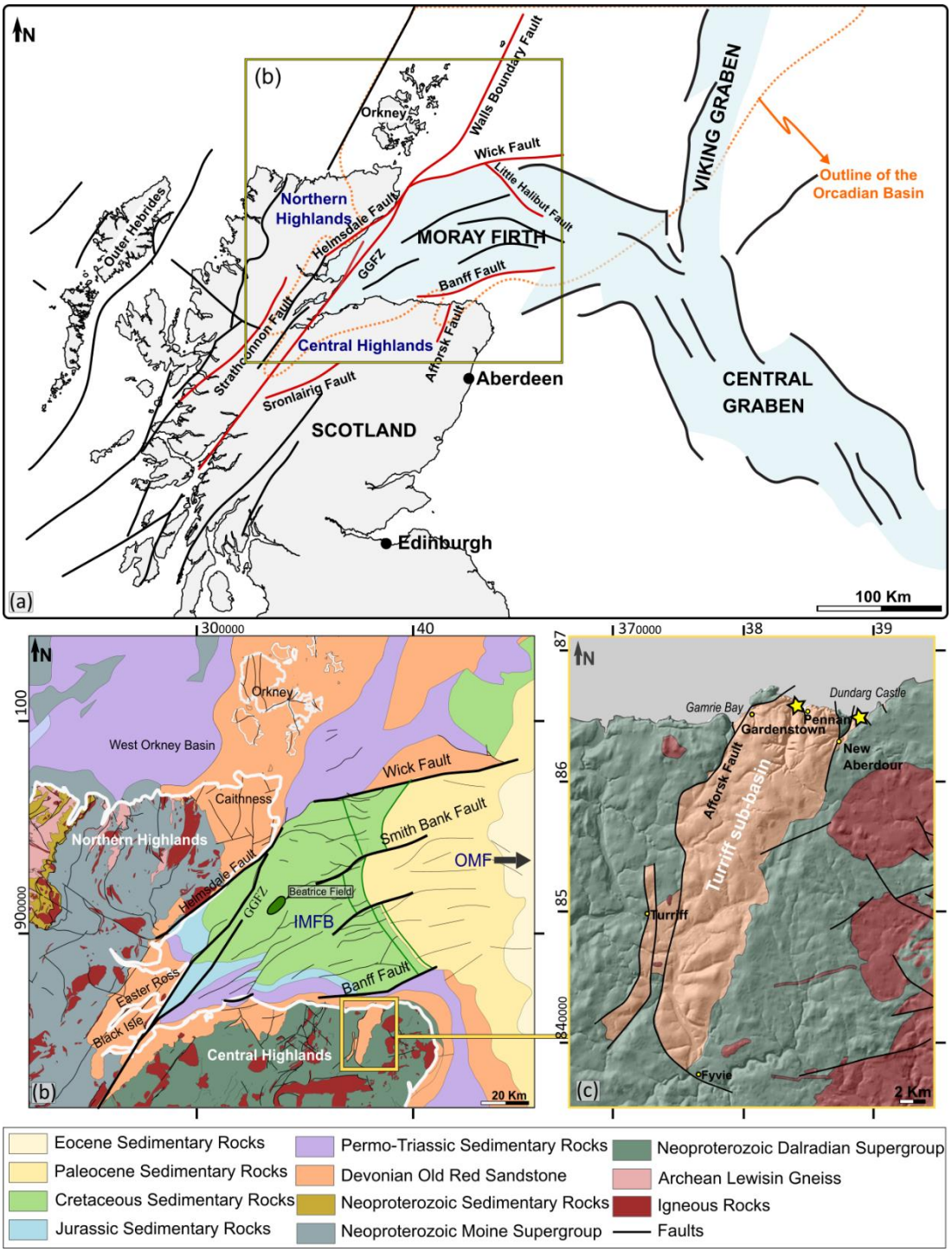

Fig. 3. 1: (a) Simplified tectonic map of Scotland and the North Sea showing the main fault systems (after Roberts and Holdsworth 1999; Zanella and Coward 2003 and Kemp et al. 2019). The faults mentioned in the text are shown in red. GGFZ, Great Glen Fault Zone. Outline of the Orcadian Basin marked in dotted orange line (after Duncan and Buxton, 1995) (b) Regional geological map of northern Scotland and associated offshore regions showing the main stratigraphy and fault systems (modified after Guariguata-Rojas and Underhill 2017 and British Geological Survey (BGS), UK. Using: EDINA Geology DigimapService, <http://edina.ac.uk/digimap. IMFB, Inner Moray Firth Basin. (c) Geological map of the Turriff sub-basin (modified after British Geological Survey (BGS), UK. Using: EDINA Geology DigimapService, <http://edina.ac.uk/digimap). Yellow stars show location of the areas of study.

The IMFB transitions eastwards into the Outer Moray Firth Basin, which links into the Central and Viking grabens in the central part of the North Sea. The IMFB is widely believed to record important episodes of Late Cretaceous- to Cenozoic-age regional uplift and faulting, including dextral reactivation of the Great Glen and sinistral reactivation of the Helmsdale faults (e.g. Underhill 1991a; Thomson and Underhill 1993; Le Breton et al. 2013).

The Mesozoic IMFB overlies the Devonian successions occupying the southern part of the Orcadian Basin (Fig. 3.1b; Johnstone and Mykura 1989; Friend et al. 2000). The earlier basin is a predominantly fluvial and lacustrine, intracratonic feature belonging to a much larger system of Devonian-Carboniferous basins that extends northwards into Shetland, western Norway, and eastern Greenland (Seranne 1992; Duncan and Buxton 1995; Woodcock and Strachan 2012).

The potential influence of older structures related to the Orcadian Basin on the geometry and kinematics of later IMFB opening has to date received little attention, partly due to the poor resolution of offshore seismic reflection data at depth, or sparse well data. It has been speculatively suggested, based on offshore data, that Orcadian Basin structures may have been reactivated in the IMFB (e.g. Norton et al.1987; Coward et al. 1989), but little compelling evidence for this inheritance has yet emerged and its potential importance remains uncertain.

3.2.1 Orcadian Basin

The Lower Devonian, basal part of the Orcadian Basin fill is represented by syn-rift alluvial fan and fluvial–lacustrine deposits. These units are mostly restricted to the western onshore-offshore parts of the IMFB (Rogers et al. 1989) and some areas of Caithness (NIREX 1994), with excellent exposures of limited extent also seen in the Turriff Sub-basin on the southern coast at Pennan-New Aberdour (Figs 3.1b, c and 3.2; e.g. Coward et al. 1989).

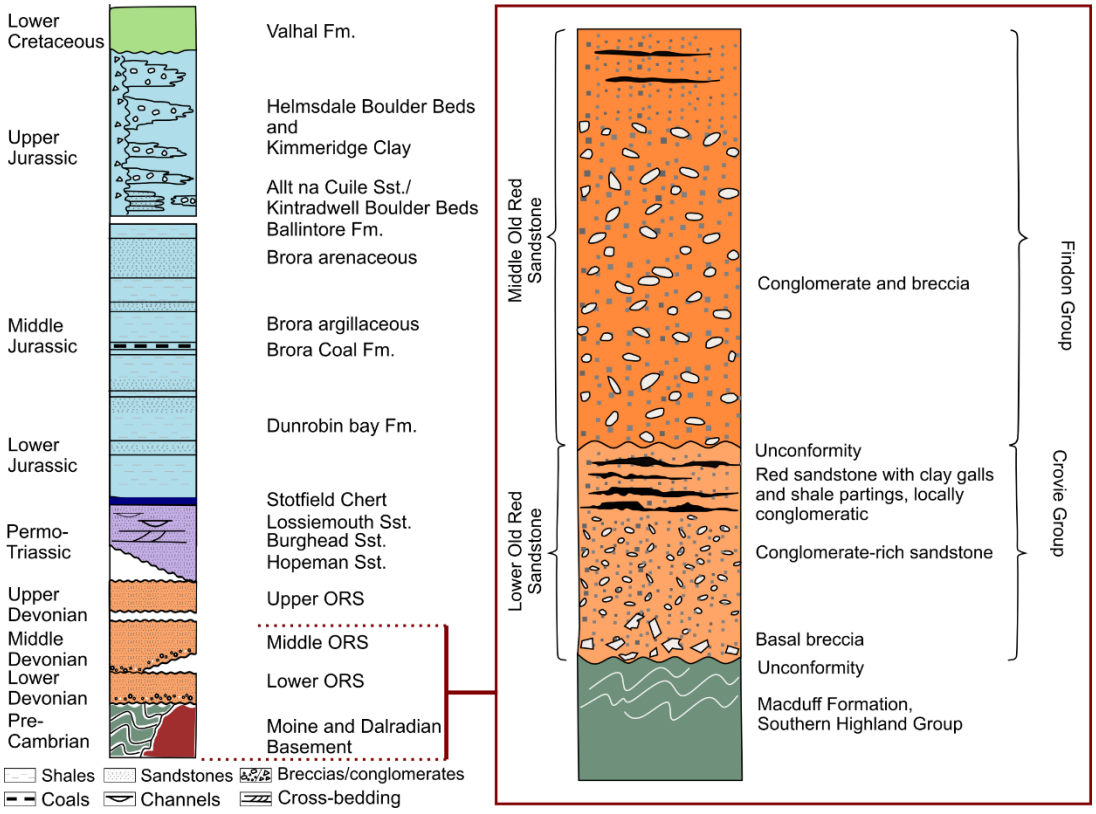

Fig. 3. 2: Left-hand column shows the general stratigraphy of the IMFB (modified after Trewin and Hurst 2009) with details concerning the Devonian sequence redrawn after Gunn et al. (2015) shown in the inset right-hand column. Not to scale, with relative thicknesses shown being notional.

Here, the Lower Devonian rocks unconformably overlie or are faulted against Neoproterozoic basement of the Dalradian Supergroup. They are thought to have been deposited in a series of small fault-bounded graben of limited extent (e.g. Friend et al. 2000). These strata are unconformably overlain by Middle Devonian syn-rift alluvial, fluvial, lacustrine and locally marine sequences. Rocks of this age dominate the onshore sequences exposed in Caithness,

Orkney and Shetland (Marshall and Hewett 2003). They are, in turn, overlain by Upper Devonian post-rift fluvial and aeolian sedimentary rocks (Friend et al. 2000). Younger Carboniferous rocks conformably overlie Devonian strata and are restricted to presently offshore regions of the Orcadian Basin. They comprise sandstones, conglomerates, and sparse claystones and siltstones interpreted as part of a regional fluvial depositional setting (e.g. Marshall and Hewett 2003).

The tectonic origin of the Orcadian and nearby West Orkney basins (Fig. 3.1b) has long been a matter of some controversy and debate. Interpretation of deep and shallow commercial seismic reflection profiles north of Scotland suggested that the West Orkney Basin comprises a series of half-graben bounded by easterly dipping normal faults (e.g. Brewer and Smythe 1984; Coward and Enfield 1987). Earlier interpretations (e.g. McClay et al. 1986; Enfield and Coward 1987) postulated that much of the basin fill here is Devonian and that the Orcadian - West Orkney basins formed due to extensional collapse of the Caledonian Orogen. More recent studies have cast doubt on these models, showing that the fill of the West Orkney Basin is mostly Permo-Triassic (e.g. Stoker et al. 1993) and that there is only limited onshore evidence for basement reactivation along the N coast of Scotland (e.g. Roberts and Holdsworth 1999; Wilson et al. 2010). Rifting in northern Scotland during the Devonian is now considered to be related to regional sinistral transtension during left-lateral shear along the Great Glen–Walls Boundary fault system (Seranne 1992; Dewey and Strachan 2003; Watts et al. 2007). However, Norton et al. (1987) argued against the dominance of strike-slip related development of the Orcadian basin and proposed a dip-slip evolution during

NW-SE extension, and used the Turriff Sub-basin as one of their case studies to support their interpretation.

The Orcadian Basin later experienced a Late Carboniferous-Early Permian inversion event, thought to be related to dextral strike-slip movements along the Great Glen-Walls Boundary fault system (e.g. Coward et al. 1989; Seranne 1992; Watts et al. 2007; Wilson et al. 2010; Dichiarante et al. 2020). This led to regional-scale N-S folding and reverse reactivation of pre-existing Devonian graben-bounding faults from the Scottish mainland to Shetland (e.g. Underhill and Brodie 1993; Dichiarante et al. 2020; Armitage et al. 2020). In Caithness these structures are then everywhere crosscut by younger, predominantly normal faults formed during a later NW-SE rifting event (Wilson et al. 2010; Dichiarante et al. 2020). Dichiarante et al. (2016) used Re-Os geochronology to date base metal sulphides in syn-tectonic normal to transtensional fault infills and veins in Devonian rocks of the Dounreay area. These yielded a mid-Permian (267.5 ± 3.4 [3.5] Ma) age of faulting, which Dichiarante et al. (2016, 2020) argued was related to the development of the offshore West Orkney Basin located just the northwest. Therefore, they viewed the latter basin as being younger, geographically separate and partially superimposed over the western flanks of the older Orcadian basin and its associated Devonian fills.

3.2.2 The Inner Moray Firth Basin

The stratigraphy of the IMFB (Fig. 3.2) is known from both surface (e.g. Hurst 1981; Pickering 1984; Frostick et al. 1988) and sub-surface studies (e.g. Andrews et al. 1990; Roberts et al. 1990). The outcrops in onshore regions to the north and south are dominated by Precambrian basement rocks and Silurian-Devonian Caledonian intrusions that are unconformably overlain by Palaeozoic (mainly Devonian, with lesser amounts of Permian strata) cover sequences (e.g. Johnstone and Mykura 1989; Stephenson and Gould, 1995). Mesozoic strata (Triassic to Jurassic) have a limited extent onshore and occur almost entirely along coastal margins (Fig. 3.1b; e.g. Trewin and Hurst 2009; Trewin 1987). Offshore, the sub-crop of the basin is dominated by Mesozoic-Cenozoic sedimentary rocks (Fig. 3.1b; e.g. Andrews et al. 1990; BGS 1995).

The IMFB is traditionally viewed as having opened during superimposed Permo-Triassic and Late Jurassic-Early Cretaceous rifting episodes, followed by episodes of subsidence, uplift and fault reactivation during the Late Cretaceous to Cenozoic (e.g. McQuillin et al. 1982; Underhill 1991a; Thomson and Underhill 1993). The importance of Permo-Triassic rifting - which is widely recognised in other parts of the North Sea (e.g. Steel and Ryseth 1990; Bell et al. 2014; Fazlikhani et al. 2020) - is debatable in the IMFB due to poor resolution of seismic reflection data at depths where Permo-Triassic strata are imaged, sparse well data, and limited onshore exposures. Early models suggested that during the Permo-Triassic, the basin evolved as a simple half-graben tilted against the Great Glen and Helmsdale faults (Frostick et al.1988). Other authors favoured a transtensional origin for the IMFB (e.g. McQuillin et al. 1982; Bird et al. 1987; Roberts et al. 1990). Such

models typically assumed that the Great Glen Fault formed the main controlling structure and suggested that the basin opened as a result of dextral movements along this structure during NE-SW extension. McQuillin et al. (1982) estimated ca. 8 km of displacement along the Great Glen Fault which then generated 5-6 km of extension between the Wick and Banff boundary faults.

The transtensional models and the role of the Great Glen Fault during basin opening were challenged based on findings in a series of later studies (e.g. Underhill 1991a; Thomson and Underhill 1993; Underhill and Brodie 1993). Largely based on detailed interpretation of seismic profiles and construction of thickness maps between key stratigraphic intervals, Underhill (1991) proposed a new model for the evolution of the IMFB. He suggested that, after a long period of thermal subsidence during the Triassic to Middle Jurassic, the basin opened mainly during the Late Jurassic under an orthogonal extensional regime. The main displacements are interpreted to lie along the Helmsdale Fault, as the synkinematic sequence thickens without change across the Great Glen Fault, and towards the Helmsdale Fault. This indicates that the former structure was inactive during the Late Jurassic. The widespread recognition of Jurassic-age syn-tectonic fault scarp breccias (locally termed the Boulder Beds) in the hanging-wall of the Helmsdale Fault onshore, along the north coast of the IMFB, further supports fault activity at this time during basin opening (e.g. Trewin and Hurst 2009; McArthur et al. 2013). In contrast to the previously suggested oblique- or strike-slip deformation under a NE-SW stress regime (e.g. McQuillin et al. 1982; Andrews et al. 1990), Underhill (1991) proposed an orthogonal NW-SE to NNW-SSE

extension direction across the Wick and Helmsdale faults. This is similar to the regime suggested by Davies et al. (2001) for the wider North Sea region during the Oxfordian and early Kimmeridgian, following a shift from E–W extension during the Bathonian and Callovian which generated N-S-trending structures in the Central Graben. The rifting in both the IMFB and wider North Sea is considered to be characterised by multiple stages of faulting separated by periods of near tectonic quiescence and is now generally thought to continue until the Early Cretaceous (e.g. Andrews et al. 1990; Davies et al. 2001; Zanella et al. 2003).

Limited information exists in the IMFB about a more detailed structural evolution and timing of fault activity, and it is also uncertain as to when rifting ended during the Early Cretaceous. Underhill (1991) suggested rifting up to the Berriasian followed by (post Berriasian) onlap and regional subsidence in an underfilled basin. Davies et al. (2001) consider that during the Kimmeridgian and Volgian, mainly NW-SE-trending faults developed under a NE-SW rifting direction, and that this extension ceased in the Berriasian. Andrews et al. (1990) imply that rifting continued until later in the Lower Cretaceous based on the preservation of thick (1.6 km) Valanginian to Albian syn-rift deposits in the hangingwall of the Little Halibut Fault (Fig. 3.1a). Roberts et al. (1990) identified the first reflector onlapping the syn-rift strata in the western part of the IMFB as near top Hauterivian. Argent et al. (2002) suggest the Smith Bank fault was active until the Hauterivian. It is generally agreed, however, that following the cessation of rifting, the basin then experienced a period of thermal subsidence during the Late Cretaceous (e.g. Andrews et al. 1990, Underhill 1991a).

From the Early Cenozoic to the present day, the IMFB is thought to have experienced episodes of uplift with regional erosion and eastward tilting, with some major faults undergoing reactivation (e.g. Underhill 1991a; Argent et al. 2002). These events have been variously related to the uplift caused by the regional development of the early Iceland mantle plume, the far field effects of the Alpine Orogeny, or to plate readjustment during the opening of the North Atlantic rift (see Le Breton et al. 2013 and references therein). The Great Glen Fault is believed to be the major controlling structure in the basin at this time (Underhill 1991a). Offshore, seismic reflection profiles show evidence for the development of strike-slip related deformation patterns including flower structures, folds and offset post-rift reflectors (e.g. Thomson and Underhill 1993; Underhill and Brodie 1993; Davies et al. 2001). Onshore evidence of Cenozoic structures supposedly includes the development of large-scale folds, of about 500m wavelength trending NW-SE, in the hangingwall of Helmsdale fault (Thomson and Underhill 1993; Thomson and Hillis 1995). In addition, minor folds and faults in the Jurassic strata exposed at Black Isle and Easter Ross (Fig. 3.1b) are considered to be Cenozoic and related to right-lateral slip of the Great Glen Fault (e.g. Underhill and Brodie 1993; Le Breton et al. 2013). The effects of Cenozoic deformation away from Great Glen Fault are less certain.

3.2.3 Turriff Sub-basin

Our study area lies in part of the N-S-trending Turriff Sub-basin (Fig. 3.1c), one of the largest Devonian outliers in the onshore Central Highlands (e.g. Stephenson and Gould 1995). The basin extends for c. 11 km along the southern coast of the IMFB from Gamrie Bay at Gardenstown to Dundarg

Castle at New Aberdour Bay and extends inland and southwards c. 40km to Fyvie (Fig. 3.1c). This location was chosen for study firstly due to the relatively good coastal exposures, and secondly because it presents a better opportunity to characterise both the Devonian and Mesozoic deformation patterns that are widely overprinted and obscured on the northern margins of the IMFB due to the effects of later supposedly Cenozoic reactivation along the Great Glen Fault zone (e.g. Le Breton et al. 2013).

The Turriff Sub-basin is a Devonian half-graben, bounded to the W by the Afforsk Fault whilst the eastern side is both faulted and locally unconformable on the Dalradian metamorphic basement (Fig 1c; e.g. Read 1923; Ashcroft and Wilson 1976; Trewin 1987). The stratigraphy, sedimentology and interpretation of depositional environments have been studied in some detail and it is generally agreed that the basin fill consists of both Lower and Middle Devonian rocks, assigned, respectively, to the Crovie and Findon groups (Fig. 3.2; e.g. Read 1923; Trewin 1987). An angular unconformity, considered the boundary between the two groups, is exceptionally well exposed at Pennan (Fig. 3.1c; BGS 1987; Trewin 1987; Gunn et al. 2015). The succession, having a total thickness of up to 800 m in the northern part and 1400 m in the southern part of the basin (e.g. Gunn et al. 2015), is dominated by breccias and conglomerates, with minor sandstones and mudstones, all of which show marked lateral facies variations. Both successions are interpreted to belong to alluvial fan systems with adjacent mudflats and playa lake deposits (e.g. Sweet 1985; Trewin 1987; Trewin et al. 1987). The breccias and conglomerates of the Crovie Group contain granitic

and felsitic clasts, while the Findon Group is dominated by clasts derived from the local Dalradian Macduff Slate (Trewin 1987).

The structural style of the Turriff Sub-basin is regarded as complex, especially on the IMFB coast (Ashcroft and Wilson 1976). The bedding is mostly gently westward dipping (e.g. Sweet 1985; Trewin 1987; Gunn et al. 2015), but Read (1923) in his detailed work noted a greater variability of dips. Several fault networks have been recognised based on surface geological mapping (e.g. Read 1923; Sweet 1985; Trewin 1987), gravity data (Ashcroft and Wilson 1976) or interpretation of nearby offshore seismic reflection profiles (e.g. Norton et al. 1987). The dominant fault strikes are predominantly NNE-SSW, parallel to the basin margins (e.g. Ashcroft and Wilson 1976; Sweet 1985; Trewin 1987; Coward et al. 1989). Ashcroft and Wilson (1976) interpreted fault development to have occurred during Devonian rifting based on comparisons with other parts of NE Scotland. Norton et al. (1987) suggested that the Devonian faults were highly arcuate along ESE-WNW, ENE-WSW and N-S trends. They proposed an overall NW-SE extension direction during the Devonian that would require a significant strike-slip component to occur along the segments of these faults which are obliquely oriented to the inferred rifting vector.

A younger set of faults trending ENE-WSW (e.g. Sweet 1985; Trewin 1987) were considered by Ashcroft and Wilson (1976) to have initiated during Permo-Carboniferous times, based on the observation that a dyke swarm interpreted by Buchan (1932) to be of that age has a similar trend across NE Scotland. These authors also noted that this ENE-WSW trend is approximately

parallel to the southern margin of the IMFB and suggested that movements along structures with this trend continued into the Mesozoic.

3.3 Methods

3.3.1 Fieldwork and stress inversion analyses

The field data described in this study focuses on the Lower and Middle Devonian coastal outcrops of the onshore Turriff Sub-basin (Fig. 3.1c). Kilometre-long exposures of Crovie and Findon groups (Read 1923; Trewin 1987) in the central and eastern part of the sub-basin show representative sequences of events and variety of brittle deformation structures. The outcrops are referred to as the Pennan and New Aberdour localities (Fig. 3.1c) here based on their proximity to nearby villages.

In-situ detailed field observations and measurements of bedding, faults, fractures, folds, fault rocks and associated mineralisation were recorded. Where accessible, the structural measurements were taken using both a Suunto geological compass/clinometer and the FieldMove™ digital mapping application on an Apple iPad™ (6th Generation). At each locality studied, the relative ages of structures were carefully assessed using cross-cutting relationships. The sense of fault movement was determined based on the presence of offset stratigraphic markers, kinematic indicators such as slickenlines, in addition to shear sense criteria such as asymmetric, en-echelon arrays of Riedel or tensile veins (e.g. Petit 1987).

Structural data processing and visualisation were carried out using Stereonet 10 (Allmendinger et al. 2012; Cardozo and Allmendinger 2013). The measurements were graphically represented using both rose diagram plots of azimuth distributions (at 10° sector angles) and equal area stereonets, lower

hemisphere projection using poles to planes where appropriate. The contouring was calculated after Kamb (Kamb 1959) at 2 and 3 sigma standard deviation above a random population.

Fault-slip slickenline data were collected in-situ from exposed fault surfaces in order to perform a palaeostress inversion. In this study, the fault data were analysed using the Angelier (1990)'s direct inversion method (INVD) implemented using the SG2PS software (Sasvári and Baharev 2014). This method estimates the reduced stress tensor and the shear stress magnitudes from the fault-slip data (Angelier 1990). The program also graphically computes the stress regime based on the stress index (R') (Delvaux et al. 1997).

3.3.1 Photogrammetry

The acquisition of UAV photography was made using a DJI Mavic Air drone, which has a digital camera with a 12-megapixel image sensor.

For horizontal exposures, we used a pre-set automated flight path and data acquisition process. This was achieved with the use of Pix4Dcapture software, used with an Apple iPad (6th generation). The acquisition parameters were a front overlap of 80% and a side overlap of 70%, and a 70° camera angle. The altitude of acquisition varied between a few centimetres to 50 meters. For the vertical or steeply inclined cliff exposures, we used a manual flight path and image acquisition process. The camera was oriented orthogonal to the exposure and we tried to achieve a similar level of overlap to the automated acquisition.

For the creation of the DOM, DEM (digital elevation models) and orthorectified models, we used Agisoft Metashape Professional™ (v.1.6.2). The 3D textured meshes (DOM), together with the dense point cloud data, were imported into Virtual Reality Geological Studio (VRGS v.2.52) software (Hodgetts et al. 2007) to allow structural interpretation and extraction of structural orientation data. These included bedding, fault and fracture orientations. Where presented together with structural data collected by hand, these readings are shown in a different colour on stereoplots. In order to reduce uncertainties regarding the positioning and orientation of the 3D outcrops and orthomosaics, several orientation measurements were ground-truthed. The orthomosaic orientation has also been cross-checked with satellite imagery data. Lineament orientation analysis was performed using FracPaQ (Healy et al. 2017), a MATLAB-based toolbox.

3.3.3 Microscopy and U-Pb geochronology

Structurally-oriented samples of calcite mineral fills associated with specific fault zones recognised during fieldwork were collected for microscopic and geochronological analysis. U-Pb analysis of four calcite fracture fills was undertaken at the University of Hull using in-situ laser ablation inductively coupled mass spectrometry (LA-ICP-MS).

Only one sample (S02) contained sufficient ^{238}U abundance (and low common lead values) in order to yield an accurate and precise date. A further sample (S01) was also analysed at the BGS Isotope Geosciences Laboratory, but did not contain sufficient amounts of ^{238}U compared with common lead to yield suitable U/Pb ratios to produce a geologically meaningful date. Analytical

protocols and analysed sample details are provided in the Supplementary Materials.

Thin sections were studied and photographed using an optical transmitted light microscope to ascertain the relative age of the mineral fills, any fault-related displacements and deformation. A key requirement here was to demonstrate that the growth of calcite could be shown to be synchronous with fault displacements recognised during fieldwork. All samples collected in the field represent calcite slickenfibres collected from the dextrally reactivated NNE-SSW-trending faults and associated Riedel shear fracture (c. 12 samples). As they show similar microstructural characteristics, thin sections from three representative samples from New Aberdour (S01-S03) are used in this paper to illustrate our findings.

For a more detailed explanation of all analytical methods, please see Chapter 2 and the supplementary files.

3.4 Results

3.4.1 Fieldwork

3.4.1.1 Pennan [Grid Reference NJ 845 654]

The village of Pennan lies in a central location along the coastal outcrop of the Turriff Sub-basin Devonian fill (Fig. 3.1c). The exposure studied here is about 1 km long and extends from Millshore [NJ 84059 65813] to Pennan Harbour [NJ 84716 65551] (Fig. 3a). The exposure comprises limited wavecut platforms and very good coastal cliff exposures 10 to 25 m high, that are fully accessible at intermediate and low tides. The rocks exposed belong to both the Crovie and Findon groups (Fig. 3.2; Read 1923; Trewin 1987). Both

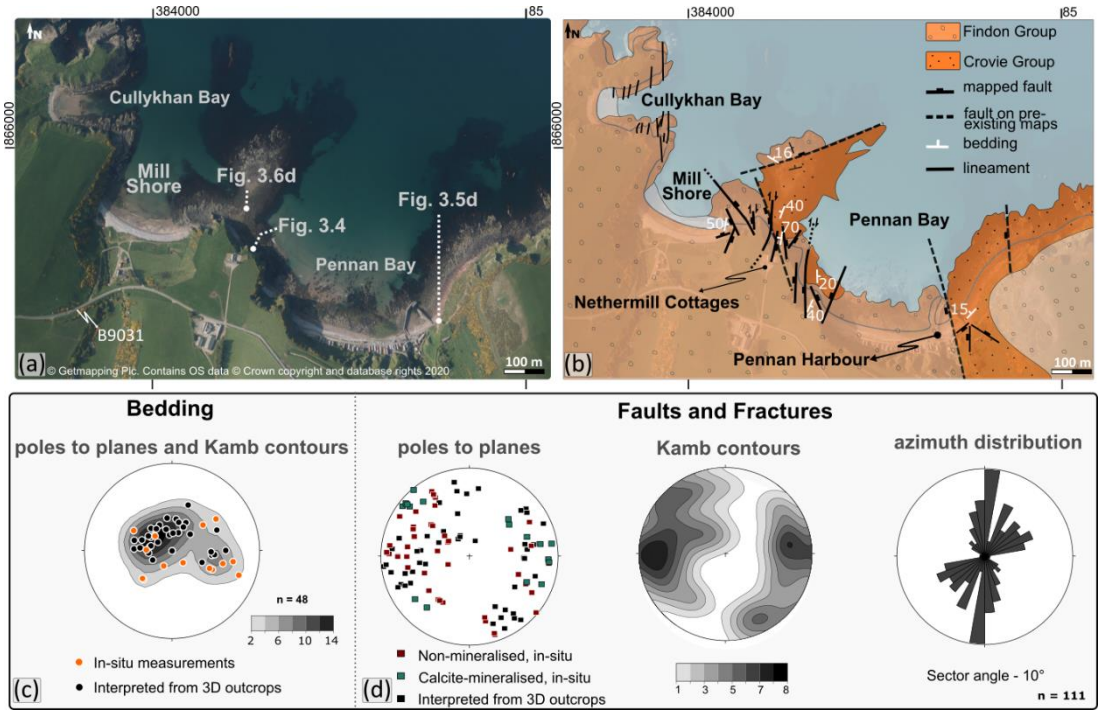

Fig. 3. 3: a) Aerial (using EdinaDigimap service © Getmapping Plc) and (b) geological map of Pennan. Field data supplemented with data digitised after Trewin 1987. (c, d) Stereonets and rose plots of structural data collected in the field. Lower hemisphere, equal area projections. The locations of Figures 4-6 are also shown in (a).

sequences here are predominantly composed of red conglomerates, breccias and sandstones and are interpreted to have formed in alluvial fan systems (e.g. Trewin 1987). The Findon Group is generally coarser grained, dominated by m-thick breccias with angular and subangular cm- to dm-scale fragments of Dalradian basement (Macduff Slates). Only a few cm-thick layers of medium-course red-coloured sandstone, usually lensoid (e.g. Fig 4b, c) can be observed, while in the older Crovie Group, red-coloured sandstones are better developed. The sandstone beds here can be more than a meter thick, but are more usually 10 to 50 cm in thickness (e.g. Figs 3.4b and 3.5). In the cliff exposure close to Pennan harbour (Figs 3.3b and 3.5c), they form a sandstone-dominated sequence with a vertical extent of at least 25 m. East of Millshore, below the Nethermill Cottages [NJ 84255 65724], an angular unconformity between the Crovie and Findon groups is beautifully exposed in coastal cliff and foreshore exposures (Fig. 3.4; see also Trewin 1987; Norton

et al. 1987). This location is traditionally considered to be the only place within the Orcadian Basin where an angular unconformity between the Lower and

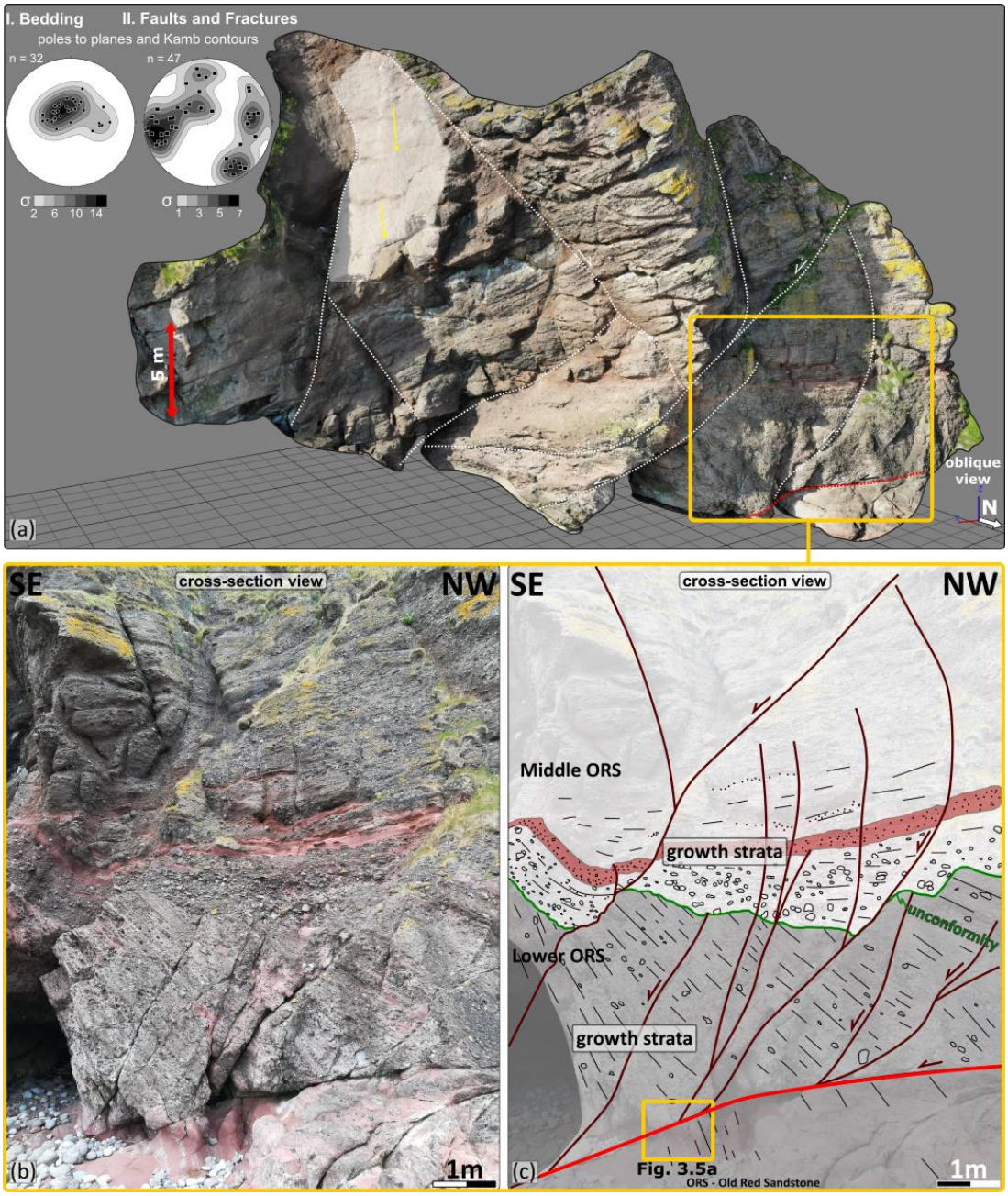

Fig. 3. 4: Cliff exposure below the Nethermill Cottages, location indicated on Fig. 3a. (a) 3D digital outcrop and inset lower hemisphere equal area stereonets derived from planes extracted from 3D photogrammetric model. Main faults are highlighted in white with senses of offset where known. Lineations on fault plane are shown with yellow lines. Locations of (b) and (c) are indicated by the yellow box. (b) Field photograph and (c) line drawing showing a cross-sectional view looking SW onto the angular unconformity between the Lower and Middle Devonian and main faults with growth strata in their hangingwall. Note the low-angle fault at the base of the outcrop. The location of Figure 5a is shown by the yellow box.

Middle Devonian sequences can be directly observed (e.g. Norton et al. 1987).

In both the Crovie and Findon groups, bedding orientations are quite variable, dipping gently to steeply (~15° to 70°) usually towards the E or W, and more locally in other directions (Fig. 3.3c). Close to Millshore, the bedding dips mainly ~30° to 50° to E or ESE (Fig. 3.3b). Walking east, in the cliffs below Nethermill Cottages, the dips steepen up to 70° and are usually inclined towards the west, whilst about 100-150 m from the cliffs to the north in the wavecut platform, the dips are shallower and are generally towards the NE (Fig. 3.3b). The beds are also more gently dipping NW on the eastern side of Pennan Bay, close to the harbour (Fig. 3.3b).

The Crovie and Findon groups are crosscut by numerous, commonly closely-spaced (decimetre to metre separation) faults, fractures or fracture corridors and veins (e.g. Figs 3.4 to 3.6). Fault displacement histories are complex, but most faults show a significant component of normal movement based on offsets of bedding markers. The main set of faults and fractures have two preferred orientations. The dominant set trend broadly N-S (~30°scatter) dipping both E and W, while a second set trend NE-SW (~60° scatter) (Fig. 3.3d). The normal fault planes typically have high to sub-vertical dips (60 to 88º), but less common, shallowly-dipping faults of about 20°- 40° are also encountered locally (Fig. 3.3d).

In the cliffs below the Nethermill Cottages, the angular unconformity between the Lower and Middle Devonian is spectacularly exposed in an outcrop 15 m wide and 20 m high, forming a local half-graben tilted towards the E (Fig. 3.4a). The sequence is affected by a series of decimetre- to metre-spaced normal offset faults (e.g. Fig. 3.4b and c). The amount of offset along individual faults is usually difficult to quantify due to the lack of stratigraphic

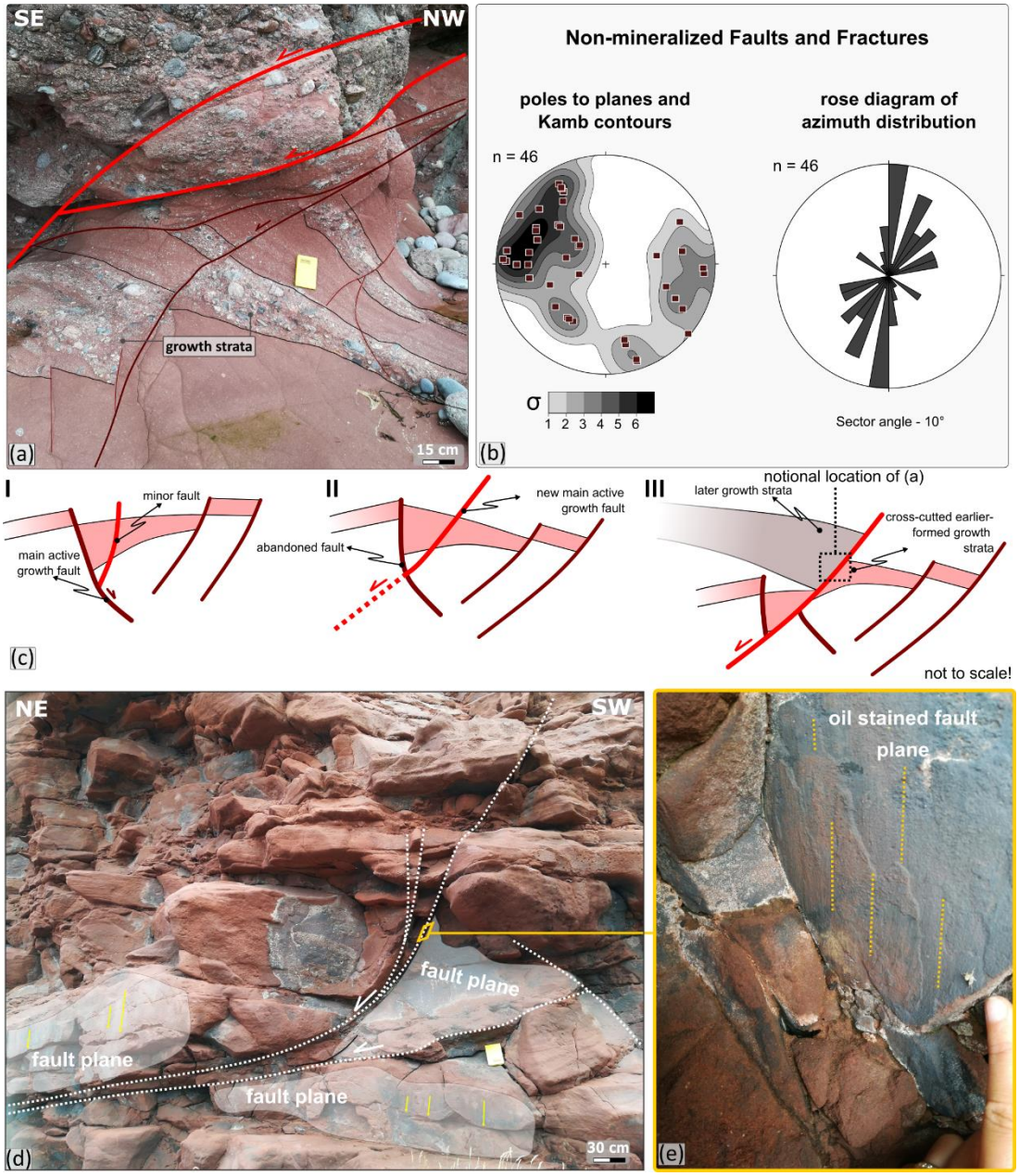

Fig. 3. 5: Non-mineralised faults and fractures at Pennan locality. (a) Oblique view showing growth packages within the tilted Lower Devonian sequence. The non-mineralised faults are highlighted in red (see location on Fig. 4b). (b) Stereonet and rose plot of the non-mineralised faults and fractures at Pennan. (c) Sketch explaining the presence of growth strata in the footwall of the bright red coloured fault in Figs 4 and 5a (d) Field photographs showing low angle and listric faults in the Lower Devonian exposure at Pennan Harbour (see location on Fig. 3a). (e) Oblique view of an exposed non-mineralised fault plane showing dip-slip kinematics. In places, oil stains are visible on the fault/fracture planes.

markers, but where it can be observed, faults show dip-slip displacements ranging from a few centimetres (e.g. Fig. 3.5a) up to several metres.

Clear thickening of the strata can be observed in the hangingwalls of faulted units both below and above the unconformity, illustrating the persistent and syn-kinematic nature of growth faulting during deposition of both the

Crovie and Findon group strata (Figs 3.4 and 3.5a). While some growth faults do not pass up into the younger Middle Devonian succession, others clearly do continue and also show growth thickening of beds into fault hangingwalls within the younger stratigraphy (Fig. 3.4). The faulted blocks show locally significant amounts of rotation (~40º), and this has contributed to the markedly angular nature of the unconformity developed between what are considered to be Lower and Middle Devonian strata (e.g. BGS 1987; Trewin 1987). The prominent low angle fault (highlighted in bright red) at the base of the outcrop in Figure 4 shows growth strata both in the hangingwall (Fig. 3.4b and c) and (apparently) in the footwall (Fig. 3.5a). This aspect can be explained by subsequent cross-cutting faulting and block rotation (Fig. 3.5c).

Close to Pennan harbour, a previously mapped (e.g. Trewin 1987; BGS 1995) major N-S-trending fault juxtaposes Middle Devonian hangingwall strata to the west against a Lower Devonian footwall to the east (Fig. 3b). The fault core is not exposed, but about 70 m east in the footwall of the fault, a ~10 m wide fault-parallel deformation zone is exposed. It is characterised by multiple decimetre-spaced faults and fractures (Fig. 3.5d). Most are shallow to steeply dipping (~10-85º), NW-SE-trending structures. Here, the low angle planes appear to be more shallowly-dipping segments of a series of curved or listric geometry faults, which have higher dips in the upper part, decreasing to (near) horizontal down dip (e.g. Fig. 3.5d).

The fault rocks and mineral fills associated with the brittle structures identified at Pennan can be divided in two main types. The first group comprises fault zones characterised by sharply-defined, clean breaks (e.g. Figs 3.5a, d, e), sometimes associated with dm-thick fault breccia infilling

dilatant jogs, and dark red or green gouges. We refer to these as '*non-mineralised faults'*. The other fault group is marked by the development of calcite-cemented breccias (Fig. 3.6a, b), calcite tensile veins (Fig. 3.6d) and

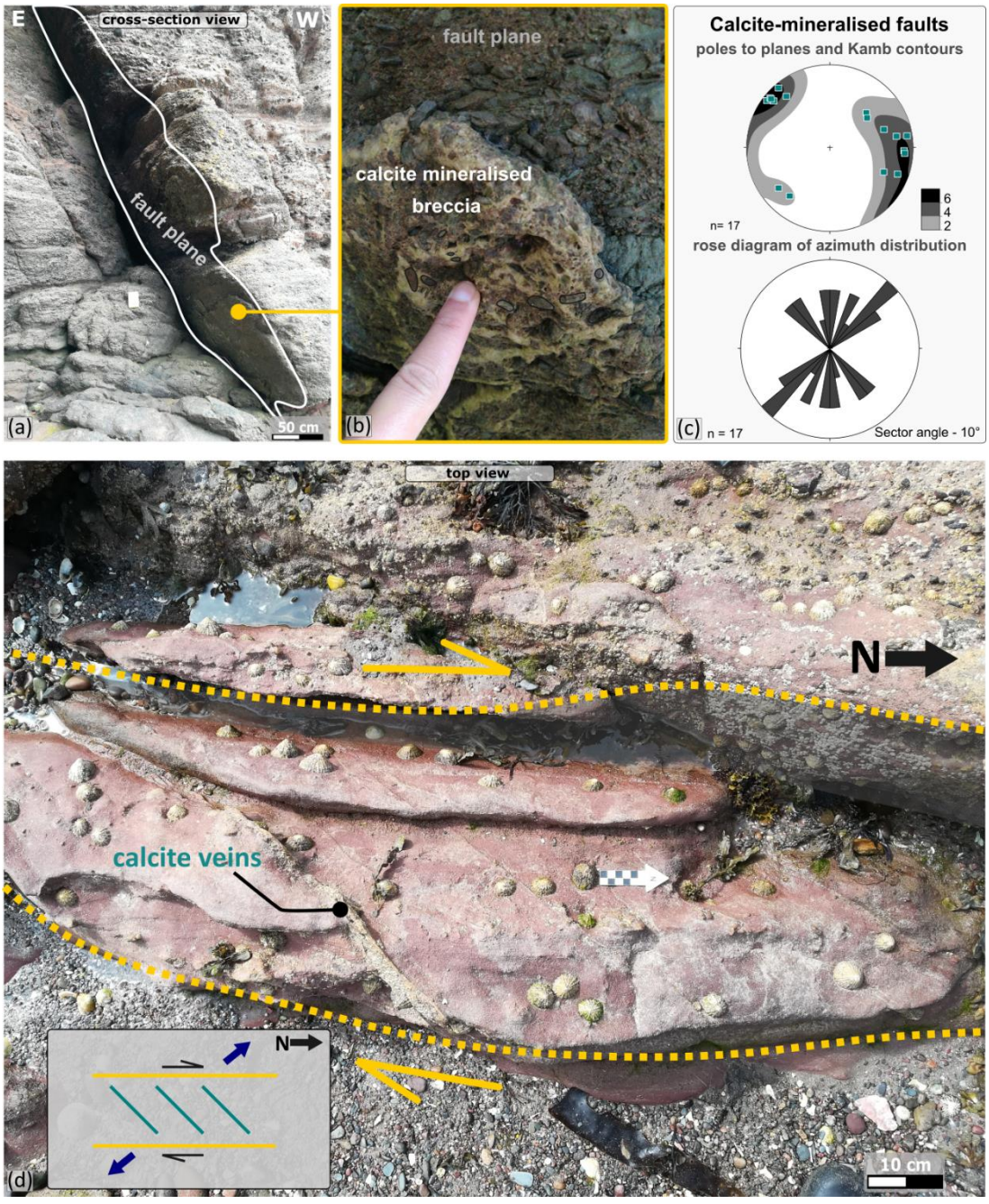

Fig. 3. 6: Calcite mineralised faults, fractures and associated structures at the Pennan locality. (a) Cross section view of a N-S-trending calcite-mineralised fault. (b) Detailed image of calcite mineralised breccia in the fault core. c) Stereonet and rose plot of calcite mineralised faults and fractures (lower hemisphere, equal area projection). d) Oblique view and sketch of tensile calcite veins associated with a N-S-trending fault indicating dextral slip along the fault.

calcite slickenfibres developed along shear plane surfaces. We refer to these as '*calcite-mineralised faults'*.

The non-mineralised faults predominantly trend N-S to NNE-SSW and NW-SE (Fig. 3.5b). Although kinematic indicators are uncommon, slickenline lineations and grooves are sometimes preserved, especially in finer-grained units of the Crovie Group (e.g. Fig. 3.5d and e). The fault panels of N-S- to NNE-SSW-trending structures typically show dip-slip to sinistral-oblique kinematics (~50° to 85° pitch), while the NW-SE-trending faults are usually dip-slip (80-90° pitch, e.g. Fig. 3.5d and e).

The calcite-mineralised faults and veins predominantly trend NE-SW, but N-S- to NNE-SSW- or NW-SE-trending faults are also present (Fig. 3.6c). Calcite mineralisation is mainly seen in patches, cementing the breccia in fault zones (Fig. 3.6a, b) or in adjacent wall rocks forming tensile veins of less than 1mm to several cm thick (Fig. 3.6d). The NE-SW trend is well represented by tensile veins observed in close proximity to N-S-trending faults (Fig. 3.6d). A key feature of the calcite mineralised faults is that, in contrast with the non-mineralised structures, the N-S- to NNE-SSW-trending faults show dextral to oblique-dextral/normal kinematics. This is indicated by both slickenlines identified on the fault panels and also by asymmetrically associated tensile veins arranged in en-echelon arrays. Figure 6d shows an example of oblique dextral slip associated with one of the major N-S-trending, steeply dipping faults (80/270) which can be traced in both the cliffs and wave-cut platform. The fault is associated with en-echelon, calcite-mineralised tensile veins trending NE-SW (Fig. 3.6d.) suggesting a component of dextral slip during NNE-SSW extension (Fig. 3.6d inset).

3.4.1.2 New Aberdour [Grid Reference NJ 884 633]

The village of New Aberdour lies on the coast about 7 km east of Pennan. The area is located close to the eastern margin of the Turriff Sub-basin (Fig. 3.1c). The investigated exposures extend about 1.5 km along the shoreline of New Aberdour Bay [NJ 885 646]. A flat-lying wave-cut platform 150-200 m wide which is accessible at low tide is present on the west side of

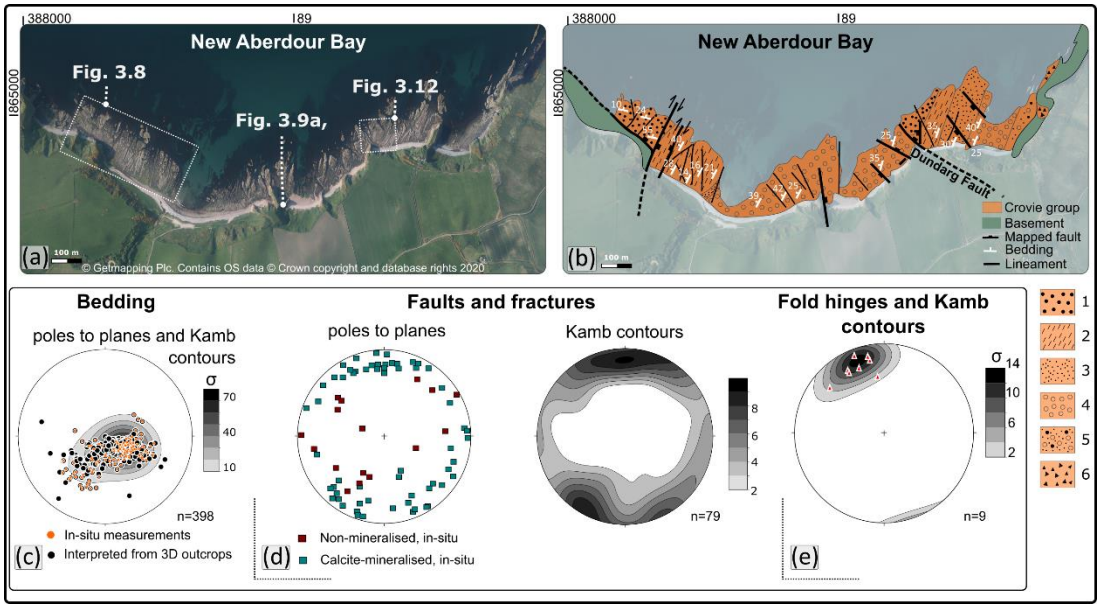

Fig. 3. 7: (a) Aerial map (using EdinaDigimap service © Getmapping Plc) and (b) geological map of New Aberdour. Lithology data digitised after Sweet, 1985: from younger to older: 1 - sandstones and siltstones; 2 - sandy mudstone, mudstone, limestone; 3 - coarse to fine sandstone; 4 - conglomeratic sandstone; 5 - conglomeratic sandstone with trough cross bedding; 6 – breccia. (c) Stereonets of structural data collected in the field. Lower hemisphere, equal area projections. Locations of Figures 8, 9a, b and 12 are also shown in (a).

the bay, while towards the east, both flat-lying platforms and cliffs up to 25 m high are exposed.

The exposed Lower Devonian rocks belong to the Crovie Group (e.g. Sweet, 1985; Fig. 3.7b). On the easternmost side of the bay, the succession unconformably overlies Dalradian basement rocks (Fig. 2b) and comprises metre-thick beds of light red, poorly-sorted breccias with angular/sub-angular clasts of Dalradian basement rocks (mainly andalusite and biotite schist), interpreted to have formed as debris-flow deposits laid down in alluvial fan systems (lithology 6, Fig. 3.7b; e.g. Sweet 1985; Trewin et al. 1987). The succession continues to the west as medium-grained fluviatile sandstones

which are conglomeratic at the base and preserve trough cross bedding locally (lithology 5, Fig. 3.7b). Based on paleocurrent data, Sweet (1985) suggested that the sediments gradually filled a NNE-SSW-trending palaeo-valley. This sequence is overlain by a meter-thick bedded conglomeratic sequence (lithology 4, Fig. 3.7b) that becomes thinner-bedded and dominated by sandstones (lithology 3) representing proximal and distal alluvial fan environments, respectively (Sweet 1985). This, in turn, passes upwards into a sequence of cm-thick, fine-grained sandstones, laminated red and green mudstones and limestones (lithology 1 and 2, Fig. 3.7b). They have been interpreted as alluvial plain/playa lake deposits (e.g. Sweet 1985; Trewin et al. 1987).

Overall, the beds are typically sub-horizontal to gently dipping (02° to 30°) to the WNW but, as seen at Pennan, steeper dips (up to 55°) and a variety of dip directions are encountered locally (Fig. 3.7b and c). The sequence is crosscut by numerous faults, fractures and veins of variable orientations (Figs 3.7b-d). These display components of normal offset along faults where this can be determined from offsets of stratal marker horizons.

A large (50,000 m^2) high resolution orthorectified image (Fig. 3.8a) and DEM (Fig. 3.8b) model obtained from UAV photography was acquired from the western side of the bay and enabled a lineament analysis to be performed that revealed the dominant structural trends. The interpretation was verified with field observations to ensure that the picked lineaments corresponded to faults, fractures and veins. 102 lineaments of more than ~10 m length were interpreted within the entire area of the model (Fig. 3.8c), while 328 lineaments of less than 10 m were measured on a smaller, well-exposed area of about

225 m^2 (Fig. 3.8d). At larger scales, NNW-SSE to NNE-SSW trends dominate, with subordinate NE-SW- and E-W- to SE-NW-trending structures also present (Fig. 3.8c.). At smaller scales, the ENE-WSW trend (40° scatter) is

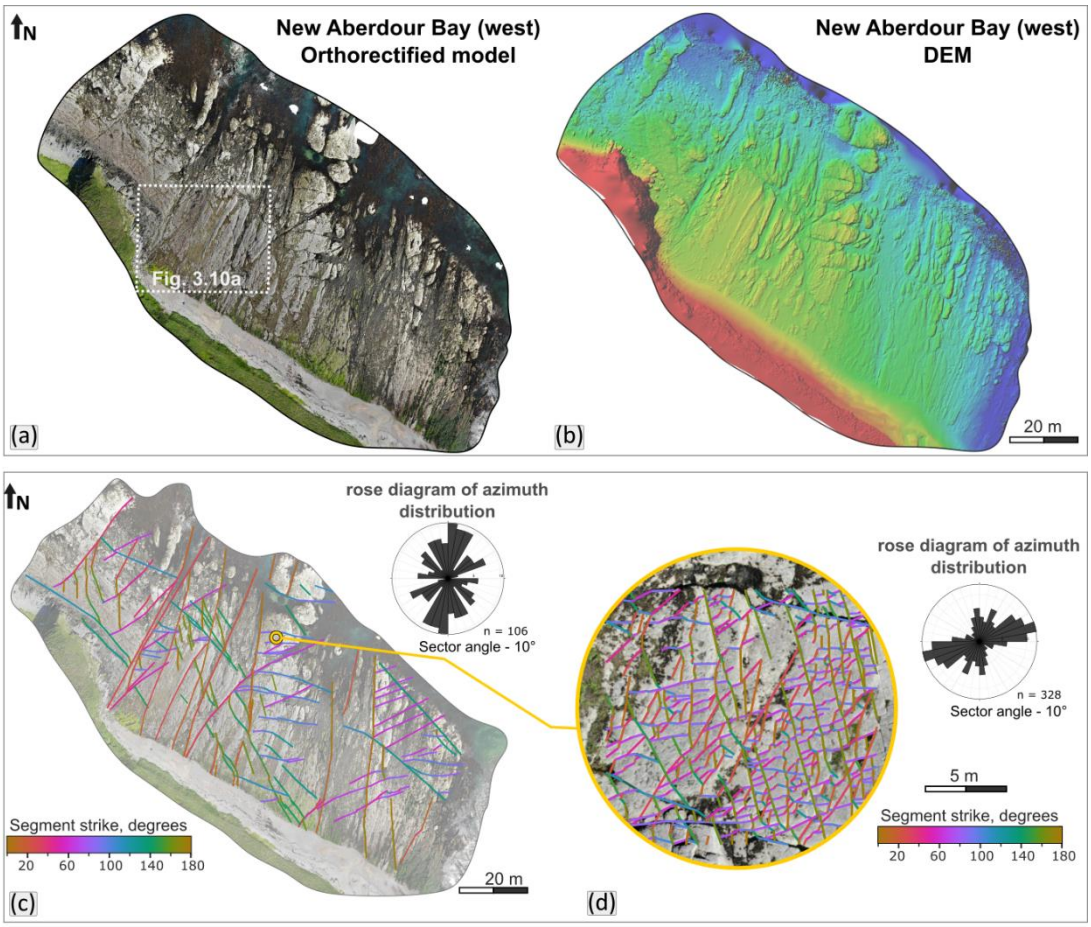

Fig. 3. 8: Overview and lineament interpretation of the western side of New Aberdour Bay. Location of the area shown in Fig 10a is also shown. (a) Orthomosaic model obtained from UAV (Unmanned Aerial Vehicle) photography. (b) DEM model, providing high resolution image for lineament interpretation. Orthomosaic models and inset rose diagram showing lineaments of (c) more than ~10m length and (d) less than ~10m length.

better represented, but lineaments trending NNW-SSE to NNE-SSW also occur (Fig. 8d).

Similar to the Pennan locality, the faults and fractures imaged and directly measured in the field can be subdivided into non-mineralised and calcite mineralised groups. The non-mineralised faults trend ESE-WNW and N-S to NE-SW (Figs 3.9a-c). The fault zones are characterised by sharply defined clean breaks (e.g. Fig. 3.9b), red/green mm- to cm-thick gouges (Fig. 3.9a) or cm- to dm-thick fault breccias. Kinematic indicators such as slickenline

lineations and grooves are sometimes preserved on exposed fault panels (e.g. Figs 3.9b and 3.10c). On ESE-WNW-trending faults, the kinematic indicators are rarely visible. Only one fault preserved indications of normal, dextral oblique-slip kinematics. On N-S to NNE-SSW trends slickenlines indicate dip-

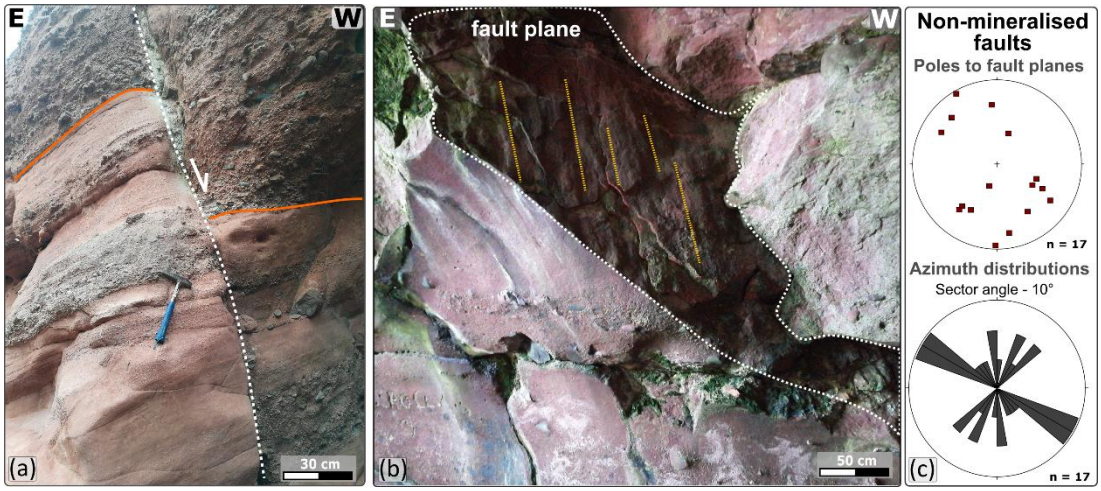

Fig. 3. 9: Example of non-mineralised structures recognised at New Aberdour locality (see location on Fig. 7a). (a) Section view of normal fault showing about 50 cm of displacement with minor quantities of green fault gouge. (b) Oblique view of clean break fault plane showing dip-slip lineations and grooves. (c) Equal area lower hemisphere stereonet and rose plot of non-mineralised faults and fractures at New Aberdour locality.

slip normal (Fig. 3.10c.) to slightly sinistral normal, oblique-slip displacements (Fig. 9b).

On the western side of New Aberdour Bay, two intersecting NNE-SSW- (Fault I in Fig. 3.10a) and NW-SE-trending faults (the latter parallel to a mafic dyke margin) juxtapose the Lower Devonian succession in their hangingwalls against the Dalradian basement slates (e.g. Figs 3.7b and 3.10a). The NW-SE-trending fault dips steeply towards the NE (dip/dip direction - 75°/320°) and poorly-preserved slickenlines suggest a normal, sinistral oblique-slip shear sense. The mafic dyke is up to 4 m wide and can be traced for about 150 m to the NW, where it becomes poorly exposed. Other similar sub-vertical (dipping >85°E) dykes have been observed locally in the Dalradian basement, but none are seen to cross-cut the Devonian succession. This suggests that the dykes most likely predate the Crovie Group and could be Ordovician as suggested

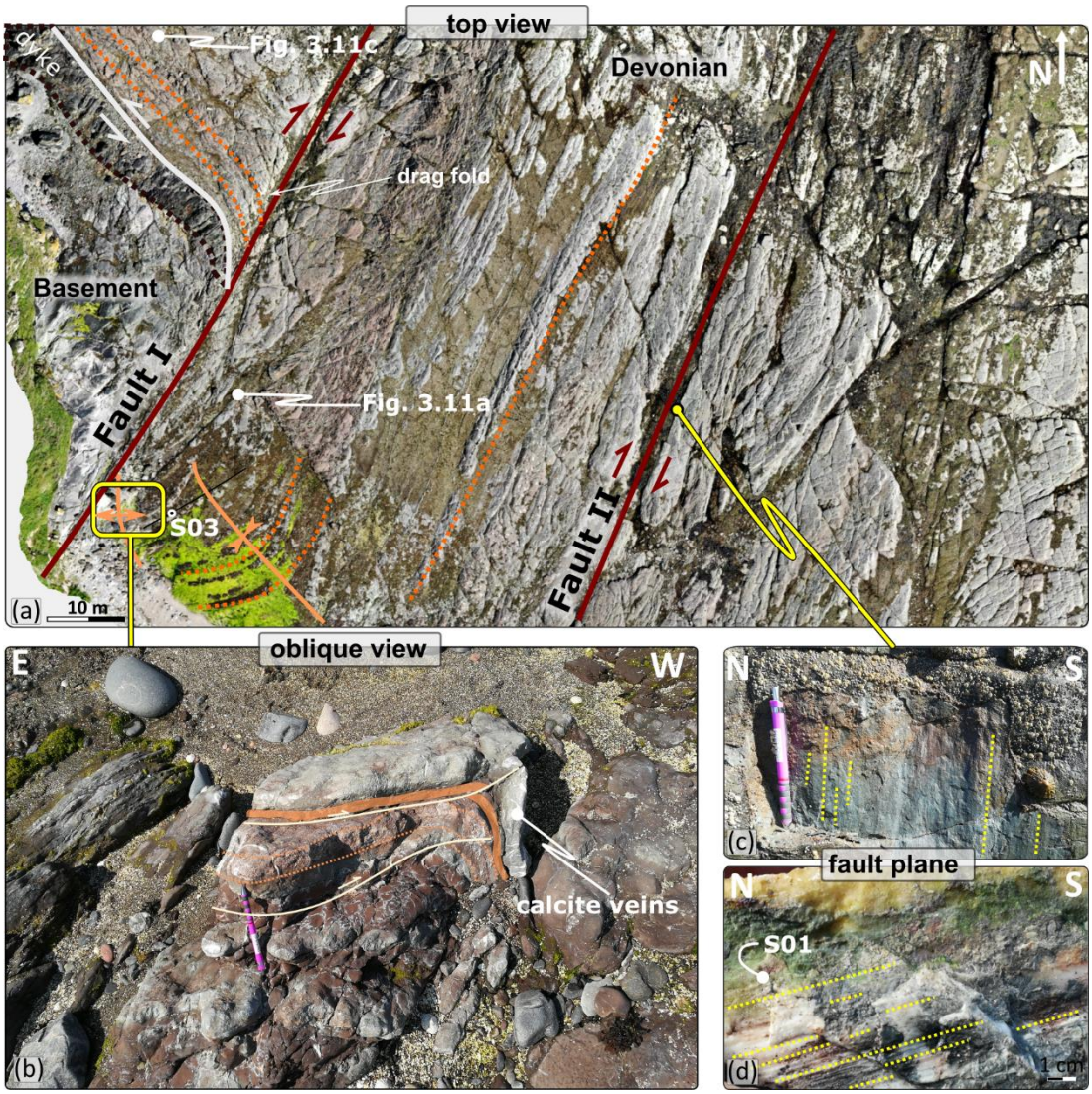

Fig. 3. 10: Examples of faulting and associated structures cross-cutting the Devonian sandstones and Dalradian basement in the western part of the New Aberdour Bay. For location see Fig 8a. a) Orthomosaic obtained from UAV (Unmanned Aerial Vehicle) photography, illustrating dextral reactivated NNE-SSW striking faults (red), oblique sinistral NW-SE striking faults (white) Bedding and fold axial traces are highlighted in orange b) NW-plunging tight folds c) Clean break N-S fault plane showing early dip-slip slickenlines and d) overprinting oblique-dextral calcite slickenfibers with the location of the S01 sample shown.

for other mafic and ultramafic intrusions in this area (e.g. Read 1923; Gunn et al. 2015). Further study is needed to better constrain the nature and age of these dykes.

The NW-SE fault separating basement and cover is crosscut by a steeply E-dipping (80°), calcite-mineralised fault trending NNE-SSW (Fault I, Fig. 3.10a). This fault has been previously interpreted as a major east-side-down normal fault together with other such faults with this trend in the area

(Sweet 1985). Although the exposed fault plane does not preserve kinematic indicators, minor structures present in a 10 m wide damage zone around the fault preserve evidence of shear sense. These include a series of mutually cross-cutting ENE-WSW-trending dextral faults (Fig. 3.11a), NW-SE sinistral faults and E-W tensile fractures. We interpret these structures as R- and R'-shears and T fractures, respectively, suggesting an overall dextral sense of movement along the main NNE-SSW-trending master fault (Fig. 3.11d). Other minor dextral N-S- to NNE-SSW-trending faults, parallel to the major fault have

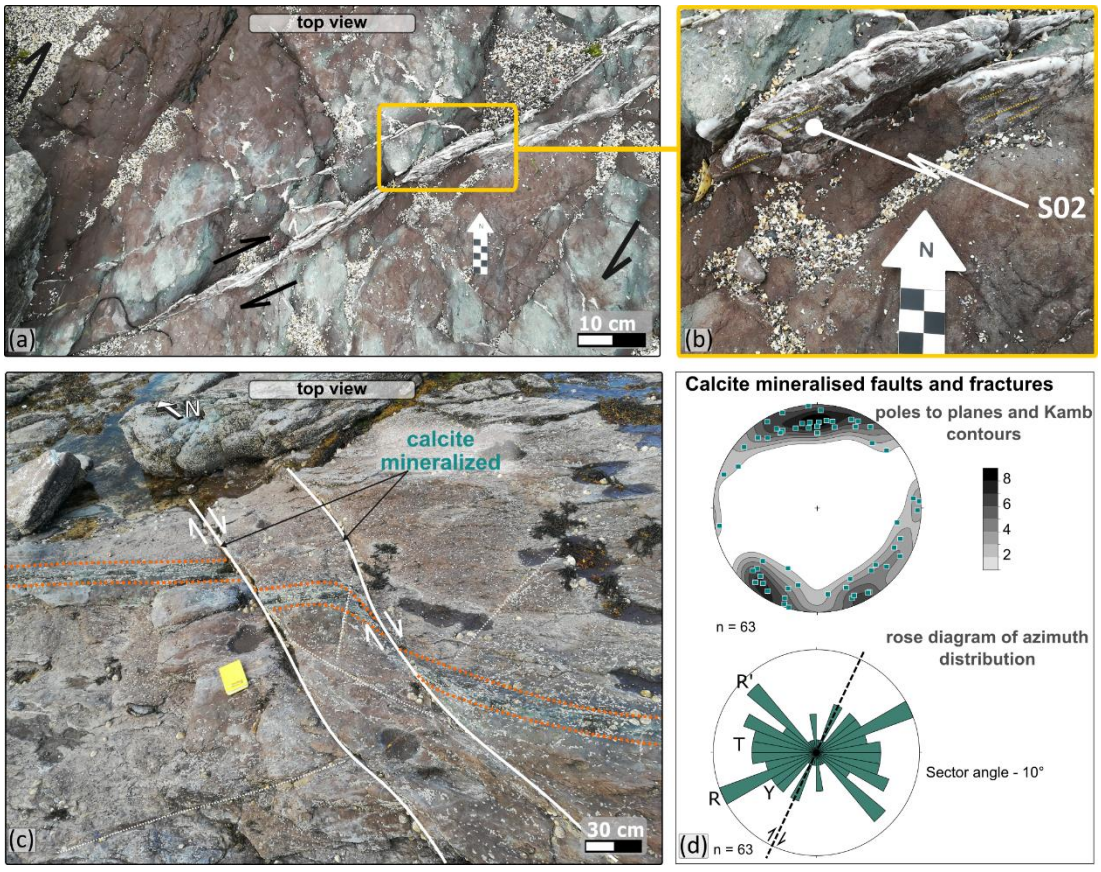

Fig. 3. 11: Examples of calcite mineralised structures from the New Aberdour locality. a) Plan view of a minor calcite-mineralised dextral fault associated with the major NNE-SSW-trending fault (Fault I in Fig 10a). b) Close-up of the calcite slickenfibers on the fault plane showing dextral slip with the location of the S02 sample shown. c) Oblique view of other calcite mineralised N-S-to NNE-SSW-trending dextral faults (white) offsetting bedding (orange). d) Stereonet (lower hemisphere, equal area projection) and rose plot of calcite mineralised structures.

also been observed (Fig. 3.11c). All of these recorded minor structures are calcite-mineralised.

Close to Fault I, drag folding of the Devonian bedding and basement foliation is observed, which is also consistent with dextral movement (Fig. 3.10a). About 60 m east from Fault I, another major, NNE-SSW tending fault steeply dipping to the E (74°/290°) occurs (Fault II, Fig. 3.10a). On the exposed fault plane, both dip-slip slickenline lineations (Fig. 3.10c) and a later set of normal-dextral calcite slickenfibres (Fig. 3.10d) are preserved, the latter suggesting that some fault movements have occurred synchronously with carbonate mineralisation. Thus the NNE-SSW-trending faults preserve evidence for two episodes of movement: an earlier phase of normal dip-slip and a later set of dextral strike-slip synchronous with calcite mineralisation.

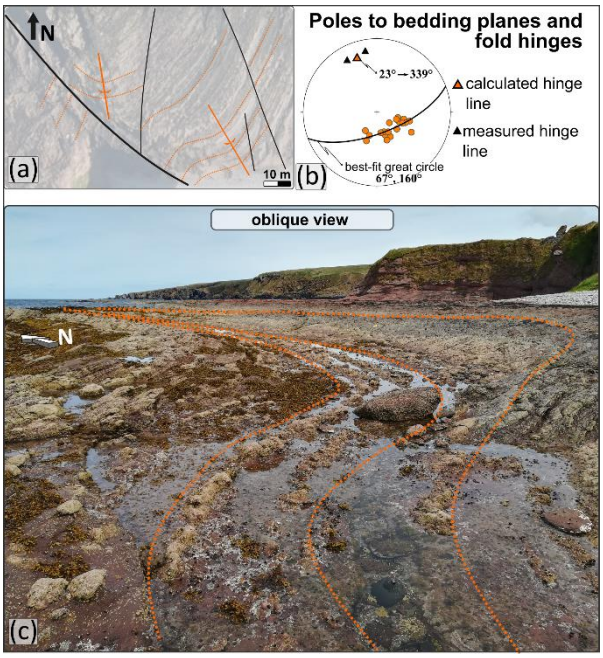

Fig. 3. 12: : a) Aerial image and line drawing showing folded strata on the eastern side of the bay. b) Stereonet showing poles to bedding and the hinge lines of the folds. c) Oblique field photograph showing the folded layers looking northeastwards.

Folds are commonly visible in the Devonian strata exposed on the flat-lying platform, both on the west and east side of the bay (e.g. Fig. 3.10a and 12a-c). They are usually gentle to open structures (interlimb angles of 120-130°) and plunge shallowly (08-23°) towards the NNW (Fig. 3.7e). Closer to faults, these folds are tighter (interlimb angles as low as 80°; Fig. 3.12b) and plunge more steeply (~40°) towards the N. Extension fractures in the outer arcs of the fold hinge zones are calcite-mineralised (Fig 10b) suggesting that the folding occurred synchronously with

calcite mineralisation and the associated faulting episode. Folds are consistently spatially associated with mappable faults (Figs 3.10b and 3.12a). Their orientation relative to these N-S to NNE-SSW faults is consistent with dextral kinematics and they have formed synchronous with carbonate mineralisation. Away from the faults, bedding is more uniformly dipping to the W (Fig. 3.7b).

3.4.2 Microscopy

Sample S01 (Fig. 3.10d) was collected from the calcite slickenfibers associated with the N-S- to NNE-SSW-trending Fault II (Fig. 3.10a). Samples S02 (Fig. 3.11b) and S03 (Fig. 3.10a) are from minor dextral shear fractures associated with Fault I (Fig. 3.10a). Further details about the samples are also provided in the Supplementary Material.

All samples show very similar microstructural characteristics (Fig. 3.13a-f) that are typical of shear veins formed synchronous with fault slip (e.g. see Passchier and Trouw 2005 and references therein). A stacked series of fault-parallel panels with sharp bounding surfaces enclose domains of crystalline and/or fibrous calcite (Fig. 3.13a and b). The shear veins are either linked together, or locally cross-cut by calcite-filled dilational veins that are consistently oriented sub-parallel to trails of wall rock and fluid inclusions that are best preserved in the fibrous domains (Fig. 3.13c). The preservation of such inclusion trails is consistent with crack-seal behaviour (Ramsay 1980) and the asymmetry of these trails, the dilational jogs and the fibre obliquity relative to the local fault planes is everywhere consistent with dextral displacements (Fig. 3.13a, b, d and e). Obliquely-oriented tensile calcite veins in sample S02 are closely associated with small gouge-bearing faults in the

wall rocks (Fig. 3.13d and e) which also locally preserve sub-millimetre-spaced Reidel shears consistent with dextral shear (Fig. 3.13f). Collectively, these

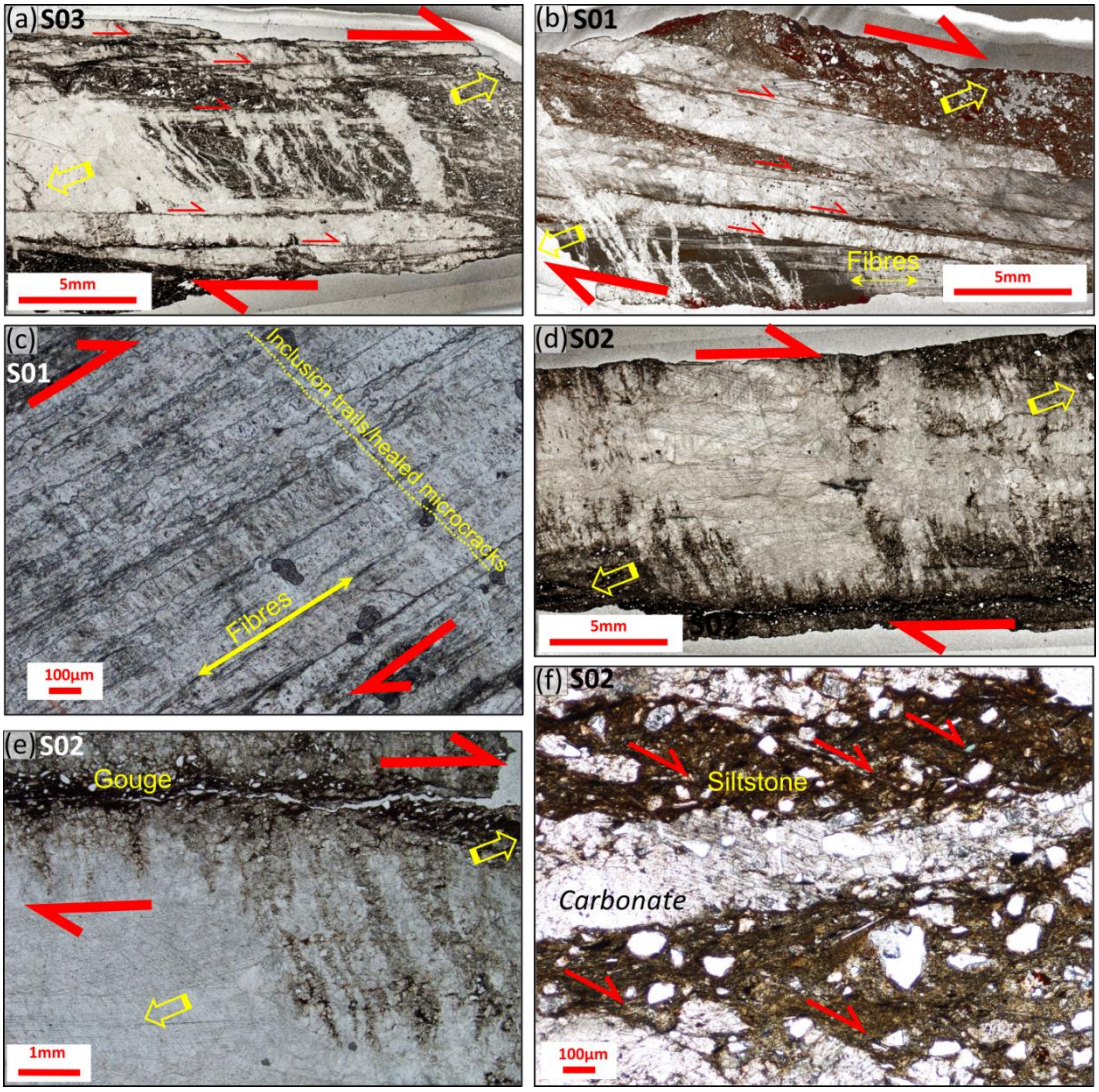

Fig. 3. 13: Photomicrographs of textures associated with calcite mineralised faults discussed in the text – all images here cut parallel to local slickenline/fibre lineations in the samples and are in plane polarized light. Red arrows show senses of shear, whilst yellow arrows show local opening and fibre directions. (a, b) Stacked shear and dilational veins in samples S03 and S01, respectively. Note oblique fibres in (b) consistent with dextral shear. (c) High power view of fibres with aligned crack-seal inclusion trails and healed microfractures – note obliquity consistent with dextral shear. Sample S01. (d, e) 'Feathered dilational vein arrays associated with gouge-bearing shear fractures consistent with dextral shear in the dated sample S02. (f) Sheared Devonian siltstone and carbonate in dated sample S02 with dextral Riedel/shear bands.

textural relationships indicate that calcite mineralisation and local right-lateral displacements along N-S- to NNE-SSW-trending faults are contemporaneous.

3.4.3 U-Pb geochronology

The ^{238}U and ^{206}Pb concentrations were analysed in five calcite-bearing samples collected in the field (e.g. Fig. 3.14a). Samples shown to have approximate concentrations of ^{238}U less than 1 ppb were not analysed any further (three samples; see Supplementary Material), whilst samples with concentrations greater than 1 ppb were mapped in detail using the methods described previously. This allowed zones of higher ^{238}U concentration to be identified and targeted for dating. Of the two samples analysed, only one - S02 (Figs 3.11b and 3.14a) - contained sufficient amounts of ^{238}U (and low enough concentrations of common Pb) to yield an accurate and precise date (note: LA-ICP-MS data for the unsuccessful sample can be found in the Supplementary Material). For sample S02, 197 spots were ablated, with 68 spots omitted due to excess common Pb or poor ablation. The remaining spot data (N = 129)

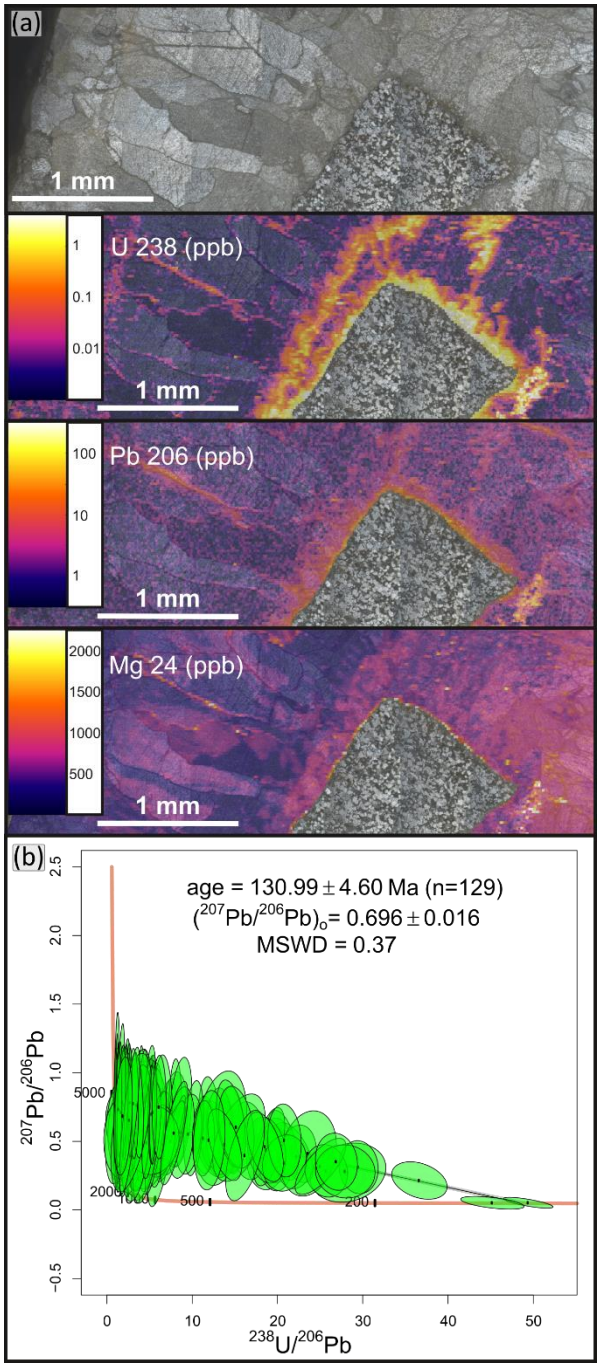

Fig. 3. 14: a) Isotopic concentration maps of 238U, 206Pb and 24Mg generated using LA-ICP-MS trace element mapping in sample S02. b) Tera–Wasserburg diagram of measured in-situ calcite 207Pb/206Pb and 238U/206Pb ratios (no common lead correction) from sample S02 (second cycle of the Manndrapselva Member) yielding a Model I discordia age of 130.99 ± 4.60 Ma (2σ, MSWD = 0.37; See text for discussion).

were plotted on a Tera-Wasserberg U-Pb plot using IsoplotR (Vermeesch 2018) which yielded a $^{238}U/^{206}Pb$ Model 1 age of 130.99 ± 4.60 Ma (2σ, $Pb_{initial}$ = 0.696 ± 0.016, MSWD = 0.37; Fig. 3.14b). The final age uncertainty is fully propagated with reference material uncertainties added in quadrature. Note that a Model 1 age of 131.06 ± 4.48 Ma (2σ, $Pb_{initial}$ = 0.700 ± 0.013, MSWD = 0.37) is yielded when the excluded data are also plotted (see Supplementary Material). The primary reference material used was WC-1 which yielded a $^{238}U/^{206}Pb$ Model 1 age of 257.22 ± 5.32 Ma (2σ, $Pb_{initial}$ anchored at 0.85, MSWD = 0.13) which is within uncertainty of the expected 255.4 ± 6.4 Ma age reported by Roberts et al. (2017). NIST612 was used as a secondary reference material which yielded isotopic concentrations (^{204}Pb = 38.40 ± 0.92, ^{206}Pb = 38.48 ± 0.15, ^{207}Pb = 38.49 ± 0.21, ^{208}Pb = 38.49 ± 0.31, ^{232}Th = 37.73 ± 0.14, ^{235}U = 37.34 ± 1.29, ^{238}U = 37.16 ± 0.48) within uncertainty of the certified values for NIST612 (38.57 ppm Pb, 37.79 ppm Th, and 37.38 ppm U); this was consistently within 2 SE of our long-term reproducibility (see Supplementary Material).

The low MSWD obtained from the dated carbonate vein sample points to a single isotopic population/mineralisation event, despite the isotopic mapping (Fig 14c) of the sample showing the heterogeneous composition of the precipitated material. The analysed carbonate is enriched in ^{238}U in the vicinity of an incorporated sandstone clast possibly suggesting leaching of metals from the host rock. Isotopic mapping also reveals a spatial link between the higher ^{238}U and ^{206}Pb concentrations with ^{24}Mg enrichment of the carbonate, with ^{238}U being particularly enriched at the interface between the high and low ^{24}Mg zones (Fig 14c). Whether this heterogeneity relates to

original fluid compositional change or to later alteration/dolomitization is uncertain, although microstructural evidence for later alteration/replacement has not been seen in the samples studied. Heterogeneous ^{24}Mg compositions occur between individual carbonate crystals on the left had side of the map with a more uniform ^{24}Mg enrichment towards the right-hand side of the image which represents the centre of the vein. This suggests that the chemical heterogeneity was a feature of the original carbonate mineralization in the vein, with the Mg (with U and Pb) becoming enriched in the remaining fluid as the vein closed (entraining the wallrock fragment). We therefore tentatively suggest that the chemical variations mapped represent original vein growth processes rather than later alteration meaning that the ^{238}U/^{206}Pb age obtained most likely reflects the time of vein formation and faulting rather than a later fluid flow event.

3.4.4 Main fault types and stress inversion analysis

The N-S to NNE-SSW striking normal to slightly sinistral faults are demonstrably syn-sedimentary based on the growth packages in their hangingwalls (Figs 3.6 and 3.7a) and are non-mineralised and characterised by clean breaks, fault gouges or breccias. Palaeostress inversion analysis of these non-mineralised fault slip data yield an ENE-WSW extension direction (Fig. 3.15a). The inversion suggests that the faults developed in a regime of near-horizontal extensional stress (σ_3) with an axis orientated 07°/061° and near-vertical compressive stress (σ_1) with an axis orientated 81°/272° (Fig. 3.15a).

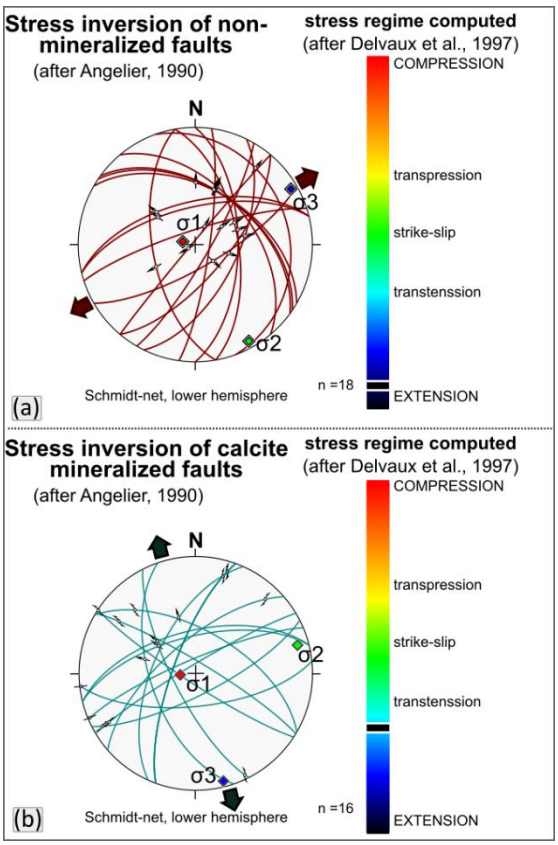

Fig. 3. 15: Stress inversion plots (after Angelier 1990) for: a) non-mineralised; and b) calcite mineralised structures.

The N-S to NNE-SSW striking faults also show evidence of dextral movements (e.g. Fig. 3.6d), while some preserve evidence of both earlier dip-slip and later dextral-oblique extensional displacement (e.g. Figs 3.10c and d). This dextral slip is everywhere associated with calcite mineralization. A palaeostress inversion performed on these calcite-mineralised faults shows that they formed during NNW-SSE rifting (Fig. 3.15b.). The faults were developed in a transtensional regime of horizontal extensional stress (σ_3) with

an axis orientated 01°/340° and steeply plunging compressive stress (σ_1) with an axis orientated 67°/247°.

3.5 Discussion

3.5.1 Timing and kinematics of faulting

3.5.1.1 Non-mineralised faulting phase

The NNW-SSE to NNE-SSW-striking faults characterised by unmineralized clean breaks, fault gouges or breccias were demonstrably established during the Lower-Middle Devonian rifting based on the preservation of very well-developed growth packages in their hangingwalls (Figs 3.6, 3.7a and Fig. 3.16a). Whilst absolute evidence concerning the age of faulting is not available, it is clear that at least two periods of growth faulting occurred prior to and following the development of the erosional unconformity that separates the supposedly Lower and Middle Devonian sequences. Different fault orientations showing the same fault rock characteristics are interpreted here as being part of the same deformation event.

The non-mineralised faults identified in the present study show normal to slightly sinistral-oblique displacements as suggested by the preservation of fault lineations and grooves on exposed slip surfaces (e.g. Fig. 3.5d and e). Palaeostress inversion analysis of these fault slip data yields an ENE-WSW extension direction (Fig. 3.15a). These results differ markedly from the NW-SE extension direction suggested by Norton et al. (1987), but are comparable to the ENE-WSW extension and similar fault kinematics documented elsewhere in the Orcadian Basin (e.g. Dewey and Strachan 2003; Wilson et al. 2010; ‘Group 1’ structures of Dichiarante et al. 2020).

We consider that our results show that the generally N-S-trending faults in the Tariff Sub-basin are related to ENE-WSW sinistral transtensional development of the Orcadian Basin during Devonian left-lateral shear along the Great Glen–Walls Boundary fault system (Seranne 1992; Dewey and Strachan 2003; Watts et al. 2007; Wilson et al. 2010). This suggests that the regional model for Devonian basin development widely recognised north of the Great Glen Fault can be extended to the southern limits of the Orcadian Basin in the Central Highlands.

We cannot exclude the possibility that some of the non-mineralised faults are younger, but we have no independent evidence to suggest this. Some could be Permo-Carboniferous structures as suggested by Ashcroft and Wilson (1976), although no faults similar to the Permo-Carboniferous 'Group 2' structures observed in Caithness (as defined by Dichiarante et al. 2020) have been identified in our study area. Those structures are typically N-S-trending reverse faults caused by localised inversion of earlier Devonian structures, and are typically associated with N-S-trending folds.

3.5.1.2 Mineralised faulting phase

The Devonian sedimentary rocks are locally cross-cut by a set of younger faults, veins and folds that are associated with widespread syn-tectonic calcite mineralisation (e.g. slickenfibres, tensile veins, Riedel shear fractures, or calcite-cemented fault rocks). Some pre-existing Devonian structures, especially the NNE-SSW-trending faults, experienced oblique-dextral reactivation during this later deformation (e.g. Fig. 3.10). Stress inversion analyses performed on the calcite mineralised faults show that they formed

during NNW-SSE transtensional deformation (Fig. 3.15b). NNW-plunging folds are locally developed in proximity to faults, and show calcite mineralised outer arc extension fractures (Fig. 3.10b). Although folding seems to be restricted to regions located closer to larger faults, folds developing in an overall transtensional regime are not uncommon (e.g. De Paola et al. 2005; Fossen et al. 2013). Likewise, the oblique-sinistral NW-SW faults are likely to have been developed during the same event as their observed kinematics are consistent with the general NNW-SSE transtensional regime.

The new U-Pb dating of the calcite in sample S02, collected from the minor dextral fault (Fig. 3.11b) interpreted as a synthetic Riedel to Fault I, yields an Early Cretaceous age of 130.99 ± 4.60 Ma (Hauterivian) (Fig. 3.14b). The field evidence (Fig. 3.11b) and microstructural observations (Fig. 3.13d-f) suggest strongly that fault displacements were contemporaneous with calcite mineralisation. It is therefore proposed that this age also constrains the timing of the younger phase of faulting recognised in the Devonian rocks along the southern coast of the IMFB.

3.5.2 Implications for the regional-scale deformation history of the IMFB

3.5.2.1 Permo-Triassic

Dextrally reactivated Devonian structures which suggest NW–SE regional rifting have been identified in the northern part of Caithness, where Re-Os geochronology of syn-tectonic fault-hosted pyrite yielded a Permian age (c. 267 Ma) (Dichiarante et al. 2016). Although somewhat similar in structural style, based on U-Pb dating, the dextral reactivation of the Devonian structures

in our study area is much younger (130.99 ± 4.60 Ma). Furthermore, the Caithness veins are widely associated with base metal sulphides in addition to calcite – such minerals have not been observed along the south coast of the IMFB. Although it is at present unclear whether the Permian deformation in Caithness extends southwards to the NW flanks of the IMFB, it does not seem to be clearly preserved in the onshore exposures on the south side of the basin. As suggested by Dichiarante et al. (2016, 2020), the deformation in Caithness is likely related to the opening of the West Orkney Basin, and may not extend south of the Helmsdale Fault. Hence, the question regarding whether there is onshore evidence for Permo-Triassic deformation in the IMFB remains unresolved.

3.5.2.2 Late Jurassic –Early Cretaceous

Much of the debate about the relative importance of strike-slip vs dip-slip tectonics in the development of the IMFB came prior to the availability of high-resolution 3D seismic data. More recent models, based on subsurface data of this kind, tend to suggest that there is little evidence for the development of syn-rift oblique-slip faults in the basin (e.g. Davies et al. 2001; Long and Imber 2010; Lapadat et al. 2018). The dextral movement of the Great Glen Fault which generated oblique- or strike-slip faults in the basin are widely considered Cenozoic as they also displace post-rift stratigraphy (e.g. Underhill 1991a; Thomson and Underhill 1993; Underhill and Brodie 1993; Davies et al. 2001). The Sronlairig Fault, located onshore south of Loch Ness (Fig. 1a), is a ENE-WSW-trending sinistral fault, considered to have developed initially as a synthetic Riedel to the sinistral Great Glen Fault during the pre-Late Devonian (428 - 390 Ma; Stewart et al. 1999). Kemp et al. (2019) used K–Ar analyses to

constrain the timing of the Sronlairig fault. The results suggest two different times of later fault movement at 296 ± 7 (Late Carboniferous–Early Permian) and 145 ± 7 Ma (Late Jurassic–Early Cretaceous), respectively. The former event coincides with a widely recognised dextral shearing event along the Great Glen-Wall Boundary fault in N Scotland, Orkney and Shetland (e.g. see Stewart et al. 1999; Armitage et al. 2020 and references therein). Kemp et al. (2019) suggested that the later age corresponds to the main phase of rifting in the IMFB in the Late Jurassic–Early Cretaceous. They proposed that the Great Glen Fault zone and related structures acted as a northern barrier to active extension at this time, thus explaining the relative absence of deformation at this time in Caithness and the Pentland Firth. Their study further confirms that well known Caledonian faults onshore may have significant Mesozoic movements and may act as barriers or transfer faults connecting or bounding younger offshore basins, as originally suggested by Roberts and Holdsworth (1999).

Our findings support the existence of oblique-dextral N-S- to NNE-SSW-trending faults, some of which are proven to have reactivated Devonian structures in the IMFB (Fig. 3.16b), during Hauterivian (130.99 ± 4.60 Ma) rifting. This is somewhat later than the Berriasian age previously proposed for the cessation of rifting in offshore areas (e.g. Underhill 1991a and b; Davies 2001), but is consistent with studies by Andrews et al. (1990), Roberts et al. (1990) and Argent et al. (2002) all of whom suggest that some faults were longer-lived. The NNW-SSE extension direction deduced from the palaeostress analysis in the present study is parallel to that suggested by Davies et al. (2001) based on offshore fault trends, but the timing proposed by

them is Late Jurassic (Oxfordian-early Kimmeridgian) rather than Early Cretaceous. During the late Kimmeridgian-Tithonian, they inferred a change to NE-SW extension in order to explain the development of NW-SW-trending faults in the basin. We suggest that this sequential model should be reassessed and that a synchronous fault development model involving the oblique reactivation of older Orcadian Basin-related structures and the development of new dip-slip faults is also feasible. This would allow multiple fault families to coexist including the main basin to sub-basin-bounding NE-SW dip-slip normal faults, in addition to smaller scale transtensional dextral N-S to NNE-SSW faults, sinistral NW-SE faults and local folds (Fig. 3.16b). Oblique kinematics and reactivation of pre-existing structures have certainly been identified elsewhere in the North Sea (e.g. Færseth et al. 1997). More generally, this model is consistent with the suggestion that simple orthogonal rifting models are less common than is generally assumed (e.g. Dewey et al. 1998; Holdsworth et al. 1997; Dichiarante et al. 2020). Further integration of high-resolution offshore 3D seismic reflection data should be used to confirm whether the trends observed onshore in the Turniff Sub-basin can be recognised offshore in the IMFB.

3.5.3 Implications for the Devonian hydrocarbon play

In the IMFB, the main reservoir-seal packages are thought to comprise Lower Jurassic to Middle Jurassic sandstones and siltstones interbedded with mudstones. The Beatrice field (Linsley 1980; Fig. 3.1b) which was the most significant field in the region, is considered to have been charged by a combination of Devonian and Jurassic source rocks (e.g. Peters et al. 1989; Greenhalgh, 2016). The Devonian source rock in the offshore IMFB is largely

thought to lie in the oil window and co-sources other fields in the Orcadian Basin (e.g. Greenhalgh 2016). Porous and fractured Devonian sandstones provide known local petroleum reservoirs elsewhere in the North Sea (e.g. Argyl, Ardmore, Claymore, Buchan, Stirling fields; Marshall and Hewett 2003). Also, the Clair field, West of Shetland is a giant oilfield hosted in fractured Carboniferous-Devonian and Precambrian basement rocks, with a Kimmeridge Clay source (Coney et al. 1993; Holdsworth et al. 2019). The development of reservoir-quality fractured sandstones and local Devonian source rocks in the oil window provide evidence that this type of play could be more extensive. Oil-stained Devonian and basement rocks have certainly been identified in many locations onshore Orkney (Parnell et al. 1998), Moray Firth (Greenhalgh 2016 and references therein) and are also locally observed in the highly fractured sandstones at Pennan (Fig. 3.5d and e).

Our findings show that the Devonian rocks underwent both Devonian and Early Cretaceous deformation, with oblique reactivation of Devonian structures during the later stage. This led to a high density of faults and fracture networks (e.g. Fig. 3.8c and d.) which are critical for the development of potential Devonian-involved plays. Although there are some similarities in terms of structural style, the reactivation events recognised in the southern part of the former Orcadian Basin are significantly younger than those recognised further to the north (e.g. Caithness, West Orkney Basin).

3.6 Conclusions

Our integrated onshore study combines structural studies with absolute U-Pb calcite dating techniques to reveal two main deformation events in the

southern part of the superimposed Inner Moray Firth and Orcadian basins.

The earliest event is demonstrably Devonian based on the preservation of growth faulting (Fig. 3.16a) and is characterised by the development of dip-slip to oblique-sinistral, non-mineralised faults predominantly striking N-S to NNE-SSW. Palaeostress inversion analyses suggest that they developed during ENE-WSW extension and are related to the opening of the Orcadian Basin during sinistral transtensional displacements along the Great Glen Fault. This suggests that the regional tectonic model recognised in the northern part of the Orcadian Basin (e.g. Wilson et al. 2010; Dichiarante et al. 2020) can be extended southwards into the Central Highlands. It is also kinematically compatible with transtensional rifting and strike slip tectonics on the Midland Valley at this time (e.g. Dewey and Strachan 2003).

These early-formed Devonian structures show evidence of later dextral reactivation during a widespread phase of NNW-SSE extension. Also, NE-SW- to WNW-ESE-, and NW-SE-striking faults (showing oblique-sinistral kinematics) and NNW-plunging folds formed at the same time (Fig. 3.16b). This later deformation is consistently associated with syn-tectonic calcite mineralisation (e.g. shear veins, slickenfibers, tensile veins and Riedel shears).

U-Pb calcite dating suggests that the timing of faulting and fault reactivation of pre-existing Devonian structures associated with calcite mineralisation is Early Cretaceous (130.99 ± 4.60 Ma). We consider this to have formed during the latter stages of the more regionally recognised Late Jurassic to Early Cretaceous opening of the IMFB (Davies et al. 2001; Argent et al. 2002). This provides the first clear evidence that strike-slip and oblique-slip faults coexist

in the IMFB during the basin opening. It also provides clear evidence that the main rift-related deformation extends beyond the Banff Fault in the southern part of the IMFB, and into the onshore Turriff Sub-basin, even though younger stratigraphy is not preserved here.

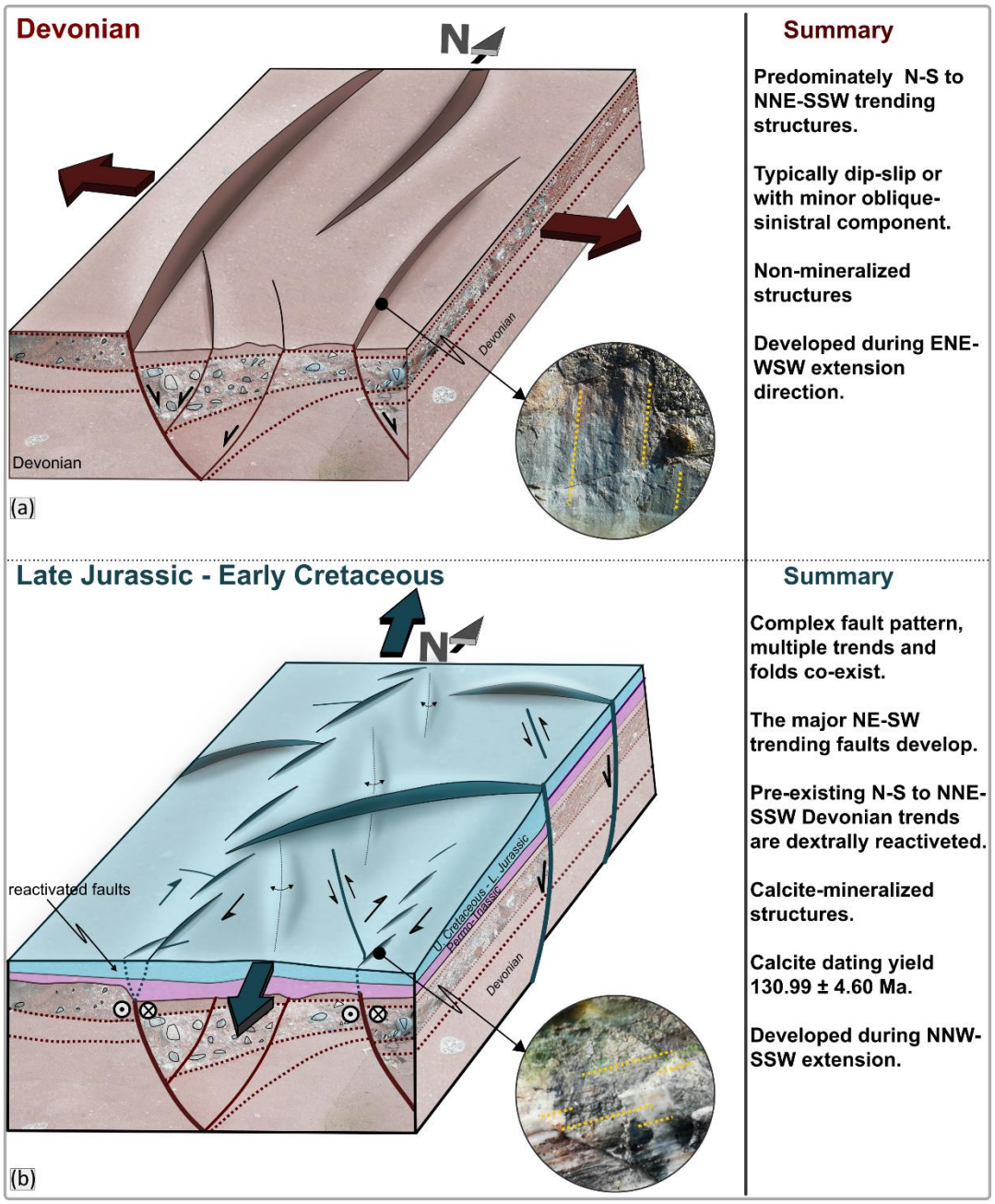

Fig. 3. 16: Summary of the structural history and schematic block diagrams illustrating the superimposed basin development during (a) Devonian and (b) Late Jurassic-Early Cretaceous.

To explain the different fault orientations associated with the Late Jurassic-Early Cretaceous deformation, we favour synchronous development of these structures during transtension and fault reactivation, rather than in-sequence

faulting due to stress rotation at different times (as suggested by Davies et al. 2001, for example). Complex fault patterns have been widely associated with transtension and oblique rifting (e.g. Wilson et al. 2006; 2010) and we believe this is the case, at least locally, in the IMFB. Thus, oblique reactivation of pre-existing faults during later rifting episodes leads to the development of highly localised regions of complex deformation that contrast strongly with intervening regions of relatively undeformed, shallowly dipping strata. The scale and kinematics of these structures are directly controlled by the location, scale and orientation of the older inherited faults at depth.

The integration of fieldwork, stress inversion analyses and absolute dating techniques shows that widespread oblique reactivation of earlier Orcadian Basin structures has occurred. This will create reservoir-scale structural heterogeneity in potential Devonian reservoirs and can be used to further explore subsurface Devonian-involved plays elsewhere in the North Sea.

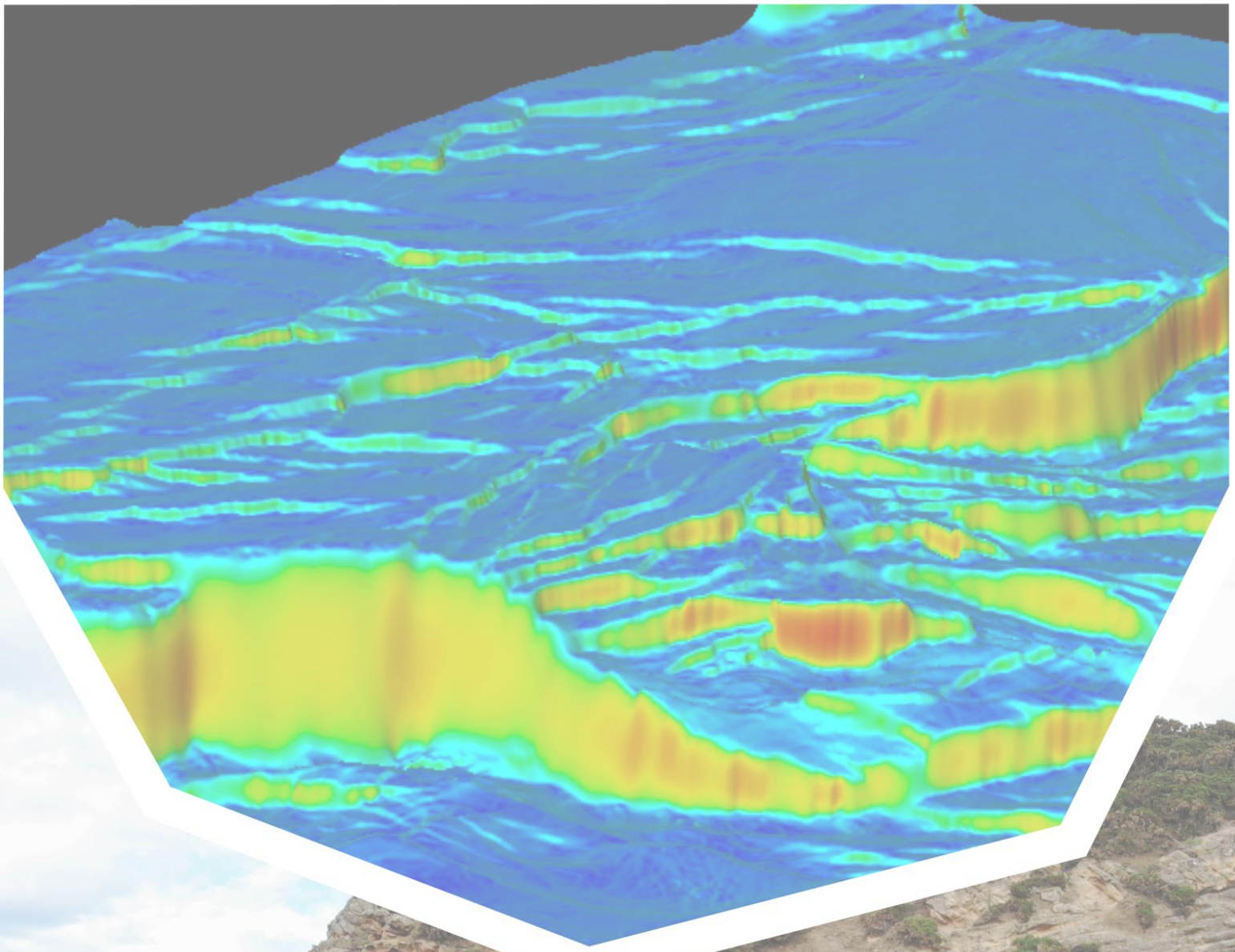

Up: Stotfield Chert map (oblique view, dip angle attribute).
Down: Clashach Cove fault.

Chapter 4

Integrating onshore fieldwork with offshore interpretation of seismic profiles to decipher the Permo-Triassic to Cenozoic history of the Inner Moray Firth Basin: the Lossiemouth Fault Zone

A version of this chapter was published as: A. Tamas, R. E. Holdsworth, J. R. Underhill, D. M. Tamas, E. D. Dempsey, D. McCarthy, K. J. W. McCaffrey, D. Selby. 2022b. ***Correlating deformation events onshore and offshore in superimposed rift basins: the Lossiemouth Fault Zone, Inner Moray Firth Basin, Scotland.*** Basin Research. Basin Research, 00, 1– 27. https://doi.org/10.1111/bre.12661
As lead author, I conducted the fieldwork, performed the seismic interpretation, analysed the data, and wrote the first draft of the manuscript.

Abstract

The separation and characterisation of different deformation events in superimposed basins can be challenging due to the effects of overprinting and/or fault reactivation, combined with a lack of detailed geological or geophysical data. This study shows how an onshore study can be enhanced using a targeted interpretation of contiguous structures offshore imaged by seismic reflection data. Two deformation events, including unambiguous evidence of fault reactivation, are recognised in the onshore part of the Lossiemouth Fault Zone (LFZ), southern-central Inner Moray Firth Basin. The basin is thought to record a history of Permian to Cenozoic deformation, but it is difficult to conclusively define the age of faulting and fault reactivation. However, structures in onshore outcrops of Permo-Triassic strata show no evidence of fault growth and new interpretation of seismic reflection profiles in the offshore area reveals that Permo-Triassic fills are widely characterised by subsidence and passive infill of post-Variscan palaeotopography. We propose that sequences of reactivated faulting observed onshore and offshore can be correlated and can be shown in the latter domain to be Early Jurassic-Late Cretaceous, followed by localised Cenozoic reactivation. The workflow used here can be applied to characterise deformation events in other superimposed rift basins with contiguous onshore (surface) - offshore (subsurface) expressions.

Key Words: fault reactivation, superimposed deformation, Inner Moray Firth Basin, North Sea

4.1 Introduction

Superimposed sedimentary basins are vertically stacked basins that partially or completely overlap. These types of basins are very common. Examples include the Colorado basin (Lovecchio et al. 2018); East African Rift (Macgregor 2015; Ragon et al. 2018); Gulf of Aden (Fournier et al. 2004); Northeast Atlantic margin (Hansen et al. 2012; Henstra et al. 2019); East Greenland rift system (Rotevatn et al. 2018); Northwest shelf of Australia (Deng et al. 2020, 2021; Deng and McClay 2021); Black See (Bosworth and Tari 2021); North Sea rift (e.g. Tomasso et al. 2008) and West Orkney Basin (Wilson et al. 2010). Isolating and characterising the age and structural styles associated with individual deformation events, in addition to assessing the role of pre-existing structures, is commonly difficult to constrain. This may be due to insufficient or ambiguous geological or geophysical data (e.g. poor seismic resolution), which can lead to uncertainties or contrasting models. Onshore areas may be limited by poor surface exposure and lack of constrain in the absolute/relative age of fault movements. A better understanding of the timing of deformation in the basin can provide key insights into basin development and potentially reduce sub-surface uncertainties. For example, in a recent study, Tamas et al. (2022a) have shown how geochronological dating of syn-tectonic calcite mineral fills associated with basin-related faults exposed onshore can be used to better constrain the age of faulting episodes in the offshore area of the Inner Moray Firth Basin, Scotland. In this paper, we use an example from the same basin to show how an alternative, but complementary approach can be used to the same ends. An integrated interpretation of offshore seismic data and onshore field evidence is used to

shed further light on the nature, age and significance of regional deformation events. This work is also highly relevant in areas where geochronological data cannot be obtained from onshore outcrops to constrain the age of faulting.

4.2 Geological overview

4.2.1 Regional structural framework

The Inner Moray Firth Basin (IMFB) is a superimposed rift basin developed on Precambrian to Caledonian metamorphic basement and Devonian-Carboniferous sedimentary rocks related to the older Orcadian Basin (Fig. 4.1). From the Permian to the lower Cretaceous, it formed the western part of the intra-continental North Sea trilete rift system (McQuillin et al. 1982; Frostick et al. 1988; Roberts et al. 1990; Andrews et al. 1990; Underhill 1991a; Thomson and Underhill 1993).

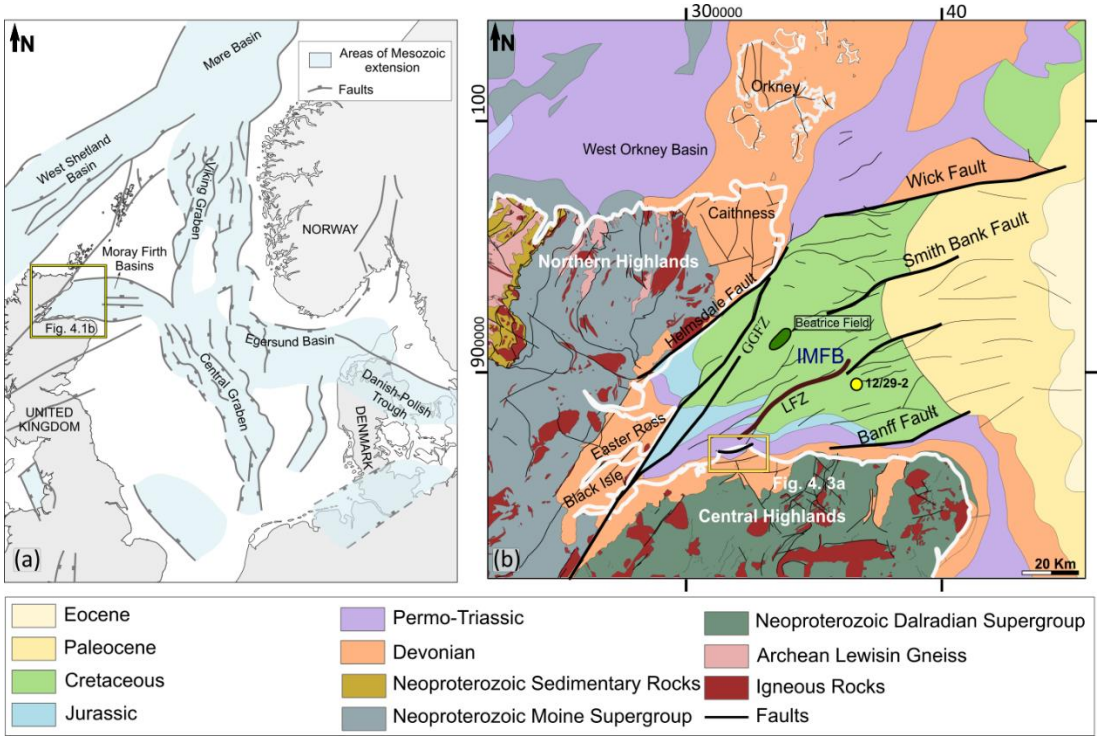

Fig. 4. 1: (a) Generalised tectonic map of north-west Europe showing the main Mesozoic rift systems (adapted after Goldsmith et al. 2003). Yellow box shows location of map in (b). (b) Regional geological map of northern Scotland and associated offshore regions (after Tamas et al. 2022a). Yellow box shows location of Fig. 3a- the onshore study area. IMFB – Inner Moray Firth Basin. LFZ – Lossiemouth Fault Zone. GGFZ – Great Glen Fault Zone.

The rift basin is controlled by major basin-bounding faults including the Banff Fault to the south, the Helmsdale and Great Glen faults to the northwest, and the Wick Fault to the north (Fig. 4.1b). The IMFB transitions eastwards into the Outer Moray Firth basin, linking with the Central and Viking graben in the central part of the North Sea (Fig. 4.1a). The IMFB is known to record important episodes of late Cretaceous - Cenozoic regional uplift and faulting, including strike-slip reactivation of major basin-bounding structures such as the Great Glen (dextral) and Helmsdale (sinistral) faults (e.g. Underhill 1991a; Thomson and Underhill 1993; Le Breton et al. 2013).

The geological history of the IMFB has, however, been a source of controversy. In particular, the Permo-Triassic history - which is widely characterised by active rifting in other parts of the North Sea (e.g. Steel and Ryseth 1990; Bell et al. 2014; Fazlikhani et al. 2020) - is debatable in the IMFB. Some authors have considered the Permo-Triassic history to be characterised by active rifting (e.g. Frostick et al. 1988; Roberts et al. 1989). Others, based on interpretations of increasingly available seismic reflection data, considered that the Permo-Triassic history was dominated by thermal subsidence (Andrews et al. 1990; Thomson and Underhill 1993).

During Late Jurassic - Early Cretaceous basin development, Roberts et al. (1990) and other authors (e.g. McQuillin, et al. 1982; Bird et al. 1987) favoured a transtensional origin for the IMFB. Such models suggested that the basin opened due to dextral movements along the Great Glen Fault during NE-SW extension.

Underhill (1991) challenged the transtensional model and proposed a new model for the evolution of the IMFB. The model suggested that, after a

long period of thermal subsidence during Triassic to Mid-Jurassic, the basin developed mainly during the Late Jurassic under a NW-SE to NNW-SSE orthogonal extensional regime. The majority of extension has been interpreted to occur along the Helmsdale Fault, with synkinematic sequence thickening observed towards the Helmsdale Fault, but not across the Great Glen Fault. This indicates that the Great Glen Fault was inactive during the late Jurassic.

Most recent studies of offshore 3D seismic reflection profiles (e.g. Davies et al. 2001; Long and Imber 2010; Lapadat et al. 2018) argue for a predominance of orthogonal rifting and suggest there is little evidence of oblique-slip faulting in the basin.

Following the cessation of rifting, the basin experienced a period of thermal subsidence during the Late Cretaceous (Underhill 1991a and b).

From the early Cenozoic to the present day, the basin is thought to have experienced episodes of uplift, eastward tilting and regional erosion, with some major faults being reactivated (e.g. Underhill 1991a; Argent et al. 2002). The Great Glen Fault is believed to be the major controlling structure in the basin at this time (Underhill 1991a). In the offshore, seismic reflection profiles show evidence of the development of strike-slip related deformations (e.g. flower-structures, folds) that offset post-rift reflectors (e.g. Thomson and Underhill 1993; Underhill and Brodie 1993; Davies et al. 2001). Cenozoic structures in the onshore area supposedly include the development of NW-SE trending large-scale folds (of about 500 m wavelength) in the hangingwall of Helmsdale Fault (Thomson and Underhill 1993; Thomson and Hillis 1995). In addition, minor folds and faults consistent with dextral kinematics, cropping out on Easter Ross coast (Fig. 4.1b), are considered to be Cenozoic and are

related to right-lateral slip along the Great Glen Fault (e.g. Underhill and Brodie 1993; Le Breton et al. 2013). The effects of Cenozoic deformation away from the Great Glen Fault, both onshore and offshore, are less certain and may be limited and/or localised.

4.2.2 Regional stratigraphic framework

The IMFB has been a depositional area since the Devonian, with up to 16 km of sedimentary rocks accumulated in the deepest parts of the basin (Andrews et al. 1990). In the offshore, the preserved stratigraphy comprises Devonian to late Cretaceous sedimentary rocks (Figs 4.1b and 4.2a). Younger, Cenozoic stratigraphy is preserved further east in the Outer Moray Firth. (Fig. 4.1b). In the onshore, the exposure is mainly represented by Devonian cover

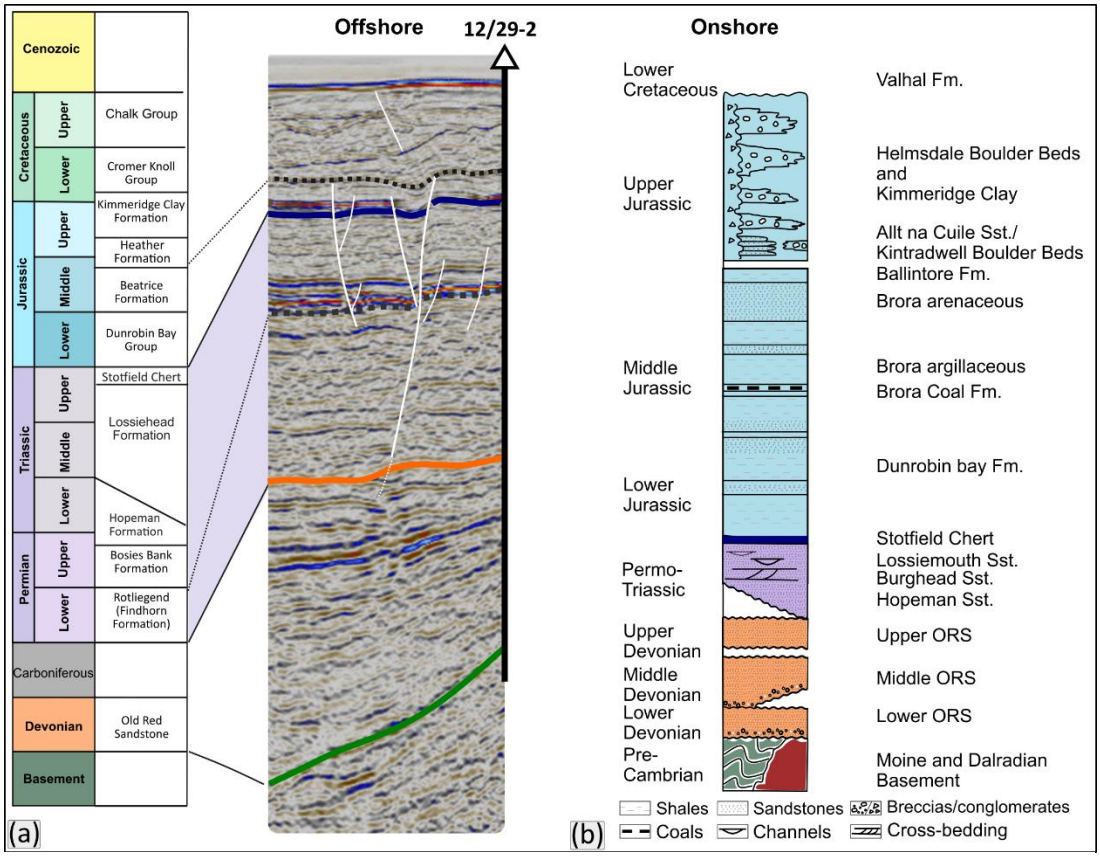

Fig. 4. 2: (a) Simplified offshore lithostratigraphic units of the IMFB (compiled after Andrews et al. 1990; Glennie et al. 2003). A representative section of seismic reflection data from a 2D survey is shown to illustrate (parts of) the typical seismic stratigraphy in the area. Formation tops are calibrated with the information in well 12/29-2, which crosses this seismic section (see well location on Fig. 4.1b). (b) Onshore stratigraphy (modified after Trewin and Hurst 2009). Not to scale, with relative thicknesses shown being notional. ORS- Old Red Sandstone.

sequences, which unconformably overlies the Precambrian Moine and Dalradian basement, together with Permo-Triassic to Jurassic cover sequences of limited extent (Fig. 4.2b).

The Devonian sequence is widely distributed both onshore and offshore (e.g. well 12/29-2, Fig. 4.2a). The succession is dominated by non-marine, red coloured alluvial and fluviatile breccio-conglomerates and conglomerates, medium- to coarse-grained sandstones or flood-plain mudstones and locally lacustrine fish-bearing flagstones (e.g. Stephenson and Gould 1995; Johnstone and Mykura 1989, and reference therein).

Permo-Triassic strata unconformably overlie the Devonian sequences. In the offshore this boundary is sometimes marked by a strong reflector referred to as the 'Variscan unconformity' (e.g. Underhill and Brodie 1993). This unconformity is thought to reflect the development of a regional erosion surface following regional-scale Variscan deformation and uplift of northern Britain in the Late Carboniferous – Early Permian (e.g. Underhill and Brodie 1993).

In the offshore, the Permian Findhorn Formation (Rotliegend Group) is dominated by sandstones and claystones of fluvial origins and is overlain by the fluvio-lacustrine deposits of the (Zechstein Group) Bosies Bank Formation (e.g. Cameron 1993; Glennie et al. 2003). The overlying Hopeman Formation forms a thick sequence of dune bedded aeolian sandstones (e.g. Peacock 1968) considered to be topmost Permian to basal Triassic (Walker 1973; Benton and Walker 1985; Clemrnensen 1987). In the onshore, the Permian deposits have a restricted coastal exposure almost entirely along the southern coast of the IMFB (Fig. 4.3a). In general, they are characterised by aeolian,

dune bedded sandstones, playa deposits and conglomerates interbedded with cross-bedded sandstones, part of a marginal fluvial sequence (e.g. Stepherson and Gould 1995).

The Triassic strata in the offshore of the IMFB comprises mainly of fluvial, alluvial fan, or lacustrine red bed sandstones and shales of the Lossiehead Formation (Goldsmith et al. 2003). In the onshore of the south coast, the Triassic is represented by the laterally equivalent fluviatile Burghead Sandstone and younger, mainly aeolian Lossiemouth Sandstone (e.g. Frostick et al. 1988). This succession is capped by the Stotfield Chert, a c. 25 m thick calcareous layer, locally dominated in south coast outcrops by microcrystalline silica (e.g. Frostick et al. 1988). This layer is interpreted as a palaeosol horizon formed during a phase of tectonic quiescence (Naylor et al. 1989), which is also recognised in offshore wells and seismic reflection profiles (Fig. 4.2a).

The overlying Lower/Middle Jurassic succession is generally represented by fluvial sandstones and shales, deltaic sandstones and coals (e.g. Linsley et al. 1980; Trewin and Hurst 2009) which in the offshore belong to the Dunrobin Bay, Beatrice and Heather formations. The following Upper Jurassic is represented by the dominantly argillaceous Kimmeridge Clay Formation. The succession is characterised by marine shales, sandstones and locally debris flow breccias. An almost complete section of Jurassic strata, with similar facies to offshore, crops out on the north-western coast of the IMFB. The Jurassic-Lower Cretaceous boundary is considered intra-formational, lying within the Kimmeridge Clay Formation (Rawson and Riley 1982).

The Upper Jurassic sequences are capped by the second most prominent seismic reflector seen offshore IMFB, which is variously termed the

'Base Cretaceous unconformity' (Thomson and Hillis 1995), '(Near) Base Cretaceous unconformity' (Long and Imber 2010) or '(Near) Base Cretaceous Event' (Underhill 1991a; Underhill and Brodie 1993). As this marker event represents both a local to regional unconformity, but also locally conformable and condensed sections are present (Rawson and Riley 1982), so we refer to it here as the Near Base Cretaceous Event (NBCE).

The Cretaceous sequence is limited to the offshore IMFB and is generally well-imaged above the NBCE seismic marker. It is characterised by onlapping reflectors, which progressively encroach onto the basin margins (e.g. Thomson and Underhill 1993). The Lower Cretaceous sequences comprise predominantly marine sandstones and calcareous shales of the Cromer Knoll Group, followed by the upper Cretaceous Chalk group comprising a thick sequence of coccolithic limestone, marls and glauconitic sandstones (e.g. Andrews et al. 1990). The Cenozoic sequence is restricted to the offshore Outer Moray Firth and extends eastwards to the Central and Viking grabens.

4.2.3 Lossiemouth Fault Zone (LFZ)

The composite sub-parallel faults forming the Lossiemouth Fault Zone (LFZ) lie on the southern side of the IMFB (Fig. 4.1b) and are thought to extend both onshore and offshore (e.g. Al Hinai et al. 2008; Farrell et al. 2014). Collectively they form a major ENE-WSW to NE-SW trending structure which represents one of the inner half-graben/horst structures of the IMFB, known as the Lossiemouth sub-basin and Central ridge, respectively (Fig. 4.3c; e.g. Andrews et al. 1990). This fault zone can be traced on seismic profiles within ~2.5 km of the southern coastline. E-W faults observed onshore between

Burghead and Lossiemouth (Fig. 4.3a) represent subsidiary strands of the main offshore trace of the LFZ (Fig. 4.3b; e.g. Al Hinai et al. 2008; Farrell et al. 2014).

Based on the interpretation of seismic reflection profiles, the LFZ has been described as an extensional, southeast dipping fault with clear Jurassic growth packages developed in its hangingwall (e.g. Fig. 4.3c; e.g. Roberts et al. 1990). The structure, which is steeper in its upper part and dipping more shallowly downwards, has been interpreted by some authors as a reactivated Caledonian thrust (e.g. Barr 1985).

4.3 Dataset and Methods

4.3.1 Onshore analysis

The field data described in this study focus on the brittle deformation associated with the LFZ recorded in the Permo-Triassic rocks cropping out along the southern coast of IMFB between Burghead and Lossiemouth (Fig. 4.3a). Detailed field observations and measurements of bedding, faults and fractures were taken using both a Suunto geological compass/clino and the FieldMove™ digital mapping application on an Apple iPad™ (6th Generation). The sense of fault movement was determined based on offset of stratigraphic markers and/or kinematic indicators such as slickenlines, lineations or grooves. To reduce the uncertainty of digital measurements, they were frequently cross-checked with the geological compass.

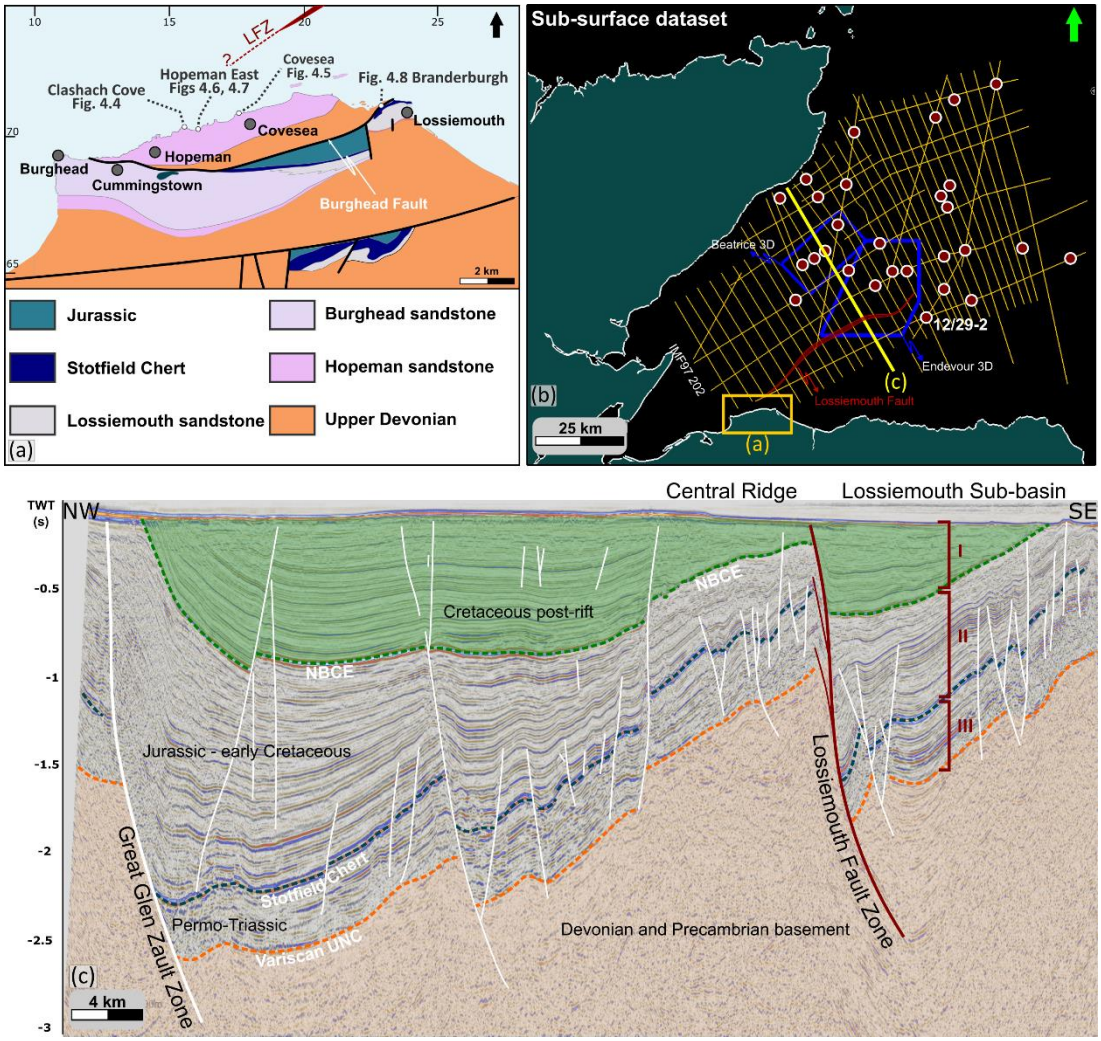

Fig. 4. 3: (a) Geological map of the onshore study area (modified after BGS 1969) The locations of Figures 3 - 7 are also shown. (b) Map of offshore data used for this study. 2D seismic lines are shown in yellow, and 3D cubes in blue. The seismic line shown in (c) is shown in bold. The red circles represent wells. The well mentioned in Fig. 1c and the text is labelled (c) Regional seismic section across the study area showing the interpreted horizons and the main faults, including the LFZ. I-III represent the investigated stratigraphic sequences referred to in the text.

Fault-slip data were collected and used to perform a palaeostress inversion. In this study, the fault data were analysed using the Angelier (1990) method implemented in the SG2PS software (Sasvári and Baharev 2014). This method is a direct inversion that estimates the reduced stress tensor from the fault-slip data and the shear stress magnitudes and orientations (Angelier 1990). The program also graphically computes the stress regime based on the stress index (R') (Delvaux et al. 1997).

The processing and visualisation of the structural measurements were carried out using Stereonet 10 (Allmendinger et al. 2012; Cardozo and Allmendinger 2013). The measurements were graphically represented using both rose diagram plots of azimuth distributions (at 10° sector angles) and equal area stereonets, lower hemisphere projections using poles to planes where appropriate. The contouring was done after Kamb (Kamb 1959) at 2 and 3 sigma standard deviation above a random population.

Oriented fault rock samples were collected from representative outcrop examples during fieldwork for microscopic analysis. Polished thin sections impregnated with blue stained epoxy were studied and photographed using an optical transmitted and reflected light microscope in order to characterise the microstructures and any mineralisation associated with faulting present.

4.3.2 Subsurface mapping offshore

The dataset used in this study comprises a compilation of 2D regional and 3D time-migrated seismic reflection surveys (Fig. 4.3b). The regional 2D seismic lines, acquired in 1997, were provided by Spectrum. Most lines (thirtytwo) are orientated NW-SE, orthogonal to the main basin-bounding structures of the IMFB (Fig. 4.3b) and have a 2 to 5 km line spacing. These lines are connected by eight ENE-WSW orientated lines with a spacing of 2 to 14 km. These lines were ideal for regional mapping and for defining the major faults in the basin.

This study also made use of two 3D time-migrated seismic surveys (Fig. 4.3b). One (Beatrice 3D) acquired over the Beatrice Field (e.g. Fig. 4.1b; Linsley et al. 1980) covers an area of 11 x 22 km and has a crossline and inline bin spacing of 12.5 m. The second (*Endeavour 3D*) is located in the central part of the basin, has an area of about 36 x 20 km and a crossline/inline bin

spacing of 12.5m/25m, respectively. This high-quality seismic survey allowed a higher-resolution analysis of fault networks and provided insights into the fault kinematics through time. In addition to the seismic reflection data, publicly available (through the National Data Repository) key exploration wells (Fig. 4.3b) were used in this study. Stratigraphic data from boreholes and checkshot/sonic logs allowed determination of the age of the mapped horizons, linking this to the stratigraphic framework for the study area.

The seismic interpretation was performed using Petrel software. The geometrical interpretation of the seismic horizons has been performed by 2D/3D manual interpretation, and 2D- and 3D-guided autotracking.

Three key horizons have been selected to illustrate the basin fill architecture and structural history, and to link this to the onshore interpretation. These are: the Variscan unconformity (labelled Variscan UNC on figures), the Triassic Stotfield Chert and the NBCE (Fig. 4.3c, Fig. 4.3cS - the uninterpreted seismic profile). Two-way time (TWT) structural maps and a TWT thickness map were generated to support structural interpretations. Multiple seismic attribute analyses were carried out on the interpreted surfaces based on the 3D reflection seismic data to assist fault interpretation and enhance small-scale fault detection and visualisation. Seismic attributes have proven to be amongst the most useful geophysical tools to highlight geological features and are routinely used to characterise fault and fracture networks (e.g. Chopra 2009; Chopra and Marfurt 2007; Di and Gao 2017). In this study, we used Variance, Edge Detection and Influential tools. In addition, horizon flattening was performed on key seismic horizons to undo the deformation (tilting, folding or faulting) and reconstruct geometries in the underlying packages.

For a detailed explanation of all analytical methods, please see Chapter 2: Dataset and Methodology.

4.4 Results

4.4.1 Onshore Fieldwork and Microscopy

We focus here on four locations at which representative sequences of events and a variety of brittle deformation styles have been encountered. The localities - Clashach Cove, Covesea, Hopeman East and Branderburgh – all lie along the southern coast of the IMFB, between Burghead and Lossiemouth (Fig. 4.3a). Large areas of Hopeman Sandstone crop out here, together with limited exposures of Stotfield Chert and Upper Devonian (Old Red Sandstone) strata (Fig. 4.3a).

The faulting and associated brittle deformation seen here is widely considered to represent the onshore continuation of the offshore LFZ (e.g. Al-Hinai et al. 2008; Farrell et al. 2014). The brittle deformations range in scale from deformation bands with slip plane offsets of millimetres, to faults with many metres to tens of metres of displacement, which juxtapose different rock formations (e.g. the Burghead Fault; Fig. 4.3a). This area has been a classic location for studying how fault-related deformation affects the anisotropy of permeability and compartmentalisation of highly porous sandstone as an analogue to similar reservoir rocks in subsurface settings (e.g. Edwards et al. 1993; Al-Hinai et al. 2008; Farrell et al. 2014).

4.4.1.1 Clashach Cove [Grid Reference: NJ 15978 70131]

The Clashach Cove locality (Fig. 4.4) is located 2 km east of Hopeman village [NJ 146 694] (Fig. 4.3a). Hopeman Sandstone is well exposed in both the cliffs and flat-lying rock platforms (Fig. 4.4a, c).

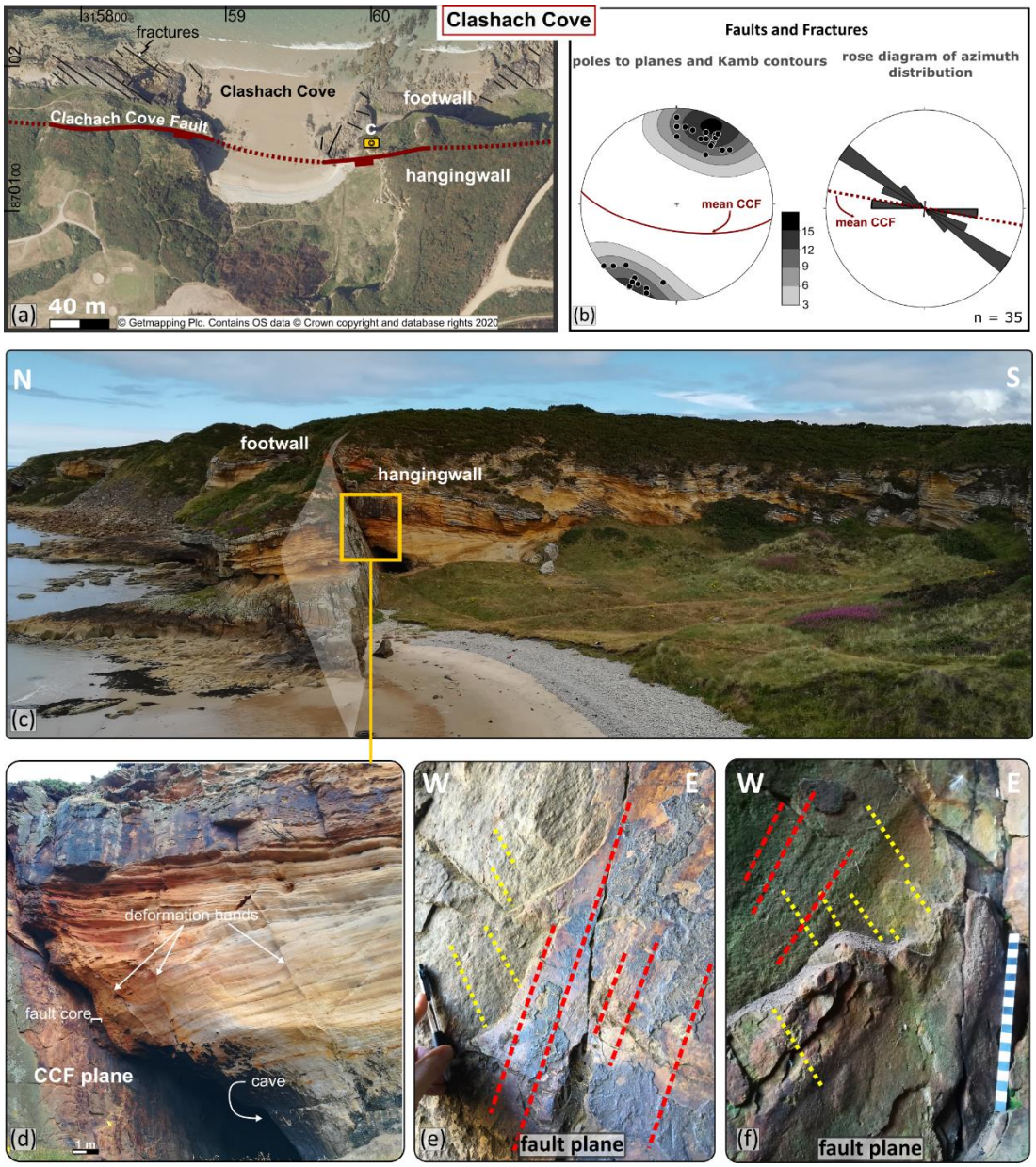

Fig. 4. 4: Structures observed at Clashach Cove locality (location indicated on Fig. 4.3a). (a) Aerial map (using EdinaDigimap service © Getmapping Plc) showing the trace of the Clashach Cove Fault (CCF). Fracture traces in fault footwall are shown in black. (b) Stereonets and rose plots of structural data collected in the field. Lower hemisphere, equal area projections. Mean orientation of the CCF is shown. Field photographs showing (c) the CCF cliff exposure on the eastern side of the bay. (d) Close-up of the fault zone looking east. (e-f) Views of CCF plane showing normal oblique-dextral slickenlines (red), polished and iron mineralized nature of fault plane and older, non-mineralized normal oblique-sinistral slickenlines (yellow). In both images, view is towards the fault footwall.

The E-W-trending Clashach Cove Fault (Fig. 4.4a-c) is the best exposed and most accessible seismic-scale fault in the area (Farrell et al. 2014). It is especially well exposed in the cliffs on the eastern side of the bay (Fig. 4.4c), displays an E-W trend (270° to 295°) and dips steeply (60° to 80°) towards the south. The fault can also be observed on the western side of the bay (Fig. 4.4a) and can be traced laterally for over 1 km. The fault throw has been estimated to be no more than 50 m, south-side-down based on the stratigraphy encountered by a nearby well (Quinn 2005).

The fault has a well-developed, 20 to 50 cm thick, fault core consisting of a heavily iron-stained brown/orange, poorly cemented fault gouge (Fig. 4.4d). The fault is surrounded by one-meter-wide damage zone dominated by cm- to dm-spaced deformation bands that are individually mm-wide, which decrease in density away from the fault core (see Farrell et al. 2014 for further details).

The footwall fault plane, which is exposed over a lateral extent of 50 m on the east side of the bay, of which 20 m are inside a cave, preserves several polished fault slip surfaces that display a dominant set of slickenlines suggesting normal- (slightly) dextral oblique-slip movements (pitching between 70° to 80 W°, Fig. 4.4e; see also Farrell et al. 2014). A previously undocumented (to our knowledge) set of lineations are also preserved on, less polished fault planes that consistently display normal-sinistral oblique-slip kinematics (pitching between 50° to 60° E; Fig. 4.4e, f in yellow). These are overprinted by the dextral normal slickenlines that suggest the Clashach Cove Fault had more than one episode of movement (Fig. 4.4e, f in red).

Immediately north of the Clashach Cove Fault, in the flat-lying platform, we can see multiple steeply-dipping (70°-90°) iron-stained tensile fractures mostly trending WNW-WSE also occur (Fig. 4.4a black lines) that appear to be consistent with the later minor dextral component of shear and associated mineralization along the master fault.

4.4.1.2 Covesea [Grid Reference: NJ 17841 70835]

This study site (Fig. 4.5) of about 1 km in length is located 500 m north of Covesea village [NJ 186 704] (Fig. 4.5.3a). The Hopeman Sandstone exposed here crops out predominantly in high coastal cliffs (c. 15-20 m high), which locally erode to form systems of caves and natural arches (e.g. Fig. 4a). The sandstones that preserve aeolian cross-bedding have been dissected by numerous faults, fractures and fracture corridors (Fig. 4a-d). The structures here have two main trends (Fig. 4h). The most prominent fault set forms as apparently conjugate faults striking E-W (e.g. Fig. 4a and b) and dipping 60° to 80° to the north and south (Fig. 4h). These faults are associated with damage zones in which well-cemented deformation bands develop (Fig. 4c and d). The deformation bands are individually 1-10 mm wide and commonly form amalgamated sets of up to 30 cm thick (Fig. 4c). They are widely associated with slip surfaces accommodating small normal throw of bedding ranging from a few millimetres to 20 cm. Exposed S-dipping slip surfaces locally preserve steeply E-pitching lineations indicating a sinistral-normal oblique-slip shear senses (pitch 65 E in Fig. 4g). The other set of structures is represented by fractures and m-wide fracture corridors striking N-S. The fractures are vertical to steeply dipping (>80°) tensile fractures which are not associated with deformation bands and show no clear offsets of bedding.

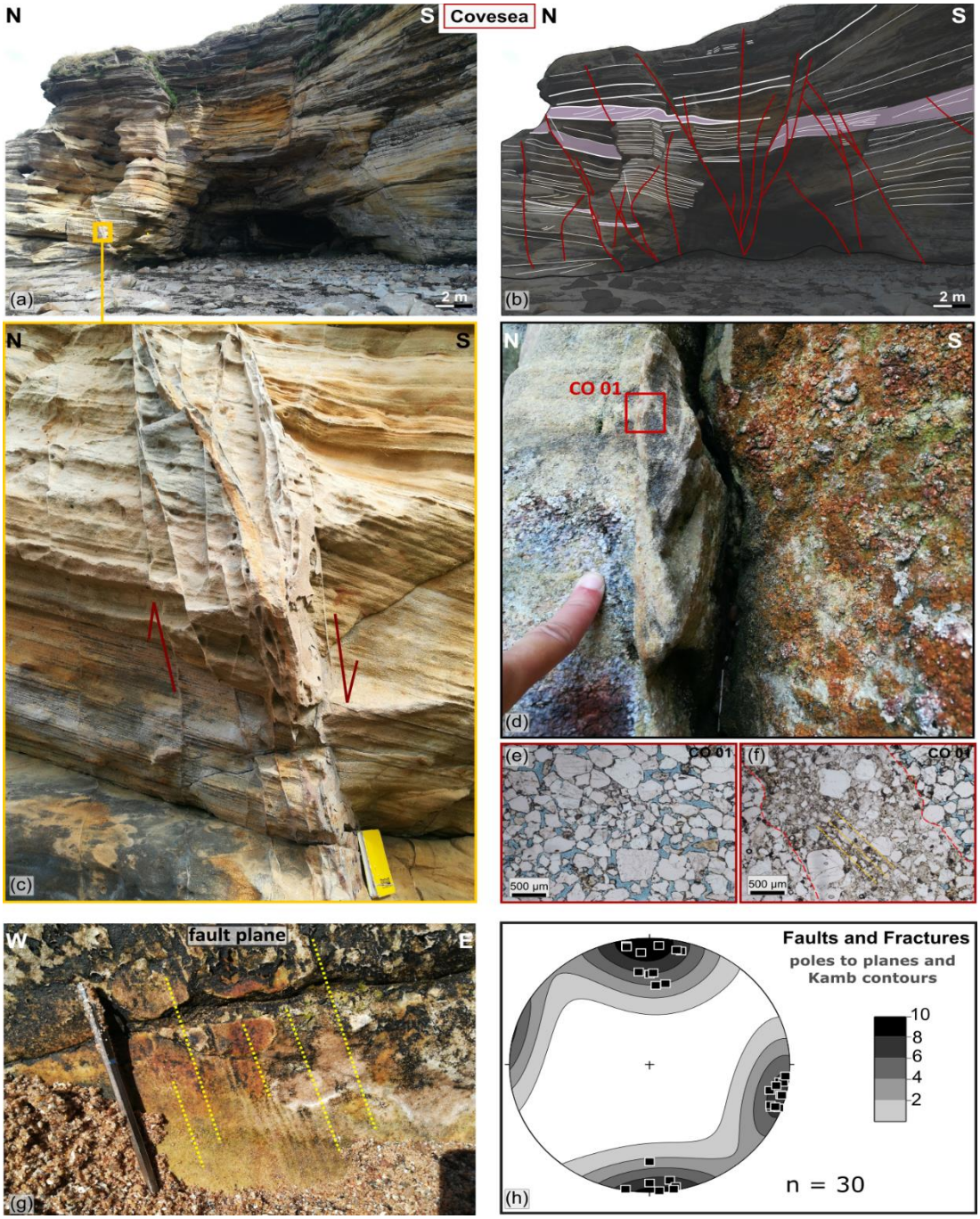

Fig. 4. 5: Structures observed at Covesea locality (location indicated on Fig. 4.4a). (a) Field photograph and (b) line drawing showing a cross-sectional view looking east at the E-W striking conjugate faults. Some marker beds which could be traced across faults are shown in purple. (c-d) Detailed views of the deformation bands associated with the E-W faults. Location of sample CO 01 shown on (d). (e) Thin section of typical undeformed Hopeman Sandstone impregnated with blue resin to highlight porosity. Rounded to sub-rounded clasts are dominated by quartz and are typical of aoelian sandstones – note hematite rims around clasts. Image in ppl. (f) Thin section through typical deformation band (margins highlighted in red) showing grainsize reduction due to cataclasis and marked reduction in visible porosity due to cementation. The central region shows a weak foliation (highlighted in yellow) due to the onset of pressure solution and possible shearing of grains during faulting. Image in ppl. (g) South-dipping fault plane viewed towards footwall showing normal oblique-sinistral slickenlines indicated by yellow dotted lines. (h) Stereonet of faults and fractures. Lower hemisphere, equal area projection.

Thin sections show that the undeformed host sandstone is mainly formed by rounded to sub-angular quartz grains with subordinate feldspar and

metamorphic clasts (mostly mylonitic quartzites) (Fig. 4e). All clastic grains are coated with thin films of iron oxide (Fig. 4e and f). Some quartz cementation and overgrowths are present, leading to a porosity reduction (Fig. 4e). The effects of cataclasis related to E-W deformation band development are widespread, leading to a significant and variable degrees of grain size reduction, compaction and cementation that is typical of such features (e.g. see Underhill and Woodcock 1987; Fossen et al. 2007). These processes lead to large decreases in porosity to virtually zero (Fig. 4f). Some more deformed regions of cataclasis have additionally developed an incipient foliation due to the weak development of solution seams and possible alignment of grains due to shearing (Fig. 4f). Such deformation band arrays are very likely to act as baffles to fluid flow in the subsurface (e.g. Shipton et al. 2002; Rotevatn et al. 2013, 2016) and their influence needs to be considered when modelling fluid storage and migration processes in sandstone aquifers or hydrocarbon reservoirs.

4.4.1.3 Hopeman East [Grid Reference NJ 15176 70163]

This location lies 500 m east of Hopeman village harbour (Fig. 4.3a). The Hopeman Sandstone crops out in a flat-lying wave-cut platform that covers an area of about 250 m by 60 m (Fig. 4.6a). The strata dip sub-horizontally to 15° and appear to be gently folded into an open, gently NE-plunging syncline (15°/050) (Fig. 4.6a).

The dominant structures observed both on aerial photographs and on the field are NNE-SSW and NW-SE trending (Fig. 4.6e).

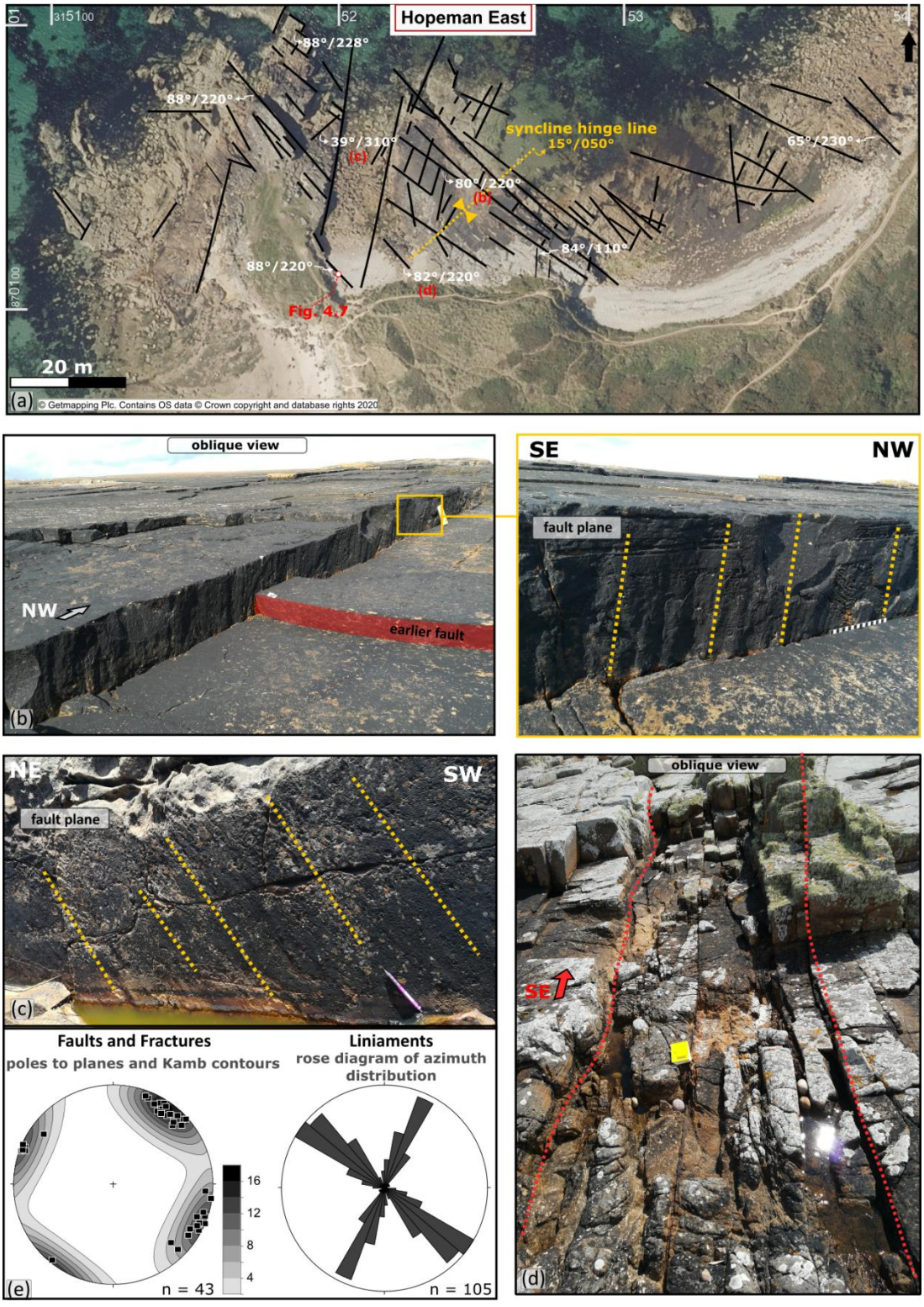

Fig. 4. 6: Structures observed at Hopeman East locality (location indicated on Fig. 4.a). (a) Aerial map (using EdinaDigimap service © Getmapping Plc) showing interpreted structural lineaments with representative faults shown as dip and azimuth. Locations of b-d and Fig. 6 also indicated. Field photographs showing - (b and inset) Oblique view of an NW-SE trending fault showing dip-slip slickenlines. (c) NW-dipping fault plane showing normal oblique-sinistral slickenlines indicated by yellow dotted lines. (d) Oblique view of an NW-SE trending fracture corridor, margins indicated by red dotted lines. (e) Left - stereonet of faults and fractures. Lower hemisphere, equal area projection. Right- rose diagram showing lineaments interpreted from the aerial map.

The NNE-SSE trending set (mean vector trending 025°) is mainly represented by steeply dipping to sub-vertical (70° to 90°) tensile joints. The NW-SE trending fracture set (mean vector trending 125°) are formed by steeply dipping (73° to 88°) single fractures or fracture corridors of about 1 m wide formed by clusters of closely spaced fractures (Fig. 4.6d) as well as small-scale faults (Fig. 4.6b and inset). The fault surfaces display down-dip slickenlines and grooves indicating dip-slip motion.

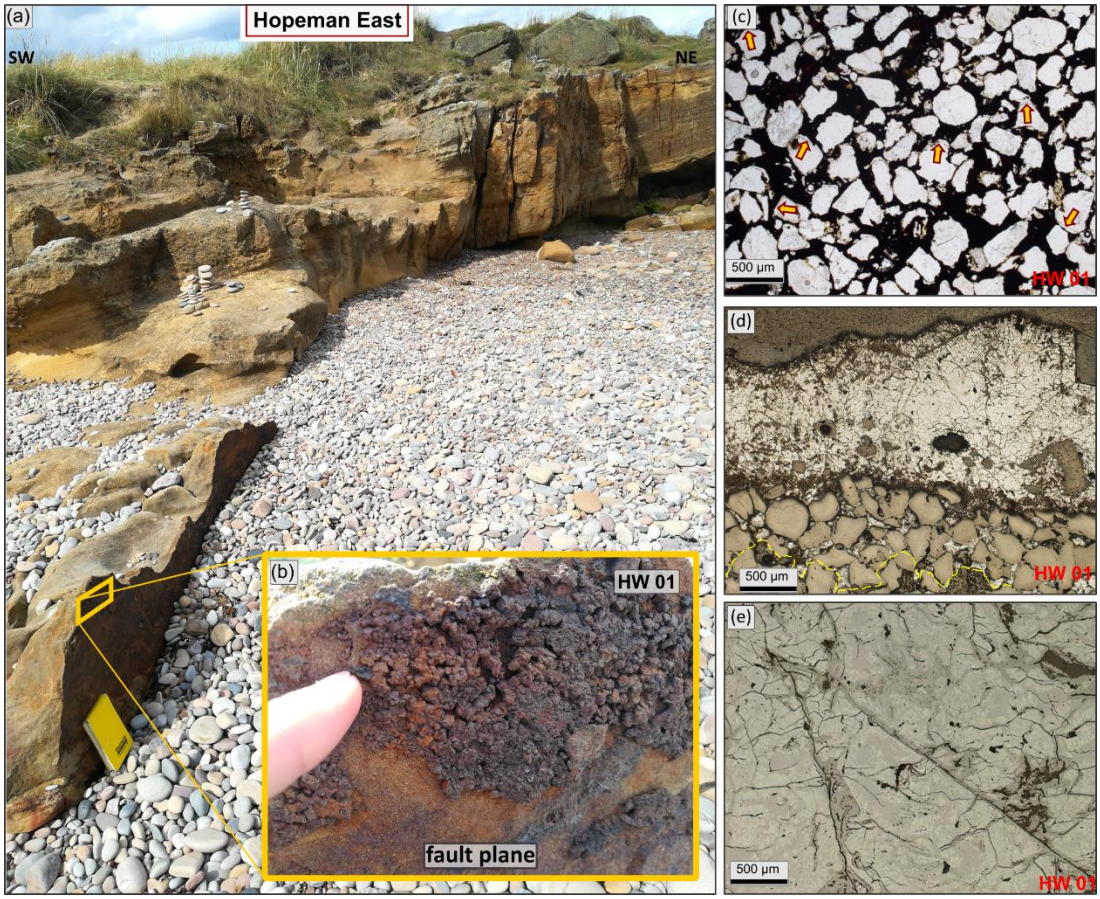

Fig. 4. 7: Structures observed at Hopeman East locality (location indicated on Fig. 5a). (a - b) Field photographs showing an NW-SE trending iron mineralised fault plane with location of sample HW 01 indicated on (b). (c) Thin section of hematite-stained undeformed Hopeman Sandstone showing how mineralization has occluded porosity (compare with Fig. 4e). Iron mineral fills post-date quartz overgrowths on clastic grains (exaples highlighted by yellow arrows). Image in ppl. (d) Thin section of zoned hematite vein (shown in (b)) in reflected light with mineralization (bright grey) extending into the pore spaces of the wall rock sanstone, with approximate limit shown by yellow dashed line. (e) High magnification thin section view of mineral vein in reflected light showing hematite (brightest grey) altered to limonite (darker greys) along fracture networks.

The faults have decimeter-scale offsets and are locally associated with the development of narrow (millimeter wide) deformation bands. NW-SE trending faults appear to locally cross-cut and offset the NNE-SSW structures (Fig.

4.6b) and could be younger. Rare examples of NE-SW trending faults are also present with moderate NW dips (40°) and oblique slickenlines indicating normal-sinistral oblique slip kinematics (pitch 70°SW; Fig. 4.6c).

The NW-SE trending faults/fractures are notably associated with iron mineralisation that is widely observed throughout the Hopeman Sandstone in the coastal sections as both diffuse patches and locally as veins up to 5mm thick (e.g. Fig. 4.7a and b). Thin sections show that the predominant iron mineral is hematite which locally almost completely occludes the pore space in otherwise high porosity sandstones (Fig 6c). Zoned hematite veining and pore-hosted mineralisation are clearly contemporaneous, with mineralising fluids locally extending out into surrounding wall rock pores (Fig. 4.7d). Iron mineralisation post-dates local quartz overgrowths (Fig. 4.7e) and has no associated grain-scale deformation.

4.4.1.4 Branderburgh [Grid Reference NJ 23021 71278]

This coastal exposure of about 200 m north of Branderburgh village (Fig. 4.5.3a) is a key outcrop location in the area as it exposes the eastern end of the Burghead Fault. Regionally, the 11-km-long fault strikes E-W and dips moderately to steeply to the south, extending from Burghead to Lossiemouth (BGS 1969; Edwards et al. 1993). It displays a maximum south-side-down displacement of 275 m (Quinn 2005), being one of the largest onshore regional faults in the area. The fault juxtaposes Upper Devonian Old Red Sandstone to the north against Upper Triassic Stotfield Chert to the south (Figs 2a and 7a).

The E-W trending (080°) fault is exposed in the tidal zone dipping 55° S and is best viewed at low tide where it can be traced for about 500 m along strike (Fig. 4.8a). Kinematic indicators are not preserved due to weathering of

the locally exposed fault plane.

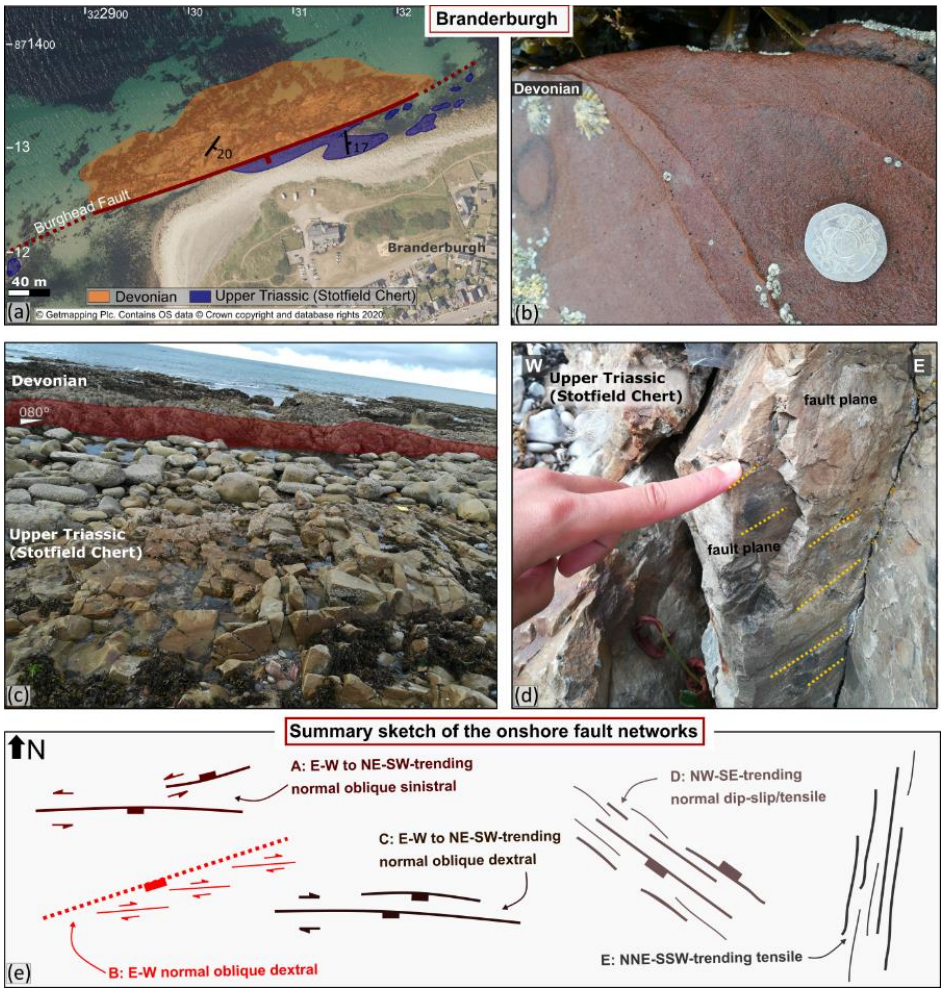

Fig. 4. 8: (a-d) Structures observed at Branderburgh locality (location indicated on Fig. 2a). (a) Aerial map (using EdinaDigimap service © Getmapping Plc) showing Burghead Fault and main geological features observed in field. Field photographs showing (b) Devonian sandstone in the footwall of the Burghead Fault. (c) Plan view of Burghead Fault represented as red plane. (d) Cross-section view of faulted Stotfield Chert in the hangingwall of the Burghead Fault. Exposed fault planes show oblique slickenlines indicated by yellow dotted lines. (e) Map-view sketch showing the variety of fault arrays observed onshore (not to scale).

The Devonian strata in the footwall are shallowly dipping (20° to 35°) to the ESE (Fig. 4.8a) and are represented by well cemented, medium to coarse-grained, red coloured sandstone with sparse deformation bands (Fig. 4.8b). The poorly exposed Upper Triassic strata (Stotfield Chert) in the hangingwall is shallowly dipping (17°) to the east. It has been highly fractured (Fig. 4.8c). A small cliff exposure located about 100 m south from the contact shows that the formation is cross-cut by E-W trending faults dipping 65° to 75° to both the north and south. Lineations preserved on exposed fault panels indicates normal-dextral oblique slip senses of fault movement (pitch 40° W, Fig. 4.9d).

4.4.1.5 Summary of onshore observations

E-W- to NE-SW-, NW-SE- and NNE-SSW-trending faults and tensile fracture (joint) sets dominate the onshore exposures of mainly Hopeman Sandstone. The E-W- to NE-SW-trending faults occur from regional scales (e.g. Clashach Fault; Fig. 4.4) to minor faults (e.g. Covesea; Fig. 4.5). They preserve evidence for early normal-sinistral oblique kinematics (e.g. Figs 4.4e and f, 4.5g and 4.8e-A). Minor E-W trending faults developed in the hanging wall of the regional Burghead Fault showing normal-dextral oblique kinematics (Fig. 4.8d, e-B), whilst the regional-scale Clashach Fault also preserves widespread evidence for a later phase of normal-dextral oblique kinematics (Fig. 4.4e,f and 4.8e-C). NW-SE trending fractures and faults show mainly dip-slip kinematics (Figs 4.6b and 4.8e-D), whilst NNE-SSW tensile fractures and fracture corridors (Fig. 4.8e-E) are generally not associated with kinematic indicators and are possibly earlier than local NW-SE trending structures based on cross-cutting relationships (Fig. 4.6b).

4.4.2 Subsurface offshore interpretation

We focus here both on the local continuation of the LFZ offshore, where the Endevour 3D seismic volume covers the fault, and regionally in the IMFB to illustrate the structural history and support interpretations made in the 3D cube.

Structures associated with the offshore continuation of the LFZ were interpreted using a series of 2D seismic profiles and key seismic horizons maps. We organised our observations based on how the imaged structures interacted with the three main stratigraphic sequences (Fig. 4.3c). The oldest is the Permo-Triassic sequence, bounded by the Variscan unconformity and

the Stotfield Chert (Fig. 4.3c-III). This package should preserve evidence of Permian and/or Triassic basin filling and rifting processes (if any). The overlying Jurassic-Lower Cretaceous sequence (Fig. 4.3c-II) between the Stotfield Chert and the NBCE should highlight the main periods of syn-rift faulting associated with the main phase development of the IMFB. The uppermost sequence (Fig. 4.3c-I) is the post-NBCE package and should highlight post-rift basin filling and deformation processes associated with (possibly) Cenozoic events.

4.4.2.1 Permo-Triassic sequence

The Variscan unconformity is locally characterised by a strong seismic reflector (e.g. Fig. 4.9a; 4.9aS - the uninterpreted seismic profile). A few wells have penetrated to the base of the succession (e.g. well 12/29-2, Fig. 4.2a), some of which are located in proximity to the studied seismic profiles, which provides enhanced confidence on the mapping of this seismic horizon.

Regionally, the Stotfield Chert at the top of the Triassic succession forms a strong, laterally continuous seismic marker horizon (e.g. Fig. 4.3). Faults observed cross-cutting the Permo-Triassic stratigraphy also displace younger stratigraphy (e.g. Figs 4.3c, 4.9a and 4.10a). Local thickness variations of the Permo-Triassic succession, seen in both the wells and on seismic profiles, has led some authors to suggest that this is due to growth faulting during a Permo-Triassic phase of rifting in the IMFB (e.g. Frostick et al. 1988; Roberts et al. 1989). It is undoubtedly true that thickness variations in the Permo-Triassic fill are seen in many seismic sections (e.g. Figs 4.9 and 4.10).

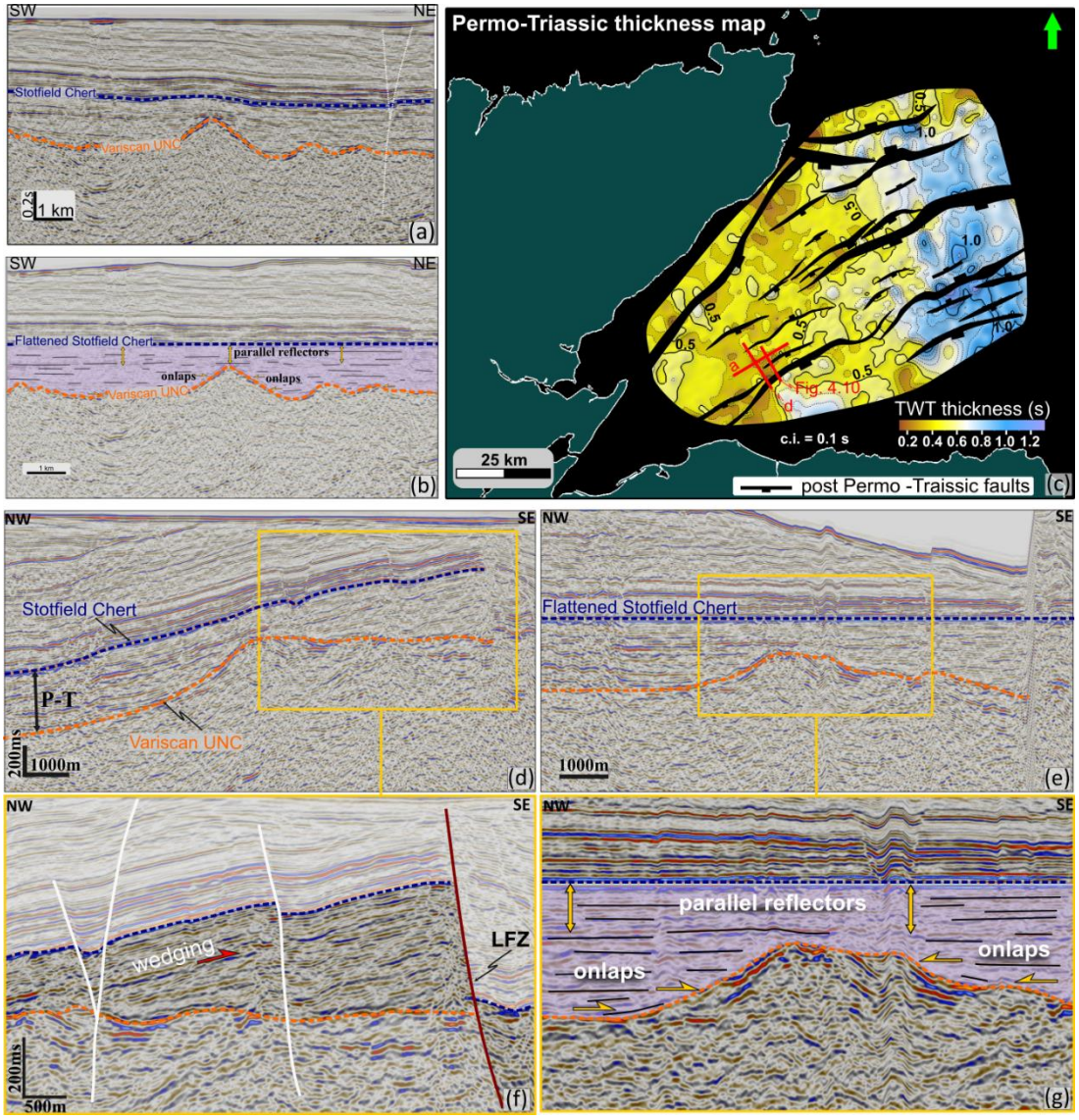

Fig. 4. 9: (a) SW-NE trending seismic profile showing Stotfield Chert and Variscan UNC horizon and (b) flattened profile at Stotfield Chert horizon. Note the palaeotopographic highs and lows of the Variscan. Location of (a) is indicated on (c). (c) Regional isochron map between Variscan Unconformity (UNC) and Stotfield Chert showing an increase of Permo-Triassic sequence towards east. Locations of (a), (d) and Figs 9 and 14 are also indicated on the map. (d) NW-SE trending seismic profile with interpretation of Variscan Unconformity (UNC) and Stotfield Chert horizon. (e) Structural flattened profile at Stotfield Chert horizon. Yellow boxes show the enlarged area in (f) and (g). (f) Enlarged detail from (d) showing apparent wedging in Permo-Triassic sequence towards the footwall of the Lossiemouth Fault Zone indicated by the red arrow. (g) Enlarged detail from the flattened seismic profile in (e) showing the Permo-Triassic sequence onlapping the Variscan palaeotopography.

However, the regional Permo-Triassic isochron map (Fig. 4.9c) shows gradual eastwards increase in overall thickness across the study area, but unambiguously fault-controlled thickness variations are not observed at a regional scale. The Variscan unconformity commonly displays a series of palaeotopographic highs and lows that are infilled by the overlying Permo-Triassic sequence (e.g. Fig. 9a and b), which therefore shows large thickness

variations (between 200ms and 500ms). Apart from a gentle folding and the presence of small displacement (~100 ms) faults that cut the stratigraphy up to the surface, the sequence appears largely undeformed (Fig. 4.9a-b). Horizon flattening was performed at the Stotfield Chert level (Fig. 4.9b) to better identify any evidence of Permo-Triassic deformation. This horizon was selected as it is interpreted as a regional palaeosol layer, associated with an overall period of tectonic quiescence (Naylor et al. 1989); hence any Permo-Triassic deformation should have ceased by that time. The resulting basin fill geometry shown in Figure 4.9b shows that the intra-Permo-Triassic reflectors are consistently sub-parallel and are clearly onlapping the palaeotopographic highs displayed by the basal Variscan unconformity.

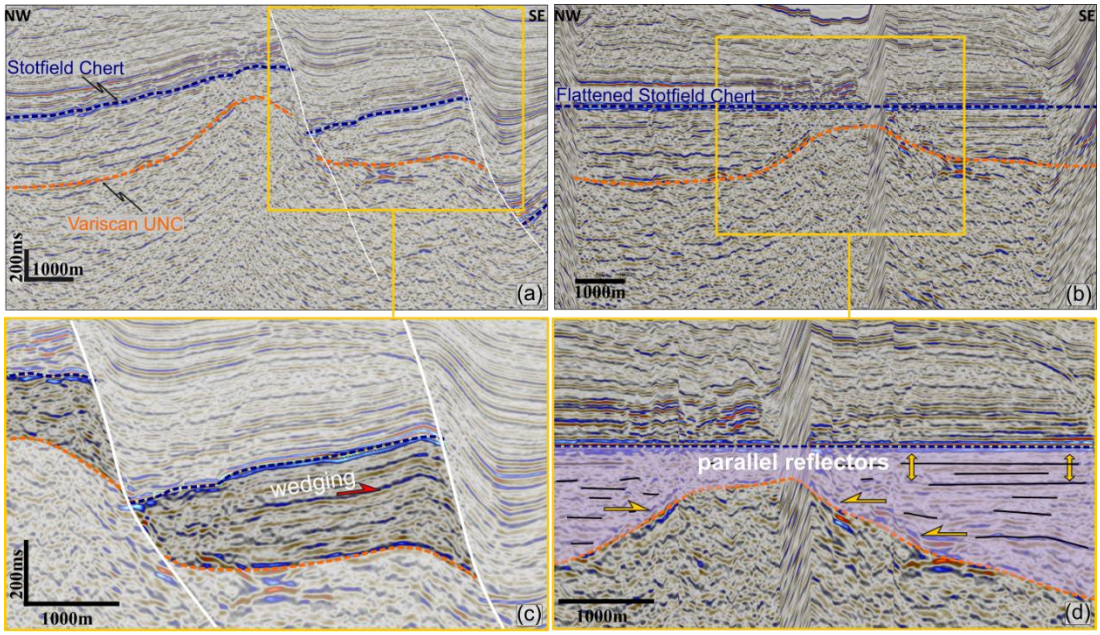

Fig. 4. 10: (a) NW-SE trending seismic profile (location shown on Fig. 4.9c) with interpretation of Variscan Unconformity (UNC) and Stotfield Chert horizon shown. (b) Structural flattened profile at Stotfield Chert horizon. (c) Enlarged detail of apparent wedging Permo-Triassic sequence towards the footwall of the Lossiemouth Fault. the direction of wedging is shown by the red arrow. (d) Enlarged detail from the flattened seismic profile showing the Permo-Triassic sequence onlapping the Variscan palaeotopography.

Other seismic reflection sections show Permo-Triassic packages apparently 'wedging' toward the SE (e.g. Figs 4.9d, f and 4.10a, c; Fig. 4.9dS and Fig. 4.10aS - the uninterpreted seismic profiles). After horizon flattening

at the Stotfield Chert horizon (Figs 4.9e, g and 4.10b, d), however, it is clear that once again the intra-Permo-Triassic seismic reflectors are sub-parallel and onlap onto the Variscan unconformity. We were unable to find any fault plane reflections or cut-offs which could prove the existence of a fault showing demonstrable Permo-Triassic fault growth geometries. Thus, in these cases, the apparent wedging geometry occurs due to onlapping of the palaeotopography at the base of the sequence. We suggest that in poor seismic data such features could easily be misinterpreted as growth strata.

4.4.2.2 Top Triassic - NBCE sequence

The regional time structure contour map of the Stotfield Chert (Fig. 4.11a), which is overlain by the Jurassic sequence, is dissected by several major ENE–WSW to NE-SW trending faults (tens of kilometres length). These faults form a series of well-defined horsts and grabens and define the main structural framework of the IMFB. The SSE-dipping LFZ, located in the southern part of the basin (Fig. 4.1b), has a mapped length of about 68 km and can be mapped to within ~2.5 km of the coast (Fig. 4.11a). It has a cumulative maximum throw of about 1600 ms (TWT) recorded at the Stotfield Chert level (Fig. 4.11b and d). The fault is last intercepted close to the coastline by the IMF97 202 line to the ENE (Fig. 4.3b), where the fault still has about 250 ms of vertical displacement. Seismic sections oriented approximately perpendicular to the LFZ (e.g. Fig. 4.11d) show that the Lower and Middle Jurassic strata overlying the Stotfield Chert are characterised by rather parallel reflectors suggesting an absence of active growth faulting at this time. The overlying Upper Jurassic to Lower Cretaceous succession has a half-graben geometry with a maximum thickness of 750 ms adjacent to the fault plane (Fig.

4.11b and d). This shows very clear evidence of syn-tectonic growth faulting in the LFZ hangingwall over this stratigraphic interval.

Whilst the regional map provides a good overview of the major, tens of

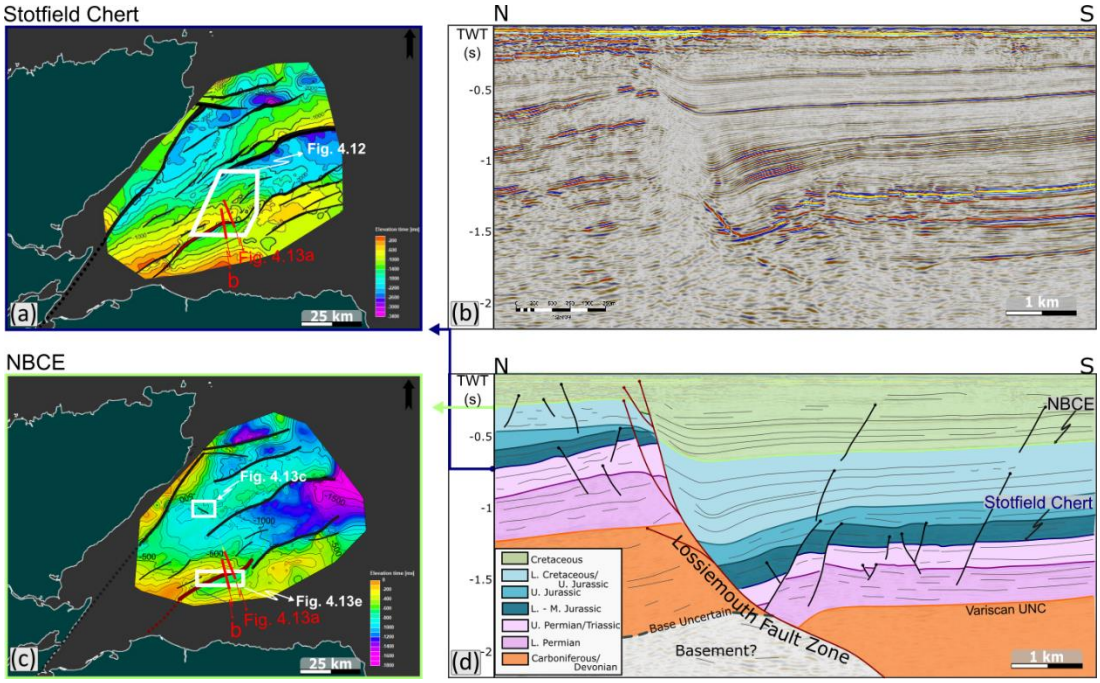

Fig. 4. 11: Regional TWT structural map of (a) Stotfield Chert horizon with location of (b), and (c) Near Base Cretaceous Event (NBCE) with location of (b), Lossiemouth Fault Zone is indicated by dark red line on both maps. (b) uninterpreted and (d) interpreted stratigraphy and faults on a N-S trending seismic profile through Lossiemouth Fault Zone.

km-length faults, the Stotfield Chert horizon mapped in the 3D Endevour seismic survey provides a well imaged sequence of minor faults (lengths about 1 to 5 km) between the major faults (Fig. 4.12a). The Stotfield Chert TWT map

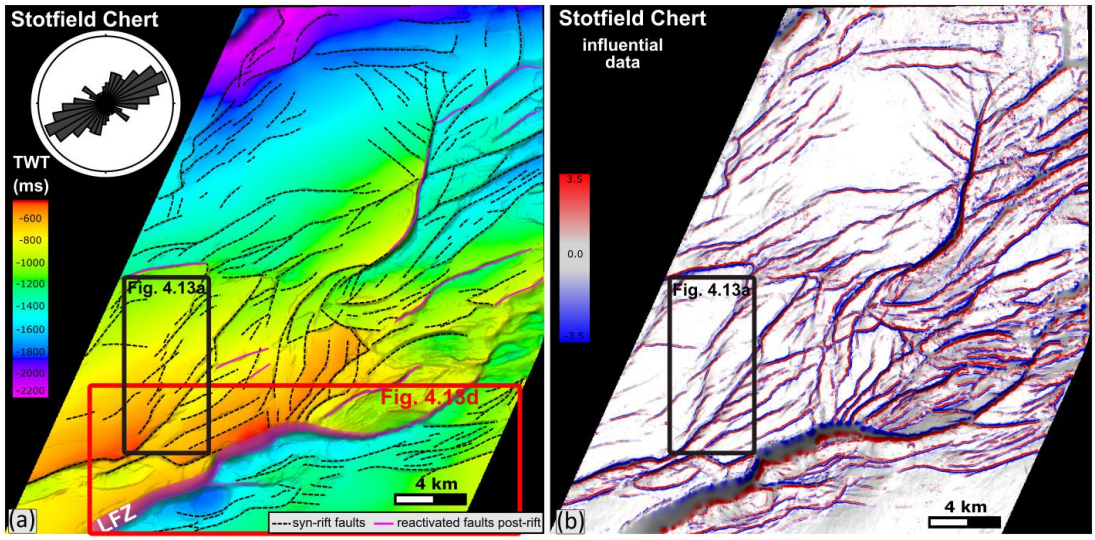

Fig. 4. 12: (a) Structural TWT map of the Stotfield chert horizon and (b) influential data attribute applied on (a). Locations of Fig. 4.13a and d are indicated on the maps.

reveals the complex structural style (Fig. 4.12). We analysed these faults also using the influential data attribute to better highlight the fault trends (Fig. 4.12b). The faults generally trend ENE-WSW to NE-SW (about 40º scatter), however occasionally en-echelon NNE-SSW-trending faults and WNW-ESE-trending faults are visible (Fig. 4.12 and inset rose plot). The en-echelon arrangement of the NNE-SSW-trending faults suggests a component of dextral strike-slip associated with these faults (Fig. 4.13a and inset).

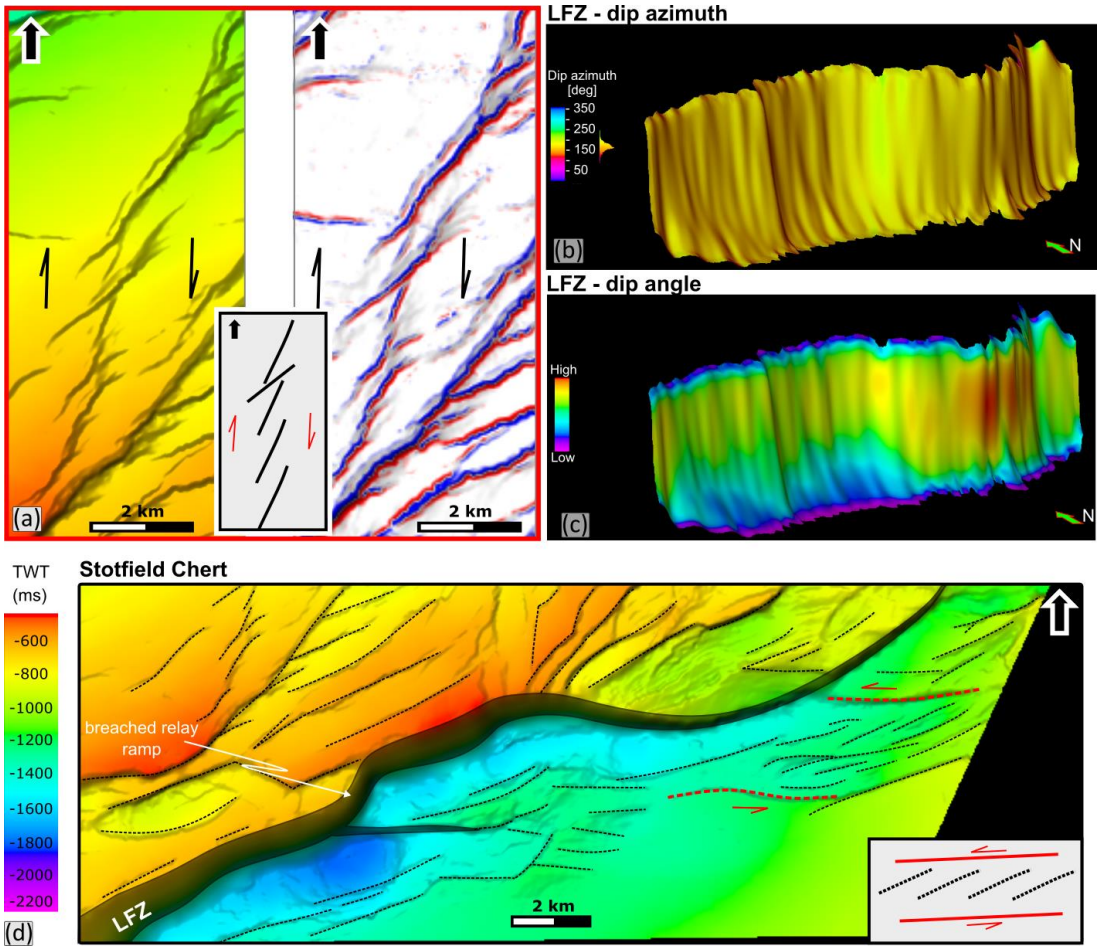

Fig. 4. 13: (a) and inset sketch showing the en-echelon NNE-SSW-trending structures on the TWT map and influential data attribute map suggesting dextral strike-slip. See location on Fig. 4.12a and b. Lossiemouth Fault surface covered by the 3D data displaying (b) dip azimuth and (c) dip angle attributes. (d) TWT structural map of the Stotfield Chert horizon interpreted based on 3D reflection data along the north-eastern end of the LFZ. Dashed lines represent minor faults. Inset sketch showing the en-echelon structures suggesting sinistral slip.

The 3D volume covers some 28 km length of the LFZ (Fig. 4.11a), which provides a detailed insight into the fault zone architecture (Fig. 4.12 and 4.13). The main fault strand, mapped in 3D steeply dips to the SSE, apparently

shallowing at depth (Fig. 4.13c and d). However, it appears that the LFZ consists of two fault segments that link through a breached relay ramp to form a through-going fault array (Fig. 4.13d). Minor faults (about 1 to 5 km in length) trending parallel to the main structure are imaged in both its hangingwall and footwall (Fig. 4.13d). Towards the western side of the fault, an array of minor ENE-WSW-trending faults developed between two parallel E-W-trending faults suggest a component of sinistral slip along these E-W-trending faults (Fig. 4.13d and inset).

4.4.2.3 Post-NBCE sequence

The Late Jurassic-Early Cretaceous syn-rift sequences are capped by the NBCE, which forms a prominent seismic reflector (e.g. Fig. 4.14a) that can be confidently mapped across most of the IMFB. On seismic reflection profiles (e.g. Figs 4.11d and 4.14b), the LFZ clearly cuts most, if not all, of the stratigraphy up to close to the seabed. The throw of the NBCE, of about 500 ms, is minor compared to the displacement of the Stotfield Chert horizon. Importantly, no thickness variation is observed in the hangingwall of the LFZ to suggest syn-kinematic growth (e.g. Fig. 4.14b). Thus, whilst the LFZ cuts through this horizon, the fault was not active during (the preserved) Cretaceous depositional period and was only later reactivated after the deposition of this sequence. More generally within the adjacent Lossiemouth Sub-basin/Central Ridge area (and regionally in the IMFB; e.g. Underhill 1991a; Thomson and Underhill 1993), the overlying Cretaceous succession clearly onlaps onto the NBCE horizon, which therefore caps the underlying syn-rift succession (e.g. Fig. 4.14a and b). This suggests that all the faults cutting this horizon post-date the (preserved) Cretaceous sequence.

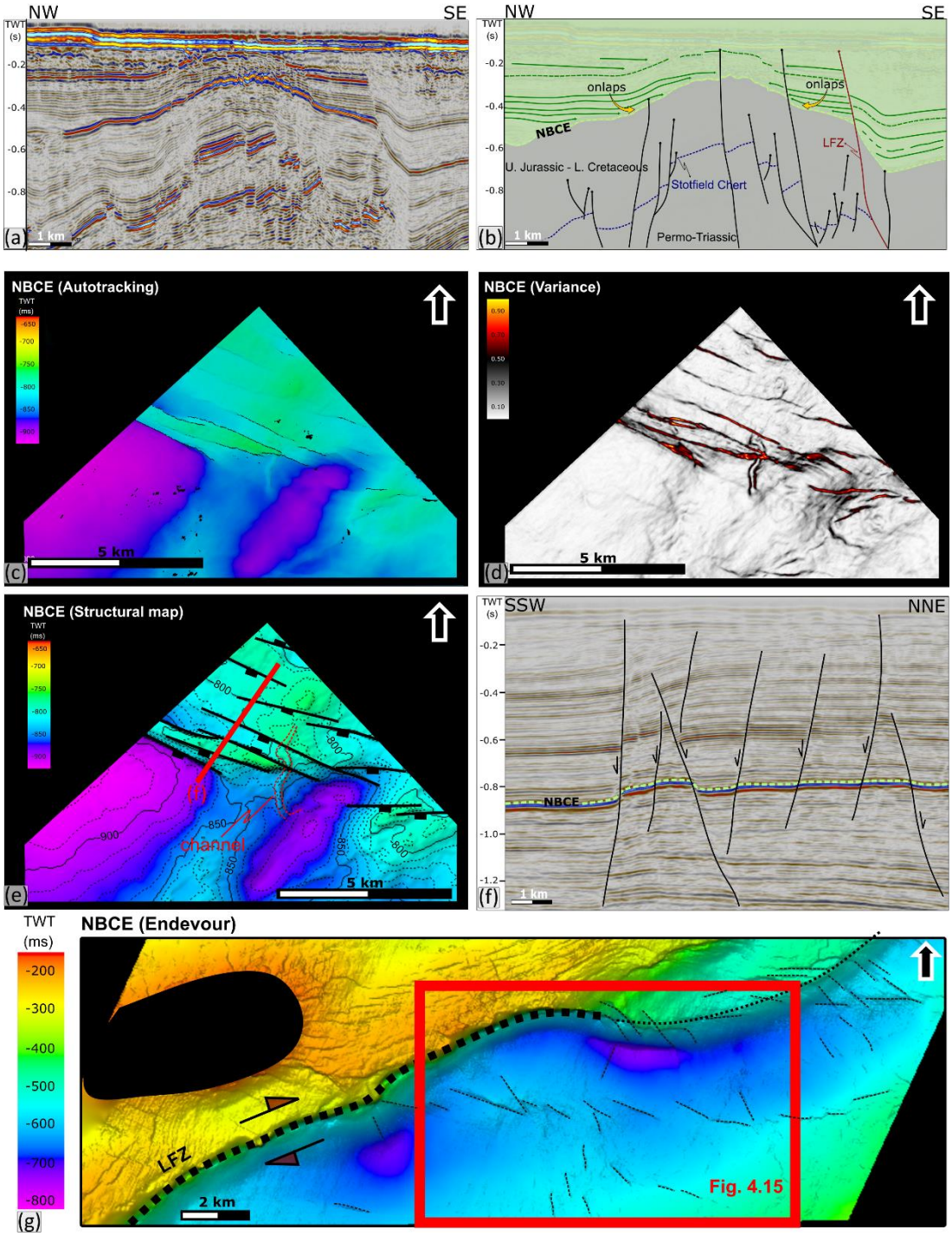

Fig. 4. 14: NW-SE-trending seismic profile (a) uninterpreted and (b) interpreted to highlight the onlapping nature of the post-NBCE sequence. The Near Base Cretaceous Event (NBCE) mapped in the Beatrice 3D cube showing the WNW-ESE-trending faults of (c) autotracked horizon, (d) variance (e) structural TWT map. (f)SSW-NNE0trending seismic profile showing a cross-section through the WNW-ESE-trending faults displacing the NBCE horizon. Location shown in (e). (g) TWT structural map of the NBCE interpreted based on the Endevour 3D reflection data, along the north-eastern end of the LFZ. Dashed black lines represent minor faults. Location of Fig. 4.15 is shown.

The regional structural map based on the 2D seismic reflection profiles (Fig. 4.11c) shows that in addition to the LFZ, many other major faults that were active as growth structures during the Jurassic-early Cretaceous were

also reactivated and displace the NBCE horizon. In the area less affected by the reactivation of the major fault, newly-formed WNW-ESE-trending faults develop (Fig. 4.14 c-f), dipping both to the SSW and NNE (Fig. 4.14 e and f).

The LFZ, which appears to be a through-going structure on the regional map (Fig. 4.11c) has a mapped strike length of about 40 km (Fig. 4.11c). In the area covered by the Endevour 3D seismic reflection data, however, the map-view expression of the LFZ becomes much more complex with a series of smaller-scale, en-echelon faults developed, especially towards its northeast termination (Fig. 4.14d; Fig. 4.14dS - the uninterpreted map).

A well imaged sequence of newly-formed, post-NBCE minor faults (lengths < 2 km) are seen developed predominantly in the hangingwall of the LFZ (Figs 4.14e and 4.15). We analysed these faults using three seismic structural attributes: 'Edge detection' (Fig. 4.15b); 'Influential data' (Fig. 4.15c); and 'Variance' (Fig. 4.15d), in order to enhance these structures which lie close to the limits of seismic resolution. Three fault populations trending NNW–SSE, NW- SE and WNW-ESE are distinguishable (Figs. 12e). These faults include NW-SE trending faults that are mostly associated with the reactivated LFZ and minor new-formed faults in the proximity of the Lossiemouth Fault trending mainly WNW-ESE and NNW-SSE, although other orientations are also present (Fig. 4.15f).

These fault populations are consistent with a dextral strike-slip Riedel system developed during local NE-SW extension (Fig. 4.15f). We suggest that the NNW–SSE trending faults (Fig. 4.15e and f in yellow) correspond to antithetic Riedel structures, the NW- SE trending features (Fig. 4.15e and f in blue) to tensile fractures/normal faults and the WNW-ESE trending faults (Fig.

4.15e and f in dark red) to synthetic Riedel structures. In addition to those main Riedel structures, occasional Y and P shear structures can also be observed (Fig. 4.15e).

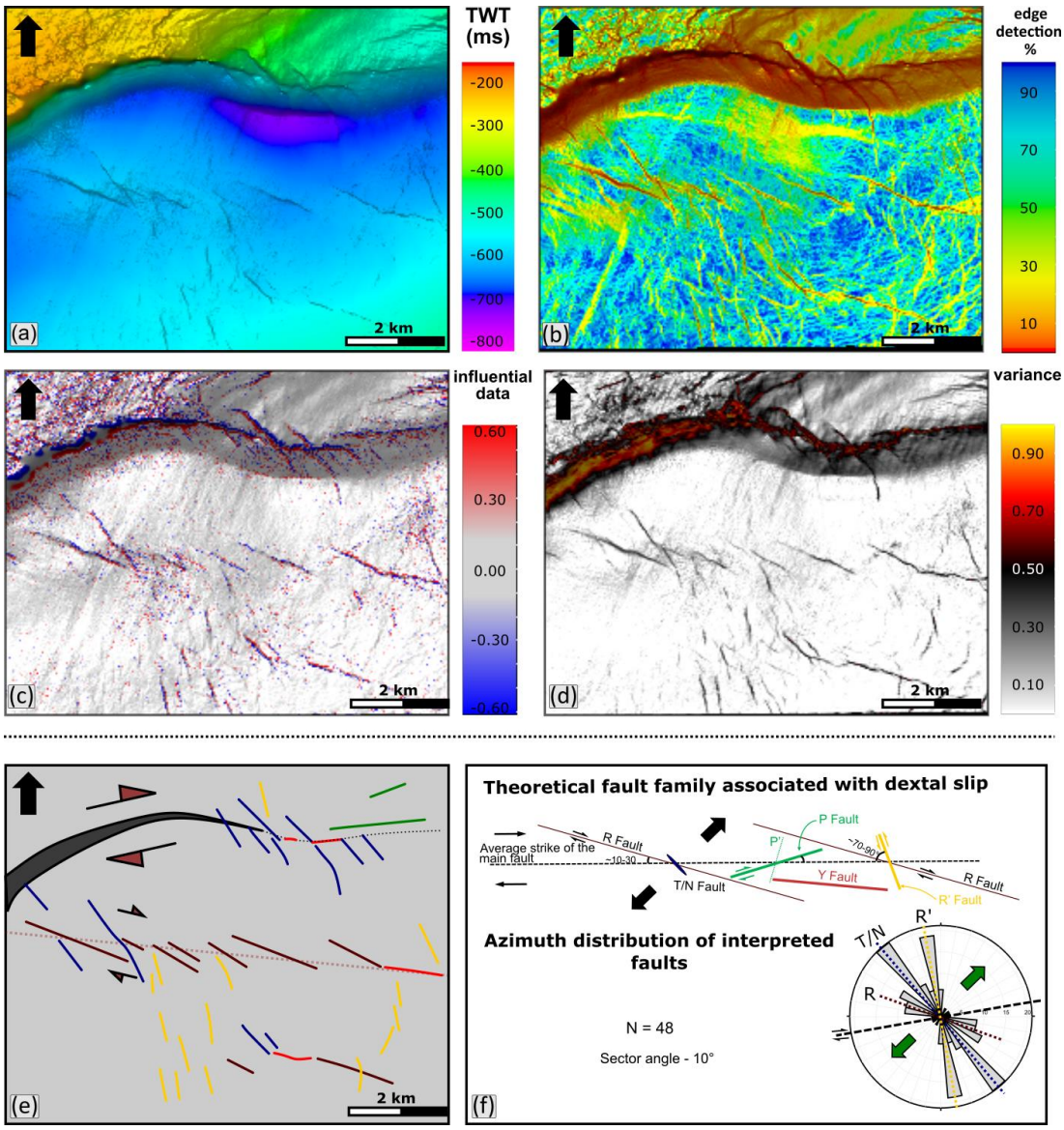

Fig. 4. 15: (a) enlarged detail of the Near Base Cretaceous Event (NBCE) TWT map interpreted based on 3D reflection data (see location on Fig. 4.14g). (a-d) Seismic attribute maps enhancing fault/fracture visualisation. (e) Interpreted structures in map view and (f) Rose diagram of azimuth distributions. The fault array geometry suggests a component of dextral movement. Theoretical fault family for dextral strike-slip is shown for comparison in (f), modified after Carne and Little 2012. Structures are colour coded in both (e) and (f) as follows: grey – main (Lossiemouth) fault; dark red – synthetic Riedels (R); yellow - antithetic Riedels (R'); blue – tensile (T) or normal (N) faults; bright red – Y fractures; green – P fractures.

4.5 Discussion

4.5.1 Onshore and offshore development of the LFZ: Linking onshore and offshore regions

The structural relationships associated with the onshore and offshore reactivation of the LFZ provide an important insight into how the various fault sets and kinematic patterns maybe correlated and separated in terms of their relative age. The offshore data show that the LFZ is a composite structure that is formed by a series of hard and soft-linked subordinate faults especially towards its lateral terminations, including onshore at its southwestern end.

Interpretation of the well-imaged minor structures associated with the LFZ imaged using the Endevour 3D seismic survey at its north-eastern end (Fig. 4.15) can be used to infer dextral kinematics (Fig. 4.15e and f) during NE-SW directed extension. This pattern is consistent with the regional understanding of Cenozoic deformation in the IMFB, which suggest widespread reactivation of intrabasinal structures (e.g. Thomson and Underhill 1993; Farrell et al. 2014; Argent et al. 2002). This reactivation occurred under a NE-SW extensional stress regime (Thomson and Hillis 1995) related to dextral reactivation of the Great Glen Fault Zone (e.g. Underhill 1991a; Thomson and Hillis 1995; Le Breton et al. 2013).

Based on the observed fault trends associated with inferred Cenozoic movements in the offshore, we suggest the following correlation with onshore structures. The E-W to ENE-WSW trending faults, which lie sub-parallel to the Lossiemouth Fault, plausibly represent either dextrally reactivated late Jurassic-early Cretaceous rift-related faults or are newly developed synthetic Riedels or Y faults (e.g. like those in Fig. 4.15e and f, in dark red and bright

red, respectively). These Cenozoic displacements could include the later phase of normal-dextral oblique slip seen along the Clashach Fault (Fig. 4.4e). Movements along the Burghead Fault have been previously inferred by Quinn (2005) to be Late Jurassic based mainly on the presence of Lower Jurassic sedimentary rocks in the hangingwall of the fault (Fig. 4.3a). It is possible that this structure did form during the main stage of Late Jurassic-Early Cretaceous rifting, but the minor dextral faults seen in its hangingwall (Fig. 4.8d) could indicate that this fault has also been reactivated or even initiated during the Cenozoic.

We further propose that the NW-SE trending faults seen onshore at Hopeman East (e.g. Fig. 4.6b and inset) are Cenozoic tensile fractures or dip-slip faults equivalent to those seen offshore (e.g. Figs 4.14e and 4.15e and f, in blue). Having grouped these onshore oblique-dextral E-W to ENE-WSW-trending and dip-slip NW-SE-trending structures and assigning them to Cenozoic stage, we are now able to perform stress inversion analysis. The faults appear to have developed during NNE-SSW extension direction (Fig. 4.16a) in a regime of near-horizontal extensional stress with a sigma 3 axis orientated 09/214° and a near-vertical compressive stress with a sigma 1 axis orientated 73°/335° (Fig. 4.16a). These results correlate well with both the inferred stress regime based on offshore fault trends along the Lossiemouth Fault (Fig. 4.15f) and with the regional Cenozoic NE-SW extensional stress regime inferred for the Cenozoic events (e.g. England 1988; Thomson and Underhill 1993; Thomson and Hillis 1995). It is unclear if the NE-SW-plunging fold observed at Hopeman East (Fig. 4.6a) is due to tectonic deformation or reflects the presence of large-scale dune cross bedding in the area. However,

such orientation would fit the dextral strain ellipse proposed for the Cenozoic deformation.

The remaining structures seen in the onshore area comprise E-W to ENE-WSW trending faults, sub-parallel with the regional Lossiemouth Fault, which preserves evidence for normal-sinistral oblique slip. These include the earlier phase of normal-sinistral oblique movement episode along the Clashach Fault (Fig. 4.4f), and the normal-sinistral minor faults present at Covesea (Fig. 4.5g) and Hopeman East (Fig. 4.6c). In the offshore, these fault trends are typical of Late Jurassic-Early Cretaceous syn-rift faults (Fig. 11a). Whilst many recent models, based on interpretations of seismic reflection data tend to suggest that there is little evidence for the development of syn-rift oblique-slip faults in the basin (e.g. Davies et al. 2001; Long and Imber 2010; Lapadat et al. 2018), some component of sinistral shear can be infer along the LFZ (Fig. 4.13d). A limited degree of strike-slip movement along any of the main half-graben bounding faults was also suggested by Underhill (1991).. More recently, Tamas et al. (2022a) have proposed that hitherto unrecognised transtensional components may be associated with fault reactivation during basin development.

A palaeostress inversion analysis of the slickenline lineations associated with the E-W to ENE-WSW trending structures showing normal-sinistral oblique movements yields an NNW-SSE extension direction (Fig. 4.16b). The faults were developed in a regime of near-horizontal extensional stress with a sigma 3 axis orientated 04°/157° and near-vertical compressive stress with a sigma 1 axis orientated 72°/052° (Fig. 4.16b). This extension direction correlates well with the NW-SE extension direction proposed by

Davies et al. (2001) based on offshore fault trends during the Oxfordian-early Kimmeridgian period. This is also parallel to the NNW-SSE extension direction seen during later phases of faulting (131 Ma) in onshore Devonian strata of the Turriff basin located on the southern margin of the IMFB, ~70 km east of the study area (see Chapter 3).

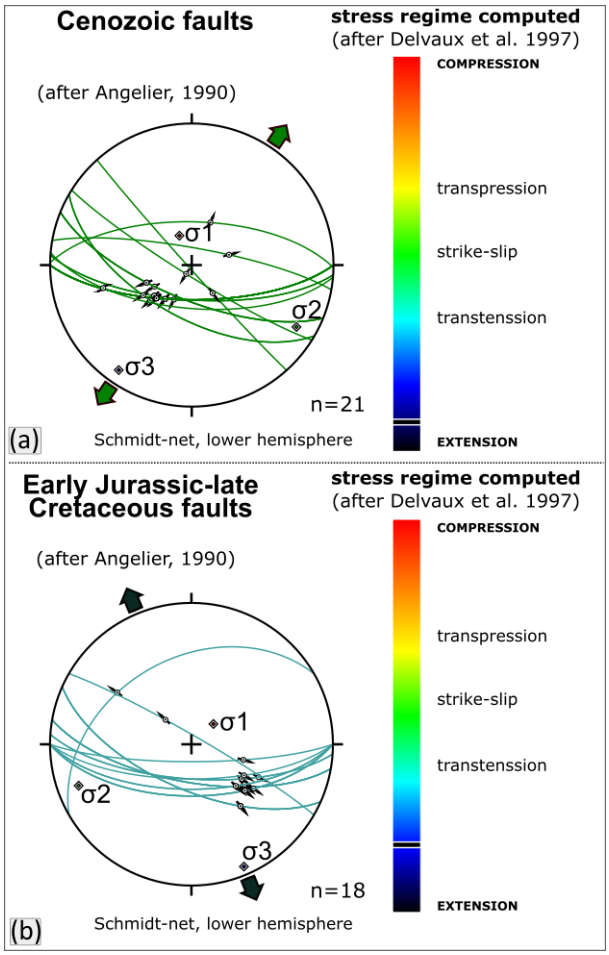

Fig. 4. 16: Stress inversion plots (after Angelier 1990) of: a) oblique-dextral; and b) oblique-sinistral normal faults from onshore study area – see text for further details.

The NNW-SSE to N-S trending faults identified onshore in our study area are also locally visible on the top Stotfield Chert map offshore (e.g. Fig. 4.13a). Although we were unable to recognise any kinematic indicators on these structures onshore, Edwards et al. (1993) have described dextral oblique slip on N-S- to NNE-SSW-trending faults in the Cummingstone area, near the western end of Burghead fault (Fig. 4.3a). Such oblique-dextral reactivation along NNE-SSW trending faults has also been identified in the Devonian strata in the Turriff sub-basin (see Chapter 3; Tamas et al. 2022a). U-Pb calcite dating of syn-kinematic mineralisation associated with these structures revealed that they likely formed during the Early Cretaceous (130.99 ± 4.6 Ma) under NNW-SSE extension (see Chapter 3). In the Turriff sub-basin, this leads to dextral

reactivation of pre-existing N-S- to NNE-SSW-trending Devonian rift faults and normal-sinistral oblique faulting along E-W to ENE-WSW trending structures. On the basis of the above observations and correlations, it is suggested that the earlier E-W trending sinistral normal and NNW-SSE-N-S trending, possibly dextral structures are related to the main phase(s) of Late Jurassic to Early Cretaceous rifting during the development of the IMFB. Unfortunately, no syn-tectonic calcite veins were observed in the area, which could be dated in order to confirm this suggestion.

4.5.2 Structural-stratigraphic relationships associated with the Permo-Triassic.

Interpretation of the offshore seismic reflection profiles (Figs 4.8 and 10) suggests that the Permo-Triassic sequence is largely characterised by onlapping onto a pre-existing post-Variscan palaeotopography and a seismic facies comprising parallel reflectors (e.g. Fig. 4.8b). Apparent wedge-like thickness variations have been shown - after horizon flattening at the Stotfield Chert Formation level and removal of deformation related to younger events - to be artefacts of Late Jurassic-Early Cretaceous and Cenozoic tilting and faulting (e.g. Fig. 4.9e). Coincidently, wedging is also observed in the footwall of major syn-rift (Late Jurassic-Early Cretaceous) faults (e.g. Fig. 4.10a). This implies that Permo-Triassic faults (presumably) having the same strike directions were not reactivated during Late Jurassic-Early Cretaceous, but were cross-cut by new oppositely dipping faults. Although this is not an impossible scenario in fault development, the lack of seismic evidence of a fault pane (e.g. fault plane reflection) and combined with the results of horizon flattening, which suggest parallel reflectors and onlaps (Figs 4.9b, g and

4.10d), we lean towards apparent growth strata. Additionally, Andrews et al. (1990) argue that previously cited Permo-Triassic wedges in the IMFB are, in fact, Devonian and Upper Jurassic. A passive subsidence and infilling of a pre-existing topography during the Permo-Triassic supports the regional models proposed by Thomson and Underhill (1993) and Andrews et al. (1990). Therefore, we suggest that none of faults and fractures observed onshore are the product of Permo-Triassic faulting. This is supported by the absence of local variations of the thickness of the Permo-Triassic sequences across the Burghead Fault in the onshore (Quinn 2005).

4.5 Conclusions

Onshore and offshore studies of the region associated with the LFZ on the southern margin of the IMFB have revealed the presence of NE-SW to E-W, N-S to NNE-SSW and NW-SE striking faults/fractures, creating a complex, composite

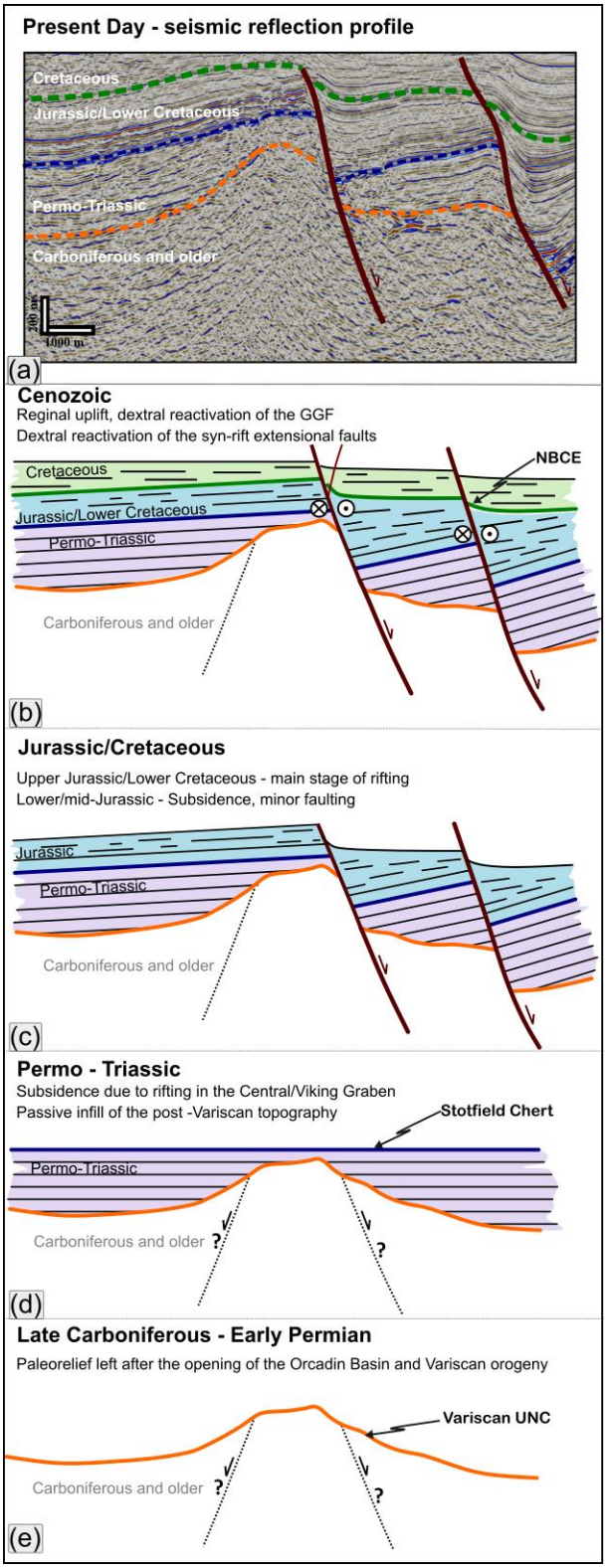

Fig. 4. 17: Summary of basin development using a representative 2D seismic profile (Fig. 4.10a).

reactivated structure. An onshore -offshore integrated analysis has revealed the following structural history summarised in Figure 4.17:

1) *Pre-rift:* Interpretations of offshore seismic data and lack of observed changes in sediment thickness across major exposed faults onshore (Quinn 2005) lead us to conclude that the Permo-Triassic basin development was not associated with active faulting, at least in the southern part of the IMFB. The basin at this time was characterised by sag-like regional subsidence and passive infilling of a pre-existing Variscan palaeotopography (14e, d). Local thickness variations within the Permo-Triassic sequences are related to this infilling process. Later faulting and tilting of these packages can produce wedge-like geometries that may resemble syn-kinematic growth strata, particularly in older, lower resolution 2D seismic sections (e.g. Figs 4.9f and 4.10c).

2) *Syn-rift:* Major E-W to NE-SW trending faults develop, including the LFZ (Fig. 4.17c). Offshore, they show strong association with wedge-shaped upper Jurassic-lower Cretaceous seismic packages (Fig. 4.11b and d), confirming their relative timing and syn-rift nature. Minor en-echelon, NNE-SSW trending faults occur (Fig. 4.13a) which could be related to dextral reactivation of Devonian structures as seen onshore in the Turriff basin further to the east (see Chapter 3). In the onshore study area, typically normal-sinistral oblique E-W to ENE-WSW trending faults develop under an NNW-SSE extension direction. Such faults include the Clashach Fault (Fig. 4.4f), minor faults at Covesea (Fig. 4.5) and most likely the Burghead Fault (Fig. 4.8a and c). We also interpret the NNE-SSW trending (possibly dextral) structures as being related to this deformation event.

3) *Post-rift:* This likely Cenozoic event is largely associated with the reactivation of the earlier formed major NE-SW to E-W trending fault complexes in the IMFB (Fig. 4.17b). Evidence of fault reactivation is encountered both onshore and offshore. Offshore, the LFZ shows evidence of dextral-normal reactivation, attested by newly formed minor en-echelon E-W to ENE-WSW, NW-SE, and NNW-SSE to N-S trending faults, interpreted as Riedel structures which fit a dextral reactivation model (Fig. 4.15e and f). Onshore, NNE-SSW-directed extension resulted both in the oblique dextral reactivation of the E-W to ENE-WSW trending faults and the development of other minor dextral E-W to ENE-WSW or dip-slip NW-SE-striking faults. Major faults such as Clashach Fault have been reactivated during this episode (Fig. 4.4e). This interpretation suggests that the Cenozoic deformation extends to the southern margins of the IMFB and is not simply limited to the north-western shore close to the Helmsdale and Great Glen fault zones (e.g. Underhill and Brodie 1993; Le Breton et al. 2013).

The present case study demonstrates the prevalence of structural inheritance and fault reactivation during superimposed faulting episodes associated with the geological evolution of the IMFB. It also highlights the value of integrating and correlating onshore surface and offshore sub-surface data to better assess the timing and kinematics of basin development. For example, in this study, the application of the strike-slip strain-ellipse model to interpret the offshore faulting patterns in plan view is now better justified as equivalent structures are seen onshore in surface exposures where kinematic evidence for components of dextral and/or sinistral movement are preserved.

This significantly reduces uncertainties in the interpretation of sub-surface datasets.

Old Red Sandstone at Sarclet Haven

Chapter 5

Combining geochronology and high-resolution photogrammetry to analyse the structural evolution of a superimposed basin: the northern margin of the Inner Moray Firth Basin, Scotland

Abstract

Constraining the age of formation and movement along fault arrays in superimposed basins helps us to better unravel the kinematic history as well as the role of bounding faults or inherited structures in basin evolution. The Inner Moray Firth Basin (IMFB, western North Sea) is a superimposed basin overlying rocks of the Caledonian basement, the pre-existing Devonian-Carboniferous Orcadian Basin and a regionally developed Permo-Triassic North Sea basin system. The IMFB rifting occurred mainly in the Upper Jurassic – Lower Cretaceous after a long period of subsidence followed by localised uplift in its eastern parts due to thermal doming in the central North Sea (in the middle Jurassic). The rift basin later experienced further episodes of regional tilting, uplift and fault reactivation during Cenozoic.

The Precambrian basement to Upper Jurassic cover successions exposed onshore along the North coast of IMFB preserve a variety of fault orientations and structures. At present, these minor structures, some related to the major fault zones bounding the IMFB (e.g. Helmsdale and Great Glen faults), lack precise age constraints for the timing of faulting/reactivation. Their timing and relationship to the structural development of the wider Orcadian and IMFB are poorly understood.

In this study, new detailed field observations augmented with drone photography and creation of 3D digital outcrops, coupled with U-Pb geochronology of synfaulting calcite-mineralised veins, are used to constrain the absolute timing of fault populations and decipher the kinematic history of the basin opening. In addition, these findings help to better identify deformation structures associated with earlier basin forming events.

This holistic approach allows up to six deformation events to be identified regionally: Devonian rifting associated with the older Orcadian Basin; Variscan inversion; Permian thermal subsidence with some evidence of minor fracturing; Late Jurassic – Early Cretaceous rifting; possible Late Cretaceous rifting; and Cenozoic reactivation and local inversion. We were also able to isolate characteristic structures, fault kinematics, fault rock development and associated mineralisation types related to many of these events.

5.1 Introduction

The IMFB is a superimposed sedimentary basin that has experienced a complex structural history with many deformation episodes of regional or local extent. Strictly, the IMFB rift is thought to have formed during the Late Jurassic-Early Cretaceous as the western arm of the intra-continental North Sea trilete rift system (Fig. 5.1; e.g. Andrews et al. 1990; Tamas et al. 2022b). However, the basin is superimposed on post-orogenic Devonian-Carboniferous sedimentary rocks related to the Orcadian Basin and a Permian to possibly mid-Jurassic basin widely characterised by thermal subsidence (Andrews et al. 1990; Underhill 1991a; Thomson and Underhill 1993; see also Tamas et al. 2022a and b and references therein for further details). Also, post-rift, the basin experienced subsequent regional tilting, uplift and fault reactivation episodes during Cenozoic (e.g. Underhill 1991a; Thomson and Underhill 1993; Le Breton et al. 2013).

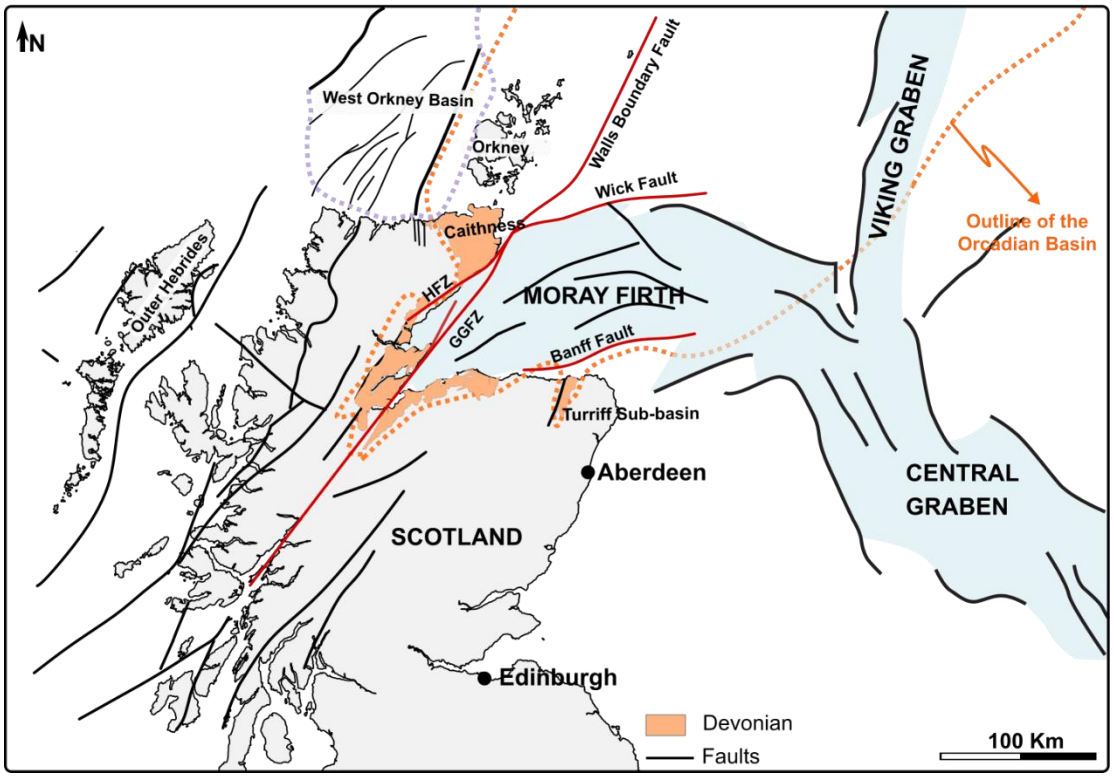

Fig. 5. 1: Generalised tectonic map of Scotland and the northern North Sea region showing the main Mesozoic rift systems (adapted after Goldsmith et al. 2003). The faults mentioned in the text are shown in red. GGFZ, Great Glen Fault Zone, HFZ, Helmsdale Fault Zone. Outline of the Orcadian Basin marked in dotted orange line (after Duncan and Buxton, 1995) and outline of the West Orkney Basin is marked in dotted purple line (after Bird et al. 2014).

The resulting multiple, superimposed structures can be challenging to separate and characterise. Offshore, the basin fills provide some constraints over the timing of events. However, observations are limited by the scale resolution of seismic reflection datasets and also by the fact that fault kinematics can be difficult to ascertain. Onshore, these aspects are well preserved, but limitations arise due to restricted exposure, complex kinematic histories and a lack of information concerning the absolute (as opposed to relative) timing of fault movements. In many cases, however, the deformation episodes may be associated with diagnostic syn-tectonic mineral fills (e.g. calcite, zeolite or base metal sulphides). Some of these can be dated using radiometric methods (e.g., U-Pb calcite, Re-Os sulphides) to constrain the absolute timing (e.g. see the approach used by Dichiarante et al. 2016; Roberts et al. 2020a; Tamas et al. 2022a).

This study focuses on the timing, nature, and regional significance of tectonic structures present in the onshore Devonian and Jurassic successions of the north-western IMFB and south-eastern Orcadian Basin. New detailed field observations coupled with U-Pb dating of syn-kinematic calcite mineralisation are used to document and characterise the timing and kinematic history of faulting and associated deformation. We also explore how these tectonic events in the IMFB may be correlated with those seen in northern Caithness and with offshore structures to the southeast and those seen onshore along the southern coast of the basin.

These findings reveal hitherto unrecognised constraints for the timing and kinematic history of faulting and fault reactivation, providing a potential new structural template for interpretation of the subsurface basin architecture in the offshore IMFB. These findings have important potential applications in other superimposed rift basin settings worldwide and also in areas of regionally contemporaneous onshore-offshore basin development.

5.2 Geological Overview

The study area lies along the north coast of IMFB (Figs 5.2a, b). Thick deposits of Devonian sedimentary rocks belonging to the underlying Orcadian basin are well exposed here as well as in the northern part of Caithness, unconformably overlying Moine and Lewisian metamorphic rocks and Silurian-Devonian plutons such as the Helmsdale granite (Fig. 5.2b). Limited Triassic

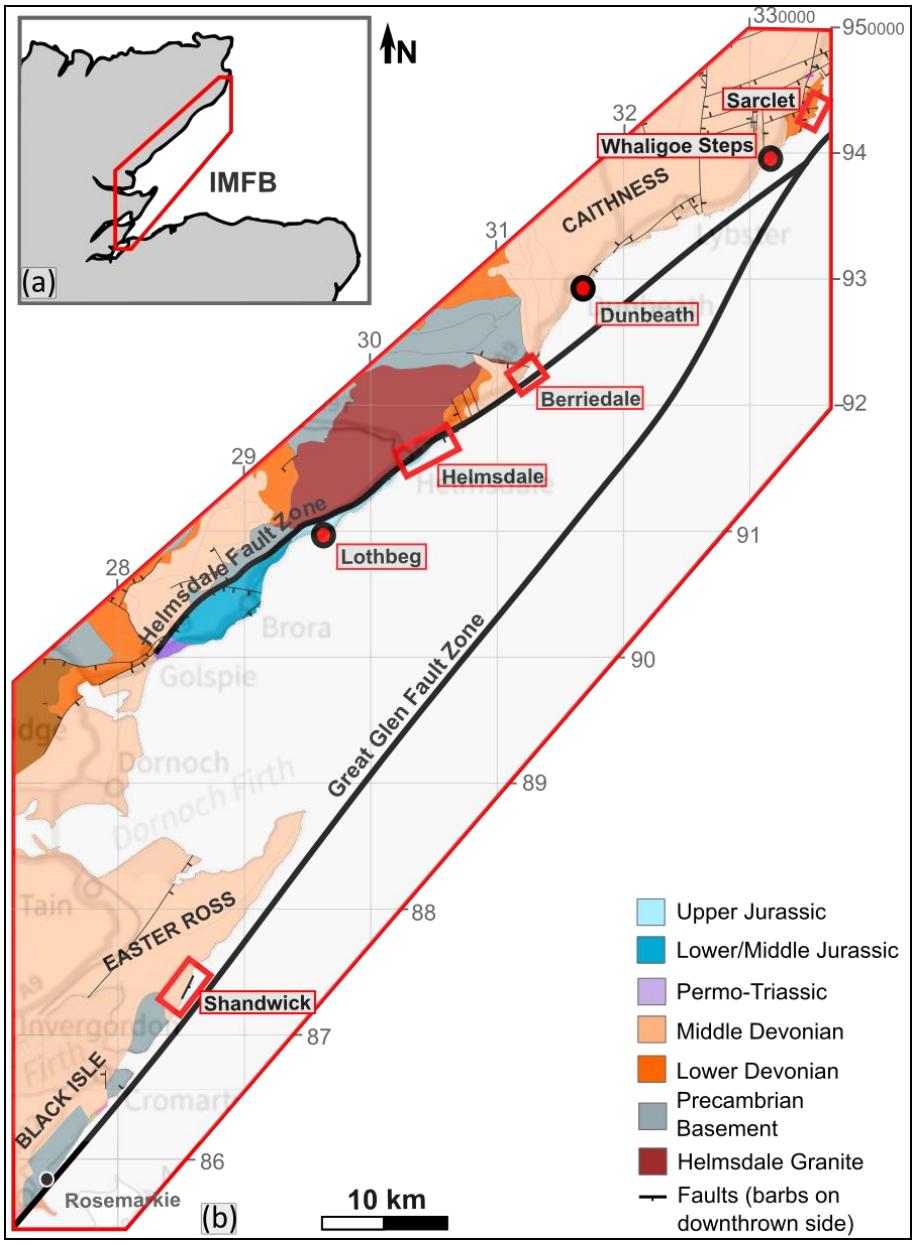

Fig. 5. 2: (a) Outline of the IMFB with red polygon showing the location of the study area. (b) Simplified regional geological map of the north-western coast of the IMFB showing the main onshore stratigraphy and fault systems (modified after Guariguata-Rojas and Underhill 2017 and British Geological Survey (BGS), UK. Using: EDINA Geology DigimapService, <http://edina.ac.uk/digimap. IMFB - Inner Moray Firth Basin. Red boxes and dots show the localities described in this chapter.

to Upper Jurassic rocks are exposed in the hangingwall of the Helmsdale fault and locally at Shandwick (Fig. 5.2b).

This margin is strongly controlled by the Helmsdale and Great Glen faults (Fig. 5.2b), which together with the Banff Fault and Wick Fault are the main bounding structures of the IMFB (Fig. 5.1). For more details about the general IMFB setting and stratigraphy, please see section 1.3.1.

5.2.1 Stratigraphic framework

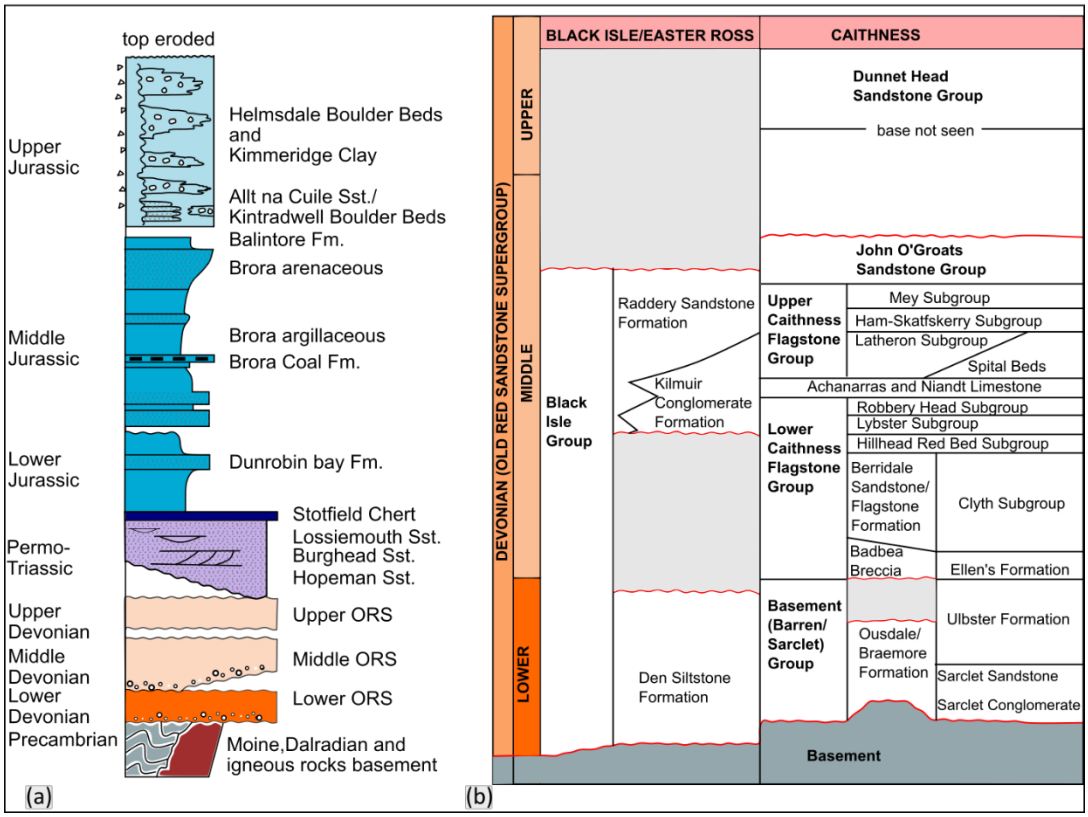

Fig. 5. 3: (a) Summary of onshore stratigraphy (modified after Trewin and Hurst 2009). Not to scale, with relative thicknesses shown in a notional fashion. ORS - Old Red Sandstone. (b) Simplified stratigraphy and correlation chart of the Lower to Upper Devonian from Caithness to Black Isle (compiled after Johnstone and Mykura 1989; Fletcher et al. 1996; Trewin and Thirlwall 2002).

The stratigraphy of the exposed rocks forming the north-western margin of the IMFB is predominantly Middle Devonian with minor Lower Devonian deposits of the Orcadian Basin, unconformably overlying Moine and Lewisian metamorphic basement and Helmsdale granite. Limited Permo-Triassic to

Upper Jurassic strata crop out in the hangingwall of the Helmsdale Fault and to the southwest at Shandwick (Fig. 5.3a).

In the Black Isle and Easter Ross areas, the Lower to Middle Devonian Old Red Sandstone (ORS) forms part of one large group – the Black Isle Group - while in Caithness it is divided into four main groups, namely the Basement (Barren/Sarclet), Lower Caithness Flagstone, Upper Caithness Flagstone and John O'Groats groups (Fig. 5.3b; e.g. Donovan et al. 1974; Johnstone and Mykura 1989 and Fletcher at al. 1996).

The Black Isle Group is about 4800 m thick and comprises Lower Devonian basal conglomerates and breccias with green and grey shales, calcareous and bituminous beds, laminated siltstones, and sandstones (Den Siltstone Formation). These have been interpreted as fluvial units, marginal sediments of a playa lake and lacustrine deposits (e.g. Fletcher et al. 1996). This succession is unconformably overlain by middle Devonian thick conglomerates and sandstones - part of alluvial fan deposits (Kilmuir Conglomerate Formation) – and a thick sandstone succession with thin lenses of conglomerate and mudstones of the Raddery Sandstone Formation (Fletcher et al. 1996).

In Caithness, the Lower Devonian belongs to the Basement (Barren/Sarclet) Group (Fig. 5.3b). The succession comprises predominantly fluvial conglomerates, which contain rounded clasts of granite, schist, and gneiss (Sarclet Conglomerate Formation), overlain by thick medium-grained red/brown sandstones (Sarclet Sandstone Formation). The Sarclet formations are overlain by a rhythmic lacustrine sequence of green mudstones, marly siltstones with some interbedded fluvial red sandstones. These represent the

main basin depocenter succession and form the Ulbster Formation (Donovan et al. 1974; BGS 1985; Trewin and Thirlwall 2002). The Sarclet and Ulbster formations are thought to be laterally equivalent to the Ousdale/Braemore Formation (Fig. 5.3b). The Ousdale/Braemore Formation is mainly a conglomeratic unit which crops out immediately north and south of the Helmsdale granite and is thought to represent the deposits of at least a partially isolated sub-basin from the main Orcadian depocenter (Trewin and Thirlwall 2002).

The middle Devonian is generally dominated by flagstones (grey-green shales, fine-grained laminated sandstone, dark-grey organic-rich shales) deposited in a cyclic lacustrine environment within the Orcadian Lake (e.g. Donovan et al. 1974; Trewin and Thirlwall 2002). The Lower Caithness Flagstone and Upper Caithness Flagstone groups are separated by Achanarras and Niandt limestone beds with abundant fish fauna, forming a regional marker horizon. The overlying John O'Groats and Upper Devonian Dunnet Head groups are represented by fluviatile red/yellow cross-bedded sandstones interbedded with lacustrine mudstones with fish fauna and do not crop out in the study area.

The Triassic is poorly exposed at Golspie and comprises fluvial and aeolian yellow sandstones overlain by mudstones with calcretes and silcretes thought to be a lateral equivalent of the regionally developed Stotfield Chert (see Chapter 4 for more details; Trewin 2009).

Lower (Dunrobin Bay Formation) and middle to Upper Jurassic strata (Brora Coal, Brora Argillaceous, Brora Arenaceous and Balintore formations) are generally represented by alluvial conglomerates, fluvial sandstones and

shales, deltaic sandstones and coal beds with lagoonal units and shallow marine incursions (e.g. Linsley et al. 1980; Trewin 2009; Hurst 2009).

The Upper Jurassic strata (Kintradwell Boulder Beds, Allt na Cuille Sandstone, Kimmeridge Clay, Helmsdale Boulder Beds) follow and are represented by marine shales, sandstones, and localised active fault-related debris flow breccias (e.g. Trewin 2009; Hurst 2009).

5.2.2 Previously recognised structural framework

Devonian-age faults and fracture systems, usually sinistral strike-slip to dip-slip NW-SE- to NNE-SSW-trending faults, are thought to have formed during the regional opening of the Orcadian Basin. They have been recognised both in the outcrops of northern Caithness (e.g. Wilson et al. 2010; Dichiarante et al. 2016, 2021 – their Group 1 structures) and on the southern coastal region of the IMFB, in the Turriff Sub-basin (see Chapter 3). In north Caithness, these structures are locally overprinted by later N-S trending folds and thrusts of (possible) Late Carboniferous-Permian age (Group 2 structures) and NE-SW trending Permo-Triassic dextral transtensional faults (Group 3 structures) related to the formation of the West Orkney Basin (Fig 1) further to the north (Dichiarante et al. 2016, 2021). Local reactivation of earlier formed structures is localised in effect, but is regionally widespread in Caithness.

The Permo-Triassic history of the IMFB is thought by most authors to be characterised by thermal subsidence and passive infill of the pre-existing topography, although Permo-Triassic rifting occurred in the other arms of the North Sea trilete rift (see Chapter 4 and references therein). The Late Jurassic – Early Jurassic rifting, which led to the opening of the IMFB, is widely characterised by the development of km-long, predominantly NE-SW-trending

growth faults. In the Turriff Sub-basin, the Devonian N-S to NNE-SSW trends are locally dextrally reactivated during Lower Cretaceous rifting (see Chapter 3; Tamas et al. 2022a).

Late Cretaceous- to Cenozoic-age regional uplift and faulting in the IMFB are thought to have led to widespread but localised fault reactivation, including dextral reactivation of the Great Glen and sinistral reactivation of the Helmsdale faults (e.g. Underhill 1991a; Thomson and Underhill 1993; Le Breton et al. 2013). While the timing of this reactivation is traditionally viewed as Cenozoic, this is commonly just assumed based on indirect evidence and correlation with regional events (e.g. Le Breton et al. 2013).

It is important to note that the post-Devonian faulting histories on either side of the Helmsdale fault appear to differ significantly, suggesting that the fault acts as a regional boundary restricting the effects of Mesozoic faulting to the IMFB (Dichiarante et al. 2016).

5.2.2.1 *The Helmsdale Fault (HF)*

The HF forms the north-western margin of the IMFB and consists of a c. 100 km long NE-SW-striking fault segment (Figs 5.1 and 5.2b; e.g. BGS 1998) steeply dipping to the SE. The fault trends onshore for about half of its length. An almost continuous succession of Triassic to Upper Jurassic rocks are exposed onshore in its hangingwall downfaulted to southeast against basement rocks of the Helmsdale Granite and overlying Devonian successions to the northwest (Fig. 5.2b; e.g. BGS 1998; Trewin 2009). Previous studies suggest that the HF formed initially as a dip-slip normal fault structure during the Late Jurassic - Early Cretaceous basin opening (e.g. Underhill 1991a; Thomson and Underhill 1993). Thickening towards the fault

is observed offshore in multiple seismic profiles and wells, revealing the syn-kinematic nature of Upper Jurassic - Lower Cretaceous strata (e.g. Underhill 1991a). The Upper Jurassic syn-rift succession is well exposed onshore, especially at Helmsdale (Fig. 5.2b). It consists of deep marine deposits, including the debris flow breccias known as the 'Boulder Beds', widely considered syn-tectonic fault scarp breccias formed in response to the movement along the HF (e.g. Bailey and Weir 1932; Pickering 1984; Macdonald 1985; Underhill 1994; Hudson and Trewin 2002; Fraser et al. 2003; McArthur et al. 2013).

The Upper Jurassic sequence outcropping in the hangingwall of the HF is modified by a series of open NW-SE-trending folds of about 500 m wavelength, consistent with sinistral shear along the HF (MacDonald 1985; Thomson 1993; Thomson and Underhill 1993; Thomson and Hillis 1995). This deformation is considered by most authors to be related to a later sinistral reactivation during the Cenozoic, when the basin was also tilted and uplifted (Thomson 1993; Thomson and Underhill 1993; Hillis et al. 1994; Le Breton et al. 2013). Calcite veins have been described from the Jurassic rocks in the hangingwall of the HF, trending sub-parallel with the main fault trace (e.g. MacDonald 1985; MacDonald and Trewin 2009). These veins are generally considered to have formed after the sediments in the hangingwall of HF were fully lithified (e.g. MacDonald and Trewin 2009) and also to be later and unrelated to the folds (MacDonald 1985). Le Breton et al. (2013) view their formation as being Cenozoic.

5.2.2.1 *The Great Glen Fault (GGF)*

The GGF is an inherited basement structure active at least since the Late Silurian (e.g. Holgate 1969; Stewart et al. 1999, 2000). During the opening of the Orcadian basin, the fault had an initial left-lateral movement (e.g. Dewey and Strachan 2003; Mendum 2010), whilst in the Late Carboniferous – Early Permian, the fault is thought to have been reactivated dextrally (Coward et al. 1989; Seranne 1992; Watts et al. 2007; Wilson et al. 2010; Dichiarante et al. 2020).

In the IMFB, the GGF consists of a series of prominent sub-vertical NNE-SSW striking segments which form the southwestern margin of the IMFB in the Black Isle and Easter Ross. It then continues north-eastwards into the basin, intersecting the HF and ultimately linking to the Walls Boundary Fault in Shetland (Flinn 1961; Appleby 1961; Fig. 5.1).

The GGF was initially considered the primary controlling structure during the Mesozoic opening of the IMFB (e.g. McQuillin et al. 1982; Roberts et al. 1990). Such models typically assumed an oblique-slip opening of the basin due to dextral movements along this fault. The transtensional models and the role of the GGF during basin opening were challenged based on findings in a series of later studies (e.g. Underhill 1991a; Thomson and Underhill 1993; Underhill and Brodie 1993). Largely based on detailed interpretation of seismic profiles, Underhill (1991a) proposed that the basin opened mainly during the Late Jurassic under an orthogonal extensional regime. The main displacements are interpreted to lie along the HF, as the synkinematic sequence thickens without change across the GGF and towards the HF. This indicates that the GGF was inactive during the Late Jurassic -

Early Cretaceous. Subsequent studies (e.g. Thomson and Underhill 1993; Underhill and Brodie 1993; Davies et al. 2001) demonstrated that the fault which shows evidence for strike-slip related deformation patterns (e.g. flower-structures, folds) on the offshore seismic reflection profiles, clearly offsets post-rift reflectors. Hence, the dextral reactivation of the GGF is now widely regarded as being Cenozoic (Underhill 1991a; Thomson and Underhill 1993; Underhill and Brodie 1993; Davies et al. 2001).

A splay of the GGF (GGFS) is exposed onshore at Easter Ross and Black Isle coast (Fig. 5.2b), juxtaposing Jurassic strata to the east against Devonian and Precambrian metamorphic basement rocks to the west (e.g. BGS 1973; Underhill and Brodie 1993; Jonk et al. 2003; Le Breton et al. 2013). Minor folds and faults in the Jurassic strata here are considered to be Cenozoic and related to right-lateral slip along the Great Glen Fault (e.g. Underhill and Brodie 1993; Le Breton et al. 2013). It is generally believed that the GGF reactivated right-laterally in a time interval from the Late Eocene to Late Oligocene, c. 37–26 Ma (Le Breton et al. 2013).

5.3 Methods

Structural fieldwork and sampling were carried out in seven key exposures located along the north-western coast of IMFB, from Sarclet in Caithness to Shandwick in Easter Ross (Fig. 5.2b). In-situ detailed field observations and measurements of bedding, faults, fractures, folds, fault rocks and associated mineralisation were recorded. Structural data processing and visualisation were carried out using Stereonet 10 (Allmendinger et al. 2012; Cardozo and Allmendinger 2013). The measurements were graphically

represented using both rose diagram plots of azimuth distributions (at 10° sector angles) and equal area stereonets, lower hemisphere projection using poles to planes where appropriate. Fault-slip slickenline data were collected in-situ from exposed fault surfaces in order to perform a *palaeostress inversion*. In this study, the fault data were analysed using the direct inversion method (INVD) of Angelier (1990) implemented using the SG2PS software (Sasvári and Baharev 2014). This method estimates the reduced stress tensor and the shear stress magnitudes from the fault-slip data (Angelier 1990).

UAV photography was collected using a DJI Mavic Air drone, which has a digital camera with a 12-megapixel image sensor. For the creation of the DOM, DEM (digital elevation models) and orthorectified models, we used Agisoft Metashape Professional™ (v.1.6.2). The structural data were extracted using VRGS™.

Calcite samples were collected for microstructural and geochronology studies. Polished thick sections were analysed using laser ablation–inductively coupled plasma–mass spectrometry (LA-ICP-MS) at the BGS Isotope Geosciences Laboratory (Nottingham, UK) and University of Hull, using standard methods for calcite U-Pb geochronology (Roberts and Walker 2016; Roberts et al. 2017; Tamas et al 2022a). From the samples selected, 15 thick sections were screened for U-Pb dating, of which 12 were successfully dated.

For a more detailed explanation of all analytical methods, please see Chapter 2.

5.4 Results

We focus here on seven locations at which representative sequences of events and a variety of brittle deformation styles have been encountered. The localities – Sarclet, Whaligoe Steps, Dunbeath, Berridale, Helmsdale, Lothbeg and Shandwick – all lie along the north-western coast of the IMFB (Fig. 5.2b). Large areas of Devonian rocks crop out here, together with more limited exposures of Jurassic strata (Fig. 5.2b).

5.4.1 Sarclet [Grid Reference: ND 35096 43332]

5.4.1.1 Onshore Fieldwork Observations

Sarclet locality is located in the cliffs ~500 m east of Sarclet village [ND 343 439] (Fig. 5.4a). The investigated exposure extends about 300 m north along the coast from the natural harbour known as the Haven until the cliffs at Muiri Geo (Fig. 5.4b). A large orthorectified model across the entire area was obtained from the UAV to enable data visualisation, interpretation, and display (Fig. 5.4b), especially as most of the cliffs are inaccessible due to height and the presence of deep sub-vertical gullies. The Lower Devonian Sarclet Sandstone Formation (Fig. 5.4a, BGS 1985) of the Sarclet Group (Fig. 5.3b) is well exposed here in high cliffs (of about 20-30 m height) and flat-lying rock platforms about 20-30 m wide (Fig. 5.4b). The succession conformably overlies the Sarclet Conglomerate Formation, which crops out further to the south of our area of interest (Fig. 5.4a). Sarclet Sandstone Formation comprises cm- to m-thick beds (of about 10 cm to 4 m) of red coloured, well cemented medium-grained sandstone showing parallel laminations and local

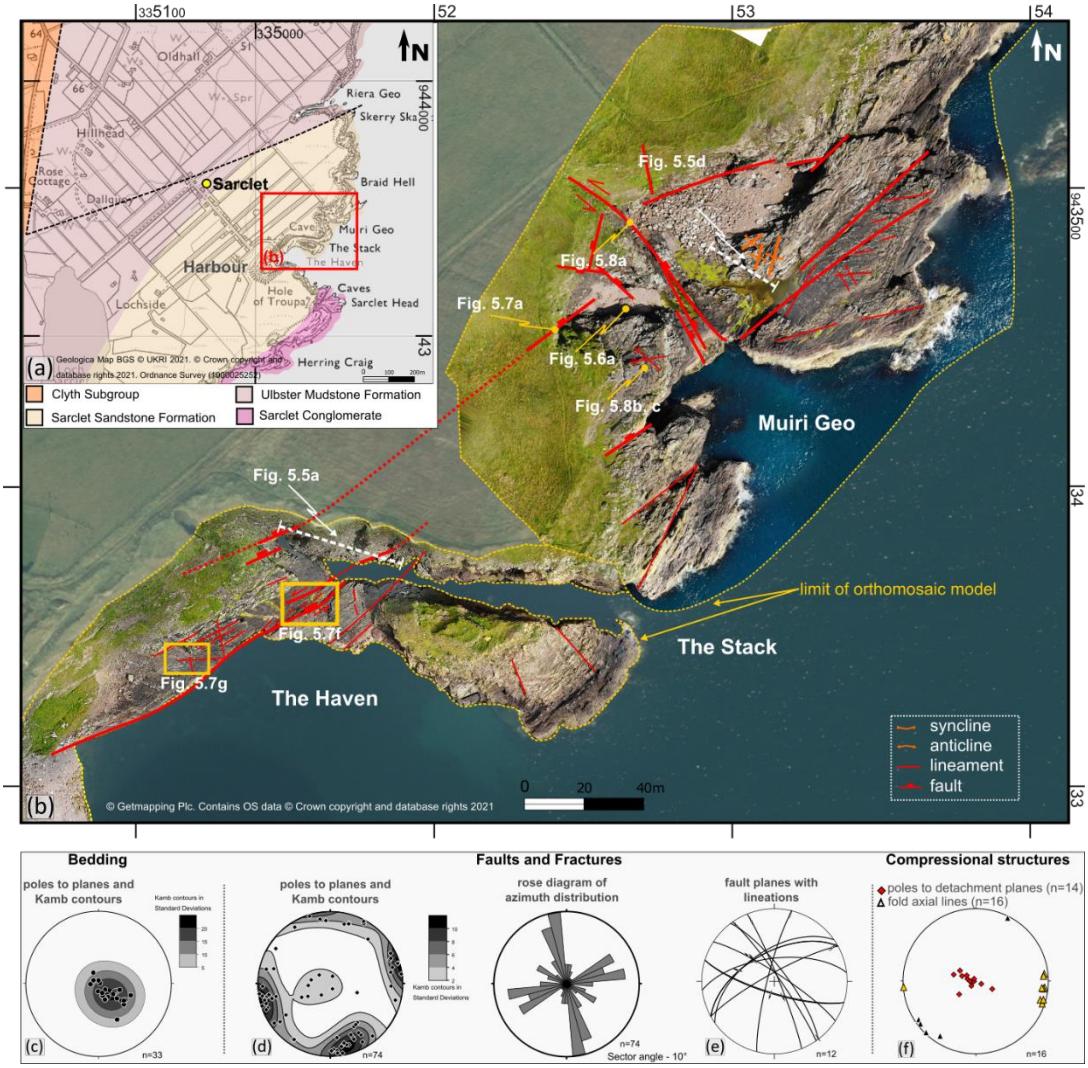

Fig. 5. 4: (a) Geological map of Sarclet area (using EdinaDigimap service and BGS 1985) showing the location of (b) – the studied exposure. (b) Orthomosaic model obtained from UAV (Unmanned Aerial Vehicle) photography overlapped on aerial map (using EdinaDigimap service © Getmapping Plc) showing the main structural trends. The locations of Figures 5.5a and d, 5.6a, 5.7a, f and g, and 5.8 are also shown. (c-f) Stereonets and rose plots of structural data collected in the field. Lower hemisphere, equal-area projections.

cross-bedding. Previous authors have interpreted these as braided river/meandering river deposits (Johnstone and Mykura 1989) with aeolian influences (Trewin 2009).

Overall, the beds are typically sub-horizontal to gently dipping (02° to 30°) predominantly to the NW (Fig. 5.4c). The stratigraphy is cross-cut by numerous, commonly closely spaced (decimetre to metre separation) shallowly-dipping to high angle faults, fractures/fracture corridors and veins of multiple orientations and kinematics (e.g. Fig. 5.4d and e). The dominant set trends broadly NNW-SSW (~20°scatter) dipping both E and W, a second set

trends NE-SW to E-W (~40° scatter) and a third (less well represented) is NW-SE trending (Fig. 5.4d). The fault planes typically have high dips (55 º to 89º), but less common, shallowly dipping (of about 3°- 36°) detachment faults and thrusts are also encountered locally, usually associated with folds (Fig. 5.4f). These shallow dipping (often bedding-parallel) compressional detachment planes are generally N-S- to NNE-SSW-trending and display top-to the WNW movements (Fig. 5.4f). These compressional structures are rarely accessible and are mostly seen high in the cliffs.

One good example can be observed in the high cliff face immediately north of the harbour (Fig. 5.5a and b), where approximately mid-section and to the east of the cliff, a large fold (of about 13 m amplitude) can be observed. The layers in the core of the fold (Fig. 5.5b) are truncated against a sub-horizontal detachment plane dipping 3º-5º to the E, subparallel to the underlying beds (Fig. 5.5b). The outer zone of the fold (Fig. 5.5b in green) extends to the west, where it forms small-scale west-verging imbricates (Fig. 5.5b). This structure formed most likely as part of a 'staircase' thrust system with a ramp-flat-ramp geometry (Fig. 5.5c). The large fold seen in Figure 5.5b most likely represents a fault-bend fold developed over the ramp, which cuts through the lower stratigraphy (Fig. 5.5c in grey). With further shortening, more thrusts appear to have developed in the upper stratigraphy forming the imbricate thrusts (Fig. 5.5c in green). The hanging wall of these imbricates are later truncated against a top-to-the E thrust which can represent a backthrust to the generally top-to-the W to WNW thrust system (Fig. 5.5c).

Top-to-the WNW thrust and folded structures of a smaller scale are also present at Muiri Geo (Fig. 5.5d). The syncline in the footwall is NE-SW

trending, while the hangingwall anticline and syncline are NNE-SSW-trending (Fig. 5.5b). Where accessible, these detachment planes are associated with fault breccia that shows no mineralisation (Fig. 5.5e).

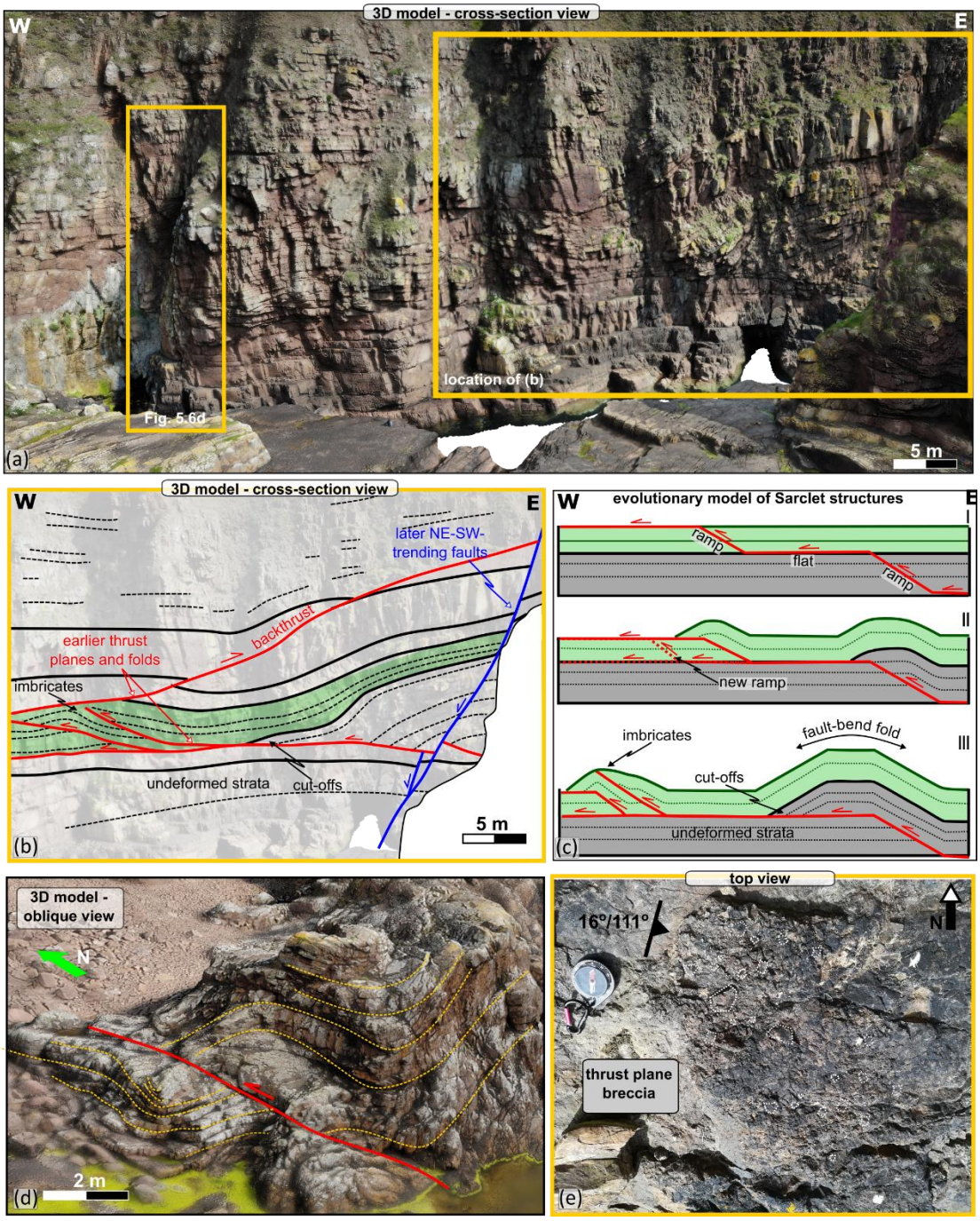

Fig. 5. 5: (a) 3D digital outcrop model of the cliff exposure at Sarclet Haven (see location on Fig. 5.4b) showing the folded and faulted Devonian strata. The location of (b) and Fig. 5.6d are indicated on the 3D outcrop. (b) Line drawing showing the interpreted early compressional structures offset by later NE-SW-trending faults. (c) Forward model explaining the possible evolution of the compressional structures. (d) 3D digital outcrop model of the compressional structures present at Muiri Geo (see location on Fig. 5.4b). (e) Field photograph showing the low-angle thrust plane associated with fault breccia.

Two different types of mineralised structures have been identified at Sarclet. In the field, the mineralisation reacted with hydrochloric acid, indicating that calcium carbonate (most likely calcite) was present, making it suitable for sampling and potentially dating. An earlier N-S-trending set of translucent/white calcite tensile veins (Fig. 5.6a-c) is developed, whilst later, pink-coloured zeolite (identified as zeolite later in thin sections; see below 5.4.1.2 section) and calcite mineralisation is associated with NE-SW- to E-W-trending fault planes and fractures (Fig. 5.6d and e).

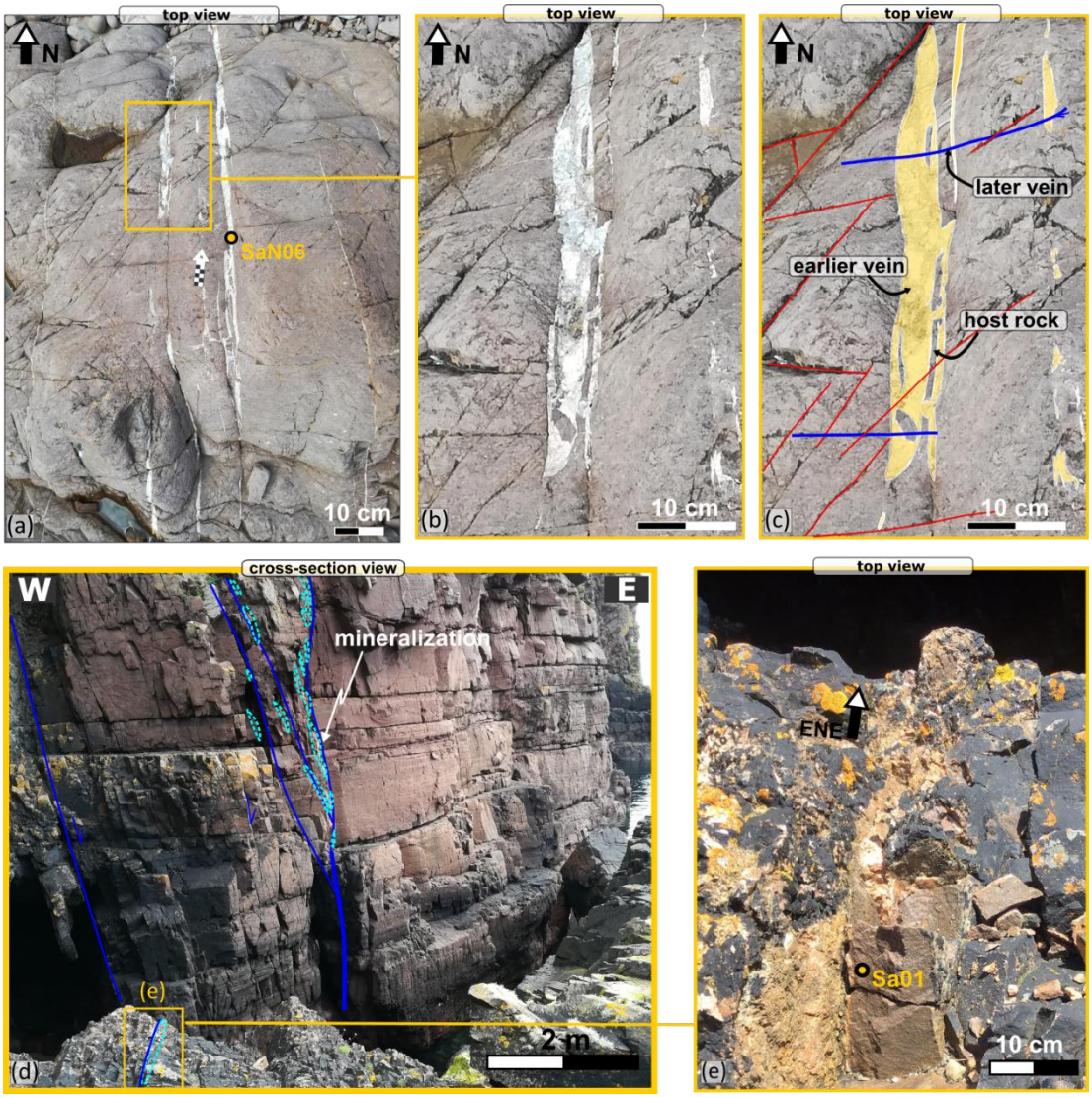

Fig. 5. 6: (a-b) Field photographs and (c) line drawing snowing the N-S-trending calcite mineralised veins with location of sample SaN06 indicated on (a). Note the N-S-trending vein is crosscut by a later ENE-WSW-trending vein. (d and e) Field photograph showing the later NE-SW-trending faults which are associated with pink-coloured zeolite-calcite-quartz mineralisation. Location of sample Sa01 is indicated on (e).

The N-S-trending veins, locally visible at Muiri Geo, are mm to c. 5 cm wide tensile veins containing jigsaw inclusions of Devonian host rock (Fig. 5.6a). One sample, SaN06, was selected from this type of vein for microstructure and geochronology study (Fig. 5.6a). These N-S-trending veins are cross-cut by E-W-trending zeolite and calcite veins and NE-SW-trending fractures (Fig. 5.6b and c). These zeolite and calcite mineralised faults are best observed in the cliffs at the Haven, where the mineralisation seems to fill tension gashes (Fig. 5.5d). Locally they are accessible in the flat platform, forming 1 to 7 cm wide ENE-WSW-trending tensile veins (Fig. 5.5e). One sample from such a mineralisation, Sa01, was selected for microscopy and geochronology (Fig.5.5e). These later NE-SW to E-W trending faults are usually the most prominent features in outcrops (Figs 5.6d and 5.7). In addition to zeolite and calcite mineralisation, they are usually associated with m-wide damage zones. These faults everywhere cross-cut the earlier low angle detachments and folds (Fig. 5.5a and b). The ENE-WSW-trending faults show a significant component of normal to sinistral oblique-slip movement based on offsets of bedding markers (e.g. Figs 5.5b and 5.6b) and kinematic indicators showing dip-slip (e.g. Fig.5.7b and c) to oblique-sinistral slip (62° to 84° pitch). The faults usually have a well-developed fault core of about 20 cm to 1 m thick (Fig. 5.7a and d) formed by a well- to poorly-cemented fault gouge and breccia (Fig. 5.7b and e). Some of these faults are also surrounded by an m-wide damage zone dominated by a network of closely spaced (cm to dm) fractures which decrease in density away from the fault core. This fracture system in the damage zone is best exposed at The Haven, around a generally ENE-WSW-trending fault (Fig. 5.7f and g). This major ENE-WSW-trending fault has a 6 to

10 m wide damage zone (Fig. 5.7f). The associated fracture populations here are dominantly trending NE-SW (Fig. 5.7f, g and i in blue) but, ENE-WSW- (Fig. 5.7f, g and i, in red) N-S to NNW–SSE- (Fig. 5.6f, g and i in yellow), E-W- (Fig. 5.7f, g and i, in green) and NW-SE- (Fig. 5.7f, g and I, in dotted green) trends are also distinguishable.

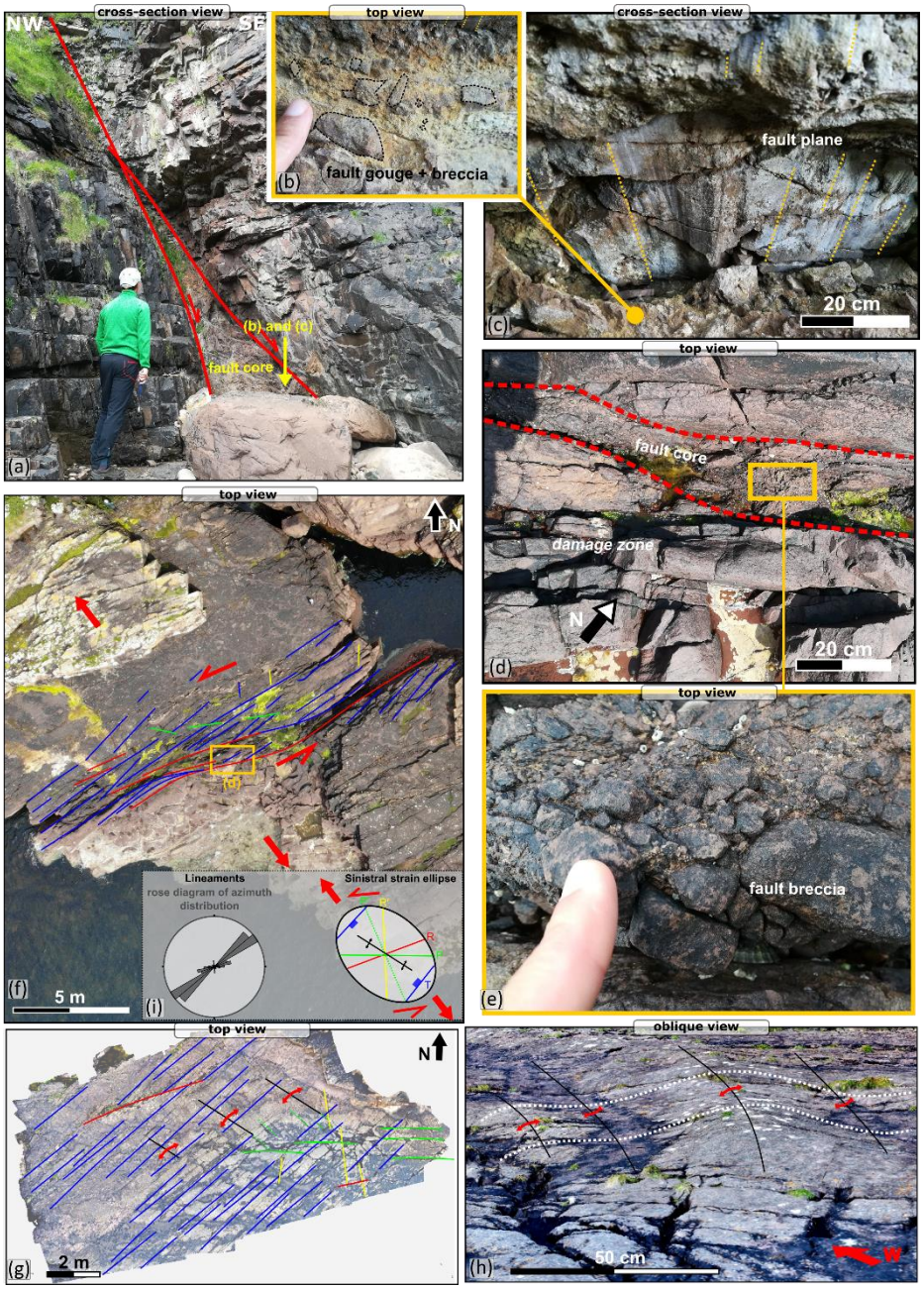

Fig. 5. 7: Field photographs of a (a) major NE-SW-trending fault present in the cliffs at Muiri Geo (see location on Fig. 5.4b), (b) detail view of the associated fault rock and (c) dip-slip lineations and grooves on the NE-SW-trending fault. (d) fault core and (e) detail of fault breccia associated with (f) a major NE-SW-trending fault, note the wide highly damage zone with en-echelon fractures array showing sinistral shear. (g) Orthomosaic model along strike of (f; see location on Fig. 5.4b) showing en-echelon fractures array and small-scale folds also shown in oblique view in (h). (i) Rose diagram of azimuth distributions and strain ellipse showing fault array geometry suggesting a component of sinistral shear movement. Colours match the colours in (f) and (g).

In addition, small-scale shallow plunging NW-SE-trending folds (Fig. 5.4f, fold axis in yellow) of about 20-30 cm amplitude also develop in the damage zone, about 9 m away from the fault trace (Fig. 5.6h). These fault and fold populations are consistent with a sinistral strike-slip Riedel system developed during NW-SE extension (Fig. 5.7i). We suggest that the NE–SW-trending faults correspond to tensile fractures/normal faults (Fig. 5.7i T, in blue), ENE-WSW -trending to synthetic Riedel structures (Fig. 5.7i R, in red), N-S to NNW–SSE-trending to antithetic Riedel structures (Fig. 5.7i R', in yellow), and E-W- and NW-ES-trending to P shear and antithetic P shear structures, respectively (Fig. 5.7i P and P', in green). The NW-SE-trending folds (Fig. 5.7h) also fit relative to the proposed sinistral strain ellipse model (Fig. 5.7i).

A different and possibly the earliest (see section 5.4.1.4 below) set of strike-slip faults and en-echelon fracture systems resembling Riedel shear structures are also present at Muiri Geo locality (Fig. 5.8). Here, steeply dipping (80º to 90º) NW-SE-trending fault planes show strike-slip kinematics (e.g. Fig. 5.8a). Where exposed on bedding planes, NW-SE-trending faults are associated with small scale (cm to dm) en-echelon fracture systems resembling Riedel shear structures showing sinistral slip (Fig. 5.8c). Likewise, ENE-WSW-trending faults are associated with en-echelon fracture systems resembling Riedel shear structures showing dextral slip (Fig. 5.8b). Those two sets, dextral and sinistral, developed at about 60º to each other (Fig. 5.8d). They can represent the first order Riedel shear structures developing simultaneously, as part of the same strike-slip system, during NNE-SSW extension and WNW-ESE compression, while the smaller scale Riedel shear

fractures associated with their movement are most likely second order Riedel shear fractures (Fig. 5.8d).

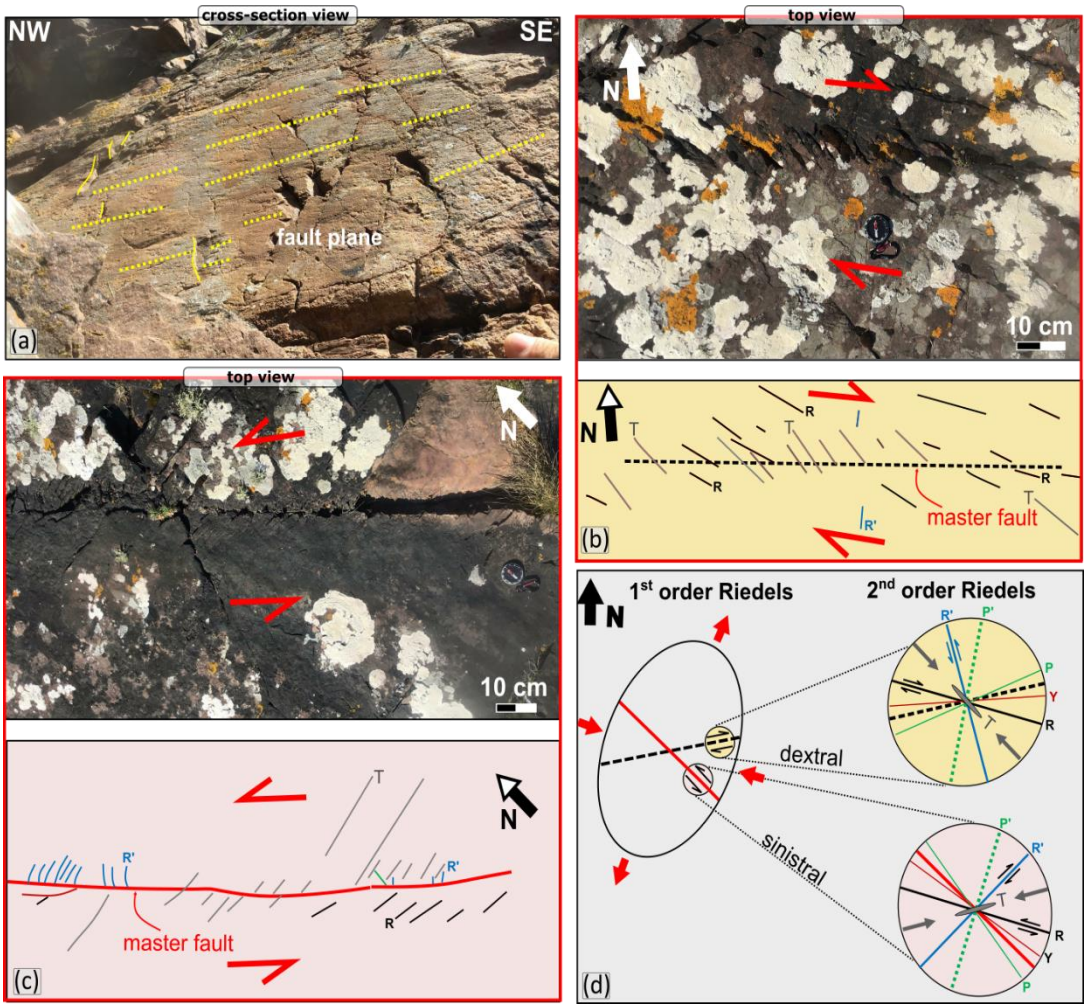

Fig. 5. 8: (a) Field photographs of a NW-SE-trending fault plane showing sub-horizontal slickenline lineations (pitch 10°NW) suggesting strike-slip kinematics. (b) Field photograph and interpreted fracture network of a small-scale dextral fault. (c) Field photograph and interpreted fracture network of a small-scale sinistral fault. (d) strain ellipse showing the predicted fault orientation and associated second-order structures matching the two Riedel shear sets in (b) and (c).

5.4.1.2 Microscopy

Two different vein samples from Sarclet locality have been investigated for microstructural characteristics and dating: Sa01 and SaN06 (Fig. 5.9).

The SaN06 sample (Fig. 5.9a) was taken from a N-S-trending white calcite vein (Fig. 5.6a), which on the basis of observed cross-cutting relationships, appears to be the earliest vein set seen in the outcrops. In thin section, the veins are curviplanar and have local mesh-like offshoots (Fig.

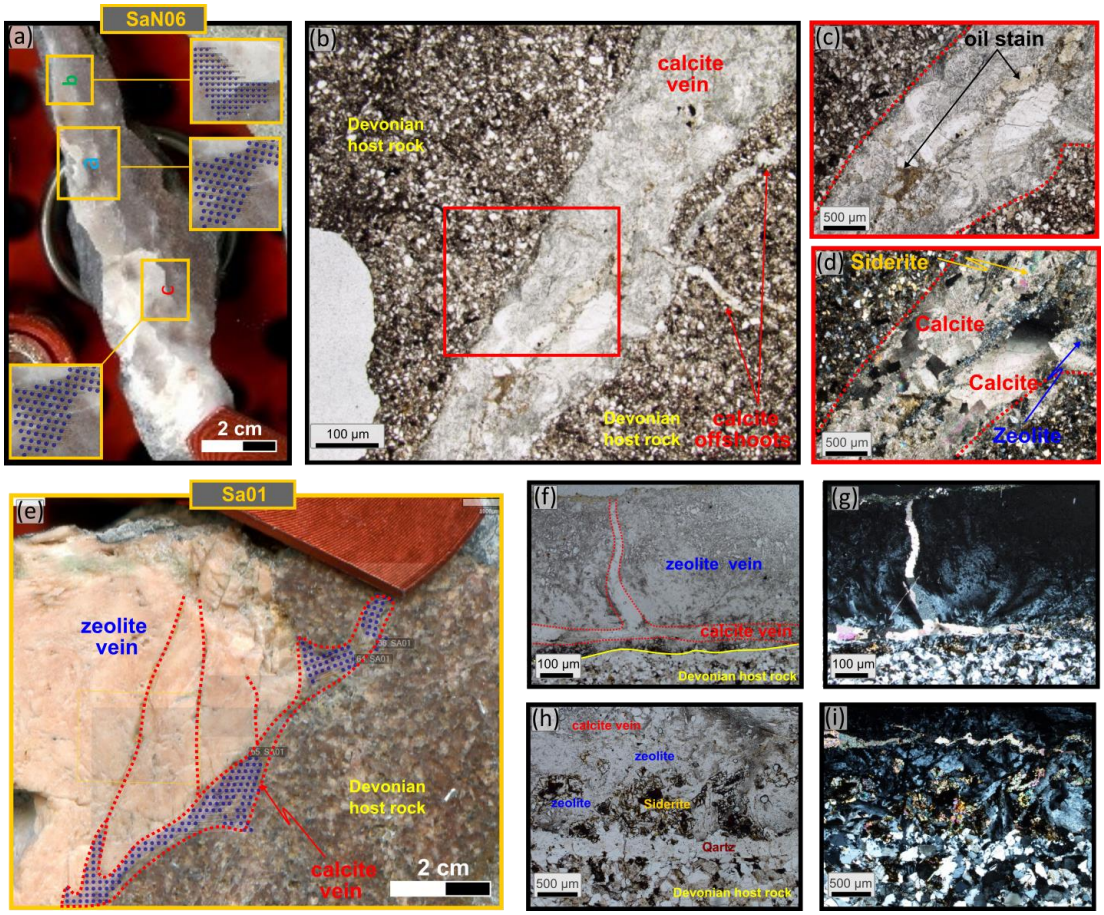

Fig. 5.9: (a) Polished thick section of SaN06 sample showing the laser ablation spots (blue dots). (b) microphotograph and detail of the calcite vein showing (c) oil stains and (d) occurrence of associated intergrown siderite and zeolite. (e) Polished thick section of mainly zeolite (pink) and calcite (grey) Sa01 sample also showing the laser ablation spots (blue dots). (f-i) representative thin section microphotographs of Sa01 sample showing (f)- in plane polarised light and (g)- crossed polarised light the vein formed almost entirely of zeolite with thin calcite vein present at the boundary with Devonian host rock and as offshoots in the main zeolite vein. (h)-in plane polarised light and (i)- crossed polarised light, rare occurrence of early formed siderite and quartz along vein margins.

5.9b). Larger veins are composite and likely syntaxial with finer calcite outer zone, coarser sparry calcite inner zone and fine central mixture of calcite, zeolite and local siderite (Fig. 5.9c and d, only seen locally). Most offshoots are the sparry variety of calcite (Fig. 5.9b). The youngest fills - including zeolite and siderite in places - are lightly oil-stained, notably in the region adjacent to the contact region of the zeolite-bearing fill (Fig. 5.9c). This is possibly a sign of local brittle deformation and dilatancy during final vein opening.

The Sa01 sample (Fig. 5.9e) was collected from an ENE-WSW-trending tension gash (Fig. 5.6e) associated with an ENE-WSW-trending fault

which is best observed in the cliffs (Fig. 5.6b). The vein is characterised by dominantly pink-coloured zeolite and calcite mineralisation (Fig. 5.9e). These pink veins, mm to cm thick, cross-cut older white calcite vein sets in outcrops of Lower Devonian sandstone/siltstone (Fig. 5.6d).

Thin sections of this vein show that the mineral fill is composite, predominantly zeolite (Fig. 5.9e-g), with marginal quartz (only preserved on one vein margin, Fig. 5.9h and i). This zone is followed by a mixture of zeolite and siderite (seen on both sides of the vein), followed by a central domain of pure zeolite which forms about 80% of total vein mineralisation (Fig. 5.9h and 1). This appears to be the relative age sequence (oldest to youngest), e.g. syntaxial growth. All are then cross-cut by a mesh of later thin white calcite veins (Fig. 5.9e-i), some of which are parallel to earlier vein contacts (Fig. 5.9h and i), with high angle offshoots locally intruding into the central part of the zeolite vein (Fig. 5.9e-g).

5.4.1.3 Geochronology

The ^{238}U and ^{206}Pb concentrations were analysed in the Sa01 and SaN06 calcite-bearing samples collected in the field. From the Sa01 sample, the later calcite veins that cross-cut the zeolite fills have been targeted for dating (Fig. 5.9a see locations of ablation sites on the thick section), while from SaN06, three dated sites have been chosen (SaN06a, SaN06b and SaN06c, see ablation sites in Fig. 5.9f). Both samples analysed contained sufficient amounts of ^{238}U (and low enough concentrations of common Pb) to yield an accurate and precise dates.

For SaN06a (Fig. 5.9a), 84 spots were ablated and plotted on a Tera Wasserberg U-Pb plot which yielded a $^{238}U/^{206}Pb$ age of 255.20±2.46

(2σ, $Pb_{initial}$ = 0.3086±0.0029, MSWD = 4.5; Fig. 5.10a).

For SaN06b (Fig. 5.9a), 62 spots were ablated and plotted on a Tera-Wasserberg U-Pb plot which yielded a $^{238}U/^{206}Pb$ age of 258.89±6.06 (2σ, $Pb_{initial}$ = 0.3455±0.0034, MSWD = 5.1; Fig. 5.10b).

For SaN06c (Fig. 5.9a), 40 spots were ablated and plotted on a Tera-Wasserberg U-Pb plot which yielded a $^{238}U/^{206}Pb$ age of 257.51±5.21 (2σ, $Pb_{initial}$ = 0.3546±0.0044, MSWD = 4.8; Fig. 5.10c).

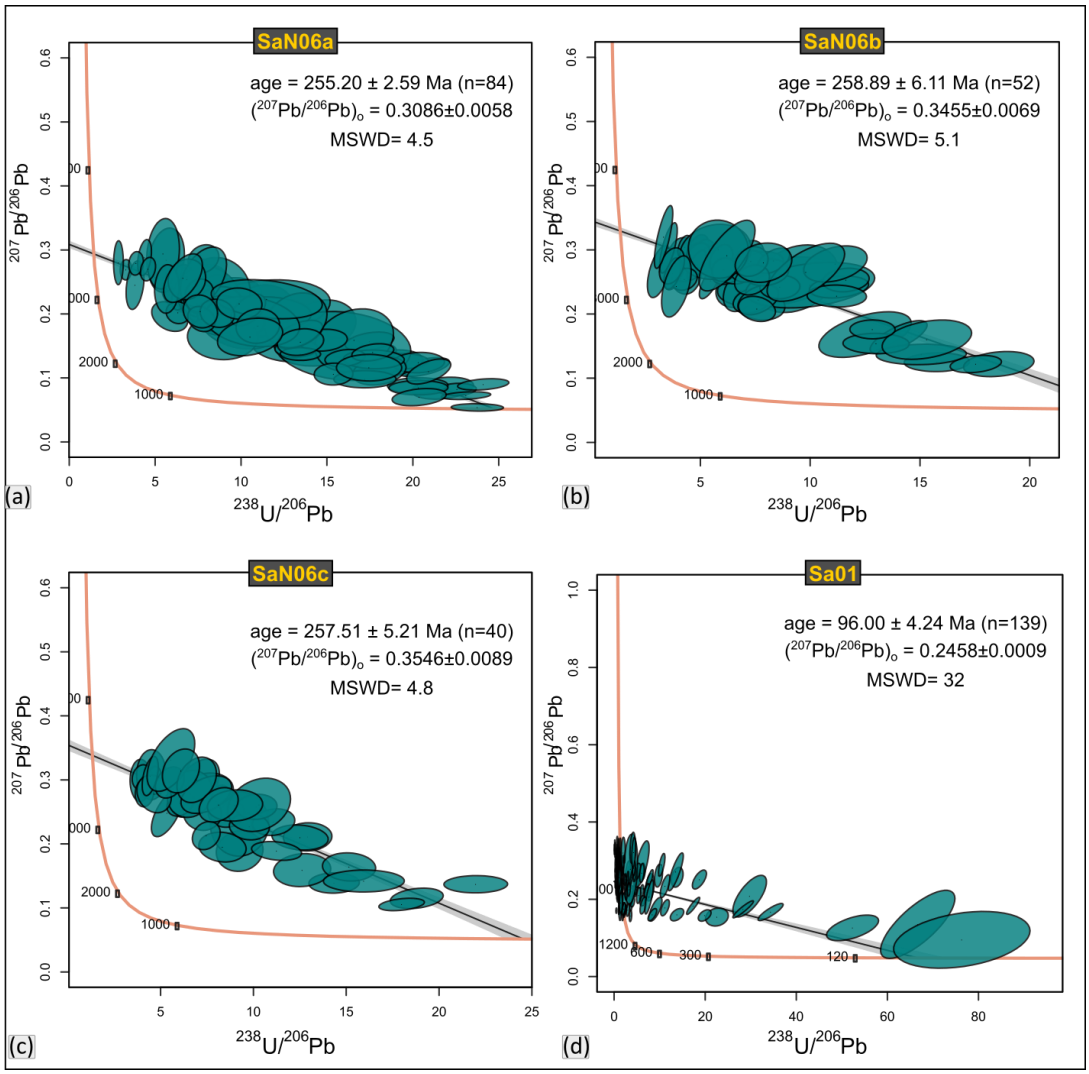

Fig. 5. 10: Tera–Wasserburg diagram of measured in-situ calcite 207Pb/206Pb and 238U/206Pb ratios (no common lead correction) from (a) sample SaN06a yielding a Model I discordia age of 255.20 ± 2.59 Ma (2σ, MSWD = 4.5) (b) sample SaN06b yielding a Model I discordia age of 258.89 ± 6.11 Ma (2σ, MSWD = 5.1) (c) sample SaN06c yielding a Model I discordia age of 257.51 ± 5.21 Ma (2σ, MSWD = 4.8) (d) sample Sa01 yielding a Model I discordia age of 96 ± 4.24 Ma (2σ, MSWD = 32). Error ellipsoids of spot analysis are plotted in green and represent 2σ uncertainties. MSWS = mean standard weighted deviation.

For sample Sa01 (Fig. 5.9e), 139 spots were ablated, with 87 spots omitted due to excess common Pb or poor ablation. The remaining spot data (n=52) were plotted on a Tera-Wasserberg U-Pb plot using IsoplotR (Vermeesch 2018), which yielded a $^{238}U/^{206}Pb$ age of 96.00 ± 4.24 Ma (2σ, $Pb_{initial}$ = 0.2885 ± 0.0015, MSWD = 4.8; Fig. 5.10d).

5.4.1.4 Interpretation of structural history

The deformation at Sarclet is complex and characterised by multiple episodes of faulting of different orientations and kinematics. The highly deformed nature of the rocks at this exposure was attributed tentatively by some authors (e.g. Trewin 2009) to its proximity with the converging HF, GGF and Wick Fault immediately offshore (c. 1 km). The combined outcrop observations of structural features, microstructures and geochronology, integrated with pre-existing studies across the Orcadian and IMFB, aid in establishing the possible geological relationships between the structures seen at Sarclet and link them to the wider regional events.

First, the calcite dating revealed two dated episodes of calcite mineralisation (c. 258 and 82 Ma) respectively pre-dating and synchronous with a phase of zeolite (+/- siderite and minor hydrocarbon) mineralisation. Thus, the ages obtained are consistent with the observed cross-cutting and contact relationships in the field and thin section.

The N-S-trending veins (Fig. 5.6a) are the earliest mineralised structures seen in the outcrops and of Permian age (c. 258 Ma). This date is close to being within error of Re-Os pyrite age for veins in northern Caithness (c. 267 Ma; Dichiarante et al. 2016). Those veins in northern Caithness formed

as a result of Permian NW–SE extension related to the opening of the offshore West Orkney Basin (Group 3 structures of Dichiarante et al. 2021).

The NE-SW- to ENE-WSW-trending veins predominantly containing pink zeolite and lesser amounts of calcite are, at least in part, Cenomanian in age (c. 96 Ma). Those NE-SW- to ENE-WSW- trending faults have the same orientation as the offshore structures associated with the opening of the IMFB during the Late Jurassic - Early Cretaceous (e.g. Andrews et al. 1990; Underhill et al. 1991). It is likely that these onshore NE-SW- to ENE-WSW-trending faults correlate with the offshore faults and were potentially formed during an earlier Late Jurassic to Early Cretaceous episode. This episode possibly led to the formation of the fault core breccia and wide damage zone indicating oblique-sinistral slip and could have been associated with the zeolite/siderite mineralisation. Repetitive later motions during the Cenomanian may have led to fault reactivation associated with calcite mineralisation, but this episode is quite unclear.

Two sets of structures remain unresolved by absolute dating as they are not associated with mineralisation; the compressional structures associated with the detachments (Fig. 5.5) and the complex strike-slip Riedel shear system observed at the Muiri Geo locality (Fig. 5.8).

The folds and thrusts at Sarclet are possibly the earliest structures identified at Sarclet as they are cross-cut by later steeply-dipping ENE-WSW- to NE-SW-trending faults. Similar structures have been previously observed within the Orcadian Basin, including at Sarclet Haven (e.g. Einfield and Coward 1987; Trewin 2009; Utley 2020; Dichiarante et al. 2021), although not all the studies discuss their timing and nature. Enfield and Coward (1987)

suggest that contractional structures showing a transport direction dominantly to the WNW, observed in Orkneys and Caithness (including those at Sarclet Haven), formed sometime during Late Devonian – Late Permian as they pre-date a phase of Permian dyke intrusion. Similar N-S-trending compressional structures with movement towards west to west-northwest have been described by Parnell et al. (1998) in western Orkney. There, the compressional structures commonly reactivate earlier extensional structures (Devonian rift-related faults), particularly on low-angle decollement planes. Thus, listric normal faults become later low-angle thrust ramps, sometime during Permo-Carboniferous, process facilitated by the presence of hydrocarbons along slip planes (Parnell et al. 1998). Compressional structures characterised by m- to km-scale N-S-trending folds and thrusts, often are developed close to earlier Devonian syn-rift faults have been documented from the Scottish mainland to Shetland (e.g. Underhill and Brodie 1993; Armitage et al. 2020; Dichiarante et al. 2020, 2021). Overall, these structures are interpreted as the result of a Late Carboniferous–Early Permian east-west inversion possibly related to dextral strike-slip reactivation of the Great Glen Fault (e.g. Coward et al. 1989; Seranne 1992; Watts et al. 2007; Wilson et al. 2010; Dichiarante et al. 2020, 2021) due to the far-field effects of the Variscan orogenic event. These structures were named Group 2 by Dichiarante et al. (2021). It is very likely that the compressional structures observed at Sarclet are part of the same Group 2 structures of Dichiarante et al. (2021), formed in a similar manner as those described by Parnell et al. (1998) in west Orkney.

The timing of the strike-slip Riedel shear system observed at Muiri Geo locality (Fig. 5.8), which include NW-SE-trending sinistral and dextral ENE-

WSW-trending faults, is more difficult to constrain. If those structures formed simultaneously, as suggested, during NNE-SSW extension, then their timing could be Cenozoic. This is due to a good correlation of this stress regime with both local stress regime interpreted onshore and offshore along the Lossiemouth Fault and inferred as Cenozoic (see Chapter 4 for more details). Also, their proximity to the GGF would favour such an interpretation with dextral ENE-WSW-trending representing synthetic Riedel shear structures to the GGF and the NW-SE-trending sinistral, representing antithetic Riedel shear structures, formed during Cenozoic dextral reactivation on the GGF.

5.4.2 Whaligoe Steps [Grid Reference ND 32140 40249]

5.4.2.1 Onshore Fieldwork Observations

The Whaligoe Steps locality lies ~200 m south of Whaligoe village [ND 320 404] (Fig. 5.11a and b). The investigated exposure is formed almost entirely of steep cliffs (about 50-60 m high), the bottom of which can be accessed during low tide using the 'Whaligoe steps' (Fig. 5.11b). A large 3D model across the entire area was obtained using the UAV to enable data visualisation, interpretation, and display (Fig. 5.11c), especially as most of the cliffs are inaccessible on foot. The middle Devonian Whaligoe Formation of the Clyth Subgroup (Fig. 5.11a; BGS 1985) is well exposed in the high cliffs and very narrow, flat-lying rock platforms. The succession comprises predominantly mm- to cm-thick beds (of about 5 mm to 10 cm) of light to dark grey alternating fine sandstones, siltstones and mudstones. Symmetrical ripple marks (Fig. 5.11g) and subaerial desiccation cracks are widespread and are usually observed on exposed bedding planes. This succession has been interpreted as shallow lake mudflats with some stream/river influx deposits,

part of the larger Orcadian Lake (e.g. Donovan et al. 1974).

The bedding is mostly sub-horizontal to shallowly dipping to the SW (average

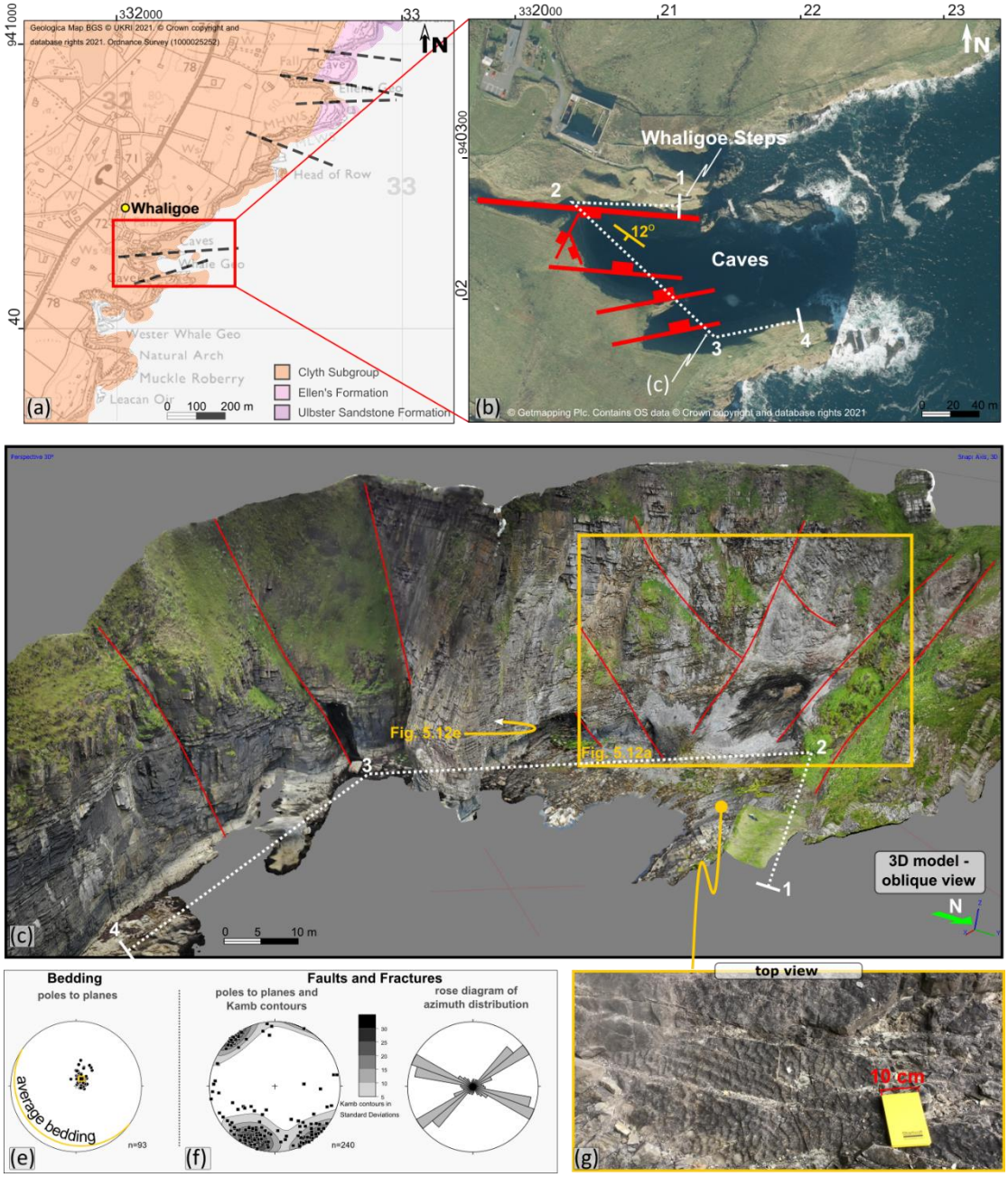

Fig. 5. 11: (a) Geological map of Whaligoe Steps area (using EdinaDigimap service and BGS 1985) showing the location of (b) aerial map (using EdinaDigimap service © Getmapping Plc) of the studied exposure showing the main structural trends. Approximate orientation of (c) is also indicated by the numbered white dotted line. (c) 3D digital outcrop model of the cliff exposure with location of (g) and Figs 5.12a and 5.13e indicated on the image. (e-f) Stereonets and rose plots of structural data collected in the field. Lower hemisphere, equal-area projections. (g) bedding surface with ripples

bedding dipping 12º/215º; Fig. 5.11e). The succession is intensely fractured and faulted by two dominant sets of structures. The first set is ESE-WNW-trending, dipping moderately to vertical (31º to vertical) predominantly to the

SSW, while the second dominant set is NE-SW- to ENE-WSW-trending dipping from moderately to vertical (46º to vertical) both to the SE/SSE and NW/NNW (Fig. 5.11f). Subordinate sets of N-S-, NNW-SSE- and NNE-SSW-trending faults also occur, mostly visible higher up in the cliffs (Fig. 5.12a). The N-S, NNW-SSE trends (Fig. 5.12a and b in dark red) seem to be cross-cut by the NNE-SSW-trending fault (Fig. 5.12a and b in bright red).

All these sets are then cross-cut by the ESE-WNW- and NE-SW- to ENE-

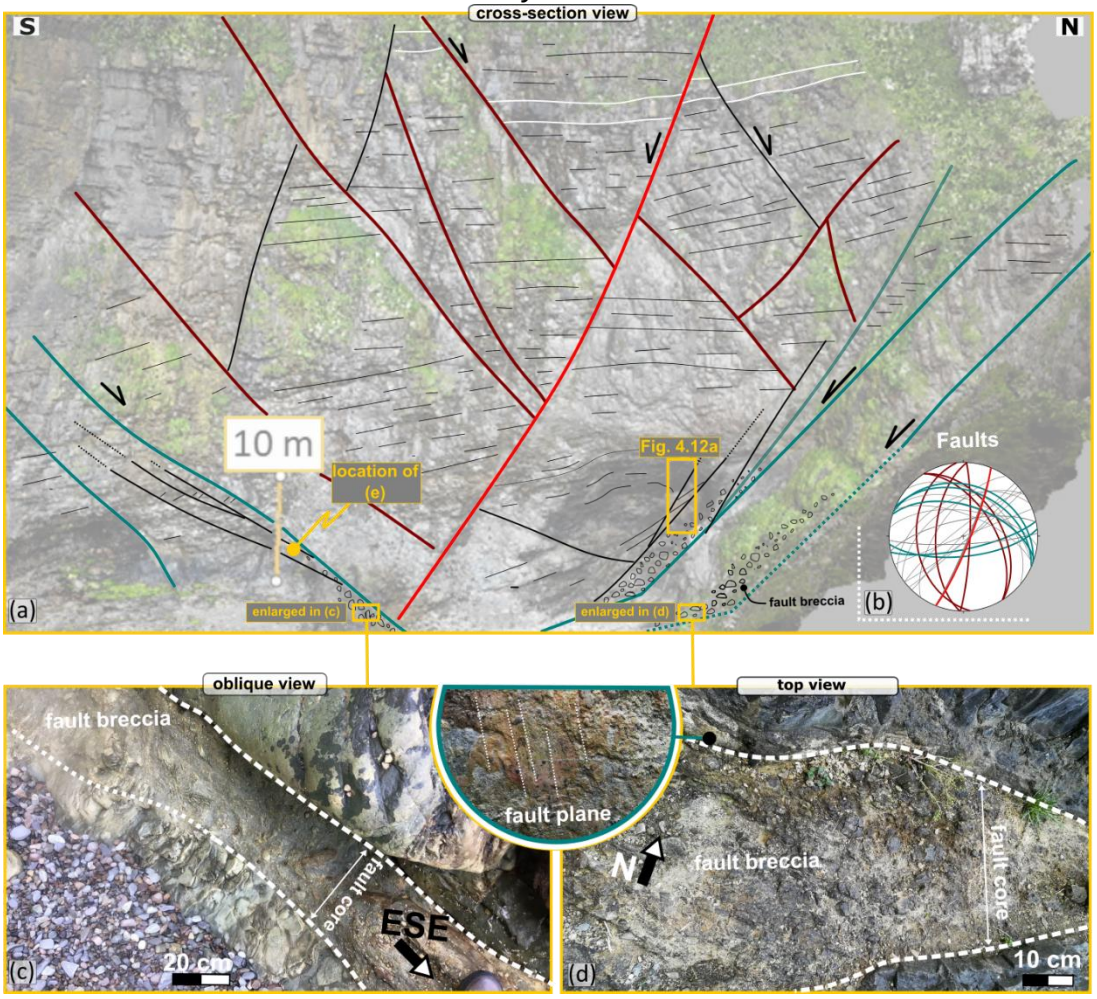

Fig. 5. 12: (a) Detailed interpretation of fault networks on the N-S-trending cliff face (see location on Fig. 5.11c) and (b) Stereonet showing the orientation of visible faults in (a) in the same colours. Faults in green are ENE-WSW- to ESE-WNW-trending and are crosscutting the NNW-SSE- to NNE-SSW-trending faults. These later faults are associated with fault breccia (c-d), gouge (see Fig. 13a) and calcite mineralisation (see Fig. 13b-d). (c-d) field photographs showing fault breccia in the fault core of the faults shown in (a) and (d-inset) dip-slip/slightly oblique-sinistral slickenlines on the exposed slip planes.

WSW-trending faults (Fig. 5.12a and b in green). Both these later ESE-WNW- and NE-SW- to ENE-WSW-trending fault sets show similar characteristics.

They are associated with a well-developed fault core formed by a cohesive fault breccia of about 20 cm to 50 cm thick (Fig. 5.12c and d) or c. 3-4 m-wide shear zone with multiple strands of fine-grained grey and yellow fault gouge (Fig. 5.13 a). Very stretched, boudinaged beds can be observed in this fault zone (Fig. 5.13a).

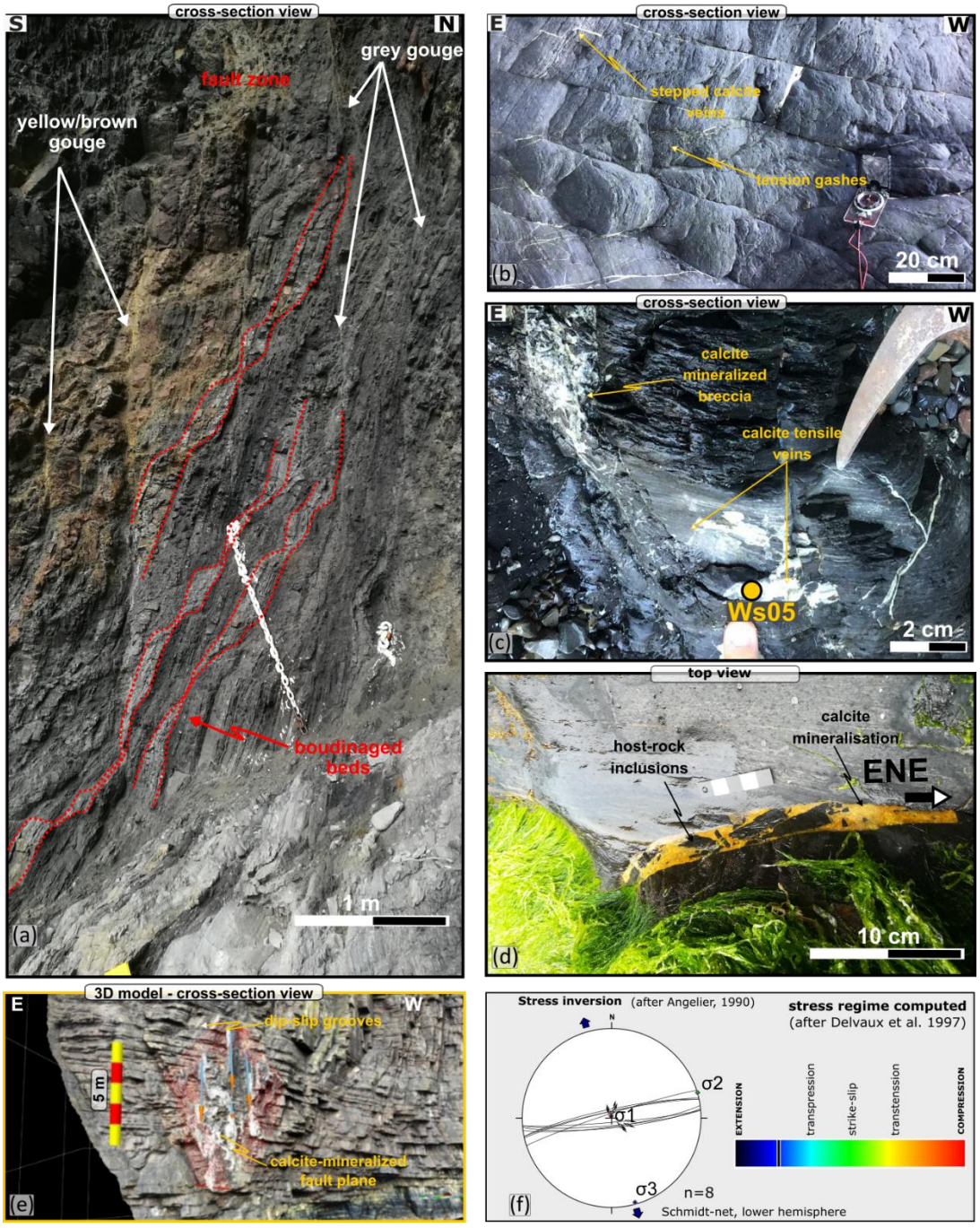

Fig. 5. 13(a) Field photograph showing a c. 3 m wide fault zone associated with a ENE-WSW-trending fault (see location on 5.12a) showing multiple strands of fault gouge. (b-d) calcite mineralisation associated with the ESE-WNW-trending fault shown in (a). Location of sample Ws05 is indicated on (b). (e) detail from 3D digital outcrop model showing an E-W trending fault plane with dip-slip grooves. (f) Stress inversion plot (after Angelier 1990) of fault lineation data.

Immediately next to the fault core a damage zone of about 2-3 m occurs with extensive calcite veining. In this zone, multidirectional calcite veins (submillimetre to mm), tension gashes, explosive calcite-cemented breccia and mm to c. 5 cm wide tensile veins often containing jigsaw inclusions of Devonian host rock (Fig. 5.12e) occur. These mineralised structures could represent local explosive hydrofractures synchronous with faulting. One sample from such a mineralised feature, Ws05, was selected for microscopy and geochronology (Fig. 5.13c).

These faults show a significant component of normal movement based on offsets of bedding markers and kinematic indicators showing dip-slip lineations and grooves on the slip planes (e.g. Fig. 5.12d inset and e). A palaeostress inversion analysis of the slickenline lineations associated with these faults yields an NNE-SSW extension direction (Fig. 5.13f).

5.4.2.2 Microscopy

The Ws05 sample (Fig. 5.14a) was taken along the ENE-WSW-trending vein set (Fig. 5.13c) sub-parallel with the major ENE-WSW-trending fault illustrated in Figure 5.13a. These veins are white and translucent in outcrop and hand specimen with large sparry calcite crystals surrounded by a finer grey matrix/cement (Fig. 5.14a). Thin sections were cut both normal to the vein (Fig. 5.14b and c) and at low angles to the vein walls (Fig. 5.14d-g) to better investigate both the sparry crystals and the finer fill. Two distinct fills are visible in thin sections. An earlier sparry zoned calcite with local intergrown pyrite crystals, and a later 'dusty', inclusion-rich, fine-grained carbonate with local

large calcite overgrowths (e.g. Fig. 5.14b and c). These are sometimes formed

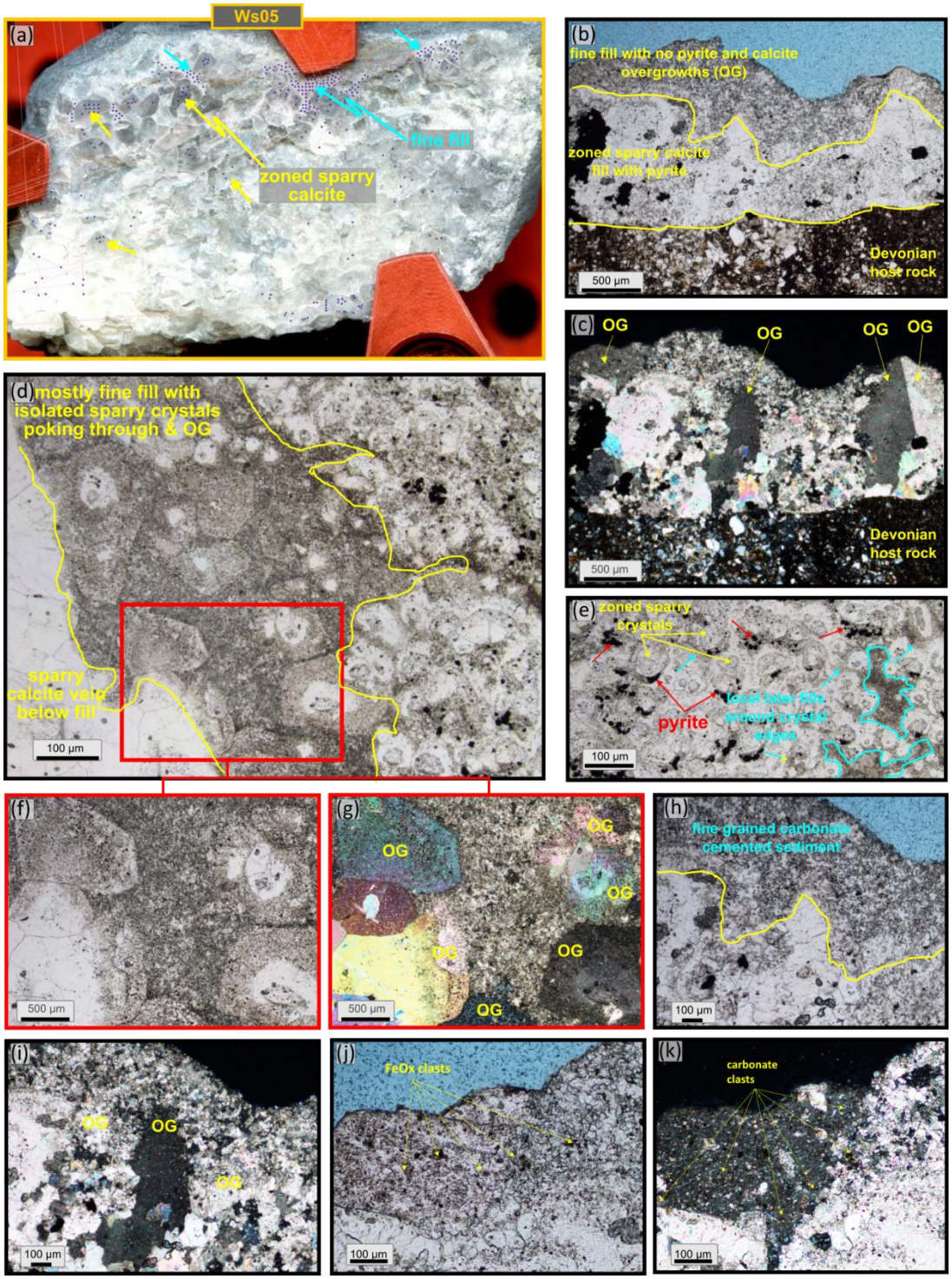

Fig. 5. 14: (a) Polished thick section of mainly calcite Ws05 sample also showing the laser ablation spots (blue dots). (b-k) representative thin section microphotographs of Ws05 sample. (b)-in plane polarised light, (c)- crossed polarised light and the enlarged (h-k) are cut normal to vein and show an earlier sparry zoned calcite with local pyrite crystals, and a later 'dusty' inclusion-rich, fine-grained carbonate with local large calcite overgrowths (OG). (d-e - in plane polarised light) and the enlarged (f)- in plane polarised light and (g)- crossed polarised light, are cut at a low angle to the vein and show how the younger fill appears to infill vuggy cavities lined by early fill sparry zoned calcite. Fine inclusions including clastic carbonate and Fe oxide are visible in (j)-plane polarised light and (k)- crossed polarised light.

in optical continuity with the older sparry calcite crystals (Fig. 5.14c).

The younger fill is interpreted as a fine-grained carbonate-cemented sediment (Fig. 5.14h-i). It appears to infill vuggy cavities lined by early fill sparry zoned calcite crystals (e.g. Fig. 5.14e) and contains many fine clastic inclusions, including carbonate grains and Fe oxide (Fig. 5.14j and k).

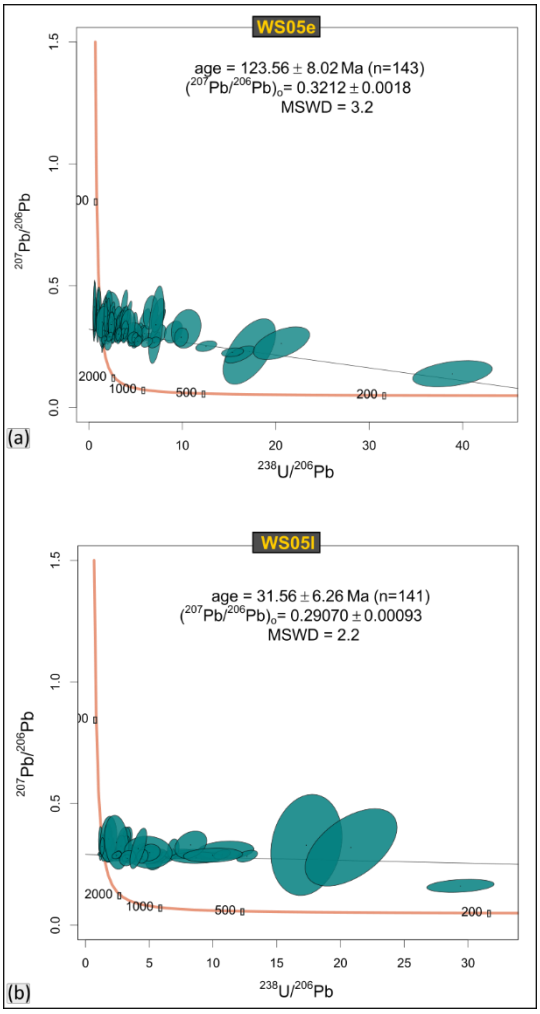

Fig. 5. 15: Tera–Wasserburg diagram of measured in-situ calcite 207Pb/206Pb and 238U/206Pb ratios (no common lead correction) from (a) sample WS05e yielding a Model I discordia age of 123.56 ± 8.02 Ma (2σ, MSWD = 3.2) (b) sample WS05l yielding a Model I discordia age of 31.56 ± 6.25 Ma (2σ, MSWD = 2.2). Error ellipsoids of spot analysis are plotted in green and represent 2σ uncertainties. MSWS = mean standard

5.4.2.3 Geochronology

The ^{238}U and ^{206}Pb concentrations were analysed in both early sparry fill (Ws05e) and later fine fill (Ws05l). Both analysed zones contained sufficient amounts of ^{238}U (and low enough concentrations of common Pb) to yield accurate and precise dates.

For sample Wa05e, 143 spots were ablated and were plotted on a Tera-Wasserberg U-Pb plot using IsoplotR, which yielded a $^{238}U/^{206}Pb$ age of 123.56±7.98 Ma (2σ, $Pb_{initial}$ = 0.3212±0.0018, MSWD = 3.2; Fig. 5.15a).

For sample Wa05l, 141 spots were ablated and were plotted on a Tera-Wasserberg U-Pb plot using IsoplotR, which yielded a $^{238}U/^{206}Pb$ age of 31.56±6.21Ma (2σ, $Pb_{initial}$ = 0.29070±0.00093, MSWD = 2.2; Fig. 5.15b).

5.4.2.4 Interpretation of structural history

The N-S, NNW-SSE and NNE-SSW-trending faults (Fig. 5.12a) are the earliest structures observed at Whaligoe Steps based on cross-cutting relationships in the field. Faults with such orientation have been widely documented across the Orcadian basin, both to the north (Dichiarante et al. 2021 Group I structures and references therein) and to the south (see Chapter 3; Tamas et al. 2022a). These faults often display growth strata in their hangingwalls (e.g. Dichiarante et al. 2021; Tamas et al. 2022a) and are associated with the transtensional opening of the Orcadian basin during the Early-middle Devonian (Seranne 1992; Dewey and Strachan 2003; Watts et al. 2007).

The later ESE-WNW- and NE-SW- to ENE-WSW-trending faults most likely represent a polymodal set of faults (fractures) formed simultaneously (e.g. Healy et al. 2006, 2015). Two dated episodes of calcite mineralisation are recognised from the WS05 sample collected from an ENE-WSW-trending fracture. An older Aptian (Early Cretaceous) age (c. 124 Ma) is similar to the age of the calcite fill obtained at New Aberdour (see Chapter 3; Fig. 3.14). Their structural orientation is consistent with the Late Jurassic- Early Cretaceous syn-rift faults, which led to the opening of the IMFB (e.g. Andrews et al. 1990; Underhill 1991a; Davies et al. 2001). However, the timing is somewhat later than the Berriasian age previously proposed for the cessation of rifting in offshore areas (e.g. Underhill 1991a and b; Davies et al. 2001), but is consistent with studies by Andrews et al. (1990), Roberts et al. (1990) and Argent et al. (2002), all of whom suggested that some faults were longer-lived, and may have been active during the Albian (Andrews et al. 1990).

The younger Oligocene age (ca 32 Ma) is so far unique in the IMFB, and the style of fill is more consistent with a near-surface fissure filled with carbonate cemented sediment. Thus, it is not necessarily associated with a phase of active tectonism.

5.4.3 Dunbeath Bay [Grid Reference ND 16801 29272]

5.4.3.1 Onshore Fieldwork Observations

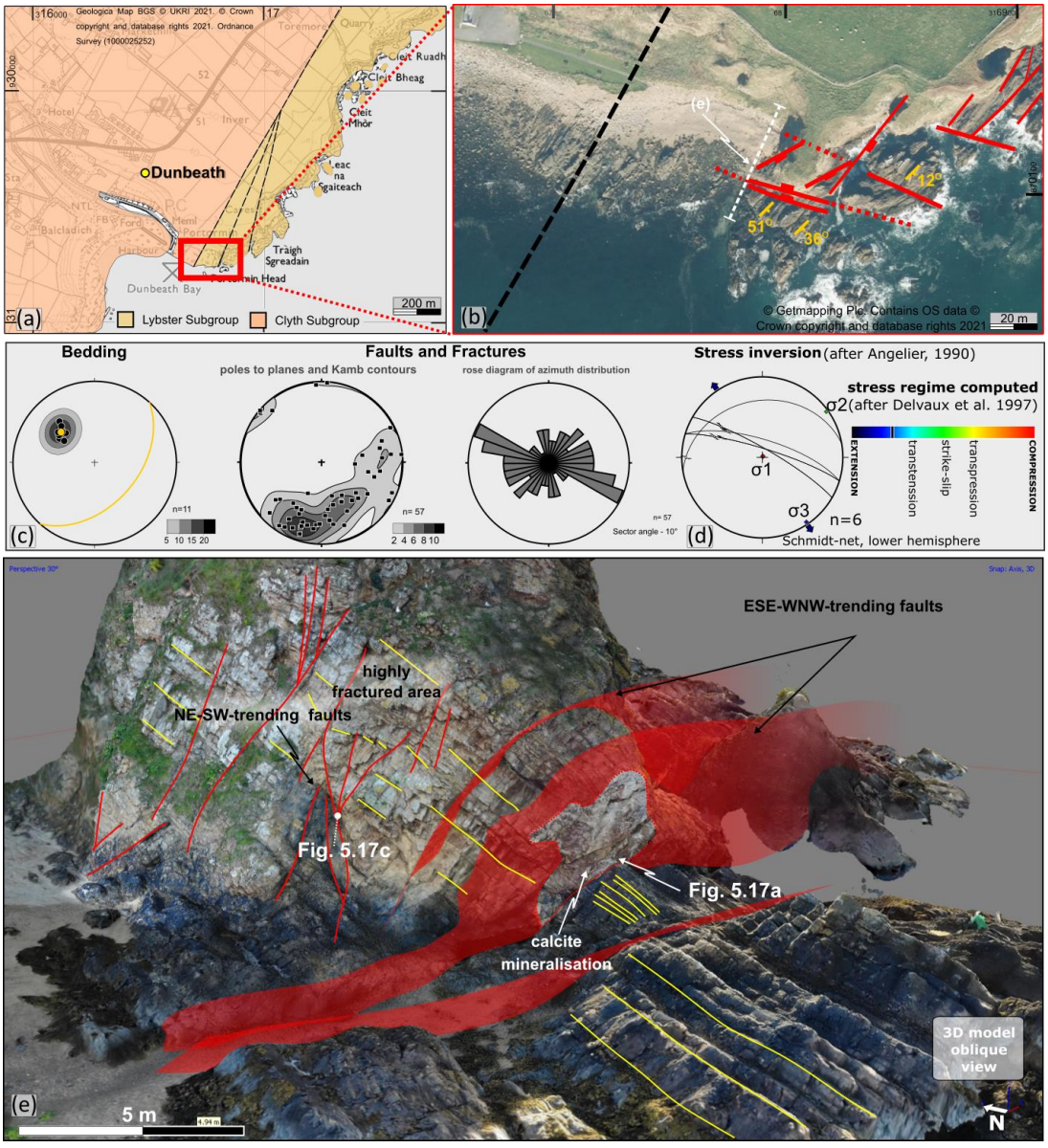

Fig. 5. 16: (a) Geological map of Dunbeath area (using EdinaDigimap service and BGS 1985) showing the location of (b) aerial map (using EdinaDigimap service © Getmapping Plc) of the studied exposure showing the main structural trends. Approximate orientation of (e) is also indicated by the white dotted line (c) Stereonets and rose plots of structural data collected in the field. Lower hemisphere, equal-area projections. (d) Stress inversion plot (after Angelier 1990) of fault lineation data (e) 3D digital outcrop model of the cliff exposure showing the ESE-WNW trending faults and NE-SW-trending structures. Location of Fig. 5.17a and c are also indicated on the image.

The Dunbeath Bay exposure is located ~1 km southeast of Dunbeath village [ND 16 29] (Fig. 5.16a and b). The investigated exposure is formed almost entirely of cliffs up to 20 m high with some limited rock platforms which can be accessed at low tide. A large 3D model across the entire area was obtained using the UAV to enable data visualisation, interpretation, and display (Fig. 5.16f).

The Middle Devonian Lybster Subgroup crops out here separated by a NNE-SSW-trending set of faults from the Clyth Subgroup to the west (Fig. 5.16a; BGS 1985). The Lybster Subgroup, ESE of the fault, comprises predominantly of cm- to dm-thick beds (of about 5 to 50 cm) of grey mudstones and fine laminated yellow/brown and grey sandstones. This succession most likely represents mudflat deposits with some coarser stream/river influx deposits, as is typical for the Lower Caithness Flagstone Group (e.g. Donovan et al. 1974).

The bedding is mostly shallowly to steeply dipping (up to 51°) to the SE with an average bedding of 46°/137° (Fig. 5.16c). The succession is deformed by a dominant, moderately to steeply dipping (34° to 80°), ESE-WNW-trending fault and fracture set (Fig. 5.16d). The ESE-WNW-trending faults are usually associated with sinistral normal oblique-slip slickensides lineations (pitch between 35-50W). A stress inversion analysis of the slickenlines associated with these faults yielded a NNW-SSE extension direction (Fig. 5.16e). The largest fault in the exposed cliff is ESE-WNW-trending, steeply dipping (80°) to the NNE (Figs 5.16f and 5.17a). This fault has a well-developed fault-core of about 1-1.5 m thick containing 30-50 cm thick, pink-coloured mineralisation (Figs 5.16f and 5.17a and b). Large, blocky crystals strongly reacting to hydrochloric acid revealed that the mineralisation is at least in part calcite

and/or siderite. The fault plane preserves evidence of sinistral normal oblique-slip slickensides lineations (pitch 50W) (Fig. 5.17a inset).

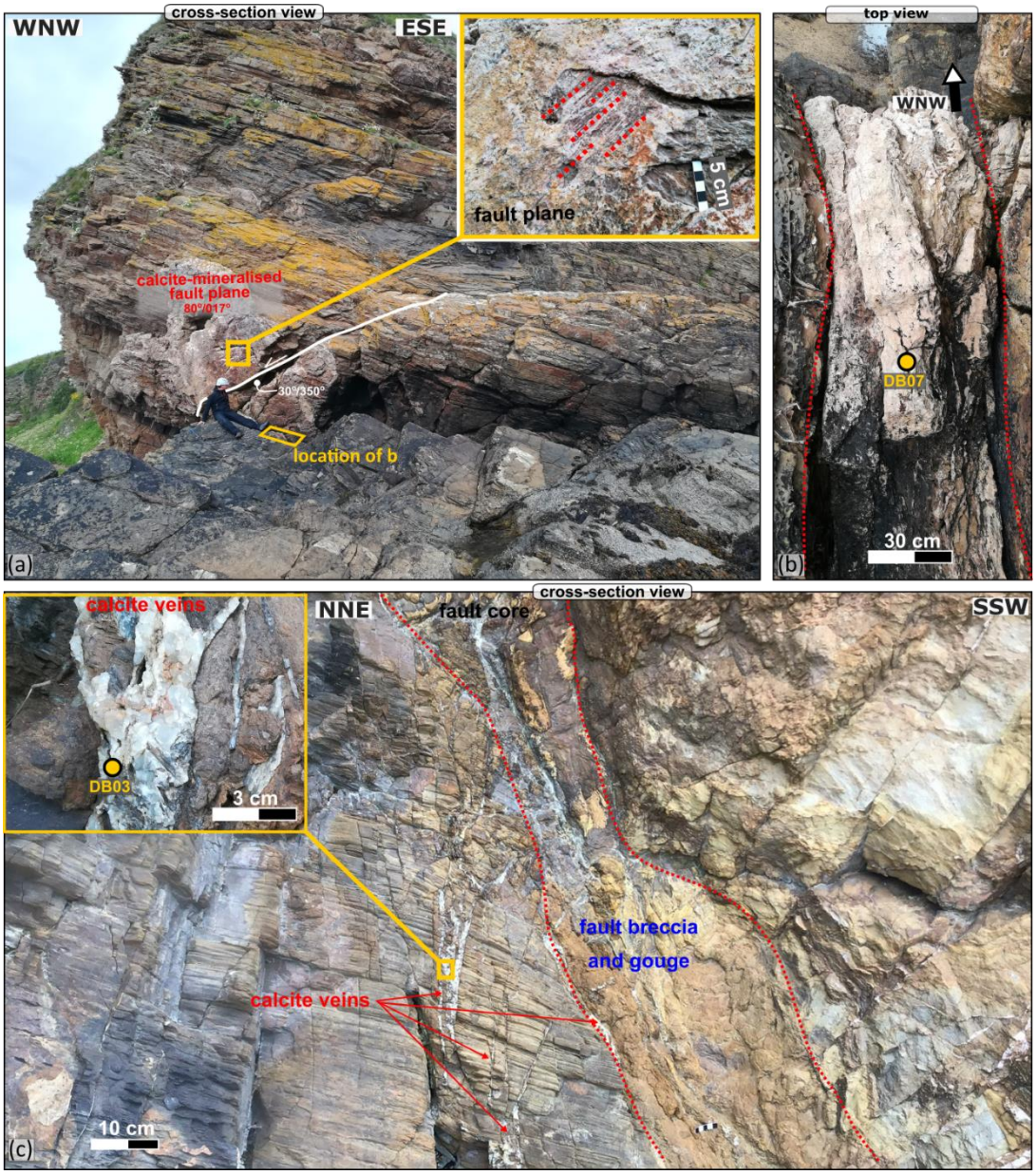

Fig. 5. 17: Field photographs showing (a) ESE-WNW-trending fault with sinistral oblique kinematics (inset) on mineralised (calcite) fault plane. (b) detailed field photograph of the thick pink calcite vein associated with the fault in (a), location of sample DB07 is also indicated. (c) NE-SW-trending faults and fracture corridors associated with fault gouge and breccia, and vuggy calcite mineralisation (inset). Location of sample DB03 is also indicated on picture.

A sample has been selected from this calcite-mineralised fault core (DB07; Fig. 5.16b) for further microscopy study and possible dating. Other faults and fracture sets, more scattered in orientation (c. 40º scatter), are moderately to vertical dipping (34º to vertical) and E-W- to NE-SW-trending.

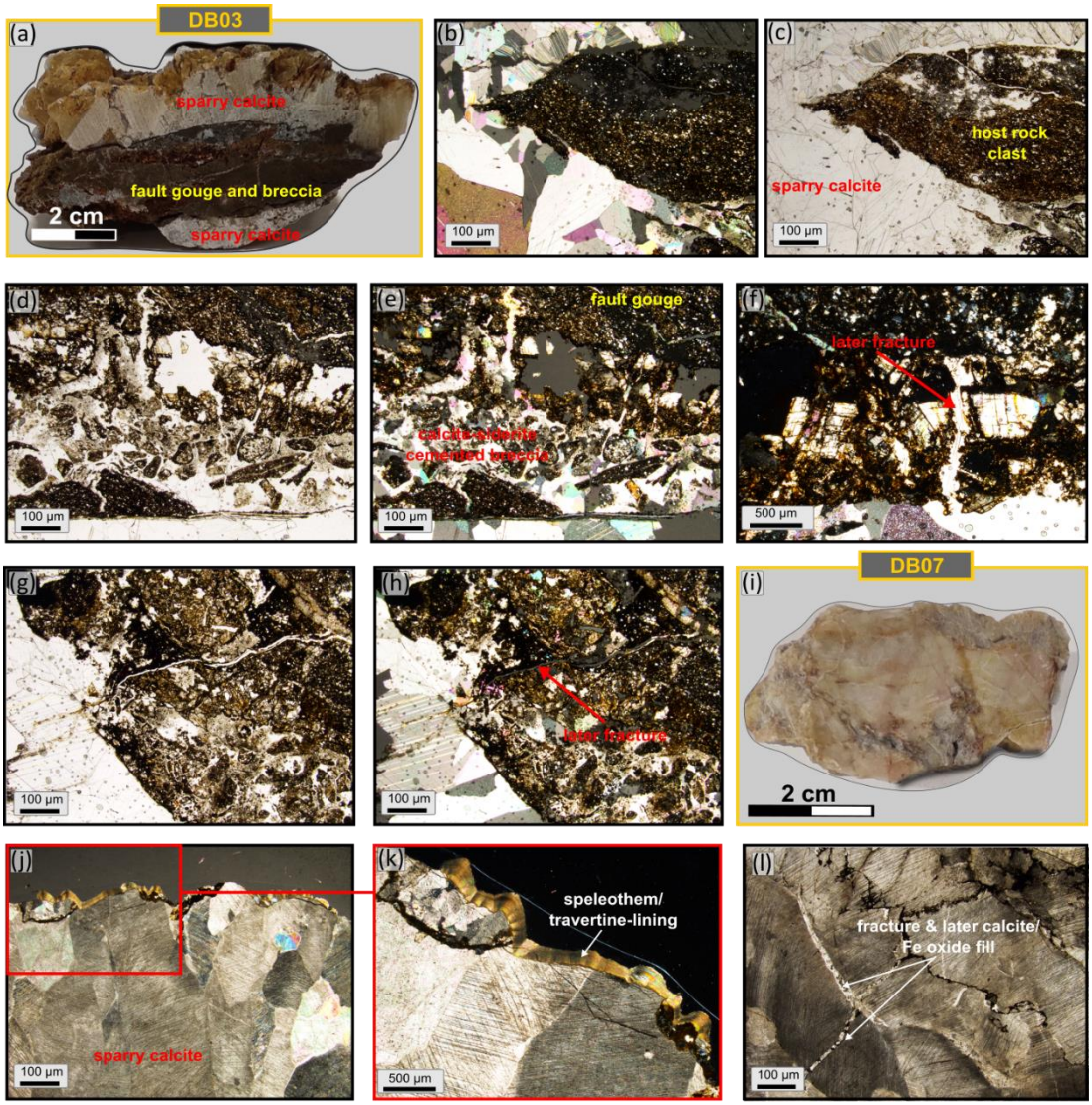

Fig. 5. 18: (a) Polished DB03 hand specimen of fault rock breccia and gouge with large euhedral calcite crystals. (b-h) representative thin section microphotographs of DB03 sample showing a dark gouge derived from sheared host rock cut and brecciated by complex calcite-siderite cemented breccia and veins, which are in turn crosscut by clean sparry calcite veins. (c, d and g) - in plane polarised light and (b, e and f) - crossed polarised light. (i) Polished DB07 hand specimen of pink calcite vein. (j-l) representative thin section microphotographs of DB07 sample showing sparry calcite vein with evidence of late fracturing and mineralisation including calcite-iron oxide fills and travertine/speleothem overgrowths. Images in crossed polarised light.

Subordinate, moderately to vertical (42º to vertical) NNE-SSW- to NNW-SSE-trending fractures also occur (Fig. 5.16d). The E-W- to NE-SW-trending normal faults and fracture corridors are best observed in the hangingwall of the major ESE-WNW-trending fault (Fig. 5.15d). These set appears to be younger as it cross-cuts the ESE-WNW-trending fault (Fig. 5.17a). The faults are associated with a 10-30 cm wide zone of incohesive yellow/brown fine-grained gouge and breccia (Fig. 5.17c). In this fault zone, some vuggy calcite veins with large

euhedral white/translucent calcite crystals are observed (Fig. 5.16c inset). One sample from the vuggy white calcite was collected for microscopy and possible dating (DB03; Fig. 16c inset).

5.4.3.2 Microscopy

The DB03 sample (Fig. 5.17a) shows large sparry calcite crystals in irregular veins cutting a dark gouge derived from sheared Devonian siltstone/sandstone host-rock (Fig. 5.17a-e). This gouge is cut and brecciated by complex calcite-siderite cemented breccia and veins (Fig. 5.17d and e), which are in turn cross-cut by clean sparry calcite veins (Fig. 5.17f-h).

The DB07 sample (Fig. 5.17i) is a big sparry calcite vein with blocky elongated crystal (Fig. 5.17j). Speleothem/travertine overgrowths can be observed at the margins on the faces of the calcite crystals (Fig. 5.17j and k) most likely formed due to long-term exposure in open, air-filled vuggy cavities. Evidence of late fracturing and mineralisation, including calcite-iron oxide fills, are observed locally (Fig. 5.17l).

5.4.3.3 Geochronology

The ^{238}U and ^{206}Pb concentrations were analysed in both samples. Both samples contained sufficient amounts of ^{238}U (and low enough concentrations of common Pb) to be dated, but unfortunately, no sample yielded an accurate and precise date. The sample DB03 is not further discussed.

Three regions of the DB07 sample were analysed (DB07a, DB07b and DB07c; Fig. 5.17a). The DB07b and DB07c regions were targeting some later fractures (Fig. 5.17a).

For sample DB07a, eight spots were ablated and were plotted on a Tera-Wasserberg U-Pb plot using IsoplotR, which yielded a $^{238}U/^{206}Pb$ inaccurate age of 54.6 ± 66.8 Ma, note the very large error bar of ± 66.8 Ma (2σ, $Pb_{initial}$ = 0.2817 ± 0.0059, MSWD = 0.38; Fig. 5.18a).

For sample DB07b, 19 spots were ablated and were plotted on a Tera-Wasserberg U-Pb plot using IsoplotR, which yielded a $^{238}U/^{206}Pb$ age of 1.55±3.76 Ma (2σ, $Pb_{initial}$ = 0.26263±0.00096, MSWD = 2.1; Fig. 5.18b).

For sample DB07c, 29 spots were ablated and were plotted on a Tera-Wasserberg U-Pb plot using IsoplotR, which yielded a $^{238}U/^{206}Pb$ age of 2.64 ± 5.97 Ma (2σ, $Pb_{initial}$ = 0.25536±0.00074, MSWD = 2.7; Fig. 5.14c).

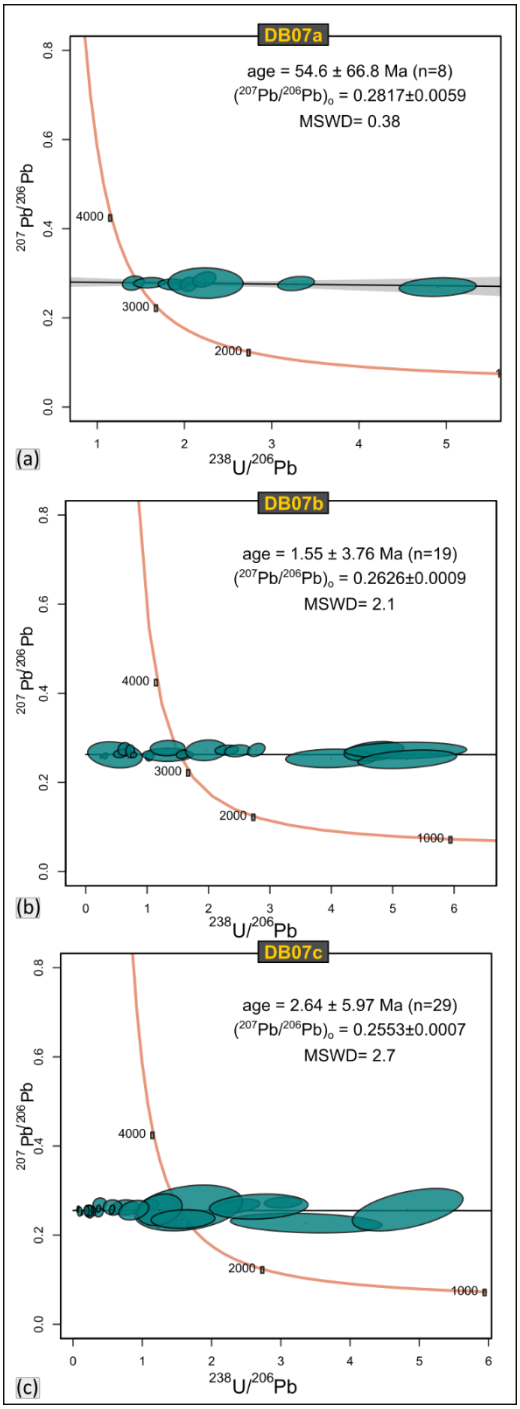

Fig. 5. 19: Tera–Wasserburg diagram of measured in-situ calcite 207Pb/206Pb and 238U/206Pb ratios (no common lead correction) from (a) sample DB07a yielding a Model I discordia age of 54.6 ± 66.8 Ma (2σ, MSWD = 0.38). Note the large error bar, which suggests an inaccurate measurement (b) DB07b yielding a Model I discordia age of 1.55 ± 3.76 Ma (2σ, MSWD = 2.1) (c) DB07c yielding a Model I discordia age of 2.64 ± 5.97 Ma (2σ, MSWD = 2.7). Error ellipsoids of spot analysis are plotted in green and represent 2σ uncertainties. MSWS = mean standard weighted deviation.

The widespread younger fractures and indicators of relatively recent long-term exposure in air filled

vuggy cavities seen in the thin sections might be responsible for the disrupted and inaccurate dates seen in DB07a.

5.4.3.4 Interpretation of structural history

As seen in the previous outcrops, the NNE-SSW- to NNW-SSE-trending structures, subparallel to the previously mapped (BGS 1985) major NNE-SSW-trending juxtaposing the Clyth against Lybster subgroups, most likely formed during the opening of the Orcadian Basin during Early-middle Devonian (Seranne 1992; Dewey and Strachan 2003; Watts et al. 2007; Dichiarante et al. 2021 – their Group 1 structures).

The mineralised NE-SW- and ESE-WNW-trending faults were sampled and dating was attempted, unfortunately they did not yield any reliable dates. This is most likely due to some widespread younger (Quaternary age) fracturing and associated fluid fluxing. However, the NE-SW-trending faults have the same orientation as the typical synrift faults observed offshore, hence they could have formed sometime during the Late Jurassic – Early Cretaceous.

The ESE-WNW-trending faults associated with sinistral normal oblique-slip slickensides lineations formed during NNW-SSE extension direction, are somewhat atypical compared to the other structures observed along the north coast of the IMFB, and their timing is more difficult to constrain. However, the NNW-SSE extension direction, which seems typical for the Late Jurassic - Early Cretaceous rifting, could indicate that these faults formed also during this main stage of rifting. In addition, sinistral normal NW-SE-trending faults, inferred to be Late Jurassic – Early Cretaceous, were also encountered on the

southern coast of IMFB, in the Turriff basin, where they reactivate an earlier basement dyke margin (see Chapter 3, Fig. 3.10a).

5.4.4 Berridale [ND 12195 22654]

*5.4.4.1 **Onshore Fieldwork Observations***

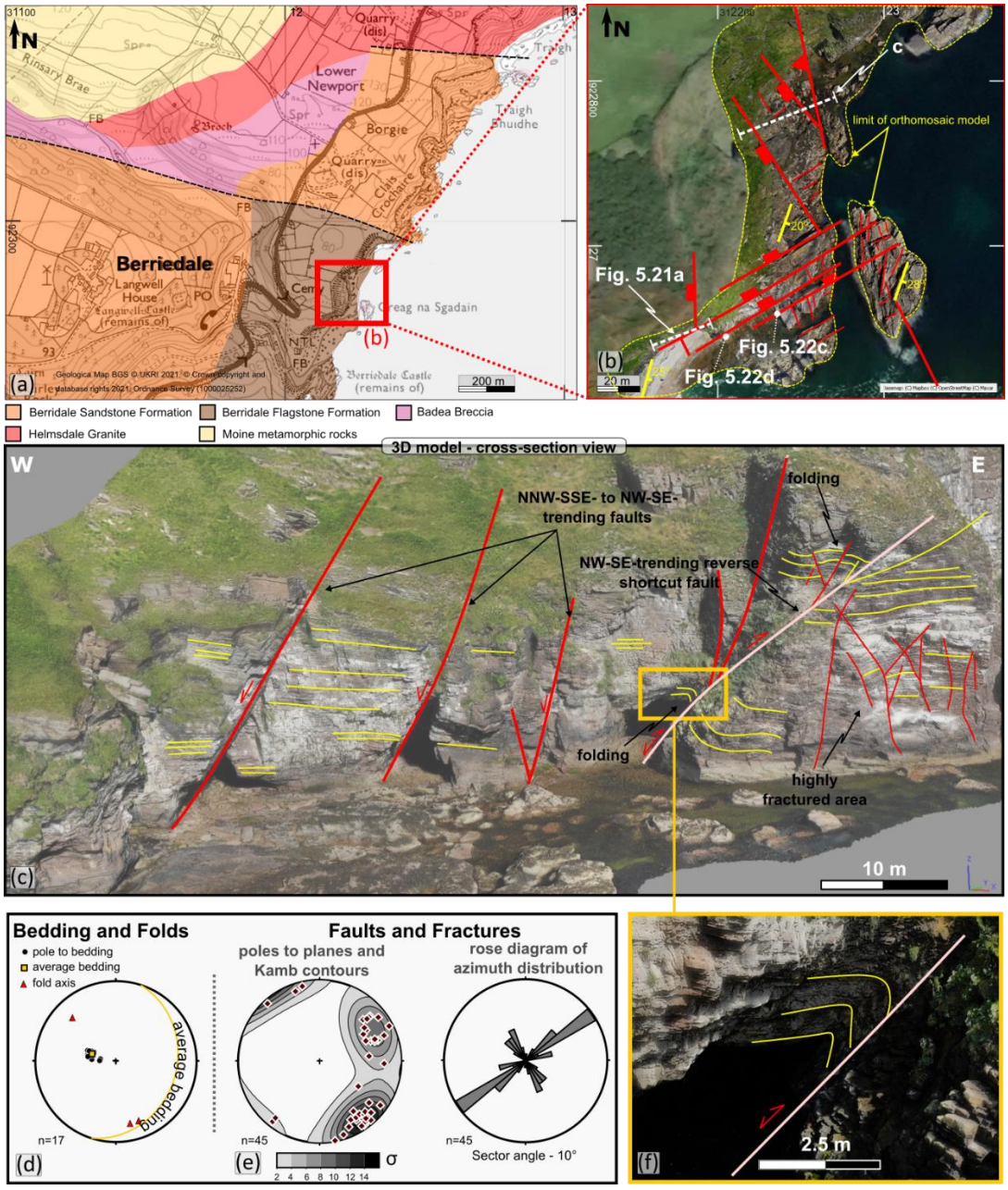

Fig. 5. 20: (a) Geological map of Berridale area (using EdinaDigimap service and BGS 1985) showing the location of (b) - orthomosaic model obtained from UAV (Unmanned Aerial Vehicle) photography overlapped on aerial map (using EdinaDigimap service © Getmapping Plc) of the studied exposure showing the main structural trends. Approximate orientation of (c) and Fig. 5.21a is also indicated by the white dashed line. (c) 3D digital outcrop model of the cliffs in the northern part of the exposure showing faults and folds occurring at Berridale. Location of (f) is also indicated on the model. (d-e) Stereonets and rose plots of structural data collected in the field. Lower hemisphere, equal-area projections. (f) detail from 3D digital outcrop model showing the folded strata in the hangingwall of a NW-SE-trending fault.

The Berridale outcrops are located on the coast ~300 m east of Berridale village [ND 117 227] (Fig. 5.20a and b). The investigated exposure is c. 600 m long and is formed almost entirely of high cliffs (30 to 80 m high) and narrow rock platforms, some of which can be accessed at low tide. A large orthomosaic (Fig. 5.20b) and 3D model (Figs 5.20c and 5.21a) across the entire area were obtained using the UAV to enable data visualisation, interpretation, and display, as large portions of the outcrop are inaccessible on foot. The Berridale Flagstone Formation of the Lower Caithness Flagstone Group (Fig. 5.3; Middle Devonian) crops out here (Fig. 5.20a; BGS 1985) and comprises predominantly of cm- to dm-thick beds (about 5 to 50 cm) of laminated grey mudstones and fine laminated red/brown and grey sandstones. These deposits have previously been interpreted as low energy, fluvio-lacustrine sequence laid down on the southwestern margin of the Orcadian basin (Donovan 1993). The bedding is mostly shallowly dipping (15º to 30º) to the ESE (average bedding 25 º /108 º; Fig. 5.20d).

Two sets of faults and fractures are dominant. The first set is ENE-WSW- to NE-SW-trending, moderately to steeply dipping (47º - 89º) predominantly to the NW, while the second dominant set is NNW-SSE- to NW-SE-trending moderately to steeply dipping (51º - 88º) to the WSW (Fig. 5.20e). The cliffs on the northern side of the exposure (Fig. 5.20c) could not be accessed on foot, and measurements were made based on the 3D outcrop using VRGS software. Mainly NNW-SSE- to NW-SE trending faults can be observed at this location, steeply dipping to the WSW/SW. Towards the eastern side of the outcrop, a NW-SE-trending fault cross-cuts through the stratigraphy dipping at a lower angle (c. 40º; Fig. 5.20c in pink). Here, the strata

are locally folded in its hangingwall and footwall (Fig. 5.20c and f), suggesting a reverse sense of movement (top-to-the-NE). The fault seems to be an inverted pre-existing steeper fault, which has been shortcut by a reverse fault oriented at a lower angle.

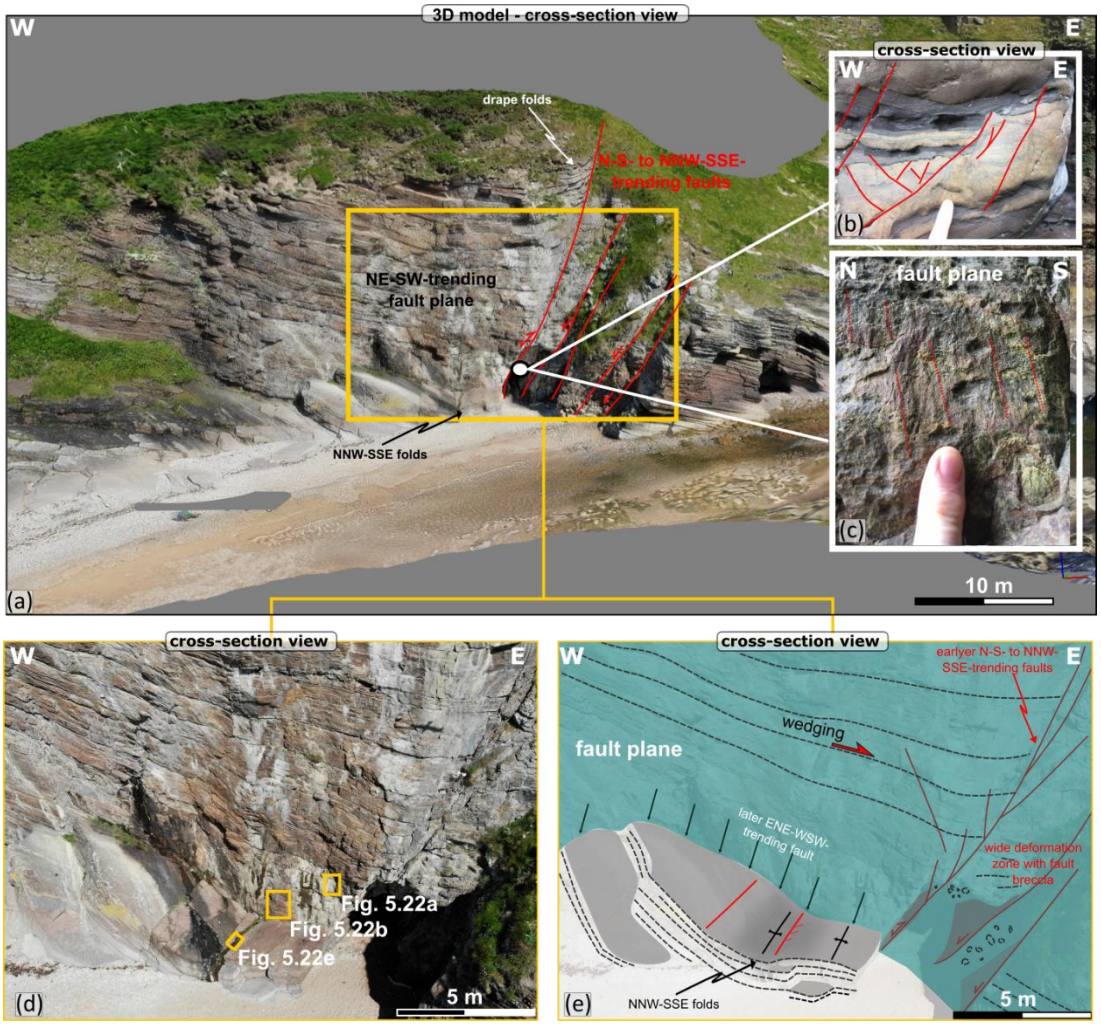

Fig. 5. 21: (a) 3D digital outcrop model of the cliffs in the southern part of the exposure (see location on Fig. 5.20) showing the main structures. (b) field photograph showing the deformation bends associated with the N-S-trending fault zone and (c) dip-slip kinematics observed on the main fault plane. (d) Field photograph and (e) line drawing showing the crosscutting relationship between the sets of structures recognised at Berridale. Location of Fig. 5.22a, b and e are indicated on (d).

On the southwestern side of the exposure (Fig. 5.21), a wide deformation zone of about 5 meters can be observed in the high cliffs. In the deformation zone, N-S- to NNW-SSE-trending faults moderately dipping (57º-64º) to the W can be observed. These faults are non-mineralised and are associated with fault breccia and widespread deformation bands with mm to

cm normal displacements based on offset bedding (Fig. 5.21b). The fault planes of these N-S- to NNW-SSE faults show dip-slip lineations (Fig. 5.21c). The strata in the hangingwall seem to gently thicken towards the fault (Fig. 5.21d and e). Also, in the hangingwall, some NNW-SSE-trending, m-scale folds (Fig. 5.21d and e) and small-scale (cm- to dm-scale) folds and thrusts (Fig. 5.22a) are developed. This suggests that the faults, which show evidence of an early dip-slip normal slip episode, are later compressionally reactivated during ~ E-W shortening.

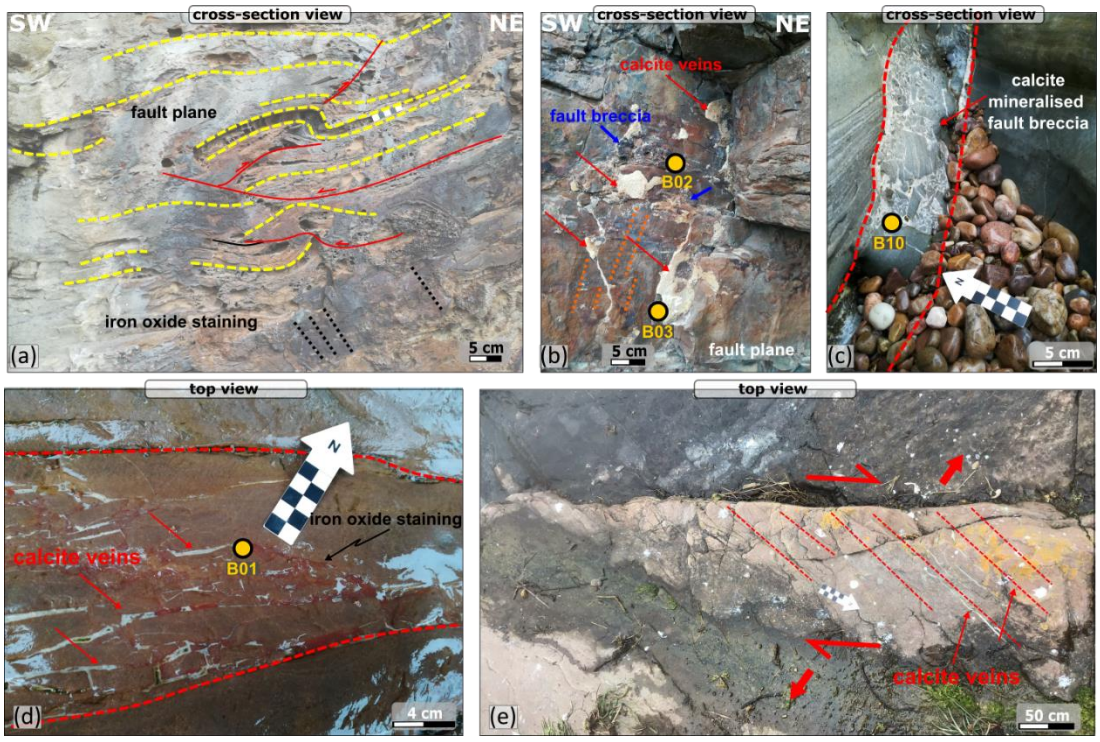

Fig. 5. 22: (a) Field photograph showing the ENE-WSW-trending fault plane. Note the small-scale fold and thrusts in the Devonian layers intersected by the fault. Dextral oblique- kinematics can be observed on the Fe-oxide mineralised fault plane (black dotted lines). (b) Field photograph showing the sinistral oblique kinematics (orange dotted lines) on the same ENE-WSW-trending fault plane as well as fault breccia and calcite mineralisation associated with the fault. Location of samples B03 and B02 are indicated on the image. (c) ENE-WSW-trending fault associated with calcite-mineralised fault breccia. Location of B10 sample is indicated on the image. (d) ENE-WSW-trending fault zone with tensile calcite veins and red-coloured sediment fill. Location of sample B01 is indicated on image. (e) En-echelon N-S-trending calcite veins consistent with dextral kinematics.

On an exposed bedding plane (Fig. 5.22e), an array of mm-thick N-S-trending white calcite tensile veins are observed. Their en-echelon arrangement suggests dextral kinematics under E-W extension direction (Fig. 5.22e).

Both N-S- to NNW-SSE-trending faults and folds are then cross-cut by later ENE-WSW- to NE-SW-trending faults and fractures (Fig. 5.21d and e). The cliff face of this outcrop represents such a fault plane (Fig. 5.21e shown in green). Some of these fault planes are heavily iron oxide-stained and are associated with iron oxide-stained fault breccia (Fig. 5.22a and b) and mm-thick white/yellow calcite mineralisation (Fig. 5.22b). Two samples were selected from this iron-mineralised fault plane, one from the iron-mineralised fault breccia (B02) and one sample from the calcite vein (B03) (Fig. 5.22b). Two differently oriented kinematic indicators are preserved on the fault plane, suggesting two episodes of movement. One, associated with normal slightly sinistral oblique-slip slickenlines and calcite slickenfibres (Fig. 5.22b; pitch between 70-82SW) and the other, dextral- normal oblique-slip slickenlines (pitch between 46-52NE) observed on the iron oxide films (Fig. 5.22a).

Other similarly oriented faults (ENE-WSW- to NE-SW-trending) in the area are associated with 10-20 cm wide calcite mineralised fault breccia (Fig. 5.22c) or 10-15 cm calcite-mineralised fracture zones with mm-thick white veins calcite and fine, red-coloured sediment infills (Fig. 5.22d). Both types of structures were sampled for microstructural study and possible dating (B10 – from the calcite mineralised breccia and B01 – from the thin veins with sediment infill).

5.4.4.2 Microscopy

The B02 sample (Fig. 5.23a) is a hematite-rich and noticeably calcite-poor, partially cemented vuggy breccia, with large clasts (mm to cm) of Devonian sandstone wall rocks. Porous hematite cements (Fig. 5.23b) show

widespread marginal alteration to limonite, possibly due to weathering in the open cavities (Fig. 5.23c). Small areas of earlier sediment fill, preserved locally, are post-dated by brecciation and hematite fill (Fig. 5.22d). Several open cavities are lined with thin rinds of orange-brown fibrous speleothem/travertine possibly formed late due to relatively recent mineral precipitation in open cavities (Fig. 5.23e and f). One definite silicified echinoderm stereom (Fig. 5.23g) (implying a marine input) and other possible fossils, including circular and angular shell fragments, can be observed in the fracture fill (Fig. 5.23h).

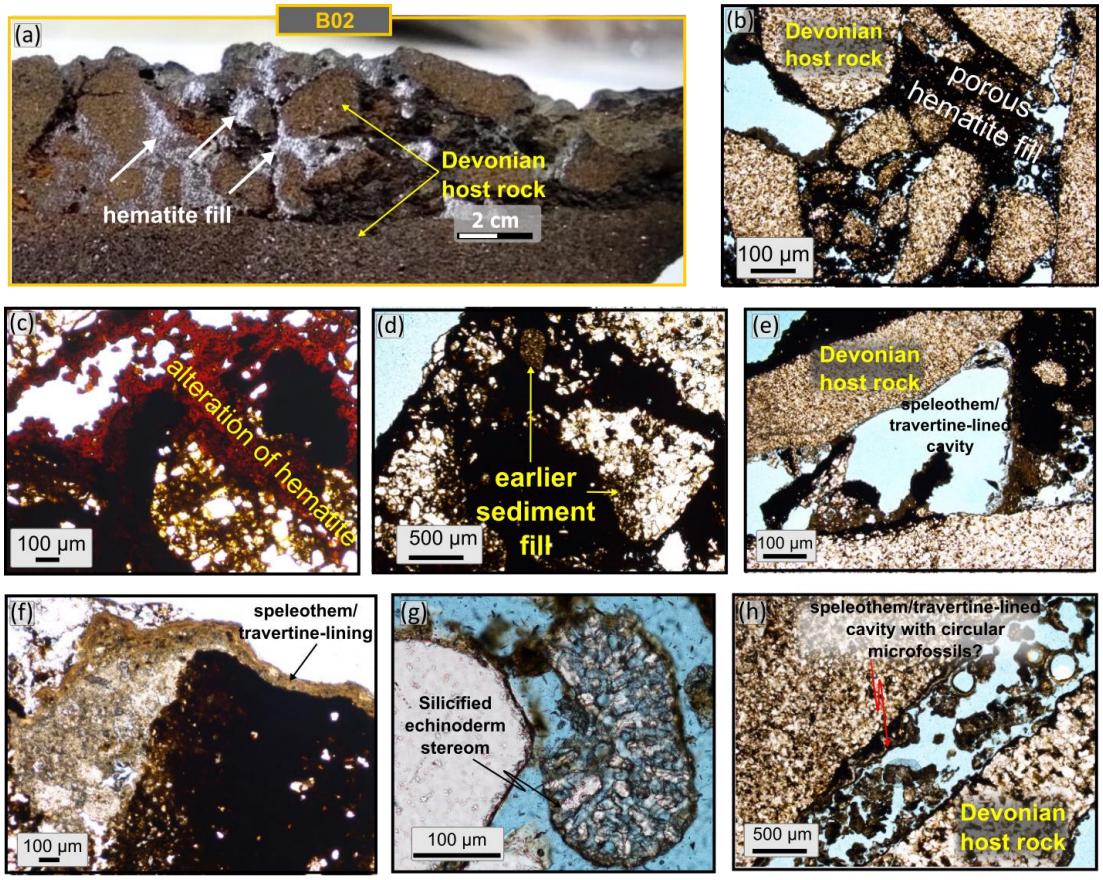

Fig. 5. 23: (a) Polished B01 hand specimen of fault breccia (b-h) representative thin section microphotographs of B01 sample showing the brecciated host rock with the pore space filled with (b) hematite and local (c) alteration of hematite to limonite (d) earlier sediment fill and (e and f) travertine/speleothem lining. (g-h) microfossils can also be observed in the cavities.

The B03 sample (Fig. 5.24a) represents a composite tensile sparry calcite vein with syntaxial growth, with at least three texturally distinct fills (Fig. 5.24b and c). Earlier ones are generally zoned, inclusion rich, including

hydrocarbon inclusions (Fig. 5.24c and d), whilst later fills are clean sparry calcite locally intergrown with hematite (Fig. 5.24c). Also, a later fracture with irregular, cataclastically deformed calcite (Fig. 5.24e) with deformation twins in the surrounding vein material (Fig. 5.24e) can be observed. This may indicate a later minor shearing event.

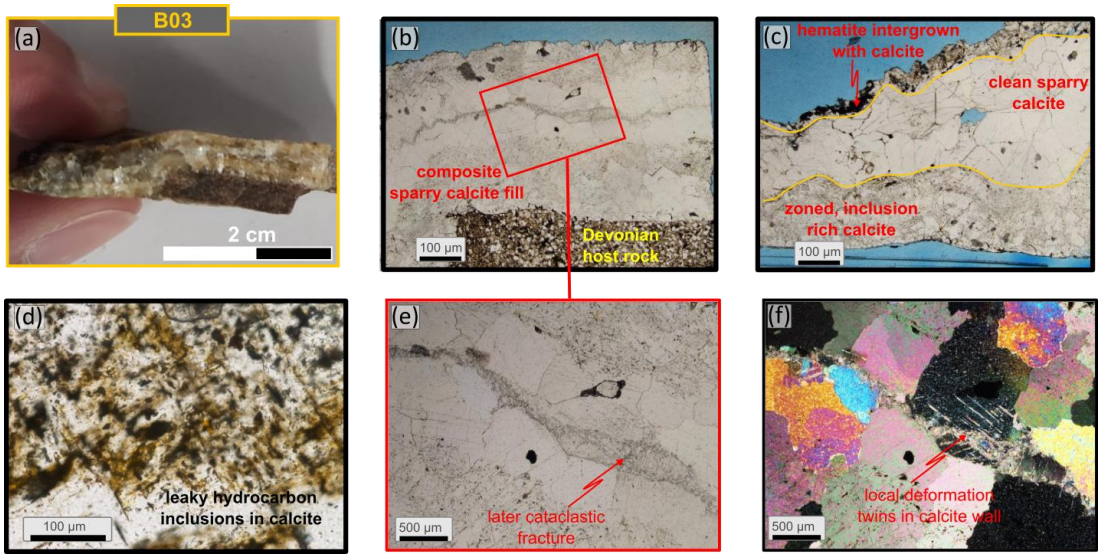

Fig. 5. 24: (a) B03 hand specimen of calcite vein. (b-f) Representative thin section microphotographs of B03 sample showing (b and c - plane polarised light) composite sparry calcite fill with light (d- plane polarised light) hydrocarbon inclusions and (e - plane polarised light) later cataclastic fracture with (f -crossed polarised light) local deformation twins in the calcite wall.

The B01 sample (Fig. 5.25a) comprises an irregular network of fine-grained red sediment fills with patches of calcite fill/veins often hosted in the same fracture (Fig. 5.25b). Sediment fills are generally earliest and rich in Fe oxide (but not hematite). Other minerals present are rare patches of pyrite (Fig. 5.25c) and flakes of colourless low relief zeolite (Fig. 5.25d), both of which are intergrown with calcite. The pyrite darkens the colour of the local sediment fill (Fig. 5.25b).

The fractures trend at various angles to bedding in the host Devonian fine sandstone and often display geopetal filling geometries in several places, all giving consistent younging sense relative to bedding in host rocks (Fig. 5.25e).

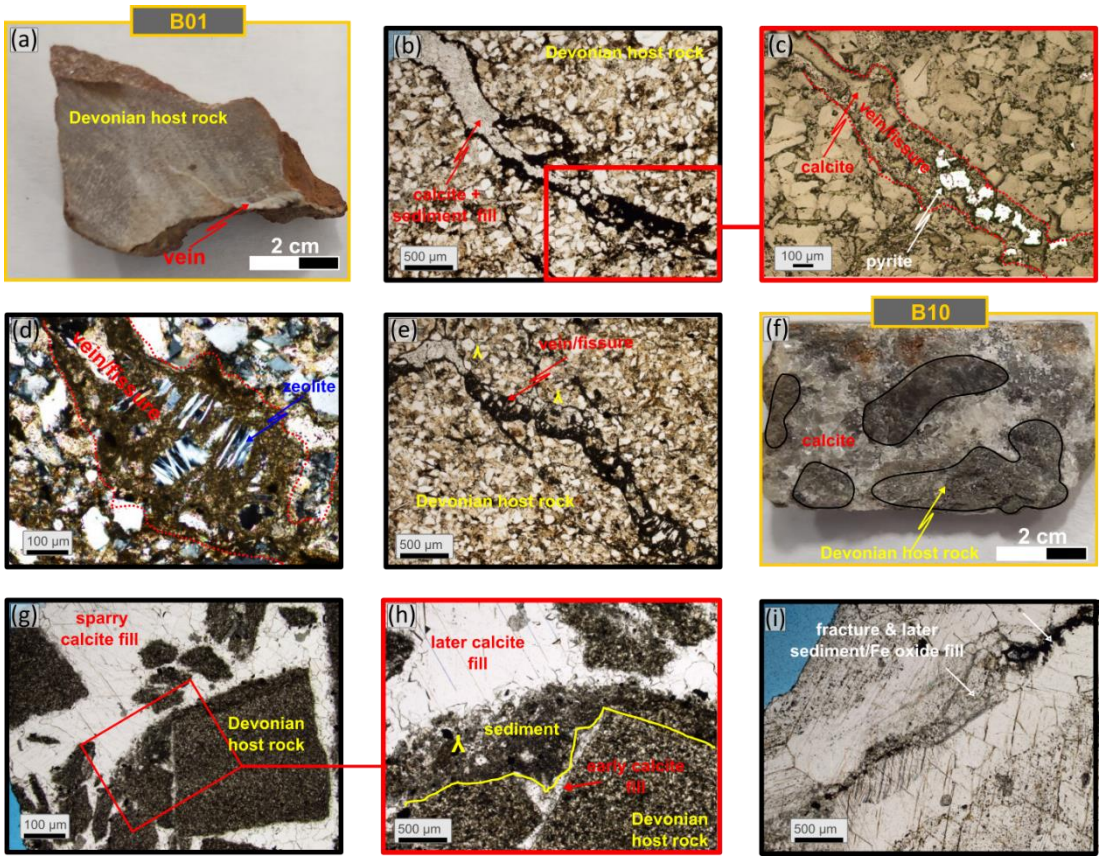

Fig. 5. 25: (a) Polished B01 hand specimen of fault breccia (b-h) representative thin section microphotographs of B01 sample showing the brecciated host rock with the pore space filled with (b) hematite and local (c) alteration of hematite to limonite (d) earlier sediment fill and (e and f) travertine/speleothem lining. (g-h) microfossils can also be observed in the cavities.

The B10 sample (Fig. 5.25f) represents a relatively 'clean' sparry calcite-filled jigsaw breccia with syntaxial growth patterns (Fig. 5.22m and n) and local development of zoning defined by dusty inclusion trails and small intergrown grains of pyrite (Fig. 5.25g). In places (Fig. 5.25h), there is also evidence of an earlier sparry calcite fill post-dated by a pale brown calcite-cemented sediment fill. Both of these are then brecciated by later calcite fill; both sediment and calcite fills carry sparse pyrite, but not the Devonian host (Fig. 5.25h). Some areas of zoned fill show later fracturing and possible later sediment or Fe Oxide fill (Fig. 5.25i).

5.4.4.3 Geochronology

The ^{238}U and ^{206}Pb concentrations were analysed in three samples. All samples contained sufficient amounts of ^{238}U (and low enough concentrations of common Pb) to be dated, and they all yielded accurate and precise dates.

For sample B01 (Fig. 5.25a), 201 spots were ablated and were plotted on a Tera-Wasserberg U-Pb plot using IsoplotR, which yielded a $^{238}U/^{206}Pb$ age of 142.34 ± 4.96 Ma (2σ, $Pb_{initial}$ = 0.577 ± 0.020, MSWD = 0.17; Fig. 5.26a).

For sample B03 (Fig. 5.24a), 234 spots were ablated and were plotted on a Tera-Wasserberg U-Pb plot using IsoplotR, which yielded a $^{238}U/^{206}Pb$ age of 148.03 ± 3.19 Ma (2σ, $Pb_{initial}$ = 0.726±0.017, MSWD = 0.11; Fig. 5.26b).

For sample B10 (Fig. 5.25f), 109 spots were ablated and were

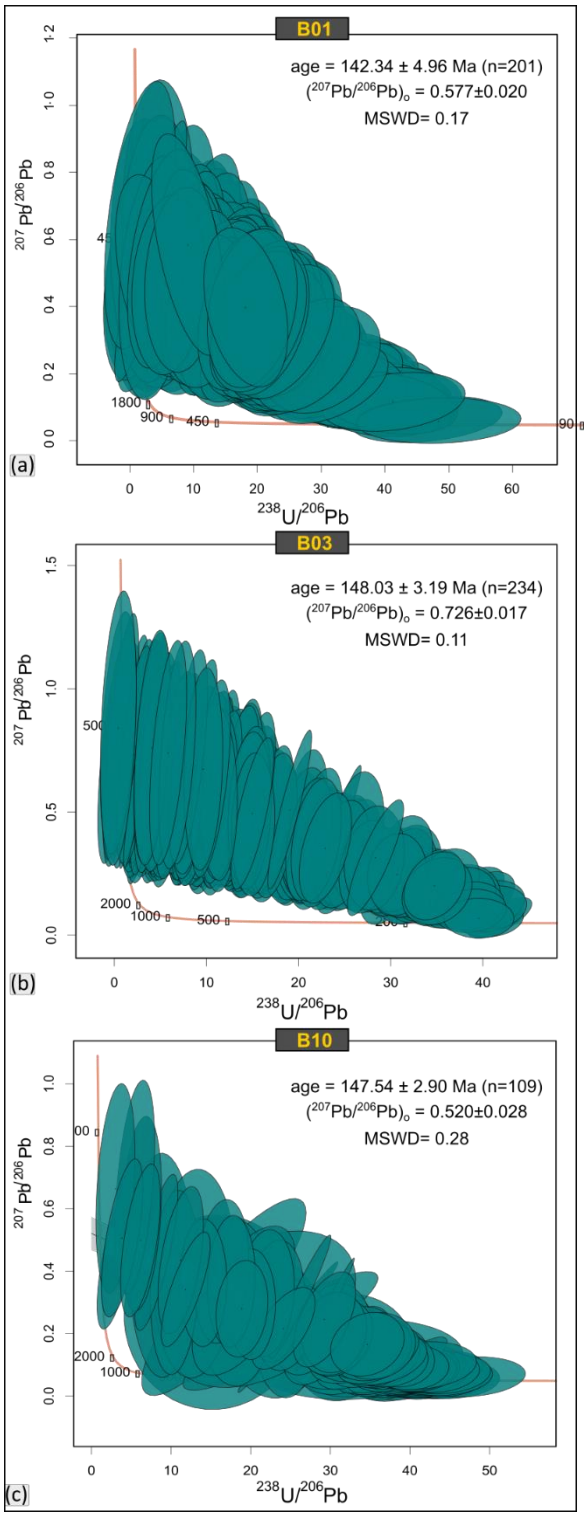

Fig. 5. 26: Tera–Wasserburg diagram of measured in-situ calcite 207Pb/206Pb and 238U/206Pb ratios (no common lead correction) from (a) sample B01 yielding a Model I discordia age of 142.34 ± 4.96 Ma (2σ, MSWD = 0.17) (b) sample B03 yielding a Model I discordia age of 148.03 ± 3.19 Ma (2σ, MSWD = 0.11) (c) sample B10 yielding a Model I discordia age of 147.54 ± 2.90 Ma (2σ, MSWD = 0.28). Error ellipsoids of spot analysis are plotted in green and represent 2σ uncertainties. MSWS = mean standard weighted deviation

plotted on a Tera-Wasserberg U-Pb plot using IsoplotR, which yielded a $^{238}U/^{206}Pb$ age of 147.54 ± 2.90 Ma (2σ, $Pb_{initial}$ = 0.5206 ± 0.028, MSWD = 0.28; Fig. 5.26c).

5.4.4.4 Interpretation of structural history

The N-S- to NNW-SSE-trending faults (Fig. 5.20e) most likely represent the earliest structures observed at Berridale. These faults show evidence of normal dip-slip and stratal thickening in their hangingwall (Fig. 5.21e), suggesting synkinematic growth faulting during deposition of the Berridale Formation (middle Devonian; Fig. 5.3b). As mentioned previously, faults with such orientation have been widely documented across the Orcadian basin in both Caithness and the IMFB (see Dichiarante et al. 2021 Group 1 structures and Chapter 3; Tamas et al. 2022a). These faults are associated with the transtensional opening of the Orcadian basin during the Early-middle Devonian (Seranne 1992; Dewey and Strachan 2003; Watts et al. 2007; Wilson et al 2010).

N-S- to NNW-SSE-trending reverse faults and folds (e.g. Fig. 5.20c) are most likely inverted earlier Devonian structures, contemporaneous with the compressional structures observed at Sarclet and elsewhere from the Scottish mainland to Shetland (e.g. Underhill and Brodie 1993; Parnell et al. 1998; Armitage et al. 2020; Dichiarante et al. 2020, 2021). These structures are interpreted as the result of a Late Carboniferous–Early Permian east-west inversion (Group 2 structures of Dichiarante et al. 2021). Likely, the compressional structures observed at Berridale are also part of the Group 2 structures of Dichiarante et al. (2021), possibly related to dextral strike-slip

reactivation of the nearby Great Glen Fault (e.g. Coward et al. 1989; Seranne 1992; Watts et al. 2007; Wilson et al. 2010; Dichiarante et al. 2020, 2021) due to the far-field effects of the Variscan orogenic event.

En-echelon mm-thick N-S-trending calcite tensile veins (Fig. 5.22e) are similar in terms of orientation and mineralisation to the N-S-trending calcite veins of Permian age (c. 258 Ma) observed at Sarclet. It is likely that these veins are also Permian. In northern Caithness, they might be associated with the opening of the West Orkney basin offshore (Dichiarante et al. 2016, 2021). In the IMFB, the Permo-Triassic history is characterised by subsidence and passive infill of the Variscan palaeotopography (see Chapter 4 for more details). However, Permo-Triassic rifting occurred in the Central/Viking graben, during E-W extension direction (e.g. Davies et al. 2001). It is possible that those veins form in response to the far-field stress related to the early rift in the Central/Viking graben.

N-S- to NNW-SSE-trending faults and folds are then cross-cut by later ENE-WSW to NE-SW trending faults and fractures (e.g. Fig. 5.21e). These faults show evidence of two episodes of movement. A normal sinistral oblique-slip event is widely associated with calcite mineralisation, and a later normal-dextral oblique-slip event is associated with iron-oxide mineralisation as concluded from field and observations thin section (e.g. Figs 5.22a and 4.25i).

As revealed by the geochronology, the calcite mineralisation associated with those ENE-WSW-trending structures is Late Jurassic-Early Cretaceous (c. 148 to c. 142 Ma) (Fig. 5.26). This falls within the main syn-rift episode, which led to the opening of the IMFB (e.g. Underhill 1990; Thomson and Underhill 1993). The B03 sample gave a c. 148 Ma age and is rich in

hydrocarbon inclusions (Fig. 5.24d), also indicating the timing of a hydrocarbon charge episode.

The later event characterised by normal-dextral reactivation of the pre-existing normal-sinistral ENE-WSW-trending fault is widely associated with iron-oxide staining and is inferred as Cenozoic. This is because heavily iron oxide-stained fault planes were also observed on the southern coast at Hopeman (see Chapter 4) where a very similar sinistral-normal Late Jurassic - Early Cretaceous syn-rift fault was dextrally reactivated during Cenozoic. Cataclastically deformed calcite with deformation twins and fracturing with possible later sediment or iron oxide fill (Fig. 5.25i) were also encountered in thin section and may be related to these Cenozoic events.

The heavily hematite-cemented fault breccia (Fig.5.23a) shows widespread alteration to limonite (Fig. 5.23c), orange-brown fibrous speleothem/travertine lining (Fig. 5.23f) and marine fossils (5.23g), suggesting a complex fault history. The fault breccia could have formed earlier, related to the Jurassic - Early Cretaceous faulting, as a silicified echinoderm stereom and other marine fossil shells are found in fracture cavities. The position of the outcrop in the footwall of the HF would agree with Trewin and Hurst (2009), who suggest that echinoderms probably lived on a rock substrate at the top of the HF scarp, which formed a shallow marine high energy shelf during the Jurassic. The enrichment in iron-oxides and the hematite cement could have happened during the Cenozoic, while the alteration to limonite and the speleothem/travertine lining are most likely the results of weathering in open cavities and could be due to Quaternary exposure, as seen at Dunbeath.

5.4.5 Helmsdale [Grid Reference ND 04068 15596]

5.4.5.1 Onshore Fieldwork

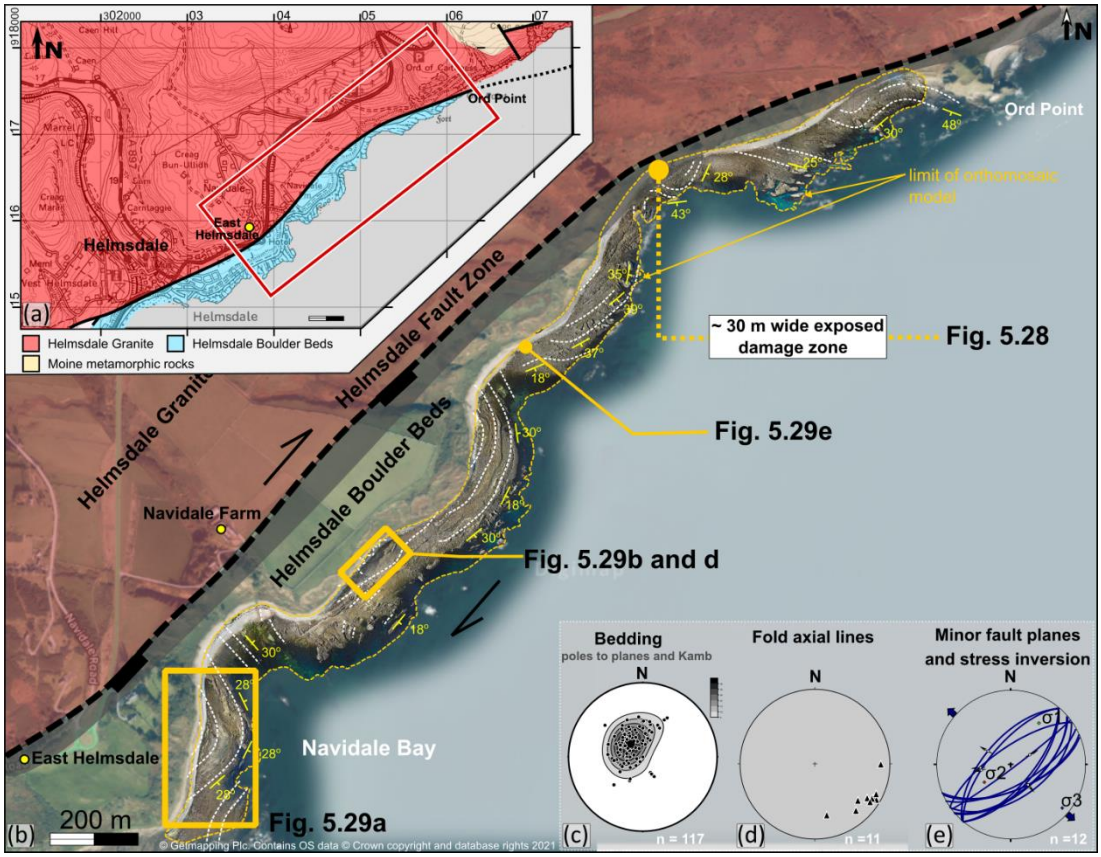

Fig. 5. 27: (a) Geological map of Helmsdale area (using EdinaDigimap service and BGS 1998) showing the location of (b) - orthomosaic model obtained from UAV (Unmanned Aerial Vehicle) photography overlapped on aerial map (using EdinaDigimap service © Getmapping Plc) of the studied exposure showing the main structural trends. Location of Figs 5.28 and 5.29a-e is also indicated on (b). (c) Stereonets and rose plots of structural data collected in the field. Lower hemisphere, equal-area projections.

Helmsdale outcrops are located along the coast, ~1 km east of Helmsdale village [ND 028 154], extending c. 2.5 km from Helmsdale East [ND 04068 15596] to Ord Point [ND 05864 17209] (Fig. 5.27a and b). The investigated exposure is formed almost entirely of rock platforms of about 100 m wide, which can be accessed at low tide, and some limited high cliffs (about 30 m in height). The section follows the trace of the Helmsdale Fault Zone, which exposes the Upper Jurassic Boulder Beds in the hangingwall, downfaulted to the SE against the Helmsdale granite (Fig. 5.27). This has been a location of great interest for both structural (e.g. Thomson and Underhill

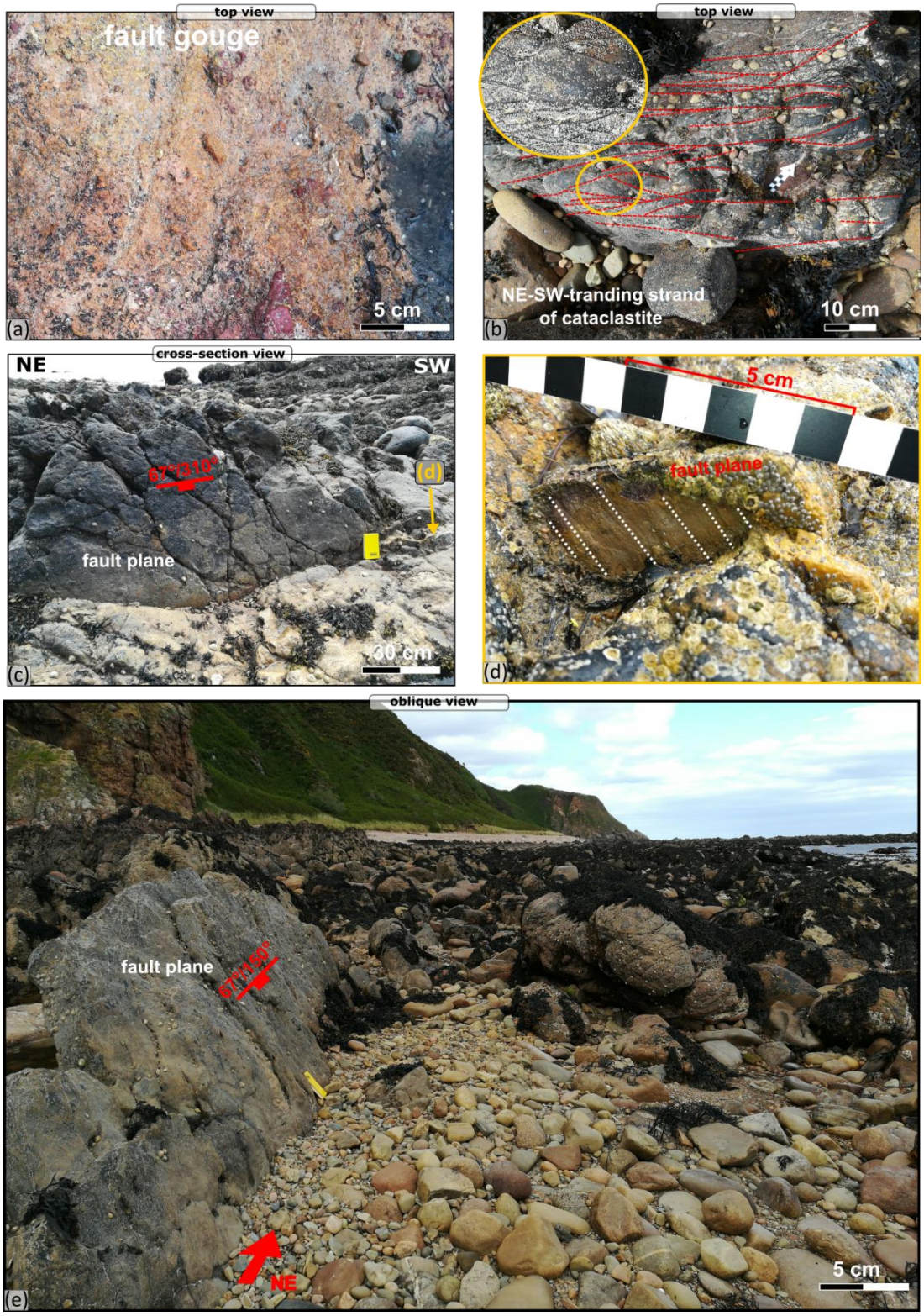

Fig. 5. 28: Field photographs of structures within the HF damage zone (a) yellow/orange fault gouge (b) NE-SW-trending strands of deformation bands shown in red and without interpretation in the inset (c) minor antithetic fault plane (dipping to the NW) (d) kinematic indicators on the slip planes of the subsidiary faults show dip-slip to slightly sinistral normal oblique-slip (e) minor synthetic fault (dipping to the SE).

1993; Hillis et al. 1994; Le Breton et al. 2003) and sedimentological aspects (e.g. Pickering 1984; Jonk et al. 2003; MacDonnald and Trewin 2009;

McArthur et al. 2013).

The Upper Jurassic Boulder Beds consist of dm- to m-thick breccias formed by angular/subangular clasts of mostly middle Devonian sandstones. These are interbedded with thin-bedded (mm- to cm-thick) light and dark grey sandstones and laminated dark shales. Slump-folds, very large Devonian blocks (m-wide) and sandstone intrusions are also present within the Boulder Beds. The origin of these Boulder Beds is widely accepted as debris flow breccias triggered by the syn-sedimentary movements of the HF and the presence of an associated fault scarp (e.g. Pickering 1984; McArthur et al. 2013).

The main slip plane of the Helmsdale fault is not exposed, but a ~30 m wide deformation zone in the hangingwall of the fault is locally exposed (Figs 5.27b and 5.28). Within the damage zone, yellow/orange fault gouge (Fig. 5.28a), 50 cm to 1 m wide NE-SW-trending strands of deformation bands (Fig. 5.26b) as well as minor synthetic (dipping to the SE; Fig.5.28e) and antithetic faults (dipping to the NW; Fig. 5.28c) can be observed. Kinematic indicators (e.g. slickenlines, grooves) on the slip planes of the subsidiary faults show dip-slip to slightly sinistral normal oblique-slip (Fig. 5.27e). Movement indicators used to infer the overall movement and kinematics of the fault minor faults within the damage zone are consistent with a NW-SE extension direction (Fig. 5.27e).

Next to the fault zone, the Upper Jurassic layers in the hangingwall are sub-horizontal to moderately dipping (Fig. 5.27c) and are folded into large- (tens of meters) to small-scale (dm to m) folds which are best exposed at low

tide. A large orthomosaic and 3D model across the entire area was obtained from the UAV to better visualise these structures (Fig. 5.27b).

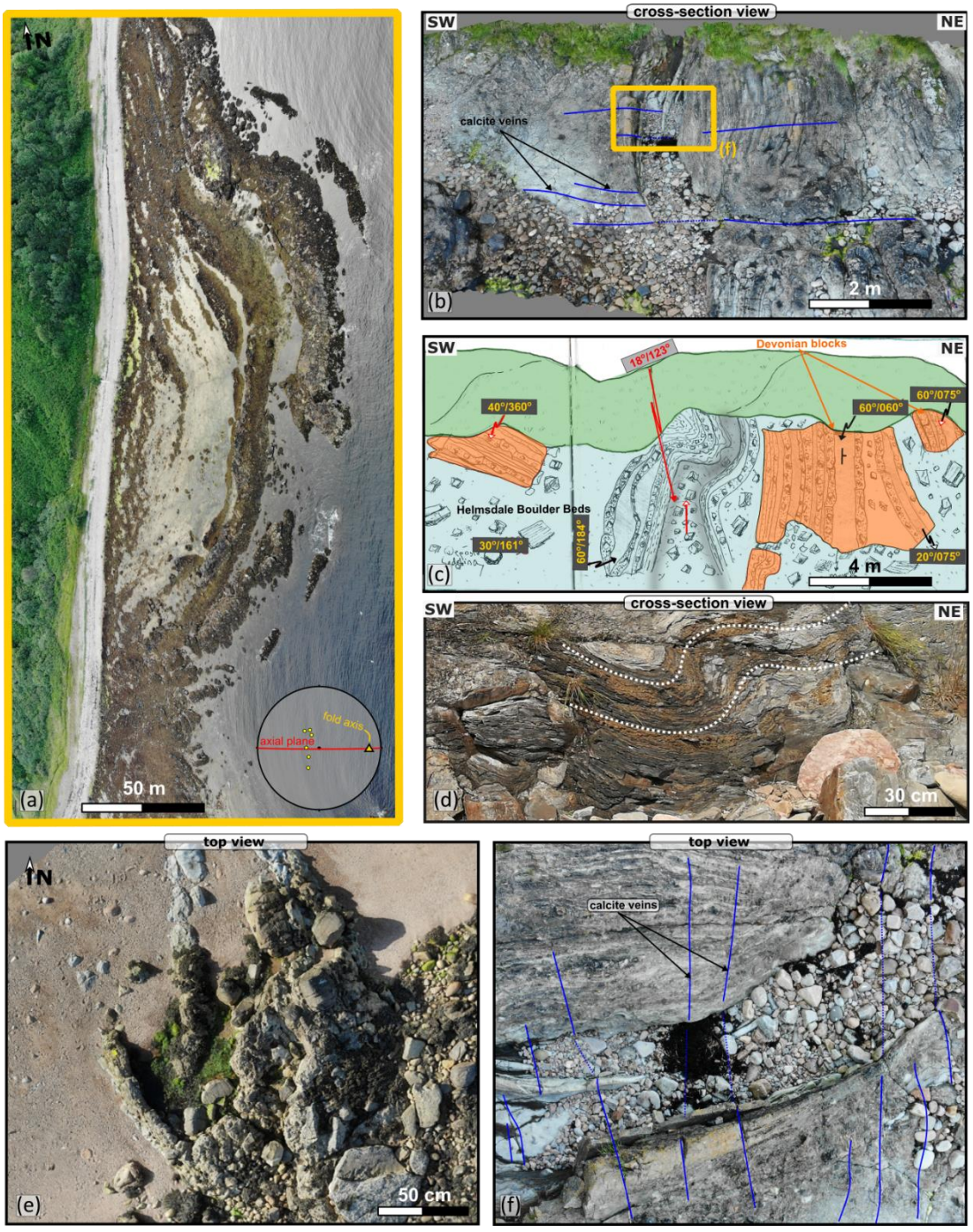

Fig. 5. 29: (a) Drone image of the large-scale fold at Navidale Bay and inset stereonet of the fold limbs bedding, hinge and axial plane (see location on Fig. 5.27b). (b) 3D model, (c) field sketch of (b), and (d) field photograph of small-scale fold within the Boulder Beds. These folds are shallow plunging to SE, similarly to the large-scale folds. Also note the large Devonian boulders dipping at different angles within the Boulder Beds in (c). (e) Drone image showing a tight fold, steeply plunging (41º) to the S. This fold most likely represents a slump. (f) calcite-mineralised tensile veins crosscutting the folded strata.

The large-scale folds (Figs 5.27b and 5.30a) are mostly gentle (interlimb angles of 140 º-160 º), shallow plunging (6º to 18º) predominantly to

the SE (Fig. 5.27d). However, the large fold cropping out at Navidale Bay plunges more to the east (Fig. 5.29a). Some smaller-scale folds (Fig. 5.29b-d) are similarly to the large-scale structures and are shallow plunging to the SE, while others are steeply plunging (41º) to the S (Fig. 5.29e).

The folds are seemingly cross-cut by calcite-mineralised tensile veins (Figs 5.29f, 5.30).

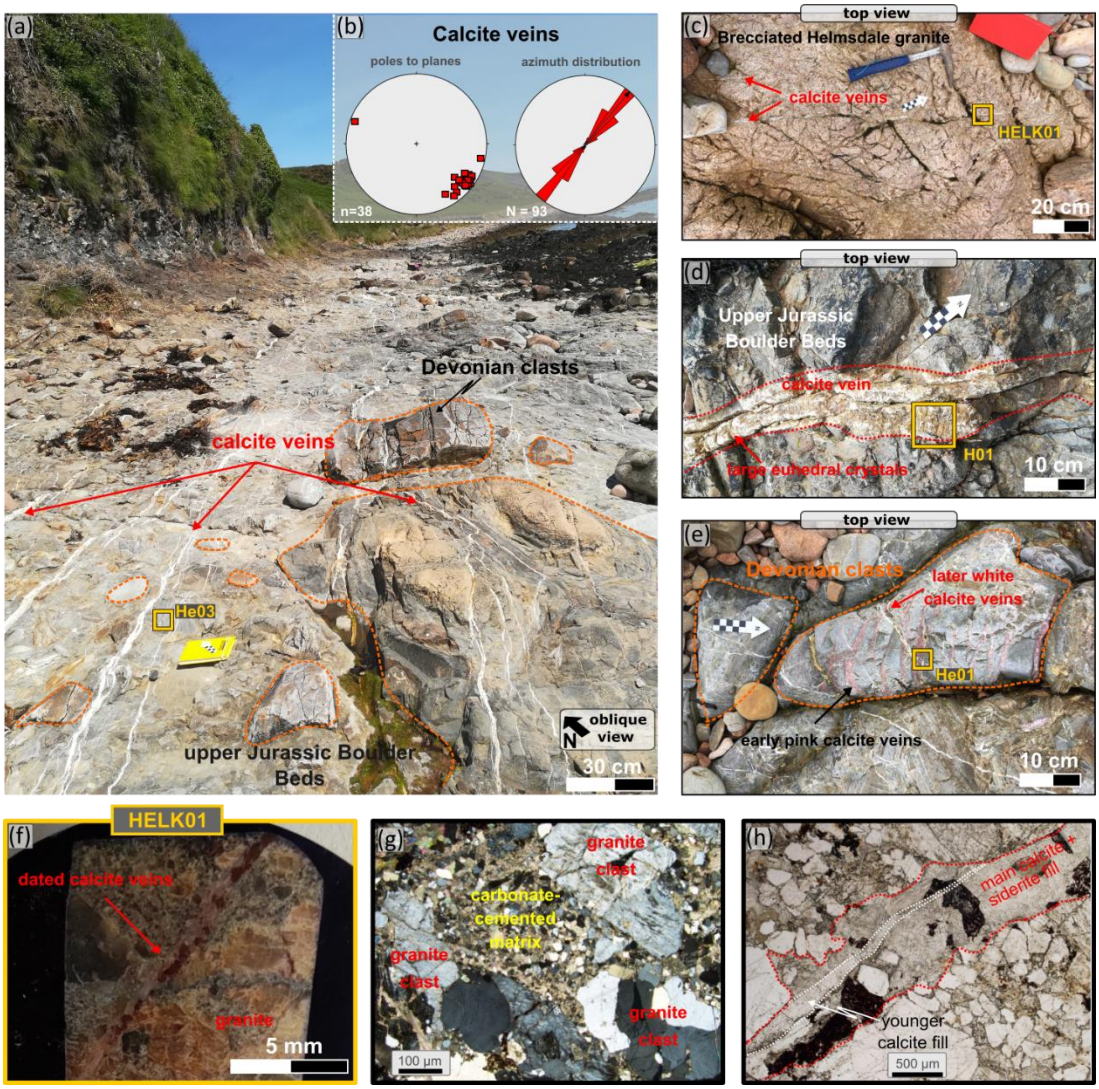

Fig. 5. 30: (a) Field photograph showing calcite-mineralised tensile veins crosscutting the upper Jurassic boulder Beds. Note the large Devonian boulders also crosscut by the calcite veins. Location of sample He03 is also indicated. (b) Stereonet (lower hemisphere, equal-area projections) and rose plot of the calcite-mineralised veins. (c) Field photograph showing calcite-mineralised tensile veins crosscutting the Helmsdale granite. Location of sample HELK1 is also indicated on the image. (d) Close-up image of a wide (c. 10 cm) calcite vein with location of sample H01 also indicated on the image. (e) Field photograph of a Devonian clast within the upper Jurassic Boulder Beds crosscut by early pink-calcite veins and later white calcite veins. (f) Polished thick section of the HELK1 sample. (g) representative thin section microphotographs of HELK1 sample showing the granite clast cemented by a carbonate matrix (crossed polarised light). (h) thin section microphotographs of HELK1 sample showing the calcite and siderite vein. Also note the younger calcite vein crosscutting the earlier one (in plane polarised light).

These veins are best exposed c. 300m southeast of the Navidale Farm [ND 04471 16177], where they concentrate within a ~7-10 m wide zone and extend laterally for about 100 m.

The veins are sub-millimetre to 10 cm wide, NE-SW-trending, sub-parallel to the HF, steeply dipping (60º to 88º) to the NW (Fig. 5.30b). Some of the wider veins are incompletely sealed and have large (mm to cm) euhedral crystals lining open vugs (e.g. Fig. 5.30d). These veins are widespread and cross-cut both the Upper Jurassic Boulder beds (Fig. 4.30a and d), including the Devonian clasts within the Boulder beds (Fig. 5.30a and e) and the Helmsdale granite (Fig. 5.30c). The Devonian clasts within the Boulder beds are also cross-cut by earlier, pink-coloured calcite veins (Fig. 5.30e). The calcite veins were sampled both from the Helmsdale Granite (HELK1; Fig. 5.30c) and the Upper Jurassic Boulder Beds (H01 and He03; Fig. 5.30a and d). One sample was also collected from Devonian clasts within the Boulder beds (He01; Fig. 5.30e) in order to investigate and possibly date both the earlier pink veins only observed in the Devonian clasts in addition to the later white calcite veins.

5.4.5.2 Microscopy

The HELK 1 sample (Fig. 5.330f) is located within the Helmsdale granite, close to contact with the Boulder Beds, and was interpreted in the field to be a brecciated granite cut by NE-SW-trending calcite veins (Fig. 5.30f). The thin section reveals that the host rock is a carbonate-cemented sedimentary (as opposed to cataclastic) breccia containing clasts of granite (Fig. 5.30g). This breccia is crosscut by later calcite-siderite tensile veins (Fig. 5.30h). The siderite is only observed within the veins (Fig. 5.30h). Locally the

veins are composite with a subordinate, later clearer calcite fill following pre-existing calcite and siderite vein (Fig. 5.30h).

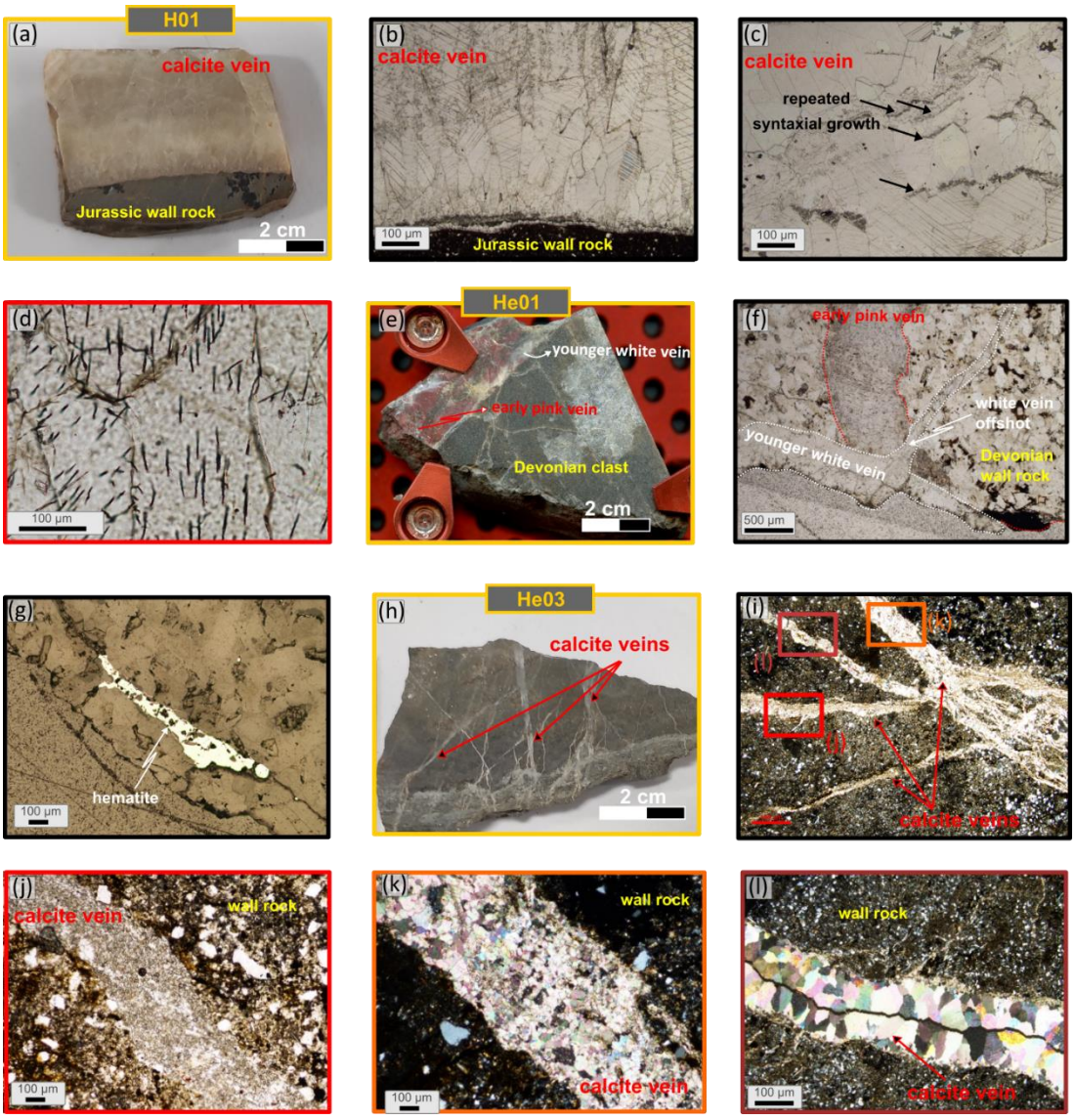

Fig. 5. 31: (a) Polished thick section of the H01 sample. (b-d) representative thin section microphotographs of H01 sample in plane polarised light showing (b) elongated calcite crystals with 'beef-like' textures. Elongation of crystals is normal to tensile fracture walls (c) Repeated syntaxial grain growth preserving evidence for past vugs which are occluded. (d) worm-like inclusions of FeOx or possibly hydrocarbon. (e) Polished thick section of the He01 sample showing the earlier pink calcite veins and later white calcite veins crosscutting the Devonian clast (f-g) representative thin section microphotographs of He01 sample showing (g) the pink veins with irregular margins which are cut by pale white veins with the later calcite fills growing in optical continuity with crystals in older veins (in plane polarised light). (g) Local fresh hematite host in the younger set (in crossed polarised light) (h) Polished thick section of the He03 sample. (i-k) Representative thin section microphotographs of He03 sample (in crossed polarised light) showing (i) at least 3 sets of veins recognised by differences in texture and crosscutting relationships namely (j) early Set i which are thin (<1mm), yellowish, fine-grained, with irregular margins and lack internal structure. (k) Set ii which are whispy, feathered veins with crack-seal textures and mostly white calcite fine sparry fills and (l) Set iii which are coarser sparry white calcite with central open fractures and typically follow earlier Set ii veins.

The H01 sample (Fig. 5.31a) is located in the main outcrop of the Boulder Beds and was collected from a yellow, c. 10 cm thick calcite fill of a

NE-SW-trending vein (Fig. 5.30d). Veins show composite fills defined by grain size and inclusion density changes, with syntaxial growth coarsening inwards to give 'beef-like' textures (Fig. 5.31c). Elongation of crystals is normal to tensile fracture walls (Fig. 5.31b). Some fills show evidence for past vugs, which are occluded, leading to repeated cycles of syntaxial grain growth (Fig. 5.31c), while others are simpler single growths. Some earlier fills host unusual tubular inclusions of FeOx(?) or possibly hydrocarbon(?) (Fig. 5.31d).

The He01 sample (Fig. 5.31e) was collected from a Devonian sandstone boulder within the Boulder Beds (Fig. 5.30e). Early pink calcite veins (only seen in Devonian boulder) are cut by pale white calcite veins, which also cut Boulder Beds matrix; thus pink veins are clearly pre-Jurassic (Fig. 5.31f). The pink veins have notably irregular margins and are everywhere cut by pale white veins with calcite fills in latter growing in optical continuity with crystals in older veins (Fig. 5.31f). The younger set also locally hosts fresh hematite (Fig. 5.31g).

The He03 sample (Fig. 5.31h) is located in the main outcrop of Boulder Beds in NE-SW vein sets. At least three sets of veins are recognised in thin section by differences in texture and cross-cutting relationships (Fig. 5.31i). Early Set i (Fig. 5.31j) are thin (<1mm), yellowish, fine-grained, with irregular margins, and lack internal structure. Set ii (Fig. 3.31k) are whispy, feathered veins with crack-seal textures and mostly white calcite fine sparry fills. Set iii (Fig. 5.31l) are coarser sparry white calcite with central open fractures and typically follow earlier Set ii veins.

5.4.5.3 *Geochronology*

The ^{238}U and ^{206}Pb concentrations were analysed in five samples, but only four samples contained sufficient amounts of ^{238}U (and low enough concentrations of common Pb) to be dated and yielded accurate and precise dates. Those samples coincide with the samples shown in the 'Microscopy' section.

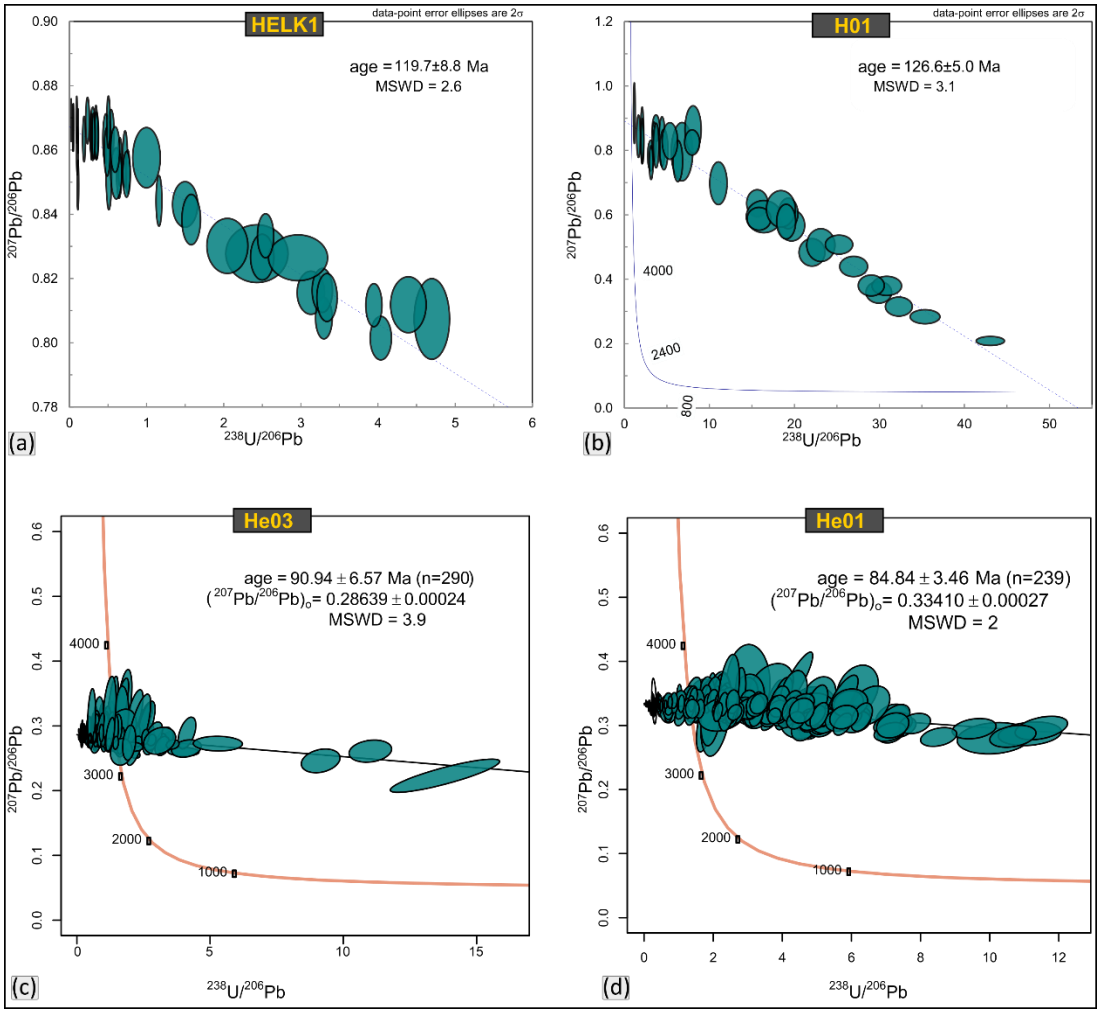

Fig. 5. 32: Tera–Wasserburg diagram of measured in-situ calcite 207Pb/206Pb and 238U/206Pb ratios (no common lead correction) from (a) sample HELK1 yielding a Model I discordia age of 119.7 ± 8.8 Ma (2σ, MSWD = 2.6) (b) sample H01 yielding a Model I discordia age of 126.6 ± 5.0 Ma (2σ, MSWD = 3.1) (c) sample He03 yielding a Model I discordia age of 90.94 ± 6.57 Ma (2σ, MSWD = 3.9). (d) sample He01 yielding a Model I discordia age of 84.84 ± 3.46 Ma (2σ, MSWD = 2). Error ellipsoids of spot analysis are plotted in green and represent 2σ uncertainties. MSWS = mean standard weighted deviation.

For sample HELK1 (Fig. 5.30f), ablation sites followed a calcite vein (Fig. 5.30f). 84 spots were ablated, of which four spots were omitted due to excess common Pb or poor ablation and were plotted on a Tera-Wasserberg

U-Pb plot using IsoplotR, which yielded a $^{238}U/^{206}Pb$ age of 119.7 ± 8.8 Ma (2σ, MSWD = 2.6; Fig. 5.32a).

For sample H01 (Fig. 5.31a), 36 spots were ablated, of which two spots were omitted due to excess common Pb or poor ablation, and were plotted on a Tera-Wasserberg U-Pb plot using IsoplotR, which yielded a $^{238}U/^{206}Pb$ age of 126.6±5.0 Ma (2σ, MSWD = 3.1; Fig. 5.32b).

For sample He03 (Fig. 5.31h), dated veins belong to the youngest Set iii (Fig. 5.31l).

290 spots were ablated and were plotted on a Tera-Wasserberg U-Pb plot using IsoplotR, which yielded a $^{238}U/^{206}Pb$ age of 90.94 ± 6.57 Ma (2σ, MSWD = 3.9; Fig. 5.32c).

For sample He01 (Fig. 5.31e), 239 spots were ablated and were plotted on a Tera-Wasserberg U-Pb plot using IsoplotR, which yielded a $^{238}U/^{206}Pb$ age of 84.84 ± 3.46 Ma (2σ, MSWD = 2; Fig. 5.32d).

5.4.5.4 Interpretation of structural history

The Upper Jurassic succession exposed onshore in the hangingwall of the HF preserves folding, veining and minor faults consistent with oblique-sinistral slip of the HF, as also suggested by previous workers (Thomson 1993). This deformation is commonly attributed to the Cenozoic (e.g. c. 37–26 Ma; Le Breton et al. 2013) post-rift fault reactivation during basin exhumation and erosion.

New fieldwork findings coupled with U-Pb analyses of synfaulting calcite-mineralised tensile veins, spatially associated with HF, yielded dates populations of 126.6 ± 5-119.7 ± 8.8 Ma (Early Cretaceous, Barremian-Aptian Age) and 90.94 ± 6.52 / 84.84 ± 3.37 Ma (Late Cretaceous, Turonian-

Santonian Age). Because the calcite veins cut the folds, it has previously been assumed that they are younger than the folds. However, the hinge-normal orientation of the veins is consistent with near fold hinge-parallel finite extension during transtensional deformation (Venkat-Ramani and Tikoff 2002; De Paola et al. 2005; Fossen 2013). So, the simplest explanation is that the sinistrally transtensional HF, folds and veins are all the same age and the veins are syn-faulting.

These radioisotope ages provide evidence that sinistral shearing and associated deformation along the HF is older than previously thought. Ages can be fitted to observed cross-cutting and contact relationships in the field and thin section since the NE-SW-trending veins are clearly composite.

Early Cretaceous veins (Aptian-Barremian) associated with veins cutting earlier carbonate-cemented HF granite scarp breccia (siderite-bearing) and yellow calcite NE-SW-trending veins plausibly equivalent to Set i seen associated with Late Cretaceous vein sets. These are locally oil-stained and are the same age within error as veins at Whaligoe Steps, Shandwick (see below), and New Aberdour on the south coast associated with dextral reactivation of a NNE-SSW-trending inherited Devonian structure (see Chapter 3). This suggests that the HF had a sinistral normal oblique-slip movement at least during a later stages of regional rifting and not during Cenozoic as had previously been assumed (Thomson 1993; Thomson and Underhill 1993; Hillis et al. 1994; Le Breton et al. 2013).

The oldest pink calcite veins, only found in Devonian boulders, are oil-stained and are cross-cut by white unstained calcite veins dated in the range

ca 91-84 Ma. This Late Cretaceous age is within error of the age obtained from the youngest veins seen at Sarclet (Fig. 5.10d).

5.4.6 Lothbeg [Grid Reference NC 96023 09511]

5.4.6.1 Onshore Fieldwork Observations

This coastal site, of about 1 km in length, is located c. 800 m southeast of Lothbeg village [NC 945 104] (Fig. 5.33a). The Upper Jurassic Alt na Cuile Sandstone exposed here crops out in high cliffs (c. 5 to 30 m hight, e.g. Fig. 4.33b and d) and flat-lying wave-cut platforms accessible only at low tide (Fig. 4.34a). The sandstones are white/yellow coloured, medium-grained, well-sorted and usually form massive (m-think) channelised beds (Fig. 5.33b). In the high cliffs below the railway line (Fig. 5.33d), the sandstone beds are interbedded with dark grey, locally slumped, siltstones and shales. The Allt na Cuile sequence, which is overall sandstone-dominated and clearly different from the laterally equivalent 'Boulder Beds', suggests a different depositional environment that previous workers attributed to a submarine channel deposit (e.g. Pickering 1984; MacDonald and Trewin 2009).

The stratigraphy is cross-cut by two dominant sets of brittle structures (faults and fractures; Fig. 5.33c). The dominant set are ESE-WNW-trending shallowly to steeply dipping (12^{o}-79^{o}) generally to the SSW, and the second set are ENE-WSW-trending shallowly to moderately (14^{o} -41^{o}) dipping to the SSE.

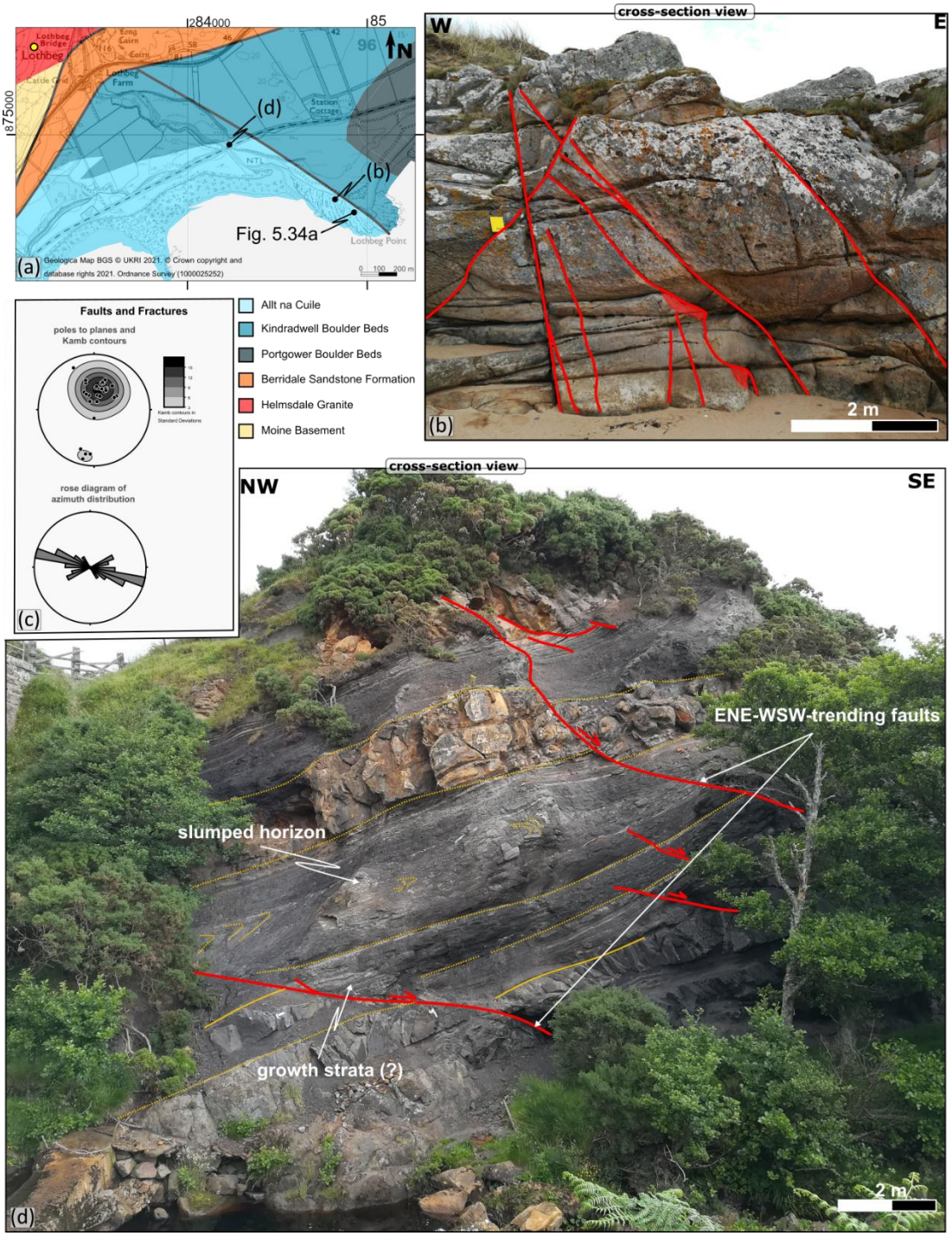

Fig. 5. 33: (a) Geological map of Lothbeg area (using EdinaDigimap service) showing the location of b, d and Fig. 5.34a. (b) Field photograph of the upper Jurassic Alt na Cuile sandstone exposed in a c. 5 m hight cliffs showing the typical channelised beds of white/yellow coloured sandstone, which are crosscut by ESE-WNW-trending faults. (c) Stereonets and rose plots of structural data collected in the field. Lower hemisphere, equal-area projections. (d) High cliffs exposure, bellow the rail line, where the sandstone beds are interbedded with dark grey, locally slumped, siltstones and shaly intervals. Note the slumped interval mid-section and the low-angle ENE-WSW-trending faults.

The ENE-WSW-trending faults are best observed in the cliffs below the rail line, where they cut the stratigraphy at low-angle (Fig. 5.33d). The faults have at least a component of dip-slip displacement judging by the normal

offsets of bedding (Fig.5.33d). Some of these faults appear to be growth features as wedging of sedimentary units is observed in the hangingwall (Fig. 5.33d).

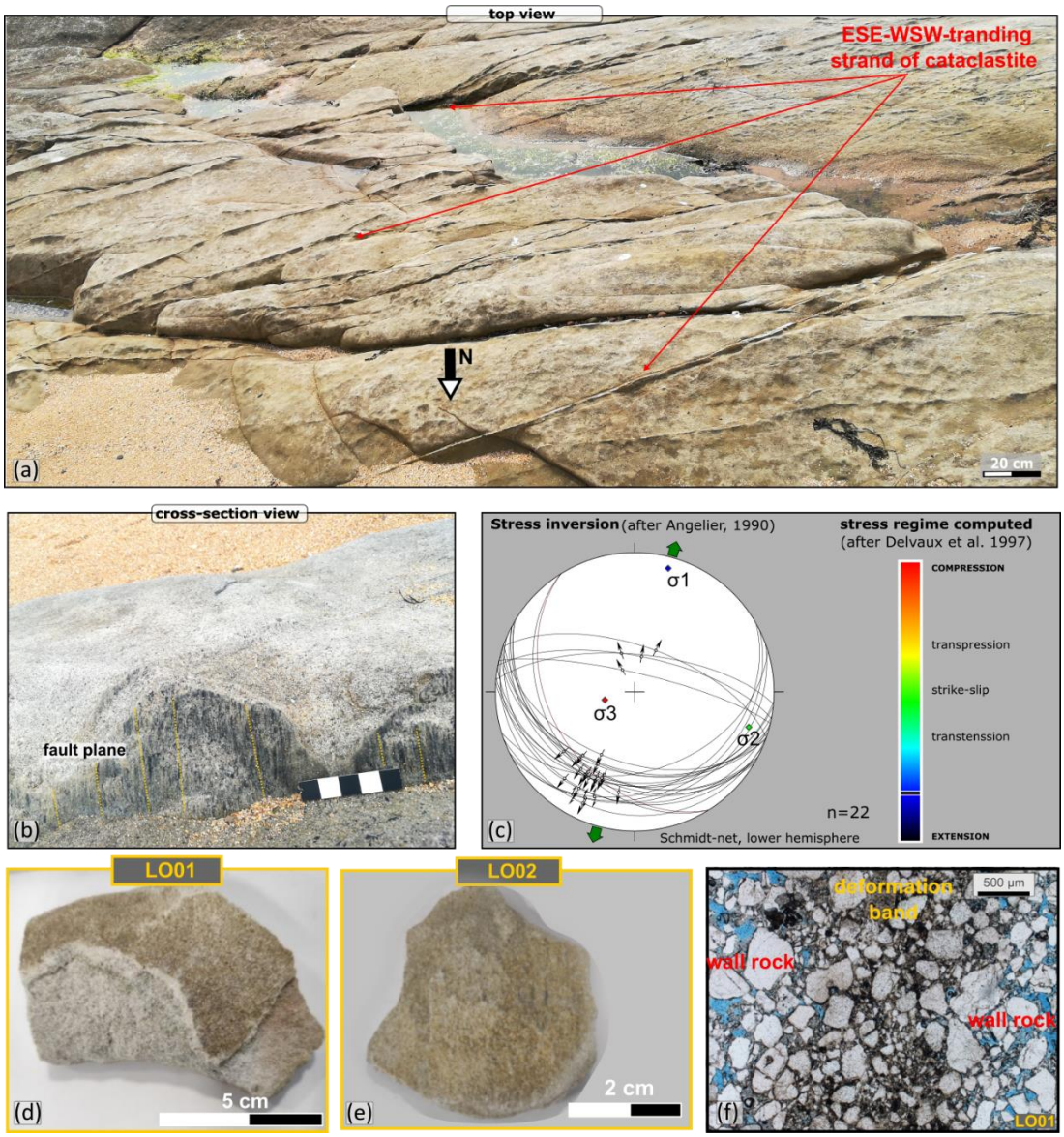

Fig. 5. 34: (a) Field photograph of the upper Jurassic Alt na Cuile sandstone exposed in flat-lying platform showing the ESE-WNW-trending strands of well-cemented deformation bands which are forming an up to 50 m wide ESE-WNW-trending damage zone. (b) Detailed field photograph of a slip plane showing dip-slip lineations. (c) Stress inversion plot (after Angelier 1990) of fault lineation data. (d and e) Hand specimens of the LO01 and LO02 samples of the deformation bands. (f) Representative thin section microphotographs of the deformation bands (in plane polarised light) showing the undeformed host sandstone dominated by sub-angular quartz grains (90%) and the cataclastic finer-grained deformation bands.

In the sandstone-dominated coastal cliffs (Fig. 5.33b) and flat-lying wave-cut platform (Fig. 5.34a), numerous strands of well-cemented deformation bands form an up to 50 m wide ESE-WNW-trending damage zone. The cataclastic deformation bands here are easily recognisable in the

field due to their resistance to weathering (Fig. 5.34a and b). The individual deformation bands within the damage zone are dominantly ESE-WNW-trending, shallowly dipping to the SSW, but ENE-WSW-trends are also common (Fig. 5.34c). The cataclastic deformation bands are 1-10 mm wide but commonly form amalgamated sets c. 10-15 cm thick. They are widely associated with slip surfaces accommodating small (mm to cm) normal offsets.

Exposed slip surfaces on the ESE-WNW-trending bands preserve steeply dip-slip lineations (pitch 85 E in Fig. 5.34b), while the ENE-WSW-trend are slightly oblique-dextral (Fig. 5.34c). A palaeostress inversion analysis of the slickenline lineations associated with these deformation bands yields an NNE-SSW extension direction (Fig. 5.34c). The faults were developed in a normal faulting regime with a near-horizontal sigma 3 axis orientated 11°/016° and near-vertical sigma 1 axis orientated 71°/250° (Fig. 5.34c).

5.4.6.2 Microscopy

Two samples of sandstone with deformation bands (Lo1 and Lo2; Fig. 4.34d and e) have been selected for microscopic study. Both are from ESE-WNW-trending dip-slip bands.

As both LO01 (Fig. 4.34d) and LO02 (Fig. 4.34e) samples show identical characteristics, they are presented together. Thin sections show that the undeformed host sandstone is dominated by sub-angular quartz grains (90%) with subordinate feldspar and metamorphic clasts (mostly mylonitic quartzites) (Figs 5.34 and 5.35a, b). Wall rock porosities are very high (>20%), with relatively sparse matrix present. Deformation bands are clearly cataclastic (Fig. 5.34e) and preserve examples of sheared clasts (Fig. 5.34f). Deformation

bands are slightly finer-grained, with more angular clasts and a zeolite + fine Fe Oxide cemented microporous matrix with many small angular grains (Fig. 5.35c-f). The effects of cataclasis related to the deformation bands lead to significant and variable degrees of grain size reduction, compaction, and cementation typical of such features (e.g. see Underhill and Woodcock 1987; Fossen et al. 2007). These processes lead to large decreases in visible porosity to (e.g. Fig. 5.34f).

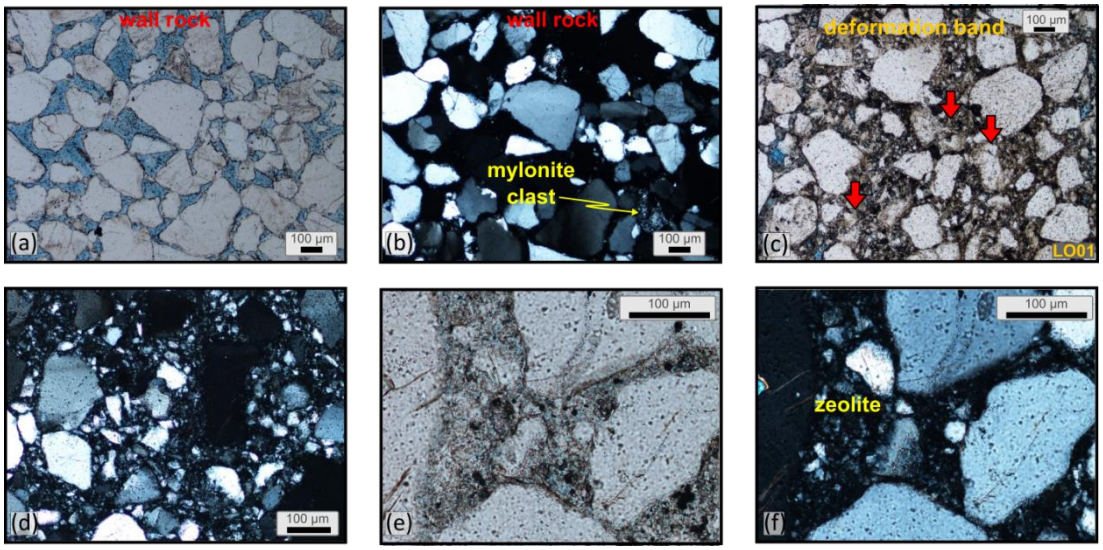

Fig. 5. 35: (a- in plane polarised light, and b- in cross polarised light) Thin section microphotographs of undeformed host sandstone which is dominated by sub-angular quartz grains (90%) with subordinate feldspar and metamorphic clasts (mostly mylonitic quartzites). Wall rock porosities are very high (>20%), with relatively sparse matrix present. (c-f) Thin section microphotographs of the deformation bands which are clearly cataclastic, note sheared clasts in (c). Deformation bands are slightly finer-grained, with more angular clasts and (e-f) zeolite + fine Fe Oxide cemented microporous matrix with many small angular grains.

5.4.6.3 Interpretation of structural history

Two types of faults are present at Lothbeg, possibly related to two different deformation events. The ENE-WSW-trending low-angle (possibly) syn-sedimentary faults visible in the cliffs under the railway line (Fig. 5.33d) could represent subsidiary faults to HF, developed during Late Jurassic – Early Cretaceous.

The dip-slip strand of ESE-WNW-trending deformation bands correlates well with similarly trending (inferred) Cenozoic normal faults seen

offshore in the Beatrice 3D seismic reflection dataset (see Chapter 4, Figure 4.14c-f). Stress inversion of fault slickenline data associated with these deformation bands suggests a NNE-SSW-directed extension. This correlates well with the NNE-SSW extension direction based on the offshore normal faults developed during Cenozoic (see Chapter 4, Figure 4.14e). Likewise, it also correlates with the NNE-SSW-directed extension, which resulted in the oblique dextral reactivation of the E-W to ENE-WSW trending faults and the development of other minor dip-slip NW-SE-striking faults onshore on the southern coast of IMFB (see Chapter 4, 4.16a for more details). It is therefore concluded that the microfaults at Lothbag developed during the Cenozoic and are related to the Cenozoic dextral reactivation of the GGF. However, these structures are not associated with calcite mineralisation hence no U-Pb-dating was perform at this location to validate their timing.

5.4.7 Shandwick [Grid Reference NH 85286 73203]

5.4.7.1 Onshore Fieldwork Observations

The studied exposure lies c. 200 m south of Shandwick village [NH 857 745] (Fig. 5.36a and b) and extends c. 1 km from Port-an-Righ towards the north (Fig. 5.36b). Here the Upper Jurassic rocks form a narrow strip in the wave-cut platform, which is exposed at low tide, downfaulted to the SE against the middle Devonian Raddery Sandstone Formation to the NW (Fig. 5.36a and b). This NNE-SSW striking fault, juxtaposing the Upper Jurassic against the middle Devonian is widely viewed as a splay of the GGF.

The middle Devonian in the footwall of the GGFS consists of gently NE-dipping (20^{o}-30^{o}) thin-bedded (5 -20 cm) dark red sandstones, which are fine-grained and very well cemented. The Devonian rocks are poorly exposed in

the section illustrated in this study, but extend to the north and south of the study area, forming extensive rock platforms and high cliffs.

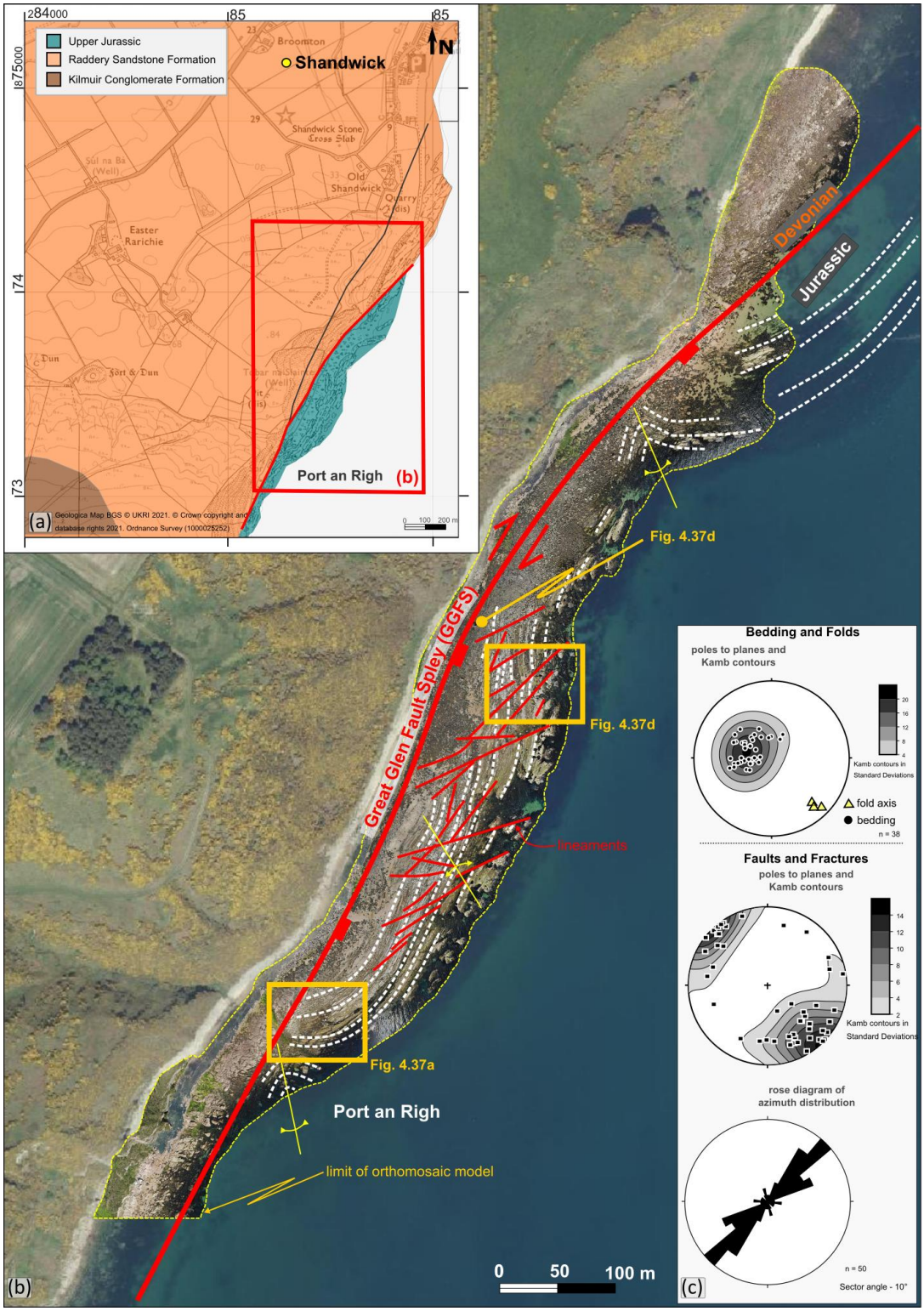

Fig. 5. 36: (a) Geological map of Shandwick area (using EdinaDigimap service) showing the location of (b) - orthomosaic model obtained from UAV (Unmanned Aerial Vehicle) photography overlapped on aerial map (using EdinaDigimap service © Getmapping Plc) of the studied exposure showing the main structural trends. Location of Fig. 5.37a, b and d are indicated on (b). (c) Stereonets and rose plots of structural data collected in the field. Lower hemisphere, equal-area projections.

The Upper Jurassic rocks exposed in the hangingwall of the GGF splay belong to stratigraphic members of Brora argillaceous (Shandwick Clay Member), Brora arenaceous (Shandwick Siltstone Member) and Balintore formations (Port-an-Righ Ironstone and Siltstone members) (Riding 2015 and references therein).

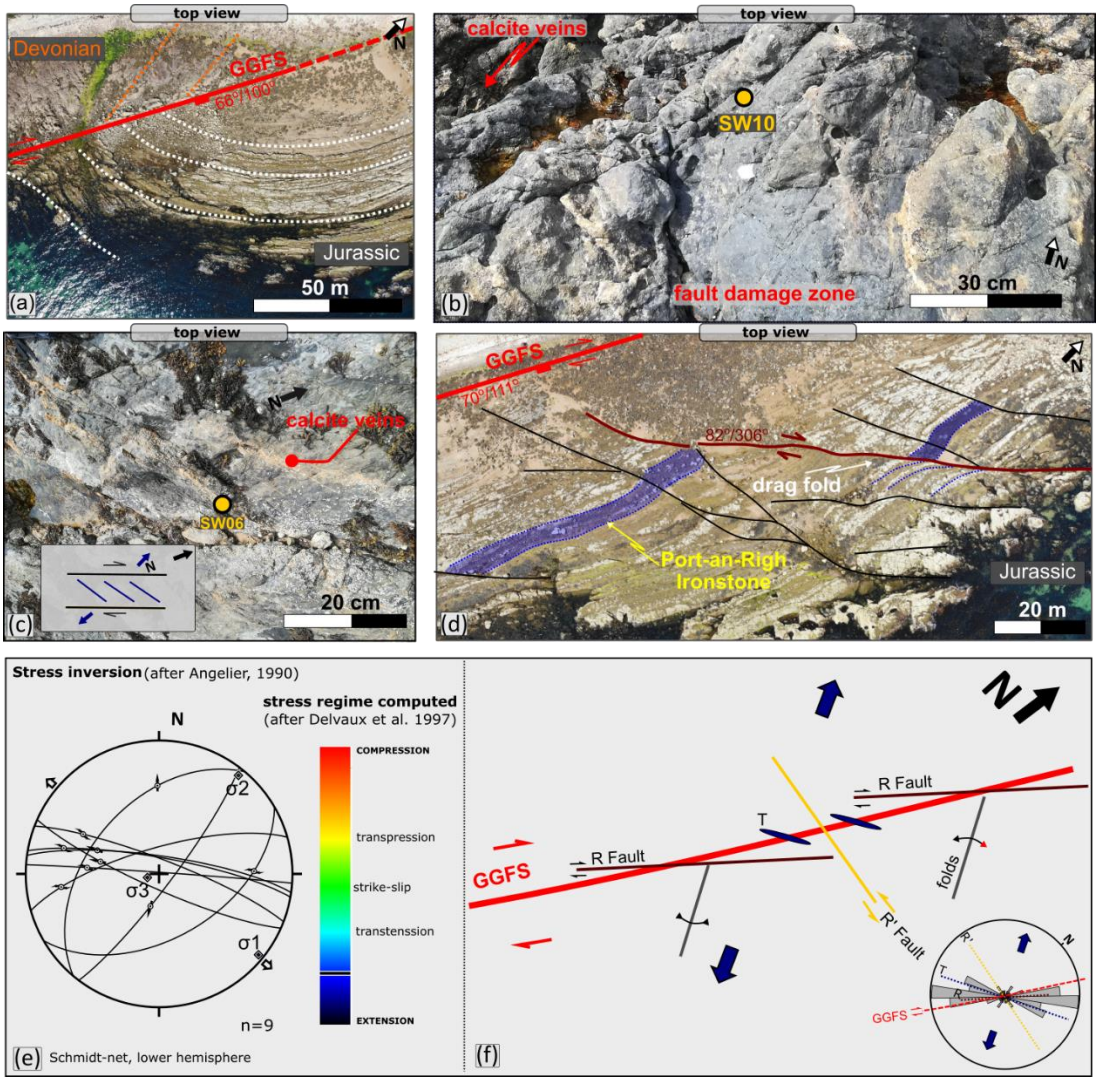

Fig. 5. 37: (a) Drone photograph of the southern section of the GGFS at Port an Righ (see location on the Fig. 5.36b). (b) Field photograph of the locally preserved damage zone associated with the GGFS. Location of sample SW10 is also indicated. (c) Field photograph and inset sketch of the en-echelon calcite-mineralised tensile veins associated with the dextral slip of the GGFS (d) Drone photograph showing a dextral high-angle fault, displacing the Port-an-Right Ironstone, most likely representing a synthetic Riedel shear to the GGFS (e) Stress inversion plot (after Angelier 1990) of fault lineation data. (f) Interpreted array of structures identified at Shandwick in map view and inset Rose diagram of azimuth distributions. Structures are colour coded in both sketch and rose diagram as follows: dashed red – main (GGFS) fault; dark red – synthetic Riedels (R); yellow - antithetic Riedels (R'); blue – tensile (T) fractures. GGFS – Great Glen Fault splay.

The strata consist of cm- to dm-thick, grey/green-coloured mudstones, sandstones, and limestones rich in marine fossils (e.g. ammonites, large

bivalves), generally accumulated in a distal shelf environment (Stephen et al. 1993; Riding 2015).

A very distinct layer comprising c. 2-2.5 m of thin-bedded (10-20 cm) red-weathered fossiliferous limestones interbedded with grey mudstone and siltstones can be locally observed in the succession. These ferruginous bands are known as Port-an-Righ Ironstone maximum flooding surface (Stephen et al. 1993; Riding 2015; Duxbury and Vieira 2018) and represent a condensed marine section of nodular glauconitic limestone, rich in ammonites (e.g. Sykes 1975; Stephen et al. 1993;). This distinctly red-coloured stratigraphic marker aids in identifying fault displacement senses, where this layer is offset.

The Upper Jurassic beds are shallow to moderately dipping (c. 12º-47°), generally to SE (Fig. 5.36c). However, on the orthomosaic map, large folds (tens of meters scale) are visible on the wave-cut platform adjacent to the GGF splay (Fig. 5.36b). The folds are gentle (interlimb angle c. 140º), upright folds (axial plane 046º/83º) shallowly plunging (10º-23º) to SE (Fig. 4.36c).

The GGF splay, as documented by previous workers (e.g. Underhill and Brodie 1993; Le Breton et al. 2013), generally trends NNE-SSW (Figs. 5.36b and 5.37a, b). There is no main fault plane observed, but rather a c. 2-5 m wide locally exposed fault zone, which is highly fractured and shows multiple cataclastic bends and calcite-mineralised slip planes (Fig. 5.37b). The subsidiary faults in the fault zone, trending parallel to the main fault zone, are generally steeply dipping (56º to 70º) to the WSW. One sample (SW10) was collected from such mineralised slip plane for microstructural study and possible dating. Throughout the Upper Jurassic, other steeply dipping to sub-

vertical calcite veins occur. Some are mm to cm wide, ENE-trending tensile veins, suggesting NNW-SSE extension direction (Fig. 5.37c and inset). Other, more NE-SW-trending, offset the Upper Jurassic strata in a right-lateral sense, having cm- to m-scale displacements. On one occasion, a 60 m dextral offset is observed, where the fault is displacing the Port-an-Right Ironstone (Fig. 5.37d). These dextral faults strike at c. 10°-25° to the GGF splay structure. Striated minor faults trending ESE-WNW, and dipping between 56° and 88°, show oblique-sinistral kinematics (pitch between 28-50 W). These oblique-sinistral faults strike at c. 80° to the GGFS.

All these minor dextral, sinistral faults, tensile veins, and folds seem genetically related to the GGF splay fault. They most likely represent a well-developed Riedel shear system associated with the dextral displacement along that structure (Fig. 5.37f) developed during NNW-SSE-directed extension. The NE-SW-trending dextral faults striking sub-parallel to the GGFS are interpreted as synthetic Riedel shear faults (R), while the ESE-WNW-trending oblique-sinistral faults are interpreted as antithetic Riedel shear faults (R')(Fig. 5.37f). The ENE-trending tensile veins and the SE plunging folds are also consistent with this kinematic model (Fig. 5.37f). A stress inversion analysis of the slickenlines associated with these minor faults yields a WNW-ESE extension direction (Fig. 5.37e). This extension direction is slightly offset then the inferred extension direction based on the orientation of the Riedel shear structures, and can reflect the limited input data which is dominated by the antithetic faults.

5.4.7.2 Microscopy

The SW06 sample (Fig. 5.48a) is a NE-SW-trending, white calcite-filled tensile vein (Fig. 5.37c) cutting the Upper Jurassic sequence a few metres SE of the GGF splay fault. The thin section reveals a blocky sparry calcite vein cutting siltstone with irregular margins and a poorly developed syntaxial growth pattern (Fig. 5.38b and c.).

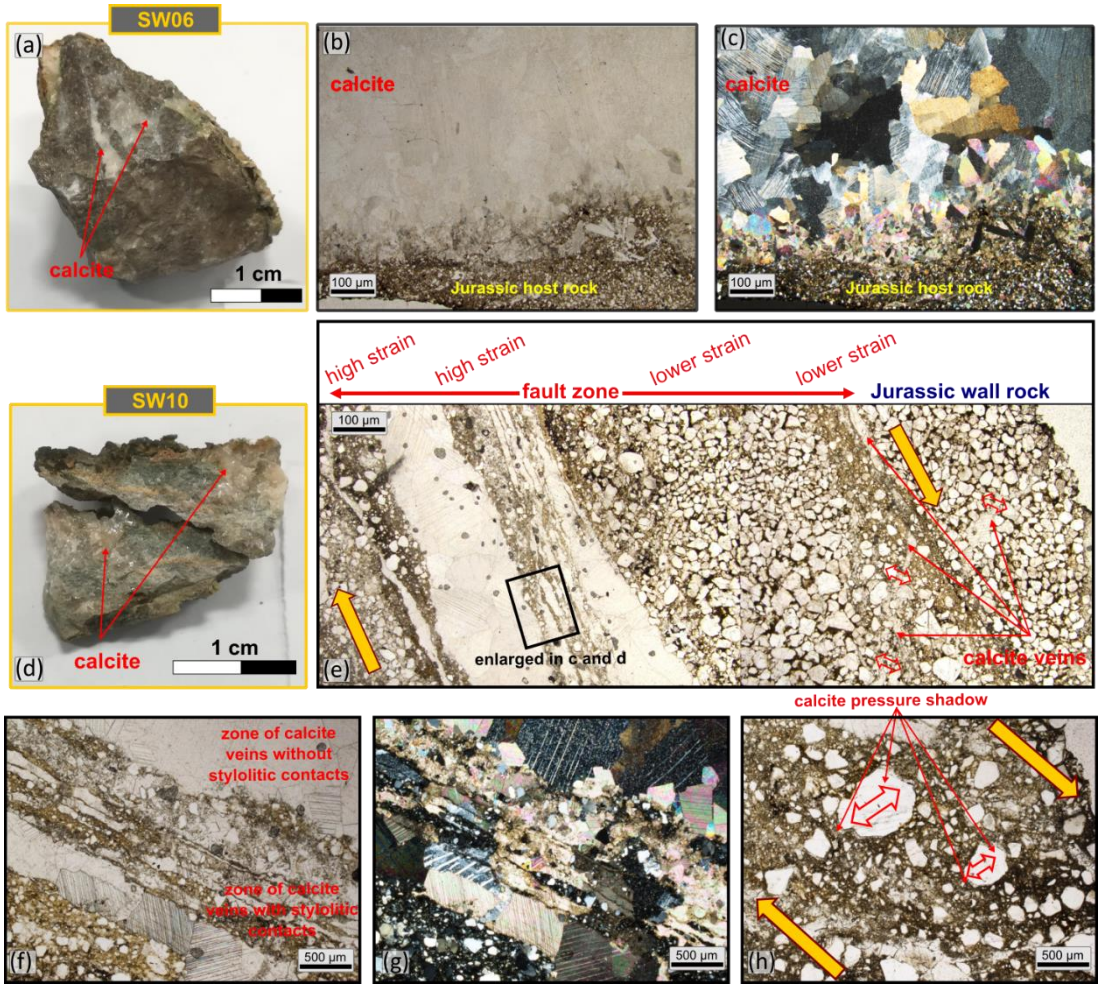

Fig. 5. 38: (a) SW06 hand specimen from a NE-SW-trending calcite vein (b-c) representative thin section microphotographs showing a blocky sparry calcite vein with irregular margins and a poorly developed syntaxial growth pattern. (d) SW10 hand specimen collected from the GGFS fault zone (e-h) representative thin section microphotographs showing (e) calcite veins which both pre-date and post-date faulting and are kinematically consistent with dextral shear (tensile jogs). (f-g) Earlier veins are cataclastically deformed and show stylolitic contacts, while the later veins are without stylolitic contacts developed in high strain areas (h) clasts in high strain regions which show obliquely oriented calcite pressure shadows. GGFS – Great Glen Fault splay.

The SW10 sample (Fig. 5.38d) comes from a NNE-SSW-trending minor fault within the main dextral normal fault zone (Fig. 5.37b) that juxtaposes Devonian rocks in its western footwall with Upper Jurassic rocks in its eastern

hangingwall (Fig. 5.36) thought to be a splay of the GGF. The veins seen in the thin section both pre-date and post-date faulting and are kinematically consistent with dextral shear (tensile jogs) (Fig. 5.38b). Earlier veins are cataclastically deformed and show stylolitic contacts, while the later veins are without stylolitic contacts (Fig. 5.38e, f and g) developed in high strain areas (Fig. 5.38e). They are consistent with fault-normal compaction, whilst clasts in high strain regions have obliquely oriented calcite pressure shadows consistent with dextral shear (Fig. 5.38h)

5.4.7.3 Geochronology

The ^{238}U and ^{206}Pb concentrations were analysed in both SW06 and SW10 samples, containing sufficient amounts of 238U (and low enough concentrations of common Pb) to be dated. They yield an accurate and precise date.

For sample SW06, 46 spots were ablated and were plotted on a Tera-Wasserberg U-Pb plot using IsoplotR, which yielded a $^{238}U/^{206}Pb$ age of 121.6 ± 14.42 Ma (2σ, Pbinitial = 0.30501±0.00041, MSWD = 2.2; Fig. 5.39a).

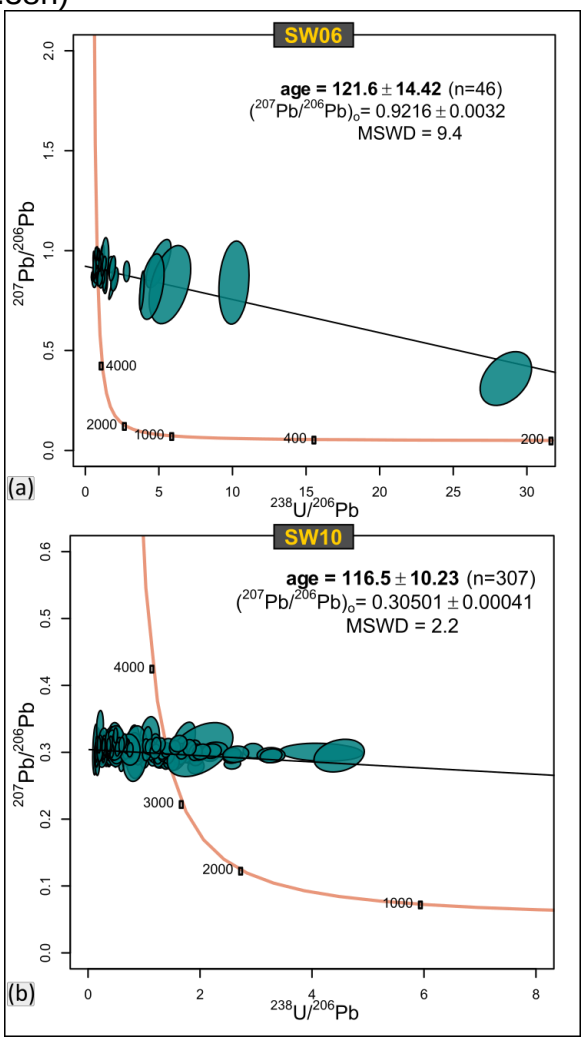

Fig. 5. 39: Tera–Wasserburg diagram of measured in-situ calcite 207Pb/206Pb and 238U/206Pb ratios (no common lead correction) from (a) sample SW06 yielding a Model I discordia age of 121.6 ± 14.42 Ma (2σ, MSWD = 9.4) (b) sample SW10 yielding a Model I discordia age of 116.5 ± 10.23 Ma (2σ, MSWD = 0.11). Error ellipsoids of spot analysis are plotted in green and represent 2σ uncertainties. MSWS = mean standard weighted deviation

For sample SW10, 307 spots were ablated and were plotted on a Tera-Wasserberg U-Pb plot using IsoplotR, which yielded a $^{238}U/^{206}Pb$ age of 116.5 ± 10.23 Ma (2σ, Pbinitial = 0.26263±0.00096, MSWD = 2.2; Fig. 5.39b).

5.4.7.4 Interpretation of the structural history

The NNE-SSW-trending splay of the GGF is associated with a well-developed Riedel shear system suggesting dextral slip under NNW-SSE extension direction (Fig. 5.37f). The SE-trending folds formed during the same time, but at an earlier stage as they are displaced locally by some on the Riedels (Fig. 5.37d).

The calcite veins and mineralisation are demonstrably synchronous with dextral movements along the NNE-SSW splay of the GGF. There is good textural evidence of cataclasis and solution-precipitation creep during fault movements (Fig. 5.38e). These observations agree with previous studies, which suggest dextral slip on this fault (e.g. Jonk 2003; Le Breton et al. 2013). However, both samples, one in the fault zone and one from the tensile vein, which cuts the Upper Jurassic host rocks yield Early Cretaceous (Aptian) ages. The calcite veins are within error of the ages obtained from Helmsdale (earlier set), Whaligoe Steps (main set) and New Aberdour (see Chapter 3). As also seen at Helmsdale, this timing is earlier than the Cenozoic timing previously proposed for the movement of this fault (e.g. early Tertiary, Underhill and Brodie 1993; Le Breton et al. 2013). This suggests that the GGF splay formed in the Early Cretaceous as a synthetic Riedel to the GGF during (possible minor) dextral movement at a later stage of basin rifting and prior to the more significant Cenozoic dextral slip estimated at c. 30 km due to the offset of the Cenozoic dykes (Holgate 1969) during tilting and uplift of the basin. During this

stage this splay was abandoned, and the deformation was accommodated more offshore in the IMFB.

4.5. Summary and conclusions

The northeastern coast of the IMFB records a complex structural history due to multiple faulting episodes with associated local reactivation of structures.

The new U-Pb analyses of synfaulting calcite-mineralised veins proved to be a very successful tool as c. 75% of the samples contained sufficient amounts of ^{238}U (and low enough concentrations of common Pb) and returned accurate results. This provided a unique opportunity to assess the absolute timing of faulting and improved understanding of the complex tectonic history of the region.

The geochronology results yielded date populations of:

- c. 258 - 255 Ma (Lopingian, Late Permian; Sarclet)

- c. 148 – 142 Ma (Berriasian – Tithonian, Late Jurassic – Early Cretaceous; Berridale)

- c. 127 - 117 Ma (Barremian-Aptian, Early Cretaceous; Whaligoe Steps, Helmsdale, Shandwick)

- c. 96 - 84 Ma (Cenomanian-Santonian, Late Cretaceous; Helmsdale, Sarclet).

- c. 32 Ma (Rupelian, Early Oligocene; Whaligoe Steps)

- c. 1.6 – 2.7 Ma (Piacenzian - Calabrian, Pliocene – Pleistocene; Dunbeath)

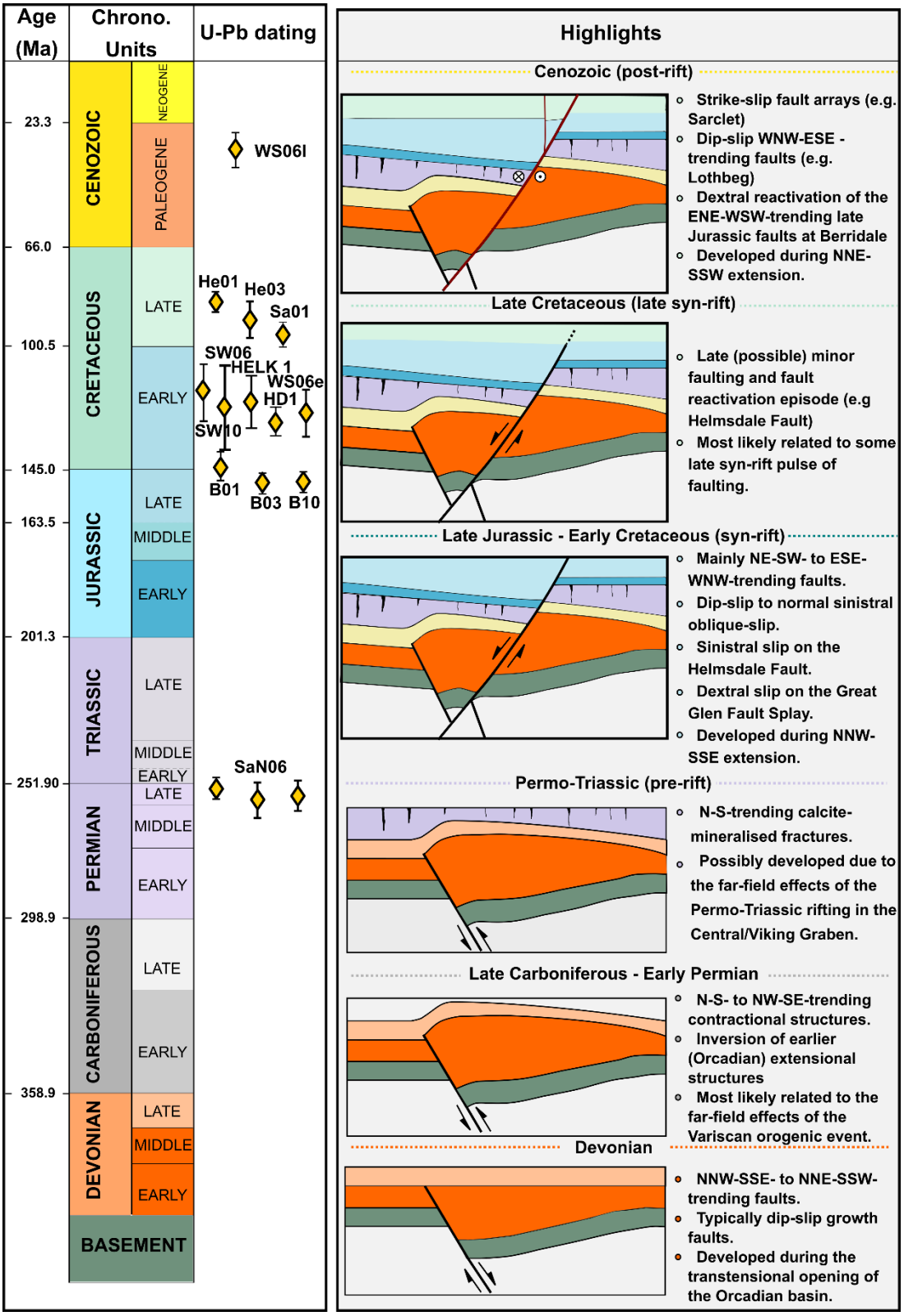

Fig. 5. 40: Summary of deformation history observed on the north-western coast of the IMFB.

The integration of geochronology results with microscopy and detailed field observations augmented with drone photogrammetry allowed up to six

deformation events to be identified, characterised and correlated with regional events elsewhere, summarised in Figure 5.40:

- **Devonian rifting**

Generally characterised by dip-slip NNW-SSE-trending faults, occasionally showing growth packages in their hangingwall. Faults with such orientation and kinematics have been wildly documented across the Orcadian basin, from Caithness and Orkney in the north (see Dichiarante et al. 2021 Group 1 structures and references therein). These structures are associated with the transtensional opening of the earlier Orcadian Basin.

Permo - Carboniferous (Variscan) **inversion**

Characterised by N-S-trending folds and thrusts. The compressional structures commonly reactivate earlier (Devonian rift-related faults) extensional structures, including low-angle decollement planes. Overall, these structures are interpreted as the result of a Late Carboniferous–Early Permian east-west inversion possibly related to dextral strike-slip reactivation of the Great Glen Fault (e.g. Coward et al. 1989; Seranne 1992; Watts et al. 2007; Wilson et al. 2010; Dichiarante et al. 2020, 2021). These structures were named Group 2 by Dichiarante et al. (2021).

Late Permian minor fracturing

This event is associated with N-S-trending calcite mineralised tensile veins. Calcite dating yielded an absolute U-Pb date of c. 258 - 255 Ma (Late Permian age). These fractures are possibly related to the early rifting event in the Central/Viking graben of the North Sea or formed as a result of Permian

NW–SE extension related to the opening of the offshore West Orkney Basin as in the northern Caithness (Group 3 structures; Dichiarante et al. 2021).

Late Jurassic – Early Cretaceous rifting

This faulting episode was documented in both Devonian strata and Jurassic strata at Helmsdale and Shandwick, where the major Helmsdale fault and the splay of the Great Glen Fault crop out, respectively. The structures are typically dip-slip to normal-sinistral oblique E-W to NE-SW-trending faults as well as dextral NNE-SSW-trending. Most of these faults and fractures are widely associated with syntectonic calcite mineralisation, which could be dated. The cluster of dated structures ranges between c. 148 and c. 117 Ma and lies within the main stage of the opening of the North Sea, including IMFB.

Late Cretaceous

This dated episode may be the onshore expression of a late syn-rift pulse of faulting. This event could be a minor late rifting episode prior to the basin uplift and inversion.

Cenozoic

This faulting episode was nowhere confirmed by calcite dating, however several structures recognised onshore can be attributed to this event. These generally include strike-slip fault arrays, including dextrally reactivated syn-rift structures, as well as WNW-ESE-trending dip-slip fault. These structures are usually associated with Fe-oxides mineralisation. These faults are most likely related to the dextral reactivation of the GGF.


Chartwell

Chapter 6

Conclusions and Way Forward

6.1 Highlights

- The regional sinistral transtensional development of the Orcadian Basin recognised in the northern part of the basin proposed by Wilson et al. (2010) and Dichiarante et al. (2020, 2021) can be extended southwards beneath the IMFB and into the Central Highlands.
- Permo-Triassic basin development in the IMFB was not associated with active faulting (at least at a scale visible on seismic reflection data). The basin at this time was most likely characterised by sag-like regional subsidence and passive infilling of a pre-existing Variscan palaeotopography.
- Seismic interpretation studies offshore and U-Pb dating of syn-faulting carbonate mineralization onshore suggest that the IMFB rifting episode and fluid flow, although more significant during the Late Jurassic - Early Cretaceous, most likely extended until the Late Cretaceous (c. 96 - 84 Ma (Cenomanian-Santonian).
- The syn-rift fault patterns are complex due to oblique kinematics, reactivation, and possibly strain partitioning of regional transtensional deformation events, with strike-slip and oblique-slip and dip-slip faults recognised both onshore and offshore.
- A significant proportion of the dextral Great Glen Fault movement and all of the (normal oblique) sinistral Helmsdale Fault movement are NOT Cenozoic features. Instead, they appear to be Lower Cretaceous based on the U-Pb dating of syn-tectonic calcite fills.

- Dextral reactivation of the Orcadian rift-related faults during the Early Cretaceous has been recognised onshore and (inferred) offshore and is also confirmed by the calcite dating onshore.
- The main rift-related deformation extends beyond the Banff Fault in the southern part of the IMFB and the Helmsdale Fault in the north-western area.
- Cenozoic deformation is widespread onshore and offshore, but perhaps not very intense. It is likely linked to the reactivation of the GGF and extends to the southern margins of the IMFB due to the reactivation of the syn-rift structures. Hence, is not simply limited to the north-western shore, close to the Great Glen Fault Zone.

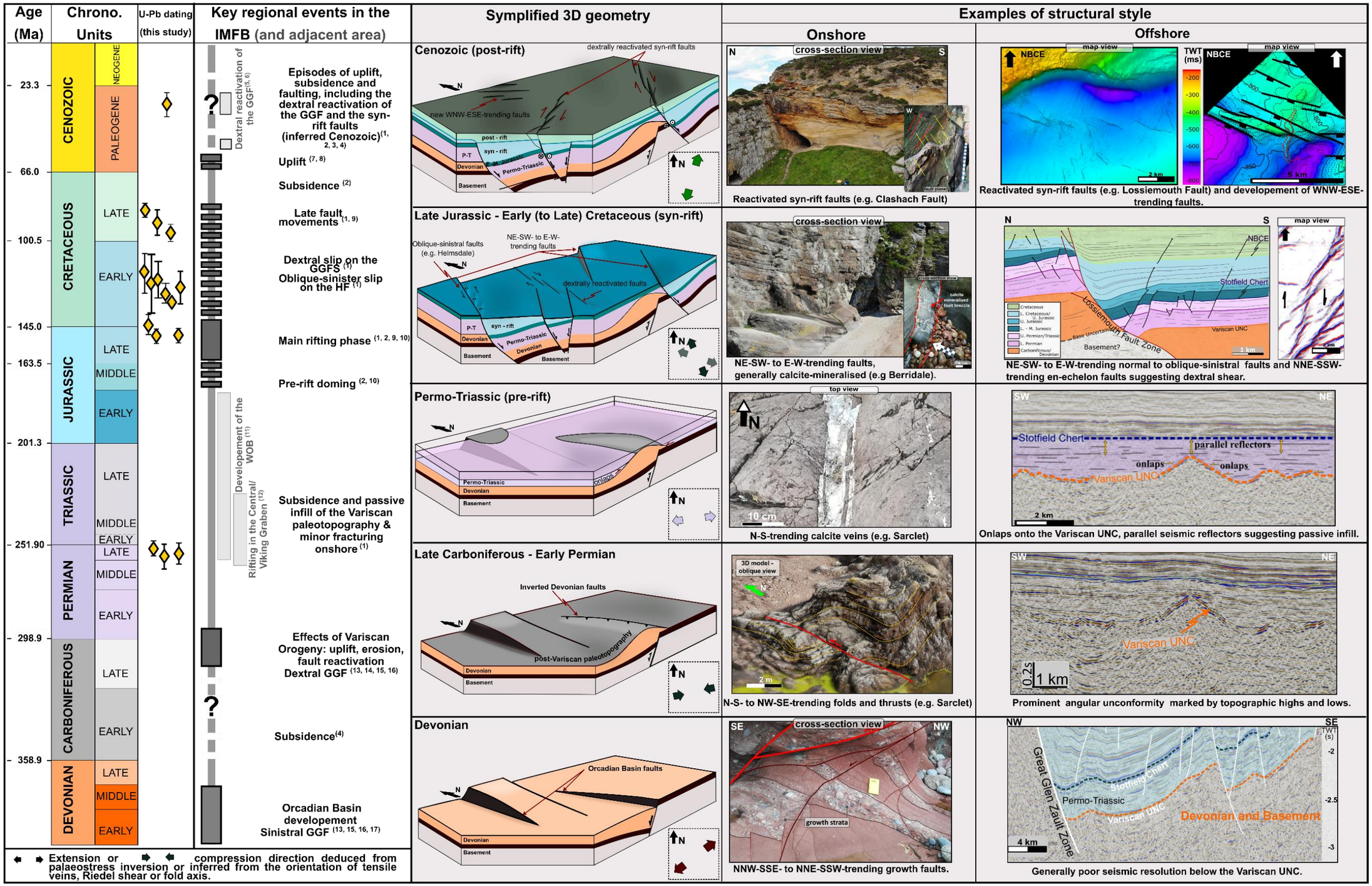

Fig. 6. 1: Summary of the superimposed basin development and associated structural style in the onshore and offshore regions. The key regional events are after [1] the results of this study compiled with [2]Underhill 1991a, [3]Thomson and Hillis 1995, [4]Zanella and Coward 2003; [5]Le Breton et al. 2013; [6]Holgate 1969; [7]Argent et al. 2002, [8]Hillis et al. 1993 [9]Andrews et al. 1990; [10]Davies et al. 2001; [11]Bird 2014; [12]Bell et al. 2014; [13]Seranne 1992; [14]Parnell et al. 1998; [15]Wilson et al. 2010; [16]Dichiarante et al. 2021; [17]Dewey and Strachan 2003. HF – Helmsdale Fault, GGF- Great Glen Fault, GGFS – Great Glen Fault splay, WOB – West Orkney Basin

6.2 Conclusions and summary

In this study, the onshore field observations were combined with the offshore interpretation of selected 2D and 3D seismic reflection data, and coupled with the thin section study of onshore fault rocks and U-Pb geochronology of syn-kinematic calcite veins or cements.

This holistic approach proved very effective in shedding new light on the nature, age, and significance of regional to local deformation events in the complex evolution of the Inner Moray Firth Basin (IMFB) and suggested the following deformation history, summarised in Figure 6.1.

6.2.1 Devonian rifting

The earliest event identified in the study area is demonstrably Devonian based on the widespread preservation of the onshore growth faulting, especially at Pennan (Fig. 6.1). This event is characterised by the development of dip-slip to oblique-sinistral, non-mineralised faults predominantly striking NNW-SSE to NNE-SSW. Palaeostress inversion analyses suggest that they developed during ENE-WSW extension. In the offshore, the Devonian succession has a limited resolution (Fig. 6.1) with low amplitude and low continuity of the seismic reflectors. The structures are difficult to map, hence the onshore outcrops are the key to understanding the structural setting and style in detail.

Faults with such orientation and kinematics have been wildly documented across the Orcadian basin, from Caithness and Orkney in the north (see Dichiarante et al. 2021 Group 1 structures and references therein) to the north-western coast of the IMFB (see Chapter 5) and in the south (see Chapter 3). These faults are thought to be associated with the sinistral transtensional

opening of the Orcadian basin during the Early-Middle Devonian (Seranne 1992; Dewey and Strachan 2003; Watts et al. 2007; Wilson et al. 2010; Dichiarante et al. 2021).

6.2.2 Permo - Carboniferous (Variscan) inversion

This event has been locally documented onshore on the north-western coast on the IMFB (e.g. Sarclet, Berridale) and is characterised by N-S- to NW-SE-trending contractional structures (folds and thrusts) showing a transport direction dominantly to the WNW. The compressional structures commonly reactivate earlier (Devonian rift-related faults) extensional structures, including low-angle decollement planes. Similar onshore structures have been previously observed within the Orcadian Basin, from the Scottish mainland to Orkneys and Shetland islands (e.g. Einfield and Coward 1987; Underhill and Brodie 1993; Parnell et al. 1998; Armitage et al. 2020; Dichiarante et al. 2020, 2021). They have been generally interpreted to have formed due to a Late Carboniferous - Early Permian east-west inversion event possibly related to dextral strike-slip reactivation of the Great Glen Fault (e.g. Coward et al. 1989; Seranne 1992; Watts et al. 2007; Wilson et al. 2010; Dichiarante et al. 2020, 2021), possibly a far-field effect of the Variscan orogenic event. These structures were named Group 2 by Dichiarante et al. (2021). It is very likely that the compressional structures observed in Devonian strata of the IMFB are part of the same Group 2 structures of Dichiarante et al. (2021).

In the offshore, this event left a prominent erosion surface (Variscan unconformity), marked by a strong seismic reflector at the boundary between the Devonian and Permian units (Fig. 6.1). This surface displays major topographic variations, which most likely represent Devonian rift shoulders or

hangingwall anticlines formed due to the Variscan inversion of the Devonian structures.

6.2.3 Permo - Triassic

In the offshore IMFB, the Permo-Triassic history is widely characterised by parallel seismic reflectors and onlaps related to subsidence and passive infill of the Variscan palaeotopography (Fig. 6.1). In the onshore, mm- to cm-wide N-S-trending calcite tensile veins have been identified at Sarclet (Fig. 6.1), suggesting an E-W-extension direction. These are the earliest mineralised structures to yield an absolute U-Pb date (c. *258 - 255 Ma,* Late Permian age).

As Permo-Triassic rifting occurred further to the east in the Central/Viking graben, during E-W extension direction (e.g. Fazlikhani et al. 2020), it is possible that those veins formed in response to the far-field stress related to that rifting episode. This date is also close to being within error of Re-Os pyrite age for veins in northern Caithness (c. 267 Ma; Dichiarante et al. 2016). Those veins in northern Caithness formed as a result of Permian NW–SE extension related to the opening of the offshore West Orkney Basin (Group 3 structures; Dichiarante et al. 2021).

6.2.4 Late Jurassic - Early Cretaceous (c. 148- 117 Ma)

In the offshore parts of the IMFB, the major (tens of km) E-W to NE-SW-trending boundary and intra-basinal faults developed during this period of time. They show a strong association with wedge-shaped Upper Jurassic - Lower Cretaceous seismic packages (Fig. 6.1), confirming their relative timing and syn-rift nature. In addition, new detailed mapping of 3D seismic data,

enhanced by structural seismic attributes (e.g. variance), revealed that at a smaller scale, en-echelon minor NNE-SSW (Fig. 6.1) and NE-SW-trending faults also formed with components of dextral and sinistral shear, respectively.

In the onshore study area, this faulting episode was documented in the Devonian strata (e.g. New Aberdour, Berridale and Whaligoe Steps), Permo-Triassic (e.g. Clashach Cove, Covesea) and in the Upper Jurassic strata at Helmsdale and Shandwick, where the major Helmsdale fault and the splay of the Great Glen Fault crop out, respectively. In the onshore study area, typically normal to normal-sinistral oblique E-W to ENE-WSW-trending faults (e.g. Clashach Cove Fault, minor faults at Covesea, Berridale, Helmsdale) as well as dextral NNE-SSW-trending (Shandwick) or dextrally reactivated Devonian faults (e.g. New Aberdour) develop. These faults developed under an WNW-ESE (e.g. Helmsdale) to NNW-SSE (e.g. New Aberdour, Whaligoe steps) extension direction. Most of these faults and fractures are widely associated with syntectonic calcite mineralisation, which could be dated. The earlier cluster of dated structures (c. 148 – 142 Ma; Tithonian - Berriasian) lies within the typical age-range proposed for the main rifting episode (e.g. Underhill 1991a; Davies et al. 2001). The younger cluster (c. 131 - 117 Ma; Hauterivian - Aptian) is somewhat later than the Berriasian age previously proposed for the cessation of rifting in offshore areas (e.g. Underhill 1991a and b; Davies et al. 2001). However, it is still consistent with studies by Andrews et al. (1990), Roberts et al. (1990) and Argent et al. (2002), all of whom suggested that some faults were longer-lived, and some have been active even during the Albian (Andrews et al. 1990). Within this younger set, the age obtained at New

Aberdour (c. 131 Ma), is related to the Lower Cretaceous dextral reactivation of a Devonian NNE-SSW-trending structure.

A very important discovery derived from the U-Pb calcite dating is that significant displacements along the Helmsdale boundary fault and the GGF splay at Shandwick are not related to Cenozoic events in the IMFB as previously assumed (e.g. Thomson and Underhill 1993; le Breton et al. 2013). The syn-tectonic tensile calcite veins associated with folds dated at Helmsdale are consistent with a component of sinistral shear along the HF. Dating shows that the HF had a sinistral-normal oblique-slip movement during the later Early to Late Cretaceous stage (c. 126 – 84 Ma) of the opening of the IMFB. Likewise, the dated syn-tectonic calcite veins associated with the GGF splay yielded an Early Cretaceous age (c. 121 – 117 Ma). This splay, consistent with dextral kinematics, most likely developed as a synthetic Riedel to the GGF during (possible minor) dextral movement of this fault at a later stage of basin rifting. This splay does not appear to record Cenozoic slip possibly because it had been abandoned during the Cenozoic dextral slip of the GGF main strand located offshore (estimated at c. 30 km due to the offset of the Cenozoic dykes; e.g. Holgate 1969) (Fig. 6.2). This evolution is typical for the development and growth of a basement-controlled shear zone (e.g. Naylor et al. 1986; Richard et al. 1995; de Joussineau and Aydin 2007). Such models typically suggest that basement-controlled strike-slip faulting creates sequential en-echelon Riedel shears in the overlying stratigraphy. With increased displacement, some segments join to form a thoroughgoing fault zone while others are abandoned, which could be the case of the GGF splay at Shandwick (Fig. 6.2).

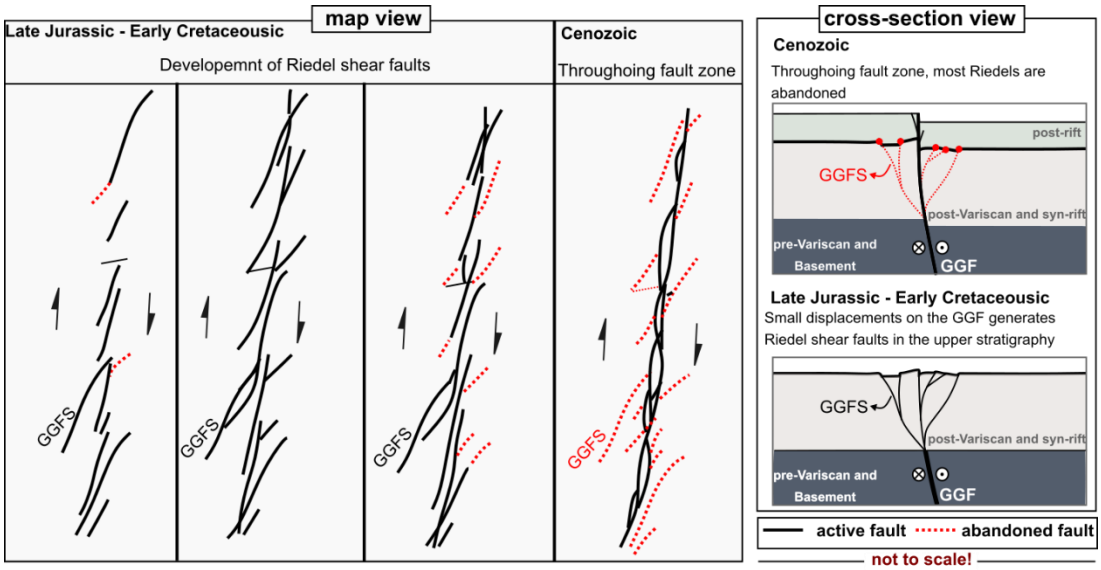

Fig. 6. 2: Conceptual cartoon explaining the sequential evolution of the Great Glen Fault (GGF) during syn- and post-rift (adapted after the sequential development of a dextral shear zone Naylor et al. 1986). (a) map view and (b) cross section view. The notional location of the Great Glen Fault splay (GGFS).

This study revealed that the syn-rift development is longer and more complex than a simple orthogonal rifting. Dip-slip, oblique-slip and strike-slip faults coexist at different times during the basin opening. This is likely the result of oblique kinematics and widespread reactivation of inherited structures. Palaeostress inversion reveal WNW-ESE to NNW-SSE extension directions are associated with the syn-rift faults. This range could either be due to stress variation in time during basin development or due to local stress perturbations related to fault kinematics and fault interference (see Lacombe 2012 and reference therein). This remains to be tested, however, through further work.

6.2.5 Late Cretaceous (c. 96 - 84 Ma)

The Late Cretaceous event recorded at Sarclet and also at Helmsdale is somehow puzzling as the Late Cretaceous is regarded as a period of subsidence (e.g. Underhill 1991a and b; Thomson and Underhill 1993). However, Andrews et al. (1990) describe minor fault movements associated

with sediment wedges of Wick and Banff faults during Late Cretaceous, including during the Maastrichtian.

It is possible that this dated episode is the onshore expression of a late syn-rift pulse of faulting. This could be minor and difficult to separate offshore due to the effects of seismic resolution.

6.2.6 Cenozoic

One of the most interesting outcomes of this study is that at least part of the dextral GGF movement and all of the (oblique) sinistral HF movement are NOT Cenozoic features as has been very widely previously assumed (e.g. Thomson 1993; Thomson and Underhill 1993; Underhill and Brodie 1993; Le Breton et al. 2013). It seems that relatively little evidence is now preserved onshore of this episode, although it is must be associated with dextral reactivation of the GGF (c. 30 km due to the offset of the Cenozoic dykes; Holgate 1969), uplift, tilting and erosion of the basin, which led to the present-day basin configuration (e.g. Underhill 1991a; Thomson and Underhill 1993; Davies et al. 2001).

The only dated example of Cenozoic mineralisation recognised so far in this study is present at Whaligoe Steps. This Cenozoic date was obtained from what looks like a micritic sediment infill of pre-existing vuggy cavity lined by early fill sparry zoned calcite crystals, which yielded a lower Cretaceous age. Thus, it is not clearly a ‘syn-tectonic’ fill.

This finding possibly confirms that (at least) Oligocene sediments were deposited onto the basin margin, possibly directly on the Devonian basement and were later removed by erosion. This would agree with Hillis et al. (1993), who suggest that the Late Cretaceous-Tertiary succession was later removed

by erosion and contra Roberts et al. (1990), who argued that the Late Cretaceous-Tertiary sequence did not extend much to the west of the current offshore limit.

Although nowhere confirmed by the calcite dating, there are structures observed in the onshore and offshore study area are inferred to be possibly Cenozoic. In the offshore, this event is characterised by dextral-normal reactivation of the earlier formed major NE-SW to E-W trending syn-rift fault (e.g. Lossiemouth Fault Zone), attested by newly formed minor en-echelon faults, interpreted as Riedel shear structures (Fig. 6.1). Also, in the area less affected by the reactivation of the major fault, newly-formed dip-slip WNW-ESE-trending faults develop (Fig. 6.1).

Onshore, inferred Cenozoic structures have been identified on both margins of the IMBF. These generally include dextrally reactivated syn-rift faults (e.g. Clashach Fault, the faults at Berridale), dip-slip WNW-ESE-trending faults (e.g. Lothbeg) or the strike-slip faults observed at Sarclet. These structures are usually associated with Fe-oxides mineralisation. Stress inversion and inferred palaeostress (based on e.g. Riedel shear arrays) suggest these structures generally formed during NNE-SSW extension. This extension direction would favour the dextral reactivation of the GGF as well as dextral reactivation of the syn-rift NE-SW to E-W trending faults and the formation of the dip-slip WNW-ESE-trending faults.

6.3 Work published and in preparation related to the PhD thesis

A. Tamas, R. E. Holdsworth, J. R. Underhill, D. M. Tamas, E. D. Dempsey, K. Hardman, A. Bird, D. McCarthy, K. J. W. McCaffrey, D. Selby. 2022a ***New***

onshore insights into the role of structural inheritance during Mesozoic opening of the Inner Moray Firth Basin, Scotland. Journal of the Geological Society, https://doi.org/10.1144/jgs2021-066.

A. Tamas, R. E. Holdsworth, J. R. Underhill, D. M. Tamas, E. D. Dempsey, D. McCarthy, K. J. W. McCaffrey, D. Selby. 2022b. ***Correlating deformation events onshore and offshore in superimposed rift basins: the Lossiemouth Fault Zone, Inner Moray Firth Basin, Scotland.*** Basin Research. (Currently pending decision after revised manuscript after review has been submitted).

A. Tamas, R. E. Holdsworth, J. R. Underhill, D. M. Tamas, E. D. Dempsey, K. Hardman, A. Bird, N. Roberts, J. Lee, D. McCarthy, K. J. W. McCaffrey, D. Selby. 2022. ***Reactivated basin-bounding faults? Are onshore Helmsdale and Great Glen faults (western North Sea) Cenozoic reactivated structures?*** Geology (in prep).

A. Tamas, R. E. Holdsworth, J. R. Underhill, D. M. Tamas, E. D. Dempsey, K. Hardman, A. Bird, N. Roberts, J. Lee, D. McCarthy, K. J. W. McCaffrey, D. Selby. 2022. ***Combining geochronology and high-resolution photogrammetry to analyse the structural evolution of a superimposed basin: the Inner Moray Firth Basin, Scotland***. Journal of Structural Geology (in prep)

A. Tamas, R. E. Holdsworth, J. R. Underhill, D. M. Tamas, E. D. Dempsey, D. McCarthy, K. J. W. McCaffrey, D. Selby. 2022. **The Mesozoic structural**

inheritance in the Cenozoic evolution of the Inner Moray Firth Basin: an offshore/onshore approach. Journal of Structural Geology (in prep).

6.4 Implications and suggestions for future research

6.4.1 Implications

The integration of subsurface interpretation of 2D and 3D seismic data, fieldwork, stress inversion analyses, and absolute dating techniques has yielded significantly improved constrains on the nature, age and significance of regional to local deformation events in the Inner Moray Frith Basin.

The recognition of dextral-oblique Early Cretaceous reactivation of faults related to the underlying and older Orcadian Basin, as well as dextral reactivation of syn-rift faults during the Cenozoic, highlights the importance of fault reactivation and structural inheritance. The pre-existing structures localise deformation and control basin- to sub-basin-scale architectures. In many cases, these structures are obliquely oriented relative to the regional extension vector and so reactivate as transtensional structures with a significant component of strike-slip in addition to dip-slip. This leads to greater structural complexity because these structures may develop in addition to ‘new’ optimally oriented rift faults. Hence, widespread oblique-slip faults have been recognised (as opposed to dominantly dip-slip faults), which influences the surface structures and the corresponding structures at depth, e.g. distribution of open fractures (von Hagke et al. 2019). These aspects are critical to any subsurface investigation (e.g. hydrocarbon resources, CO_2 storage) as they will create reservoir-scale structural heterogeneity in potential subsurface reservoirs.

The IMFB has a proven petroleum system, and its full potential is probably not yet achieved. As recently as 2019, an exploration licence was awarded to Corallian Energy during the 31st Round. Their portfolio includes prospects located in the southern part of the basin within the Middle Jurassic (Corallian Energy). Additionally, some other plays which work in other parts of the North Sea (e.g. Permo-Triassic or Devonian; e.g. Greenhalgh 2016) are underexplored in the IMFB. Better constrained structural models enhanced by the more widely available 3D seismic datasets can add valuable information to risk analysis and unlock the full potential of the area.

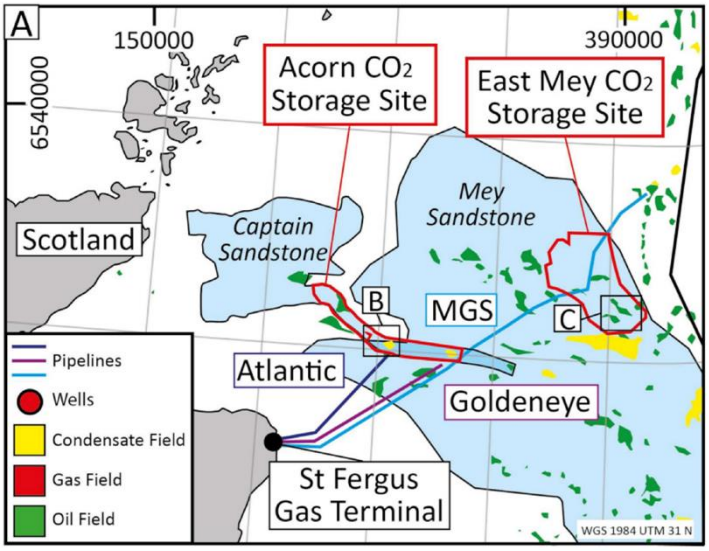

Fig. 6. 3: Offshore area of the IMFB showing the location on the Acorn CO_2 storage site and the distribution of the Captain Sandstone (after Worden et al. 2020).

Moreover, depleted oil reservoirs are ideal geological sites for CO_2 storage (see Gluyas and Mathias 2013; Hannis et al. 2017; Allen et al. 2020; Tyne et al. 2021). Several recent studies are assessing the potential for CO_2 storage in the IMFB (e.g. Williams et al. 2016; Guariguata-Rojas and Underhill 2017; Scafidi and Gilfillan 2019). The IMFB hosts the Acorn CO_2 Storage Site, which is part of Acorn pilot study aiming to capture the CO_2 at St Fergus gas terminal, transport it through Goldeneye pipeline and store it in Lower Cretaceous Captain sandstone (Fig. 6.3) of the Cromer Knoll group (see Chapter 1; Fig. 1.2; Worden et al. 2020; Allen et al. 2020). However, sedimentary basins

recording subsequent fault reactivation are less favourable for CO_2 sequestration due to fault complexities, pressure histories, or the nature of fluid transference (see Tao et al. 2022 and references therein). Understanding where these reactivation events localise is critical for assessing the full potential of the IMFB for CO_2 storage. Guariguata-Rojas and Underhill (2017) have already raised concerns regarding the injection of CO_2 in the Captain sandstone of IMFB due to potential fault-related leakage.

In addition to the IMFB-specific aspects, the workflow used here can be adapted to characterise deformation events in other rift or superimposed rift basins. For example, oblique-slip faults in the subsurface are rarely recognised as they require good 3D imaging and usually refer to analogue structures to validate the interpretation.

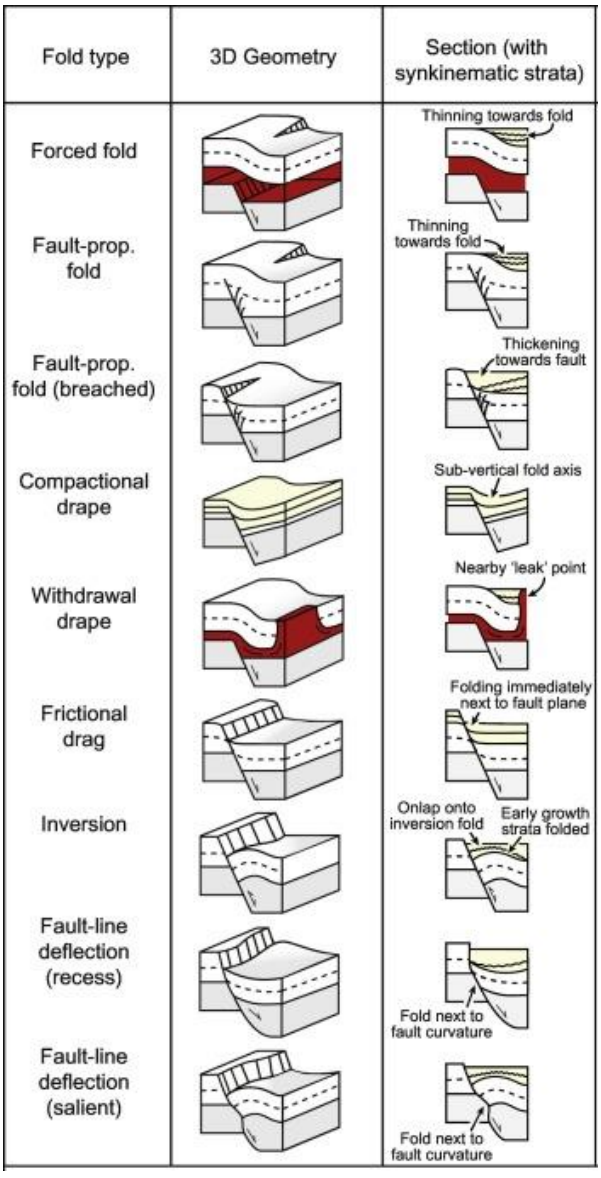

Fig. 6. 4: Fault-related folds in extensional settings (Coleman et al. 2019). Used with permission.

This study presented how a field-calibrated seismic interpretation can aid in recognising fault patterns that can be associated with oblique-slip faults. This includes the transtensional hangingwall folding at Helmsdale. In the

subsurface, hangingwall folding is typically attributed to inversion (Badley et al. 1989), fault-bend folding along irregular normal fault surfaces (e.g. Delogkos et al. 2020), vertical fault segmentation and linkage within mechanically incompetent layers (e.g. Lapadat et al. 2016), lateral segmentation (Rotevatn and Jackson 2014; Childs et al. 2016) as well as many other processes (Fig. 6.4; see Coleman et al. 2019 and references therein), but rarely with oblique kinematics. We hope this study will inspire seismic interpreters to consider the possible importance of oblique-slip deformation patterns in other basins.

6.4.2 Suggestions for future research

Potential future research to address unanswered or problematic aspects, some of which went beyond the scope of this present research and some which unfolded at a very late stage of the project, is suggested below.

- The relative age of the Devonian sequence on the south coast of IMFB (Turriff Basin) is poorly constrained. A greater understanding of the stratigraphic framework in that area will improve the interpretation of the relative timing of faulting where dating techniques are not possible.
- The calcite U-Pb dating is highly recommended for future use in age determination of calcite-mineralised structures in the IMFB as it has proved to be a very successful method. An in-depth study of deformation and mineralisation and more systematic dating will allow better constraints to be placed on the formation of the fault families which have evolved at different times within the syn-rift. This could be enhanced by detailed mapping of the minor-scale structures (e.g. below 10 km) in the offshore seismic 3D data and constructing throw-depth

profiles to better constrain the timing of faulting. Also, time (or depth)-thickness maps between the intra-rift reflectors could further aid in better understanding the timing of faulting.

- The U-Pb dating of the onshore structures revealed that the syn-rift faulting episode may have lasted longer than assumed by most previous workers. It will be significant if those events can be confirmed by further studies of the offshore subsurface data. A key step in this could be establishing the timing and relationship of the NBCE with the underlying and overlying stratigraphy.
- As Cenozoic stratigraphy is not preserved in the IMFB, and the calcite dating did not yield a convincing syn-kinematic date, the deformation associated with the Cenozoic event remains somewhat inferred. The use of a different absolute dating technique (e.g. $^{40}Ar/^{39}Ar$ of fault gouge) is recommended to shed more light into the Cenozoic deformation history.
- The present study proved that pre-existing Orcadian Basin faults were reactivated during the Mesozoic rifting of the IMFB. Likewise, the Mesozoic basin structures were reactivated during the Cenozoic. However, the role of pre-Devonian basement fabrics in the basin development was not assessed. Interestingly, in the Turriff basin, it was observed that a dyke margin within the crystalline basin was reactivated. Basement shear zones have been inferred to have a critical role in rift basins development worldwide, where they are thought to reactivate during rifting, localising stress and controlling rift configuration (e.g. Philips et al. 2016; Osagiede et al. 2020). Evaluating

the impact of pre-existing structures within the crystalline basement could shed further light on the evolution of this complex basin (see also Wilson et al. 2010).

References

Al-Hinai, S., Fisher, Q.J., Al-Busafi, B., Guise, P. and Grattoni, C.A. 2008. Laboratory measurements of the relative permeability of cataclastic fault rocks: An important consideration for production simulation modelling. Marine and Petroleum Geology, 25, 473–485. https://doi.org/10.1016/j.marpetgeo.2007.07.005

Allen, M.J., Faulkner, D.R., Worden, R.H., Rice-Birchall, E., Katirtsidis, N. and Utley, J.E.P. 2020. Geomechanical and petrographic assessment of a CO2 storage site: Application to the Acorn CO2 Storage Site, offshore United Kingdom. Int. J. Greenh. Gas Control, 94, 102923. https://doi.org/10.1016/j.ijggc.2019.102923

Allmendinger, R. W., Cardozo, N., and Fisher, D. 2012. Structural geology algorithms: Vectors and tensors in structural geology. Cambridge University Press, 302 p.

Andrews, I.J., Long, D., Richards, P.C., Thomson, A.R., Brown, S., Chesher, J.A. and McCormac, M. 1990. The Geology of the Moray Firth. United Kingdom Offshore Regional Report, British Geological Survey, London.

Angelier, J. 1984. Tectonic analysis of fault slip data sets. Journal of Geophysical Research, 89, 5835–5848. https://doi.org/10.1029/JB089iB07p05835

Angelier, J. 1990. Inversion of field data in fault tectonics to obtain the regional stress III: A new rapid direct inversion method by analytical means. Geophysical Journal International, 103, 363–376. https://doi.org/10.1111/j.1365-246X.1990.tb01777.x

Appleby, R. 1961. Continuation of the Great Glen Fault Beyond the Moray Firth. Nature, 191, 1190. https://doi.org/10.1038/1911190a0

Argent, J.D., Stewart, S.A. and Underhill, J.R. 2000. Controls on the Lower Cretaceous Punt Sandstone Member, a massive deep-water clastic depo-system, Inner Moray Firth, UK North Sea. Petroleum Geoscience, 6, 275–285.

Argent, J., Stewart, S.A., Green, P. and Underhill, J.R. 2002. Heterogeneous exhumation in the Inner Moray Firth, UK North Sea: constraints from new apatite fission track analysis and seismic data. Journal of the Geological Society, 159, 715-729. https://doi.org/10.1144/petgeo.6.3.275

Armitage, T.B., Watts, L.M., Holdsworth, R.E. and Strachan, R.A. 2020. Late Carboniferous dextral transpressional reactivation of the crustal-scale Walls Boundary Fault, Shetland: the role of pre-existing structures and lithological heterogeneities. Journal of the Geological Society, 178 (1). https://doi.org/10.1144/jgs2020-078

Ashcroft, W.A. and Wilson, C.D.V. 1976. A geophysical survey of the Turriff basin of Old Red Sandstone, Aberdeenshire. Journal of the Geological Society of London, 132, 27–43. https://doi.org/10.1144/gsjgs.132.1.0027

Badley, M.E., Price, J.D. and Backshall L.C. 1989. Inversion, reactivated faults and related structures: seismic examples from the southern North Sea Geol. Soc. Lond., Spec. Publ., 44, 201-219. https://doi.org/10.1144/GSL.SP.1989.044.01.12

Bailey, E.B. and Weir, J. 1932. Submarine faulting in Kimmeridgian times: East Sutherland. Transactions of the Royal Society of Edinburgh, 57, 429-467. https://doi.org/10.1017/S0080456800016768

Barr, D. 1985. 3-D palinspastic restoration of normal faults in the Inner Moray Firth: implications for extensional basin development. Earth and Planetary Science Letters, 75, 191-203. https://doi.org/10.1016/0012-821X(85)90101-3

Bell, R.E., Jackson, C.A.-L., Whipp, P.S. and Clements, B. 2014. Strain migration during multiphase extension: Observations from the northern North Sea. Tectonics, 33, 1936– 1963. https://doi.org/10.1002/2014TC003551

Benton, M.J. and Walker, A.D. 1985. Palaeoecology, taphonomy, and dating of Permo-Triassic reptiles from Elgin, north-east Scotland. Palaeontology, 28, 207–234.

BGS 1969. Geological map, Elgin, Scotland Sheet 95,1:63.360, Edinburgh, Scotland: British Geological Survey.

BGS 1973. Geological map, Cromarty, Scotland Sheet 94, 1:63 360.

BGS 1985. Geological map, Latheron, Scotland Sheet 110, 1:50.000.

BGS 1987. Geological map, Fraserburgh, Scotland Sheet 97, 1:50.000, Ordnance Survey, Southampton.

BGS Moray Firth (Special Sheet). 1995. 1:250.000, Edinburgh, Scotland: British Geological Survey.

BGS 1998. Geological map, Helmsdale, Scotland Sheet 103E, 1:50.000.

Bird, T.J., Bell, A., Gibbs, A.D. and Nicholson, J. 1987. Aspects of strike-slip tectonics in the Inner Moray Firth Basin, offshore Scotland. Norsk Geologisk Tidsskrift, 67, 353–369.

Bird, P. 2014. Tectono-stratigraphic evolution of the West Orkney Basin: implications for hydrocarbon exploration. PhD thesis. Cardiff University.

Bird, P.C., Cartwright, J.A. and Davies T.L. 2014. Basement reactivation in the development of rift basins: an example of reactivated Caledonide structures in the West Orkney Basin. Journal of the Geological Society, 172, 77-85. https://doi.org/10.1144/jgs2013-098

Bosworth, W. and Tari, G. 2021. Hydrocarbon accumulation in basins with multiple phases of extension and inversion: examples from the Western Desert (Egypt) and the western Black Sea. Solid Earth, 12, 59–77. https://doi.org/10.5194/se-12-59-2021

Bott, M. 1959. The mechanics of oblique slip faulting. Geological Magazine, 96(02), 109–117.

Brandes, C. and Tanner, D.C. 2013. Fault-related folding: a review of kinematic models and their application. Earth Sci. Rev. 138, 352-370. http://dx.doi.org/10.1016/j.earscirev.2014.06.008

Brewer, J.A. and Smythe, D.K. 1984. MOIST and the continuity of crustal reflector geometry along the Caledonian-Appalachian orogen. Journal of the Geological Society, 141(1), 105–120. https://doi.org/10.1144/gsjgs.141.1.0105

Brown, A.R. 2011. Horizon and Formation Attributes. In: Interpretation of Three-Dimensional Seismic Data. Society of Exploration Geophysicists and American Association of Petroleum Geologists, p. 247–282. https://doi.org/10.1190/1.9781560802884.ch8a

Buchan, S. 1932. On some dykes in east Aberdeenshire. Transactions of the Edinburgh Geological Society, 12, 323-328. https://doi.org/10.1144/transed.12.4.323

Cameron, T.D.J. 1993. Triassic, Permian and pre-Permian of the Central and Northern North Sea. In: Knox, R.WO'B. & Cordey, W.G (eds): Lithostratigraphic nomenclature of the UK North Sea 4. BGS, HMSO, Nottingham, p. 163 [4, 7,8].

Cardozo, N. and Allmendinger, R.W. 2013. Spherical projections with OSXStereonet. Computers & Geosciences, 51, 193-205. https://doi.org/10.1016/j.cageo.2012.07.021

Carne, R.C. and Little T.A. 2012. Geometry and scale of fault segmentation and deformational bulging along an active oblique-slip fault (Wairarapa fault, New Zealand). GSA Bulletin, 124(7-8), 1365–1381. https://doi.org/10.1130/B30535.1

Childs, C., Manzocchi, A., Nicol, A., Walsh, J.J., Con-neally, J.C. and Delogkos, E. 2016. The relationship between normal drag, relay ramp aspect ratio and fault zone structure. In: Childs, C., Holdsworth, R.E., Jackson, C.A.-L., Manzocchi, T., Walsh, J.J. & Yielding, G. (eds): The Geometry and Growth of Normal Faults. Geological Society, London, Special Publications, 439, 355-372. http://doi.org/10.1144/SP439.16

Chopra, S. and Marfurt, K.J. 2007. Seismic attributes for fault/fracture characterisation. SEG Technical Program Expanded Abstracts: 1520-1524. https://doi.org/10.1190/1.2792785

Chopra, S. 2009. Interpreting fractures through 3D seismic discontinuity attributes and their visualisation. CSEG Recorder, 32(8), 5-14.

Clemmensen, L.B. 1987. Complex star dunes and associated aeolian bedforms, Hopeman Sandstone (Permo-Triassic), Moray Firth Basin, Scotland. In: Frostick, L. & Reid, I. (eds) Desert Sediments: Ancient and Modern. Geological Society, London, Special Publications, 35, 213–231. http://doi.org/10.1144/GSL.SP.1987.035.01.15

Coleman, A.J., Duffy, O.B. and Jackson, C.A.-L. 2019. Growth folds above propagating normal faults, Earth-Science Reviews, 196102885. https://doi.org/10.1016/j.earscirev.2019.102885

Coney, D., Fyfe, T.B., Retail, P. and Smith, P.J. 1993. Clair Appraisal: the benefits of a co-operative approach. In: Parker, J.R., ed.: Petroleum Geology of Northwest Europe: Proceedings of the 4th Conference. Geological Society, London, Petroleum Geology Conference series, 4, 1409-1420. https://doi.org/10.1144/0041409

Corallian Energy. 2022. https://corallian.co.uk/dunrobin.

Coward, M.P. and Enfield, M.A. 1987. Petroleum geology of north west Europe: London, Heyden & Son, Third Conference on Petroleum Geology of North West Europe Proceedings, 687–696.

Coward, M.P., Enfield, M.A. and Fischer, M.W. 1989. Devonian basins of Northern Scotland: extension and inversion related to Late Caledonian - Variscan tectonics. Geological Society, London, Special Publications, 44(1), 275–308. http://doi.org/10.1144/GSL.SP.1989.044.01.16

David, M.J. 1996. History of hydrocarbon exploration in the Moray Firth. Geological Society, London, Special Publications, 114(1), 47–80. https://doi.org/10.1144/GSL.SP.1996.114.01.03

Davies, R.J., Turner, J.D. and Underhill, J.R. 2001. Sequential dip-slip fault movement during rifting: a new model for the evolution of the Jurassic trilete North Sea rift system. Petroleum Geoscience, 7(4), 371–388. https://doi.org/10.1144/petgeo.7.4.371

de Joussineau, G. and Aydin, A. 2007. The evolution of the damage zone with fault growth in sandstone and its multiscale characteristics. J. Geophys. Res., 112, B12401. https://doi.org/10.1029/2006JB004711

De Paola, N., Holdsworth, R.E., McCaffrey, K.J.W. and Barchi, M.R. 2005. Partitioned transtension: an alternative to basin inversion models. Journal of Structural Geology, 27(4), 607-625. https://doi.org/10.1016/j.jsg.2005.01.006

Delogkos, E., Saqab, M.M., Walsh, J.J., Roche, V. and Childs, C. 2020. Throw variations and strain partitioning associated with fault-bend folding along normal faults. Solid Earth, 11, 935–945. https://doi.org/10.5194/se-11-935-2020

Delvaux, D., Moeys, R., Stapel, G., Petit, C., Levi, K., Miroshnichenko, A., Ruzhich, V., and San'kov, V. 1997. Paleostress reconstructions and geodynamics of the Baikal region, Central Asia, Part 2. Cenozoic rifting, Tectonophysics, 282(1–4), 1-38. https://doi.org/10.1016/S0040-1951(97)00210-2

Deng, H., McClay, K. and Bilal, A. 2020. 3D structure and evolution of an extensional fault network of the eastern Dampier Sub-basin, North West Shelf of Australia. Journal of Structural Geology, 132, 103972. https://doi.org/10.1016/j.jsg.2019.103972

Deng, H. and McClay, K. 2021. Three-dimensional geometry and growth of a basement-involved fault network developed during multiphase extension, Enderby Terrace, North West Shelf of Australia. GSA Bulletin, 133(9–10), 2051–2078. https://doi.org/10.1130/B35779.1

Deng, H., McClay, K. and Bilal, A. 2021. Multiphase activation of the boundary fault system of the eastern Dampier subbasin, Northwest Shelf of Australia. AAPG Bulletin, 105(1), 157–188. https://doi.org/10.1306/03022019160

Dewey, J.F., Holdsworth, R.E. and Strachan, R.A. 1998. Transpression and transtension zones. Geological Society, London, Special Publications, 135(1), 1–14. https://doi.org/10.1144/GSL.SP.1998.135.01.01

Dewey, J.F. and Strachan, R.A. 2003. Changing Silurian-Devonian relative plate motion in the Caledonides: sinistral transpression to sinistral transtension. Journal of the Geological Society, 160(2), 219–229. https://doi.org/10.1144/0016-764902-085

Di, H. and Gao, D. 2017. Seismic attribute-aided fault detection in petroleum industry: A review. In: Martion D. (ed.): Fault detection: Methods, Applications and Technology. Nova Science Publishers, 53–80.

Dichiarante, A.M., Holdsworth, R.E., Dempsey, E.D., Selby, D., McCaffrey, K. J.W., Michie, U.M., Morgan, G. and Bonniface, J. 2016. New structural and Re-Os geochronological evidence constraining the age of faulting and associated mineralization in the Devonian Orcadian Basin, Scotland. Journal of the Geological Society, 173, 457-473. https://doi.org/10.1144/jgs2015-118

Dichiarante, A.M., McCaffrey, K.J.W., Holdsworth, R.E., Bjørnarå, T.I. and Dempsey, E.D. 2020. Fracture attribute scaling and connectivity in the Devonian Orcadian Basin with implications for geologically equivalent sub-surface fractured reservoirs. Solid Earth, 11, 2221–2244. https://doi.org/10.5194/se-11-2221-2020

Dichiarante, A.M., Holdsworth, R.E., Dempsey, E.D., McCaffrey, K.J.W., Utley T.A.G. 2021. Outcrop-scale manifestations of reactivation during multiple superimposed rifting and basin inversion events: the Devonian Orcadian Basin, northern Scotland. Journal of the Geological Society, 178(1). https://doi.org/10.1144/jgs2020-089

Donovan, R., Foster, R. and Westoll, T. 1974. 8. A Stratigraphical Revision of the Old Red Sandstone of North-eastern Caithness. Transactions of the Royal Society of Edinburgh, 69(8), 167-201. https://doi.org/10.1017/S0080456800015118

Duncan, W.I. and Buxton, N.W.K. 1995. New evidence for evaporitic Middle Devonian lacustrine sediments with hydrocarbon source potential on the East Shetland Platform, North Sea. Journal of the Geological Society, 152(2), 251–258. https://doi.org/10.1144/gsjgs.152.2.0251

Duxbury, S. and Vieira, M. 2018. A Stratigraphic Review of the Late Callovian to Oxfordian Interval, Fisher Bank Basin Area (UK Sector, Central North Sea). Journal of Petroleum Geology, 41, 47-65. https://doi.org/10.1111/jpg.12692

Edwards, H.E., Becker, A.D. and Howell, J.A. 1993. Compartmentalization of an aeolian sandstone by structural heterogeneities: Permo-Triassic Hopeman Sandstone, Moray Firth, Scotland. In: North, C.P. and Prosser, D.J. (eds) Characterization of Fluvial and Aeolian Reservoirs. Geological Society, London, Special Publications, 73, 339–365. http://doi.org/10.1144/GSL

Egan, S., Buddin, T., Kane, S. and Williams, G. 1997. Three-dimensional modelling and visualisation in structural geology: new techniques for the restoration and balancing of volumes. Proceedings of the 1996 Geoscience Information Group Conference on Geological Visualisation. Electronic Geology Special Volume, 67–82.

Enfield, M.A. and Coward, M.P. 1987. The Structure of the West Orkney Basin, northern Scotland. Journal of the Geological Society, 144(6), 871–884. https://doi.org/10.1144/gsjgs.144.6.0871

England, R.W. 1988. The early Tertiary stress regime in NW Britain: evidence from the patterns of volcanic activity. In: Morton, A.C. and Parsons, L.M. (eds): Early Tertiary Volcanism and the Opening of the NE Atlantic. Geological Society, London, Special Publication, 39, 381-389. https://doi.org/10.1144/GSL.SP.1988.039.01.33

Færseth, R.B., Knudsen, B.-E., Liljedahl, T., Midbøe, P.S. and Søderstrøm, B. 1997. Oblique rifting and sequential faulting in the Jurassic development of the northern North Sea. Journal of Structural Geology, 19(10), 1285-1302. https://doi.org/10.1016/S0191-8141(97)00045-X

Farrell, N.J.C., Healy, D. and Taylor, C.W. 2014. Anisotropy of permeability in faulted porous sandstones. Journal of Structural Geology, 63, 50-67. https://doi.org/10.1016/j.jsg.2014.02.008

Fazlikhani, H., Aagotnes, S.S., Refvem, M.A., Wright, J.H., Bell, R.E., Fossen, H., Gawthorpe, R.L., Jackson, C.A-L. and Rotevatn, A. 2020. Strain migration during multiphase extension, Stord Basin, northern North Sea rift. Basin Research, 33, 1474–1496. https://doi.org/10.1111/bre.12522

Fletcher, T.P., Auton, C.A., Highton, A.J., Merritt, J.W., Robertson, S., Rollin, K.E., Graham, C.C. and Robins, N.S. 1996. Geology of Fortrose and eastern Inverness district: Memoir for 1:50000 geological sheet 84W (Scotland). British Geological Survey, London.

Flinn, D. 1961. Continuation of the Great Glen Fault beyond the Moray Firth. Nature, 191, 589–591. https://doi.org/10.1038/191589b0

Fossen, H., Schultz, R.A., Shipton, Z.K. and Mair, K. 2007. Deformation bands in sandstone: a review. Journal of Structural Geology, 164(4), 755–769. https://doi.org/10.1144/0016-76492006-036

Fossen, H. 2011. 11-Folds and folding. In: Structural Geology. Cambridge University Press, 219-242. https://doi.org/10.1017/CBO9780511777806.013

Fossen, H., Teyssier, C. and Whitney, D.L. 2013. Transtensional folding. Journal of Structural Geology, 56, 89-102. https://doi.org/10.1016/j.jsg.2013.09.004

Fournier, M., Bellahsen, N., Fabbri, O. and Gunnell, Y. 2004. Oblique rifting and segmentation of the NE Gulf of Adenpassive margin. Geochem. Geophys. Geosyst., 5, Q11005. https://doi.org/10.1029/2004GC000731

Fraser, S.I., Robinson, A.M., Johnson, H.D., Underhill, J.R., Kadolsky, D.G.A., Connell, R., Johannessen, P. and Ravnås, R. 2003. Upper Jurassic. In: Evans, D., Graham, C., Armour, A. & Bathurst, P. (eds): The Millenium Atlas: Petroleum Geology of the Central and Northern North Sea. Geological Society of London, 157–189.

Flannery-Sutherland J. T. 2021. Putative arthropod trace fossils from the Orcadian Basin at Achanarras Quarry (Middle Devonian of Scotland). Journal of the Geological Society, 178. https://doi.org/10.1144/jgs2020-233

Friend, P.F., Williams, B.J., Ford, M. and Williams, E.A. 2000. Kinematics and Dynamics of Old Red Sandstone basins. Geological Society, London, Special Publications, 180(1), 29–60. https://doi.org/10.1144/GSL.SP.2000.180.01.04

Frost, R.E. and Ross, J.F. 1996. Tectonic quiescence punctuated by strike-slip movement: influences on Late Jurassic sedimentation in the Moray Firth and the North Sea region. Geological Society, London, Special Publications, 114, 145-162. https://doi.org/10.1144/GSL.SP.1996.114.01.07

Frostick, L., Reid, I., Jarvis, J. and Eardley, H. 1988. Triassic sediments of the Inner Moray Firth, Scotland: early rift deposits. Journal of the Geological Society, 145(2), 235–248. https://doi.org/10.1144/gsjgs.145.2.0235

Glennie, K.W., Higham, J., Stemmerik, L., 2003. Permian. In: Evans, D., Graham, C., Armour, A. & Bathurst, P. (eds): The Millenium Atlas: Petroleum Geology of the Central and Northern North Sea. Geological Society of London, 91-103.

Gluyas, J.G. and Mathias, S.A. 2013. Geological Storage of carbon dioxide (CO_2), Geoscience, technologies, environmental aspects and legal frameworks. Woodhead Publishing, Cambridge, 329-340.

Goldsmith, P.J, Hudson, G. and van Veen, P. 2003. Triassic. In: Evans, D., Graham, C., Armour, A. & Bathurst, P. (eds): The Millenium Atlas: Petroleum Geology of the Central and Northern North Sea. Geological Society of London, 105-128.

Greenhalgh, E. 2016. Literature Review of Devonian Source Rocks and Devonian-Sourced Hydrocarbons in the Orcadian Basin. British Geological Survey Commissioned Report, CR/16/017, 25p.

Guariguata-Rojas, G.J and Underhill, J.R. 2017. Implications of Early Cenozoic uplift and fault reactivation for carbon storage in the Moray Firth Basin. Interpretation 5(4), SS1-SS21. https://doi.org/10.1190/INT-2017-0009.1

Gunn, A.G., Mendum, J.R. and Thomas, C.W. 2015. Geology of the Huntly and Turriff Districts. Sheet description for the 1:50 000 geological sheets 86W (Huntly) and 86E (Turriff) (Scotland), British Geological Survey.

Hannis, S., Lu, J. Chadwick, A., Hovorka, S., Kirk, K., Romanak, K. and Pearce, J. 2017. CO_2 Storage in Depleted or Depleting Oil and Gas Fields: What can We Learn from Existing Projects? Energy Procedia, 114, 5680-5690. https://doi.org/10.1016/j.egypro.2017.03.1707

Hansen, J.-A., Bergh, S.G. and Henningsen, T. 2012. Mesozoic rifting and basin evolution on the Lofoten and Vesterålen Margin, North-Norway; time constraints and regional implications. Norwegian Journal of Geology, 91, 203–228. https://doi.org/10.1111/bre.12358

Healy, D., Jones, R. and Holdsworth, R. 2006. Three-dimensional brittle shear fracturing by tensile crack interaction. Nature, 439, 64–67. https://doi.org/10.1038/nature04346

Healy, D., Blenkinsop, T.G., Timms, N.E., Meredith, P.G., Mitchell, T.M. and Cooke, M.L. 2015. Polymodal faulting: time for a new angle on shear failure. Journal of Structural Geology, 80, 57-71. https://doi.org/10.1016/j.jsg.2015.08.013

Healy, D., Rizzo, R.E., Cornwell, D., Farrell, N.J.C., Watkins, H., Timms, N.E., et al. 2017. Fracpaq: A MATLAB toolbox for the quantification of fracture patterns. Journal of Structural Geology, 95, 1–16. https://doi.org/10.1016/j.jsg.2016.12.003

Henstra, G.A., Berg Kristensen, T., Rotevatn, A. and Gawthorpe, R.L. 2019. How do pre-existing normal faults influence rift geometry? A comparison of adjacent basins with contrasting underlying structure on the Lofoten Margin, Norway. Basin Research, 31, 1083–1097. https://doi.org/10.1111/bre.12358

Hillis, R.R., Thomson, K. and Underhill, J.R. 1994. Quantification of Tertiary erosion in the Inner Moray Firth using sonic velocity data from the Chalk and the Kimmeridge Clay. Mar. Petrol. Geol., 11, 283–293. https://doi.org/10.1016/0264-8172(94)90050-7

Hoareau, G., Claverie, F., Pécheyran, C., Paroissin, C., Grignard, P.A., Motte, G., Chailan, O. and Girard, J.P. 2021. Direct U–Pb dating of carbonates from micron-scale femtosecond laser ablation inductively coupled plasma mass spectrometry images using robust regression. Geochronology, 3, 67–87. https://doi.org/10.5194/gchron-3-67-2021

Hodgetts, D., Gawthorpe, R.L., Wilson, P., and Rarity, F. 2007. Integrating digital and traditional field techniques using virtual reality geological studio (VRGS). Society of Petroleum Engineers e 69th European Association of Geoscientists and Engineers Conference and Exhibition 2007. Securing the Future, 83-87.

Holdsworth, R.E., Butler, C.A. and Roberts, A.M. 1997. The recognition of reactivation during continental deformation. Journal of the Geological Society, 154(1), 73–78. https://doi.org/10.1144/gsjgs.154.1.0073

Holdsworth, R.E., Dempsey, E., Selby, D., Darling, J.R., Feely, M., Costanzo, A., Strachan, R.A., Waters, P., Finlay, A.J. and Porter, S.J. 2015. Silurian-Devonian magmatism, mineralization, regional exhumation and brittle strike-slip deformation along the Loch Shin Line, NW Scotland. Journal of the Geological Society, 172(6), 748–762. https://doi.org/10.1144/jgs2015-058

Holdsworth, R.E., McCaffrey, K.J.W., Dempsey, E., Roberts, N.M.W., Hardman, K., Morton, A., Feely, M., Hunt, J., Conway, A. and Robertson, A.

2019. Natural fracture propping and earthquake-induced oil migration in fractured basement reservoirs. Geology, 47, 700-704. https://doi.org/10.1130/G46280.1

Holdsworth, R.E., Trice, R., Hardman, K., McCaffrey, K.J.W., Morton, A., Frei, D., Dempsey, E., Bird, A. and Rogers, S. 2020. The nature and age of basement host rocks and fissure fills in the Lancaster field fractured reservoir, West of Shetland. Journal of the Geological Society, 177(5), 1057-1073. https://doi.org/10.1144/jgs2019-142

Holgate, N. 1969. Palaeozoic and Tertiary transcurrent movements on the Great Glen fault. Scottish Journal of Geology, 5(2), 97-139. https://doi.org/10.1144/sjg05020097

Hudson, J.D. and Trewin, N.H. 2002. Jurassic. In: Trewin, N.H. (ed.): The geology of Scotland. The Geological Society, London, 323-350.

Hurst, A.R. 1981. Mid Jurassic Stratigraphy and Facies at Brora, Sutherland. Scottish Journal of Geology, 17, 169-177. https://doi.org/10.1144/sjg17030169

Hurst, A.R. 2009. Bathonian to Oxfordian strata of the Brora area. In: Trewin, N. and Hurst A.R. (eds): Excursion Guide to the Geology of East Sutherland and Caithness, 2nd ed. Aberdeen Geological Society and Dunedin Press., Geological Magazine, 147(5), 798-799.

Jacques, J.M. and Reavy, R.J. 1994. Caledonian plutonism and major lineaments in the SW Scottish Highlands. Journal of the Geological Society, 151, 955-969. https://doi.org/10.1144/gsjgs.151.6.0955

Johnstone, G.S. and Mykura, W. 1989. British regional geology: the Northern Highlands of Scotland, vol. 2. HM Stationery Office.

Jonk, R., Duranti, D., Parnell, J., Hurst, A. and Fallick, E. 2003. The structural and diagenetic evolution of injected sandstones: examples from the Kimmeridgian of NE Scotland. J. Geol. Soc. London, 160, 881–894. https://doi.org/10.1144/0016-764902-091

Kamb, W.B. 1959. Ice petrofabric observations from Blue Glacier, Washington, in relation to theory and experiment, J. Geophys. Res., 64(11), 1891– 1909. https://doi.org/10.1029/JZ064i011p01891

Kane, S.J., Williams, G.D., Buddin, T.S., Egan, S.S. and Hodgetts, D. 1997. Flexural-slip Based Restoration in 3D, a New Approach. AAPG Annual Convention, Official Program, A58.

Kemp, S., Gillespie, M., Leslie, G., Zwingmann, H., and Campbell, S. 2019. Clay mineral dating of displacement on the Sronlairig Fault: Implications for

Mesozoic and Cenozoic tectonic evolution in northern Scotland. Clay Minerals, 54(2), 181-196. https://doi.org/10.1180/clm.2019.25

Koson, S., Chenrai, P. and Choowong, M. 2014. Seismic Attributes and Their Applications in Seismic Geomorphology. Bulletin of Earth Sciences of Thailand, 6(1), 1–9.

Kylander-Clark, A.R. 2020. Expanding the limits of laser-ablation U–Pb calcite geochronology. Geochronology, 2, 343-354. https://doi.org/10.5194/gchron-2-343-2020

Lacombe, O. 2012. Do fault slip data inversions actually yield “paleostresses” that can be compared with contemporary stresses? A critical discussion. Comptes Rendus Geoscience, 344(3–4), 159-173. https://doi.org/10.1016/j.crte.2012.01.006

Lăpădat, A., Imber, J., Yielding, G., Iacopini, D., McCaffrey, K.J.W., Long, J. J. and Jones, R.R. 2016. Occurrence and development of folding related to normal faulting within a mechanically heterogeneous sedimentary sequence: a case study from Inner Moray Firth, UK. Geological Society, London, Special Publications, 439, 373-394. https://doi.org/10.1144/SP439.18

Le Breton, E., Cobbold, P.R. and Zanella, A. 2013. Cenozoic reactivation of the Great Glen Fault, Scotland: additional evidence and possible causes. Journal of the Geological Society, 170(3), 403–415. https://doi.org/10.1144/jgs2012-067

Linsley, P.N., Potter, H.C., Mcnab, G. and Racher, D. 1980. The Beatrice field, Inner Moray Firth, U.K. North Sea. In: Halbouty, M. T. (ed.) Giant oil and gas fields of the decade 1968-1978. Memoir of the American Association of Petroleum Geologists, 30, 117-129.

Long, J.J. and Imber, J. 2010. Geometrically coherent continuous deformation in the volume surrounding a seismically imaged normal fault-array. Journal of Structural Geology, 32, 222–234. https://doi.org/10.1016/j.jsg.2009.11.009

Lovecchio, J.P., Rohais, S., Joseph, P., Bolatti, N.D., Kress, P.R., Gerster, R. and Ramos, V.A. 2018. Multistage rifting evolution of the Colorado basin (offshore Argentina): Evidence for extensional settings prior to the South Atlantic opening. Terra Nova, 30, 359-368. https://doi.org/10.1111/ter.12351

Lovell, J.P.B. 1991. Permian and Triassic. In: Craig, G Y (ed): Geology of Scotland. Third edition. The Geological Society, London, 421–438.

MacDonald, A.C. 1985. Kimmeridgian and Volgian fault-margin sedimentation in the northern North Sea area. Ph.D. Thesis. University of Strathclyde.

MacDonald A.C. and Trewin N.H. 2009. The Upper Jurassic of the Helmsdale area. In: Trewin, N. and Hurst A. (eds): Excursion Guide to the Geology of

East Sutherland and Caithness, 2nd ed. Aberdeen Geological Society and Dunedin Press, Geological Magazine, 147(5), 798-799.

Macgregor, D. 2015. History of the development of the East African Rift System: A series of interpreted maps through time. Journal of African Earth Sciences, 101, 232-252. https://doi.org/10.1016/j.jafrearsci.2014.09.016

Mackay, L.M., Turner, J., Jones, S.M. and White, N.J. 2005. Cenozoic vertical motions in the Moray Firth Basin associated with initiation of the Iceland Plume. Tectonics, 24, 1–23. https://doi.org/10.1029/2004TC001683

Marshall, J.E.A. and Hewett, A.J. 2003. Devonian. In: Evans, D., Graham, C., Armour, A. and Bathurst, P., Millennium Atlas: Petroleum Geology of the Northern North Sea. Geological Society, London, 64–81.

McArthur, A.D., Hartley, A.J. and Jolley, D.W. 2013. Stratigraphic development of an Upper Jurassic deep marine syn-rift succession, Inner Moray Firth Basin, Scotland. Basin Research, 25, 285-309. https://doi.org/10.1111/j.1365-2117.2012.00557.x

McCaffrey, K.J.W., Jones, R.R., Holdsworth, R.E., Wilson, R.W., Clegg, P., Imber, J., Holliman, N. and Trinks, I. 2005. Unlocking the spatial dimension: digital technologies and the future of geoscience fieldwork, Journal of the Geological Society, 162, 927-938. https://doi.org/10.1144/0016-764905-017

McClay, K., Norton, M. G., Coney, P., Davis, G. H. et al. 1986. Collapse of the Caledonian orogen and the Old Red Sandstone. Nature, 323, 147–149. https://doi.org/10.1038/323147a0

McQuillin, R., Donato, J.A., and Tulstrup, J. 1982. Development of basins in the Inner Moray Firth and the North Sea by crustal extension and dextral displacement of the Great Glen Fault. Earth and Planetary Science Letters, 60(1), 127–139. https://doi.org/10.1016/0012-821X(82)90028-0

Mendum, J.R. and Noble, S.R. 2010. Mid-Devonian sinistral transpressional movements on the Great Glen Fault: the rise of the Rosemarkie Inlier and the Acadian Event in Scotland. Geological Society, London, Special Publications, 335(1), 161–187. https://doi.org/10.1144/SP335.8

Michael, A.J. 1984. Determination of stress from slip data: faults and folds. Journal of Geophysical Research: Solid Earth, 89(B13), 11517–11526. https://doi.org/10.1029/JB089iB13p11517

Miller, H. 1841. The Old Red Sandstone. Adam and Charles Black, Edinburgh, 275 p.

Mostafa, M.E. 2005: Iterative direct inversion: An exact complementary solution for inverting fault-slip data to obtain palaeostresses. Computers & Geosciences, 31(8), 1059-1070. https://doi.org/10.1016/j.cageo.2005.02.012

Mudge, D.C. 2015. Regional controls on Lower Tertiary sandstone distribution in the North Sea and NE Atlantic margin basins. In McKie, T., et al. (eds.): Tertiary Deep-Marine Reservoirs of the North Sea Region: An Introduction: Geological Society of London Special Publications, 403, 17–42. https://doi.org/10.1144/SP403.5

Nabavi, S.T. and Fossen, H. 2021. Fold geometry and folding – a review. Earth-Science Reviews, 222, 103812. https://doi.org/10.1016/j.earscirev.2021.103812

Naylor, M.A., Mandl, G. and Supesteijn, C.H.K. 1986. Fault geometries in basement-induced wrench faulting under different initial stress states, Journal of Structural Geology, 8(7), 737-752. https://doi.org/10.1016/0191-8141(86)90022-2

Naylor, H., Turner, P., Vaughan, D.J. and Fallick, A.E. 1989. The Cherty Rock, Elgin: A petrographic and isotopic study of a Permo-Triassic calcrete. Geological Journal, 24(3), 205-221. https://doi.org/10.1002/gj.3350240305

NIREX. 1994. The Geology of the Region Around Dounreay: Report of the Regional Geology Joint Interpretation Team. UK Nirex Limited Report, 657 p.

Norton, M.J., Mcclay, K.R. and Nick, A.W. 1987. Tectonic evolution of Devonian basins in northern Scotland and southern Norway. Norsk Geologisk Tidsskrift, 67, 323-338.

Nyberg, B., Nixon, C.W. and Sanderson, D.J. 2018. NetworkGT: A GIS tool for geometric and topological analyses of two-dimensional fracture networks. Geosphere, 14(4), 1618-1634. https://doi.org/10.1130/GES01595.1

Offshore Energy 2020. https://www.offshore-energy.biz/large-ep-player-interested-in-corallians-block-off-uk/

Osagiede, E.E., Rotevatn, A., Gawthorpe, R., Kristensen, T.B., Jackson, C.A-L. and Marsh, N. 2020. Pre-existing intra-basement shear zones influence growth and geometry of non-colinear normal faults, western Utsira High–Heimdal Terrace, North Sea. Journal of Structural Geology, 130, 103908. https://doi.org/10.1016/j.jsg.2019.103908

Parnell, J., Carey, P. and Monson, B. 1998. Timing and temperature of decollement on hydrocarbon source rock beds in cyclic lacustrine successions. Palaeogeography, Palaeoclimatology, Palaeoecology, 140(1-4), 121-134. https://doi.org/10.1016/s0031-0182(98)00035-2

Passchier, C. and Trouw, R. 2005. Microtectonics. Springer, Berlin, 366 p.

Peacock, J.D., Berridge, N.G., Harris, A.L. and May, F. 1968. Geology of the Elgin District. In: Memoirs of the Geological Survey. H.M.S.O, Scotland, 54-77.

Peacock, D.C.P., Nixon, C.W., Rotevatn, A., Sanderson, D.J., and Zuluaga, L. F. 2016. Glossary of fault and other fracture networks. Journal of Structural Geology, 92, 12–29. https://doi.org/10.1016/j.jsg.2016.09.008

Peters, K.E., Moldowan, J.M., Driscole, A.R. and Demaison, G.J. 1989. Origin of Beatrice Oil by Co-Sourcing from Devonian and Middle Jurassic Source Rocks, Inner Moray Firth, United Kingdom. AAPG Bulletin, 73(4), 454-471. https://doi.org/10.1306/44B49FCE-170A-11D7-8645000102C1865D

Petit, J.P. 1987. Criteria for the sense of movement on fault surfaces in brittle rocks. Journal of Structural Geology, 9, 597–608. https://doi.org/10.1016/0191-8141(87)90145-3

Petrel 2021 - Petrel Guru software support for background theory.

Phillips, T.B., Fazlikhani, H., Gawthorpe, R.L., Fossen, H., Jackson, C.A.-L., Bell, R.E., et al. 2019. The influence of structural inheritance and multiphase extension on rift development, the northern North Sea. Tectonics, 38, 4099–4126. https://doi.org/10.1029/2019TC005756

Pickering, K.T. 1984. The Upper Jurassic 'Boulder Beds' and related deposits: a fault-controlled submarine slope, NE Scotland. Journal of the Geological Society, 141, 357-374. https://doi.org/10.1144/gsjgs.141.2.0357

Pigott, J.D., Kang, M.H. and Han, H.C. 2013. First Order Seismic Attributes for clastic Seismic facies Interpretation: Examples from the East China Sea. J. Asian Earth Sci., 66, 34–54. https://doi.org/10.1016/j.jseaes.2012.11.043

Quinn, O.F. 2005. Fault Controlled Fluid Flow and Quartz Cementation in Porous Sandstones. PhD thesis. University of Edinburgh.

Ragon, T., Nutz, A., Schuster, M., Ghienne, J.F., Ruffet, G. and Rubino, J.L. 2018. Evolution of the northern Turkana Depression (East African Rift System, Kenya) during the Cenozoic rifting: New insights from the Ekitale Basin (28-25.5Ma). Geological Journal, 54, 3468–3488. https://doi.org/10.1002/gj.3339

Ramsay, J. 1980. The crack–seal mechanism of rock deformation. Nature, 284, 135–139. https://doi.org/10.1038/284135a0

Rawson, P. and Riley, L.A. 1982. Latest Jurassic-Early Cretaceous events and the late Cimmerian unconformity in North Sea area. AAPG Bulletin, 66, 2628-2648. https://doi.org/10.1306/03B5AC87-16D1-11D7-8645000102C1865D

Read, H.H. 1923. The geology of the country around Banff, Huntly and Turriff (Lower Banffshire and North-west Aberdeenshire) Explanation of Sheets 86 and 96. Memoir of the Geological Survey, Scotland. (Edinburgh: HMSO).

Richard, P.D., Naylor, M.A., & Koopman, A. 1995. Experimental models of strike-slip tectonics. Petroleum Geoscience, 1, 71-80. https://doi.org/10.1144/petgeo.1.1.71

Riding, J.B. 2005. Middle and Upper Jurassic (Callovian to Kimmeridgian) Palynology of the Onshore Moray Firth Basin, Northeast Scotland. Palynology, 29, 87–142. https://doi.org/10.2113/29.1.87

Roberts, A.M., Price, J.D. and Badley, M.E. 1989. Discussion on Triassic sediments of the Inner Moray Firth, Scotland: early rift deposits. Journal of the Geological Society, 146, 361-363. https://doi.org/10.1144/gsjgs.146.2.0361

Roberts, A.M., Badley, M.E., Price, J. D. and Huck, I.W. 1990. The structural history of a transtensional basin: Inner Moray Firth, NE Scotland. Journal of the Geological Society, 147(1), 87–103. https://doi.org/10.1144/gsjgs.147.1.0087

Roberts, A.M. and Holdsworth R.E. 1999. Linking onshore and offshore structures: Mesozoic extension in the Scottish Highlands. Journal of the Geological Society, 156, 1061–1064. https://doi.org/10.1144/gsjgs.156.6.1061

Roberts, N.M. and Walker, R.J. 2016. U-Pb geochronology of calcite-mineralized faults: Absolute timing of rift-related fault events on the northeast Atlantic margin. Geology, 44, 531–534. https://doi.org/10.1130/G37868.1

Roberts, N.M.W., Troy Rasbury, E., Parrish, R.R., Smith, C.J., Horstwood, M.S.A. and Condon, D.J. 2017. A calcite reference material for LA-ICP-MS U-Pb geochronology. Geochem. Geophys. Geosyst., 18, 2807-2814. https://doi.org/10.1002/2016GC006784

Roberts, N.M., Drost, K., Horstwood, M.S., Condon, D.J., Chew, D., Drake, H., Milodowski, A.E., McLean, N.M., Smye, A.J., Walker, R.J. and Haslam, R. 2020a. Laser ablation inductively coupled plasma mass spectrometry (LA-ICP-MS) U–Pb carbonate geochronology: strategies, progress, and limitations. Geochronology, 2, 33-61. https://doi.org/10.5194/gchron-2-33-2020

Roberts, N.M.W., Lee, J.K., Holdsworth, R.E., Jeans, C., Farrant, A.R., and Haslam, R. 2020b. Near-surface Palaeocene fluid flow, mineralisation and faulting at Flamborough Head, UK: new field observations and U-Pb calcite dating constraints, Solid Earth, 11, 1931–1945. https://doi.org/10.5194/se-11-1931-2020

Rogers, D.A., Marshall, J.E.A. and Astin, T.R. 1989. Devonian and later movements on the Great Glen fault system, Scotland. Journal of the Geological Society, 146(3), 369–372. https://doi.org/10.1144/gsjgs.146.3.0369

Rotevatn, A., Sandve, T.H., Keilegavlen, E., Kolyukhin, D. and Fossen, H. 2013. Deformation bands and their impact on fluid flow in sandstone

reservoirs: the role of natural thickness variations. Geofluids, 13, 359-371. https://doi.org/10.1111/gfl.12030

Rotevatn, A. and Jackson, C.A.-L. 2014. 3D structure and evolution of folds during normal fault dip linkage. Journal of Geological Society, London, 171, 821–829. http://doi.org/10.1144/jgs2014-045

Rotevatn, A., Fossmark, H.S.S., Bastesen, E., Thorsheim, E. and Torabi, A. 2016. Do deformation bands matter for flow? Insights from permeability measurements and flow simulations in porous carbonate rocks. Petroleum Geoscience, 23(1), 104-119. http://doi.org/10.1144/petgeo2016-038

Rotevatn, A., Kristensen, T.B., Ksienzyk, A.K., Wemmer, K., Henstra, G.A., Midtkandal, I., Grundvåg, S.-A. and Andresen, A. 2018. Structural inheritance and rapid rift-length establishment in a multiphase rift: The East Greenland rift system and its Caledonian orogenic ancestry. Tectonics, 37, 1858–1875. https://doi.org/10.1029/2018TC005018

Sasvári, Á. and Baharev, A. 2014. SG2PS (structural geology to post script converter) – A graphical solution for brittle structural data evaluation and paleostress calculation. Computers & Geosciences, 66, 81–93.

Scafidi, J. and Gilfillan, S.M.V. 2019. Offsetting Carbon Capture and Storage costs with methane and geothermal energy production through reuse of a depleted hydrocarbon field coupled with a saline aquifer. International Journal of Greenhouse Gas Control, 90, 102788. https://doi.org/10.1016/j.ijggc.2019.102788

Seranne, M. 1992. Devonian extensional tectonics versus Carboniferous inversion in the northern Orcadian basin. Journal of the Geological Society, 149(1), 27–37. https://doi.org/10.1144/gsjgs.149.1.0027

Shipton, Z.K., Evans, J.P., Robeson, K.R., Forster, C.B. and Snelgrove, S. 2002. Structural heterogeneity and permeability in faulted eolian sandstone: Implications for subsurface modeling of faults. AAPG Bulletin, 86(5), 863-883. https://doi.org/10.1306/61EEDBC0-173E-11D7-8645000102C1865D

Soper, N.J., Strachan, R.A., Holdsworth, R.E., Gayer, R.A. and Greiling, R.O. 1992. Sinistral transpression and the Silurian closure of Iapetus. Journal of the Geological Society, 149, 871–880. https://doi.org/10.1144/gsjgs.149.6.0871

Spang J. 1972. Numerical method for dynamic analysis of calcite twin lamellae. GSA Bulletin, 84(2), 467-472. https://doi.org/10.1130/0016-7606(1972)83[467:NMFDAO]2.0.CO;2

Steel, R. and Ryseth, A. 1990. The Triassic — early Jurassic succession in the northern North Sea: megasequence stratigraphy and intra-Triassic tectonics, Geological Society, London, Special Publications, 55, 139-168. https://doi.org/10.1144/GSL.SP.1990.055.01.07

Stephen, K.J., Underhill, J.R., Partington, M. and Hedley, R.J. 1993. The sequence stratigraphy of the Hettangian to Oxford/an sedimentary succession, Inner Moray Firth. In: Parker, J.R. (ed): Petroleum Geology of North West Europe. Geological Society Publishing House, Bath, 485-505.

Stephenson, D. and Gould, D. 1995. The Grampian Highlands, 4th ed. British Regional Geology Series, London: HMSO for the British Geological Survey. Geological Magazine, 133(4), 506-506. https://doi.org/10.1017/S0016756800007779

Stevens, V. 1991. The Beatrice Field, Block 11/30a, UK North Sea. Geological Society, London, Memoirs, 14, 245-252, 1 January 1991, https://doi.org/10.1144/GSL.MEM.1991.014.01.30.

Stewart, M., Strachan, R.A. and Holdsworth, R.E. 1999. Structure and early kinematic history of the Great Glen Fault Zone, Scotland, Tectonics, 18(2), 326-342. https://doi.org/10.1029/1998TC900033

Stewart, M., Holdsworth, R.E. and Strachan, R.A. 2000. Deformation processes and weakening mechanisms within the frictional–viscous transition zone of major crustal-scale faults: insights from the Great Glen Fault Zone, Scotland. Journal of Structural Geology, 22(5), 543-560. https://doi.org/10.1016/S0191-8141(99)00164-9

Stoker, M.S., Hitchen, K. and Graham, C.C. 1993. The geology of the Hebrides and West Shetland shelves, and adjacent deep-water areas, vol. 2. The Stationery Office/Tso.

Suppe, J. 1983. Geometry and kinematics of fault-bend folding. American Journal of Science, 283(7), 684-721. https://doi.org/10.2475/ajs.283.7.684

Sutherland, D.G. 1984. The Quaternary deposits and landforms of Scotland and the neighbouring shelves: A review. Quaternary Science Reviews, 3, (2-3), 157-254. https://doi.org/10.1016/0277-3791(84)90017-9

Sweet, I. 1895. The sedimentology of the Lower Old Red Sandstone near New Aberdour, Grampian Region. Scottish Journal of Geology, 21, 239-259. https://doi.org/10.1144/sjg21030239

Sykes, R.M. 1975. The stratigraphy of the Callovian and Oxfordian stages (Middle and Upper Jurassic) in northern Scotland. Scottish Journal of Geology, 11, 51-78. https://doi.org/10.1144/sjg11010051

Tămaș, D.M., Tămaș, A., Barabasch, J., Rowan, M.G., Schleder, Z., Krézsek, C. and Urai, J.L. 2021. Low-angle shear within the exposed Mânzălești diapir, Romania: Salt decapitation in the Eastern Carpathians fold-and-thrust belt. Tectonics, 40, e2021TC006850. https://doi.org/10.1029/2021TC006850

Tamas, A., Holdsworth, R.E., Underhill, J.R., Tamas, D.M., Dempsey, E.D., Hardman, K., Bird, A., McCarthy, D., McCaffrey, K.J.W. and Selby, D. 2022a. New onshore insights into the role of structural inheritance during Mesozoic opening of the Inner Moray Firth Basin, Scotland. Journal of the Geological Society. http:// doi.org/10.1144/jgs2021-066

Tamas, A., Holdsworth, R.E., Underhill, J.R. Tamas, D.M., Dempsey, E.D., McCarthy, D., McCaffrey, K. J. W. and Selby. D. 2022b. Correlating deformation events onshore and offshore in superimposed rift basins: the Lossiemouth Fault Zone, Inner Moray Firth Basin, Scotland. Basin Research (in review).

Tao, Z., He., Z., Alves, T.M., Guo, X., Gao, J., He, S., Zhao, W. 2022. Structural inheritance and its control on overpressure preservation in mature sedimentary basins (Dongying depression, Bohai Bay Basin, China). Marine and Petroleum Geology, 137, 105504. https://doi.org/10.1016/j.marpetgeo.2021.105504

Thomson, K. 1993. Tertiary tectonics and uplift of the Inner Moray Firth and adjacent areas. PhD thesis. University of Edinburgh.

Thomson, K. and Underhill, J.R. 1993. Controls on the development and evolution of structural styles in the Inner Moray Firth Basin. Petroleum Geology of Northwest Europe. Proceedings of the 4th Conference on Petroleum Geology of NW. Europe, London, 1167–1178.

Thomson, K. and Hillis, R.R. 1995. Tertiary structuration and erosion of the Inner Moray Firth. In: Scrutton, R.A., Stoker, M.S., Shimmield, G.B. and Tudhope, A.W. (eds): The Tectonics, Sedimentation and Palaeoceanography of the North Atlantic Region. Geological Society, London, Special Publications, 90, 249–269. https://doi.org/10.1144/GSL.SP.1995.090.01.16

Tomasso, M., Underhill, J.R., Hodgkinson, R.A. and Young, M.J. 2008. Structural styles and depositional architecture in the Triassic of the Ninian and Alwyn North fields: Implications for basin development and prospectivity in the Northern North Sea. Marine and Petroleum Geology, 25, 588-605

Totake, Y., Butler, R.W.H. and Bond, C.E. 2017. Structural validation as an input into seismic depth conversion to decrease assigned structural uncertainty. Journal of Structural Geology, Volume 95, Pages 32-47, https://doi.org/10.1016/j.jsg.2016.12.007.

Trewin, N.H. 1987. Pennan, unconformity within the Old Red Sandstone, Excursion 8, In: Trewin, N.H.T, Kneller, B.C. and Gillen, C. (eds): Excursion guide to the geology of the Aberdeen area. Scottish Academic Press, Edinburgh, 127-130.

Trewin, N.H.T., Andrews S. D. and Kneller, B.C. 1987. The Lower Old Red Sandstone of New Aberdour In: Trewin, N.H.T, Kneller, B.C. and Gillen, C. (eds): Excursion guide to the geology of the Aberdeen area. Scottish Academic Press.

Trewin, N.H. and Thirlwall, M.F. 2002. Old Red Sandstone. In: Trewin, N.H. (ed.) The Geology of Scotland, 4th edn. Geological Society, London, 213–249.

Trewin, N. 2009. The Triassic and Lower Jurassic of Golspie. In: Trewin, N. and Hurst (eds): A. Excursion Guide to the Geology of East Sutherland and Caithness, 2nd ed. Aberdeen Geological Society and Dunedin Press., Geological Magazine, 147(5), 798-799.

Trewin, N. and Hurst, A. 2009. Excursion Guide to the Geology of East Sutherland and Caithness, 2nd ed. Aberdeen Geological Society and Dunedin Press., Geological Magazine, 147(5), 798-799.

Tyne, R.L., Barry, P.H., Lawson, M. et al. 2021. Rapid microbial methanogenesis during CO2 storage in hydrocarbon reservoirs. Nature, 600, 670–674. https://doi.org/10.1038/s41586-021-04153-3

Underhill, J.R and Woodcock, N.H. 1987. Faulting mechanisms in high-porosity sandstones; New Red Sandstone, Arran, Scotland. In: Jones, M.E, Preston, R.M.F (eds), Deformation of Sediments and Sedimentary Rocks, Geological Society Special Publication, 29, 91-105. https://doi.org/10.1144/GSL.SP.1987.029.01.09

Underhill, J.R. 1991a. Implications of Mesozoic - Recent basin development in the western Inner Moray Firth, UK. Marine and Petroleum Geology, 8, 359-369. https://doi.org/10.1016/0264-8172(91)90089-J

Underhill, J.R. 1991b. Controls on Late Jurassic seismic sequences, Inner Moray Firth, UK North Sea: A critical test of a key segment of Exxon's original global cycle chart. Basin Research, 3(2), 79–98. https://doi.org/10.1111/j.1365-2117.1991.tb00141.x

Underhill, J.R. and Brodie, J.A. 1993. Structural geology of Easter Ross, Scotland: implications for movement on the Great Glen fault zone. Journal of the Geological Society, 150(3), 515–527. https://doi.org/10.1144/gsjgs.150.3.0515

Underhill, J.R. and Partington, M.A. 1993. Jurassic thermal doming and deflation: the sequence stratigraphic evidence. In: Parker, J.R. (ed.): Petroleum Geology of North-West Europe: Proceedings of the 4th Conference, 337-345.

Underhill, J.R. 1994. Discussion on palaeoecology and sedimentology across a Jurassic fault scarp, NE Scotland. Journal of the Geological Society, 151(4), 729–731. https://doi.org/10.1144/gsjgs.151.4.0729

Utley, T.A.G. 2020. Basement-Cover Relationships and Regional Structure in the Transtensional Orcadian Basin, PhD thesis, Durham University.

Venkat-Ramani, M. and Tikoff, B. 2002. Physical models of transtensional folding. Geology, 30(6), 523–526. https://doi.org/10.1130/0091-7613(2002)030<0523:PMOTF>2.0.CO;2

Vermeesch, P. 2018. IsoplotR: a free and open toolbox for geochronology. Geoscience Frontiers, 9, 1479-1493. https://doi.org/10.1016/j.gsf.2018.04.001

von Hagke, C., Kettermann, M., Bitsch, N., Bücken, D., Weismüller, C. and Urai, J.L. 2019. The Effect of Obliquity of Slip in 15 Normal Faults on Distribution of Open Fractures. Frontiers in Earth Science, 7(18). https://doi.org/10.3389/feart.2019.00018

Walker, A.D. 1973. The age of the Cuttie's Hillock sandstone (Permo-Triassic) of the Elgin area. Scottish Journal of Geology, 9, 177–183. http://doi.org/10.1144/sjg09030177

Wallace, R.E. 1951. Geometry of shearing stress and relation to faulting. The Journal of Geology, 59(2), 118-130.

Watts, L.M., Holdsworth, R.E., Sleight, J.A., Strachan, R.A. and Smith, S.A.F. 2007. The movement history and fault rock evolution of a reactivated crustal-scale strike-slip fault: the Walls Boundary Fault Zone, Shetland. Journal of the Geological Society, 164(5), 1037-1058. https://doi.org/10.1144/0016-76492006-156

Weismüller, C., Urai, J.L., Kettermann, M., von Hagke, C. and Reicherter, K. 2019. Structure of massively dilatant faults in Iceland: lessons learned from high-resolution unmanned aerial vehicle data. Solid Earth, 10, 1757-1784. https://doi.org/10.5194/se-10-1757-2019

Whiteman, A., Naylor, D., Pegrum, R. and Rees, G. 1975. North Sea Troughs and Plate Tectonics. Tectonophysics, 26, 39–54.

Williams, J.D.O., Fellgett, M.W. and Quinn, M.F. 2016. Carbon dioxide storage in the Captain Sandstone aquifer: determination of in situ stresses and fault-stability analysis. Petroleum Geoscience, 22(3), 211–222. https://doi.org/10.1144/petgeo2016-036

Wilson, R.W., Mccaffrey, K.J.W., Holdsworth, R.E., Imber, J., Jones, R.R., Welbon, A.I.F. and Roberts, D. 2006. Complex fault patterns, transtension and structural segmentation of the Lofoten Ridge, Norwegian margin: Using digital mapping to link onshore and offshore geology. Tectonics, 25(4). http://doi.org/10.1029/2005TC001895

Wilson R.W., Holdsworth R.E., Wild L.E., McCaffrey K.J.W., England, R.W, Imber, J. and Strachan, R.A. 2010. Basement influenced rifting and basin

development: a reappraisal of post-Caledonian faulting patterns from the North Coast Transfer Zone, Scotland. Geological Society, London, Special Publications, 335, 795-826. https://doi.org/10.1144/SP335.32

Woodcock, N.H. and Strachan, R.A. 2012. Geological history of Britain and Ireland. John Wiley & Sons, Ltd. http://doi.org/10.1002/9781118274064

Worden, R.H., Allen, M.J., Faulkner, D.R., Utley, J.E.P., Bond, C.E., Alcalde, J., Heinemann, N., Haszeldine, R.S., Mackay, E. and Ghanbari, S. 2020. Lower Cretaceous Rodby and Palaeocene Lista Shales: Characterisation and Comparison of Top-Seal Mudstones at Two Planned CCS Sites, Offshore UK. Minerals, 10, 691. https://doi.org/10.3390/min10080691

Zanella, E. and Coward, M.P. 2003. Structural Framework. In: Evans, D., Graham, C., Armour, A., and Bathurst, P. (eds) The Millennium Atlas: Petroleum Geology of the Central and Northern North Sea. Geological Society of London, 45-59.

Zanella, E., Coward, M.P., and McGrandle, A. 2003. Crustal structure. In: Evans, D., Graham, C., Armour, A., and Bathurst, P. (eds) The Millennium Atlas: Petroleum Geology of the Central and Northern North Sea. Geological Society of London, 35–42.